SYNTHESIS AND CHARACTERIZATION OF MESOPOROUS METAL SULFIDE AND METAL SELENIDE THIN FILMS USING LIQUID CRYSTALLINE MESOPHASES

A DISSERTATION SUBMITTED TO

THE DEPARTMENT OF CHEMISTRY

AND THE GRADUATE SCHOOL OF ENGINEERING AND SCIENCE

OF BILKENT UNIVERSITY

IN PARTIAL FULFILLMENT OF THE REQUIREMENTS

FOR THE DEGREE OF

DOCTOR OF PHILOSOPHY

By

YURDANUR TÜRKER

January 2012

I certify that I have read this thesis and have found that it is fully adequate, in scope and in quality, as a thesis for the degree of Doctor of Philosophy.

Prof. Dr. Ömer Dağ
Supervisor

I certify that I have read this thesis and have found that it is fully adequate, in scope and in quality, as a thesis for the degree of Doctor of Philosophy.

Prof. Dr. Saim Özkar
Examining Committee Member

I certify that I have read this thesis and have found that it is fully adequate, in scope and in quality, as a thesis for the degree of Doctor of Philosophy.

Assoc. Prof. Dr. Margarita Kantcheva
Examining Committee Member

I certify that I have read this thesis and have found that it is fully adequate, in scope and in quality, as a thesis for the degree of Doctor of Philosophy.

Prof. Dr. Nihal Aydoğan
Examining Committee Member

I certify that I have read this thesis and have found that it is fully adequate, in scope and in quality, as a thesis for the degree of Doctor of Philosophy.

Assist. Prof. Dr. Emrah Özensoy
Examining Committee Member

Approval of the Graduate School of Engineering and Science

Prof. Dr. Levent Onural
Director of the Graduate School

ABSTRACT

SYNTHESIS AND CHARACTERIZATION OF MESOPOROUS METAL SULFIDE AND METAL SELENIDE THIN FILMS USING LIQUID CRYSTALLINE MESOPHASES

Yurdanur Türker

Ph.D., Department of Chemistry

Supervisor: Prof. Dr. Ömer Dağ

January, 2012

In this thesis, synthesis of the mesoporous CdS and CdSe by using of liquid crystalline templating (LCT) approach has been investigated. In the first part of the thesis, the thermal and structural behavior of the $[Cd(H_2O)_4](NO_3)_2$/surfactant (P85 = $((PEO)_{26}(PPO)_{40}(PEO)_{26})$) binary lyotropic liquid crystalline (LLC) systems have been investigated towards synthesis of the mesoporous cadmium sulfide, CdS, or cadmium selenide (CdSe) directly from the mesostructured CdS (or CdSe) thin films. However, the mesostructured CdS/P85 films (at low salt concentrations), which were obtained by reacting $[Cd(H_2O)_4](NO_3)_2$/P85 LLC thin films under H_2S atmosphere, are not stable to calcination process and always produced bulk CdO and CdS domains over the thin films. More metal ion containing $[Cd(H_2O)_4](NO_3)_2$-$C_{12}EO_{10}$-CTAB mesostructured films produced vast amount of HNO_3 under the H_2S atmosphere and caused decomposition of CdS back to their nitrates.

To overcome above problems, a polymerizing agent, such as titania or silica precursors have been added to salt/surfactant LLC mesophase. Both titania and

silica overcame the collapse of the mesophase by rigidifying the structure into mesostructured solid and also by providing stability for a thermal removal of nitrates from the medium. For this investigation, both $[Cd(H_2O)_4](NO_3)_2$ and $[Zn(H_2O)_6](NO_3)_2$ salts and P123 ($(PEO)_{20}(PPO)_{70}(PEO)_{20}$) and $C_{12}EO_{10}$-CTAB couple have been used.

Well-ordered mesostructured Cd(II) titania films have been obtained up to 15.0 Cd(II)/P123 mole ratio for a 60 mole ratio of Ti(IV)/P123 by spin or dip coating of a mixture of 1-butanol-$[Cd(H_2O)_4](NO_3)_2$-P123-HNO_3-$Ti(OC_4H_9)_4$. Exposing the mesostructured Cd(II)-TiO_2 films to H_2Se under a N_2 atmosphere gave stable CdSe nanoparticles in the channels of the mesostructured rigid titania walls up to 25 mole % Cd(II)/Ti(IV). To further increase the metal ion (Cd(II) and Zn(II)) content in the structure, the $C_{12}EO_{10}$-CTAB-salt mesophase has been employed. The two surfactant-salt systems, in the presence of a titania precursor, produced sponge like mesoporous $CdTiO_3$ and Zn_2TiO_4 films up to a mole percent of 57 and 86, respectively, upon calcination. Exposing the mesoporous $CdTiO_3$ to H_2S or H_2Se atmosphere at RT produced homogeneously distributed CdS or CdSe nanocrystallites on the nanocrystalline TiO_2 pore walls, respectively. The reaction of mesoporous Zn_2TiO_4 with H_2Se produced stable ZnSe nanocrystallites on the nanocrystalline TiO_2 pore walls. The conversion of titania from $CdTiO_3$ to an anatase and brookite phase under H_2S and H_2Se atmosphere, respectively, and from Zn_2TiO_4 to a rutile phase under H_2Se were observed for the first time.

Adding a silica precursor to the two surfactants ($C_{12}EO_{10}$-CTAB)-salt mesophase produced mesostructured salted-silica, and its calcination produced sponge-like mesoporous silica-metal oxide (dumped meso-SiO_2-CdO and meso-SiO_2-ZnO) thin films. Up to ~100 % and ~50 % surface coverage could be achieved by CdO and ZnO as nano-islands over the SiO_2 pore walls. Exposing the mesoporous SiO_2-CdO and SiO_2-ZnO thin film precursors to H_2S and H_2Se at RT enabled the synthesis of mesoporous SiO_2-CdS, SiO_2-CdSe, SiO_2-ZnS, and SiO_2-ZnSe thin films. The MS or MSe nanoflakes could homogenously cover the pore walls of mesoporous silica by retaining the pore morphology of the MO precursors. The H_2S and H_2Se reactions are slow and can be monitored using UV-

Vis absorption spectroscopy and EDS to elucidate the reaction mechanism and kinetics. These data showed that the reaction starts from the top surface of the MO domains and proceeds until Si-O-M bond break. Finally, the SiO_2 walls were removed from the meso-SiO_2-CdS and meso-SiO_2-CdSe films through etching in a dilute HF solution to produce mesoporous CdS (meso-CdS) and mesoporous CdSe (meso-CdSe). Surface of the meso-CdS has been modified using PEI (polyethyleneimine) and photoluminescent meso-CdS were obtained.

Keywords: Mesoporous CdS, Mesoporous CdSe, Liquid Crystal Templating, Evaporation Induced Self-Assembly, Mesoporous Titania, Mesoporous Silica

ÖZET

SIVI KRİSTAL MEZOFAZLARI KULLANARAK MEZOGÖZENEKLİ METAL SÜLFÜR VE METAL SELENÜR İNCE FİLM SENTEZİ VE KARAKTERİZASYONU

Yurdanur Türker

Doktora, Kimya Bölümü

Tez Yöneticisi: Prof. Dr. Ömer Dağ

Ocak, 2012

Bu tez çalışmasında, mezo gözenekli CdS ve CdSe sentezi sıvı kristal kalıplama (SKK) yaklaşımı kullanılarak araştırılmıştır. Tezin ilk bölümünde, $[Cd(H_2O)_4](NO_3)_2$/yüzey aktif (P85 = $((PEO)_{26}(PPO)_{40}(PEO)_{26})$) ikili liyotropik sıvı kristal (LSK) sistemleri termal ve yapısal davranışları, mezo gözenekli CdS ve CdSe'ların mezoyapılı kadmiyum sülfür (CdS) ya da kadmiyum selenür (CdSe) ince filmlerinden doğrudan sentezi yönünde araştırılmıştır. Ancak, $[Cd(H_2O)_4](NO_3)_2$/P85 LSK ince filmlerinin H_2S atmosferi altında tepkimesiyle elde edilmiş olan mezoyapılı CdS/P85 filmler (düşük tuz konsantrasyonlarında) ısıtmaya kararlı değildir ve filmler üzerinde her zaman külçe CdO ve CdS üretmiştir. Daha yüksek metal iyonları içeren $[Cd(H_2O)_4](NO_3)_2$-$C_{12}EO_{10}$-CTAB mezoyapılı filmleri H_2S atmosferi altında büyük miktarda HNO_3 üretmiştir ve CdS'lerin nitratlarına geri dönüşmesine neden olmuştur.

Yukarıda bahsedilen sorunların üstesinden gelmek için polimerleşebilen titanyum veya silika gibi öncüler, tuz/yüzey aktif SKK mezofazına eklenmiştir. Titanyumdioksit ve silikanın ikisi de yapıyı mezoyapılı katı halinde sertleştirerek ve nitratların ortamdan termal yolla uzaklaştırılması esnasında kararlılık sağlayarak, mezoyapının çökmesini engellemiştir. Bu araştırmada,

$[Cd(H_2O)_4](NO_3)_2$ ve $[Zn(H_2O)_6](NO_3)_2$ tuzları ve P123 ($(PEO)_{20}(PPO)_{70}(PEO)_{20}$) ve $C_{12}EO_{10}$-CTAB çifti kullanılmıştır.

Oldukça düzenli yapılı Cd(II) titanyum filmleri Ti(IV)/P123 mol oranı 60 ve Cd(II)/P123 mol oranı 15.0 a kadar, 1-bütanol-$[Cd(H_2O)_4](NO_3)_2$-P123-HNO_3-$Ti(OC_4H_9)_4$ karışımının döndürmeli veya daldırmalı kaplamasıyla elde edilmiştir. Mezoyapılı Cd(II)-TiO_2 filmleri N_2 altında H_2Se gazına maruz bırakmak mezoyapılı katı titanyumdioksit kanallarında % 25 Cd(II)/Ti(IV) mol oranına kadar kararlı CdSe nanoparçacıklarını vermiştir. Mezoyapı içerisindeki metal iyon (Cd(II) ve Zn(II)) miktarını arttırmak için, $C_{12}EO_{10}$-CTAB-tuz fazları kullanılmıştır. Titanyumdioksit öncüsü varlığında ikili yüzey aktif-tuz sistemlerinin yakılması 57 Cd(II)/Ti(IV) ve 86 Zn(II)/Ti(IV) mol yüzdelerine kadar süngerimsi mezogözenekli $CdTiO_3$ ve Zn_2TiO_4 filmleri üretmiştir. Mezogözenekli $CdTiO_3$ ve Zn_2TiO_4 filmlerini H_2S veya H_2Se atmosferine oda sıcaklığında maruz bırakmak nanokristal TiO_2 gözenek duvarlarında homojen olarak dağılmış, sırasıyla, CdS veya CdSe nanokristallerini üretmiştir. Mezogözenekli Zn_2TiO_4 H_2Se reaksiyonu nanokristal TiO_2 gözenek duvarlarında kararlı ZnSe nanokristallerini üretmiştir. H_2S ve H_2Se atmosferi altında $CdTiO_3$, sırasıyla, anataz ve brokayt faza ve H_2Se atmosferi altında Zn_2TiO_4 rutayl faza dönüşümü ilk kez gözlendi.

İkili yüzey aktif ($C_{12}EO_{10}$-CTAB)-tuz mezoyapısına silika öncüsü eklemek mezoyapılı tuzlu-silika, ve yakılması süngerimsi mezogözenekli silika-metal oksit (mezo-SiO_2-CdO ve mezo-SiO_2-ZnO) ince filmlerini üretmiştir. Yaklaşık yüzde yüz ve yüzde elli oranlarına kadar, SiO_2 gözenek duvarları üzerinde CdO ve ZnO nano-adalarıyla kaplanabilir. Mezogözenekli SiO_2-CdO ve SiO_2-ZnO ince filmlerini oda sıcaklığında H_2S ve H_2Se atmosferine maruz bırakmak mezogözenekli SiO_2-CdS, SiO_2-CdSe, SiO_2-ZnS, ve SiO_2-ZnSe ince filmlerin sentezini sağlamıştır. MS veya MSe nanoplakaları mezogözenekli silika gözenek duvarlarını, MO öncülerinin gözenek morfolojilerini koruyarak, homojen kaplayabilir. H_2S ve H_2Se reaksiyonları yavaştır ve reaksiyon mekanizması ve kinetiği UV-Vis soğurma spektroskopisi ve EDS kullanılarak izlenebilir. Bu veriler, tepkimenin MO nanoplakalarının üst yüzeyinden başladığını ve Si-O-M

bağının kırılmasına kadar devam ettiğini göstermiştir. Son olarak, mezo-SiO_2-CdS ve mezo-SiO_2-CdSe filmlerin SiO_2 duvarları, mezogözenekli CdS (mezo-CdS) ve mezogözenekli CdSe (mezo-CdSe) üretmek için seyreltilmiş HF çözeltisinde aşındırma yoluyla uzaklaştırılmıştır. Mezo-CdS yüzeyi PEI (polietilenimin) kullanılarak modifiye edilerek fotonlu ışıma yapabilen mezo-CdS elde edilmiştir.

Anahtar Kelimeler: Mezogözenekli CdS, Mezogözenekli CdSe, Sıvı Kristal Kalıplama, Buharlaşma İndüklenmiş Kendiliğinden Oluşma, Mezogözenekli Titanyumdioksit, Mezogözenekli Silika

ACKNOWLEDGEMENTS

First and foremost, I want to thank Prof. Dr. Ömer Dağ for his excellent supervision and support during my Ph.D. studies. I appreciate all his contributions of time and ideas to make my Ph.D. experience productive. He has taught me, both consciously and unconsciously, how important is to be a patient and open-minded for doing a fundamental research in chemistry.

I am also grateful to my committee members, Prof. Dr. Saim Özkar and Assoc. Prof. Dr. Margarita Kantcheva, for their time and helpful comments to my thesis.

I would like to thank Cüneyt Karakaya and Halil Okur for their corporation in the research and sincere friendships. I also would like to thank present and past members of Department of Chemistry for their friendships.

I would like to thank to The Scientific & Technological Research Council of Turkey (TÜBİTAK) for the financial support during my studies.

I also wish to thank my family, who saw little of me during the years of this study, for their understanding and support. Last but of course not least, I would like to thank my love Serkan, for his never ending love, encouragement, and patience.

TABLE OF CONTENTS

LIST OF TABLES

LIST OF FIGURES

CHAPTER I

INTRODUCTION

1.1 Mesoporous Inorganic Materials

Mesoporous materials have been defined as porous inorganic solids with pore diameters in the range of 20 to 500 Å.[1] M41S family of mesoporous silica (cubic MCM-48, hexagonal MCM-41, and lamellar MCM-50 which were discovered by Kresge et. al.[2]), aerogels, and pillared clays are the known examples of mesoporous materials.[3] Presence of internal channels and cavities in mesoporous materials provide high surface areas (> 1000 m^2g^{-1}). Those internal channels allow the molecules to diffuse through large cavities in the mesoporous materials. Therefore, the mesoporous materials are advantageous to be used in catalysis, gas sensing, sorption, photovoltaics, and optics.[4] These important application fields made researchers to work to design and synthesize numerous types of mesoporous materials.

The first periodic mesoporous material (PMM) has been synthesized by using surfactant as a template by Kresge et. al. in Mobil Oil Company in 1992.[2] The former efforts produced such porous materials, which in fact cannot be classified as mesoporous materials. For example, cacoxenite, a natural ferroaluminophosphate,[5] and $AlPO_4$-8, a synthetic aluminaphosphate molecular sieve,[6] have extremely small pore sizes between 8 and 13 Å. However, the M41S mesoporous silica materials with pore sizes between 15 and 120 Å, have been an attractive topic last two decades.[2] The most famous members of this family are the MCM-41 with a 2D hexagonal mesoorder with a channel structure, MCM-48 with a cubic structure, and a MCM-50 with a lamellar structure. Since the PMMs were synthesized in a facile way by means of surfactant templating, and through a liquid crystalline to solid transformation mechanism, the importance of the liquid crystal templating has been realized for the first time.

Later in 1995, Attard et. al.[7] introduced the true liquid crystalline templating (TLCT) approach for the synthesis of mesoporous silica. Non-ionic surfactants, ($C_nH_{2n+1}(OCH_2CH_2)_mOH$), C_nEO_m, have been used in their LC phase in which the silica condensation takes place. In 1996, Stucky` s group found that nonionic surfactants and pluronics (triblock poly(ethylene oxide)-poly(propylene oxide)-poly(ethylene oxide) ($PEO_n$-$PPO_m$-$PEO_n$) polymers) can be used to synthesize the mesoporous silica with larger pores with a diameter of 20-300 Å range. Ozin` s group made the first ordered thin films of silica (0.2 – 1 μm) on a mica substrate.[8] These were key steps in making those materials desirable for use in high technology.

Another important step was the use of the mesoporous materials as templates and host for various nanoparticles. The SiGe, Si and Ag nanoparticles that have been loaded into the mesoporous silica films are some examples in this wide area of research.[9-11] Modification of the pore walls with functional groups enabled to use the channels like a "nano-chemistry lab" (this topic will be discussed later under separate title, see later). Recently, synthesis of stable hydrogen functionalized mesoporous silica, called mesoporous hydridosilica (meso-$HSiO_{1.5}$), by using triethoxysilane precursor ($HSi(OEt)_3$) as a silica source through templating method has been announced.[12] A thermal treatment of the mesoporous hydridosilica over 300 °C has enabled to produce a photoluminescent (PL) periodic mesoporous nanocrystalline silicon-silica composite (meso-ncSi/SiO_2).[12] Furthermore, it has been shown that the meso-$HSiO_{1.5}$ acts as both a host and a reducing agent for Ag(I) ions in an aqueous medium at RT to create PL Ag(0) molecular nanoclusters in its pore walls, and plasmonic Ag(0) nanoparticles on the pore surfaces.[13] These examples show that the channels and cavities in mesoporous materials can be used as nano-reactors to obtain advance materials for new applications in various fields, such as catalysis, optics, electronics, and photonics, drug delivery, energy, etc.

1.2 Liquid Crystalline Templating (LCT) Approach

Conventionally, known three phases of matter are solids, liquids and gases. The phase is defined according to strength of the forces (intra- and inter-molecular) among the molecules or atom or ionic components of the matter. Those forces define the orientation and location of the molecules or atoms or ions in space, where the physical properties of the materials change accordingly. In molecular solids, if the forces between the molecules are strong enough, then the molecules have to occupy a certain place, lattice points, having a positional order and identify the solid state of matter. The molecules, atoms or ions in the solid state have only positional order in the amorphous phases, while they present positional and orientational order in the crystalline phases. When the intermolecular forces are not strong enough to put the molecules at a certain place, molecules lose their positional and orientational order, and transform into a liquid phase. The further weakening of intermolecular forces causes the material to transform into a gas phase.

Moreover, there is a fourth state of matter, called liquid crystalline (LC) state. In the liquid crystalline state, the molecules or aggregates of molecules have some orientational order like in solids but do not have positional order in all directions like in liquids.[14] Figure 1.1 shows schematically the positional and orientational order in solids, liquid crystals (LC), and liquids.

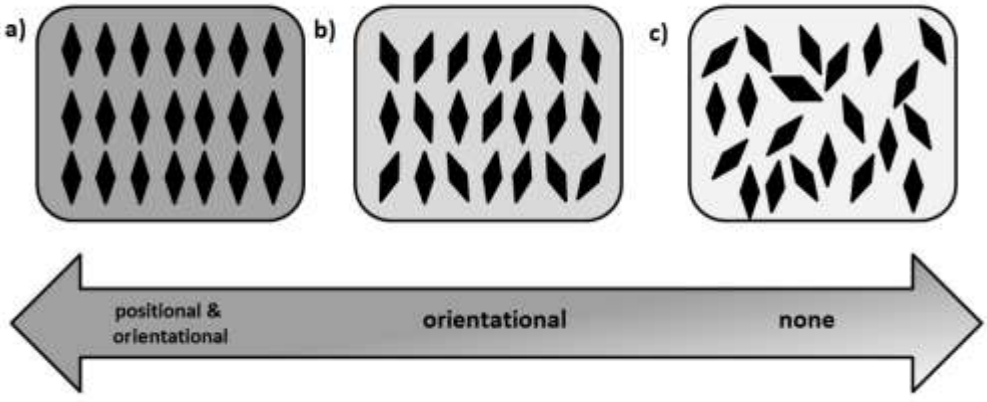

Figure 1.1 Illustration of positional and orientational order in a) solids, b) liquid crystals, and c) liquids.

The LC phase can be divided into two main groups: the thermotropic liquid crystals and lyotropic liquid crystals (LLC). The LC phase changes by a change in temperature in the *thermotropic liquid crystals*. However, *LLC phase* forms in the presence of a second component, and concentration of the components determine the phase change more effectively than temperature.[14, 15] The LLC mesophase will be further discussed later due to its importance in this thesis.

In principle, the LLC mesophase forms in an appropriate mixture of an amphiphilic molecule in a solvent.[14-16] Therefore, structure of the LLC phase is determined by the concentration of the amphiphilic molecules. Amphiphilic molecule consists of both hydrophilic (water affinity) and hydrophobic (oil affinity) parts. Existence of these parts with opposite characters leads to aggregation of the molecules into small nanoaggregates, micelles.

Surfactants are the amphiphilic molecules, which can self-assemble in a proper solvent through the interactions of hydrophilic and hydrophobic ends into micelles and LLC mesophases. Depending on the charge of their hydrophilic head groups, the surfactants can be mainly classified as ionic or non-ionic. Examples to nonionic surfactants are pluronics (triblock co-polymers of poly(ethylene oxide)-poly(propylene oxide)-poly(ethylene oxide) $(PEO)_n(PPO)_m(PEO)_n$) and oligo(ethylene oxide), $(CH_3(CH_2)_n(PEO)_m)$. The ionic amphiphilic surfactants are divided into two groups as anionic, having negative charge, and cationic, having positive charge on their head groups. (See Figure 1.)

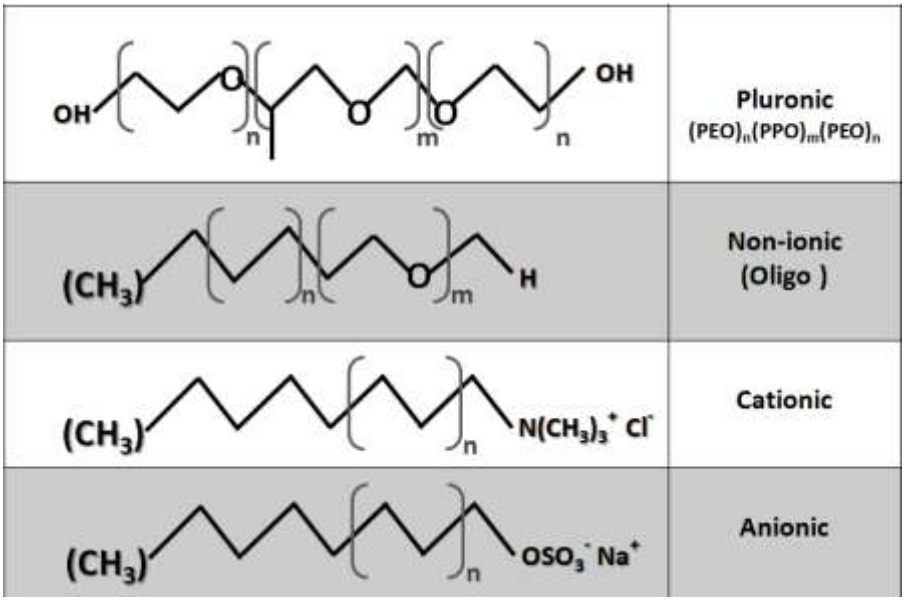

Figure 1.2 Chemical structures of various types of surfactants.

Formation of LC phases is based on a *self-assembly* process, which is a spontaneous organization process of materials in a medium through only noncovalent interactions, such as hydrogen bonding, dipole-dipole, ion-dipole, and van der Waals forces. The molecules, which can self-assemble, have inherent potential to organize themselves into well-defined supramolecular structures. Typical amphiphilic molecules are surfactants. They are called surfactants due to the active behavior of their surfaces. That means surfactants always tend to reduce surface tension of the solvent by minimizing the interfacial interaction. Therefore, when a certain concentration of surfactant is put in a polar solvent like water, they start assembling themselves into nano-spheres by directing polar head groups outside, into the solvent (usually water) and hydrophobic tail towards the center of the sphere, forming *micelles*. In another words, the main driving forces to assemble surfactants into micelles are the hydrophobic attraction and hydrophilic repulsions. The hydrophilic parts form hydrogen bonding with water molecules and so, do not prefer to stay as close as hydrophobic parts.[17, 18] As already emphasized, a certain surfactant concentration, called c*ritical micelle concentration (CMC),* has to be reached for this assembly.[14, 18, 19] Further increase in the surfactant concentration above CMC leads to self-organization of the micelles into well-defined lamellar, hexagonal and cubic mesophases, LLC

phases. Figure 1.3 shows the schematic illustration of micelles and general LLC mesophases in an aqueous medium.

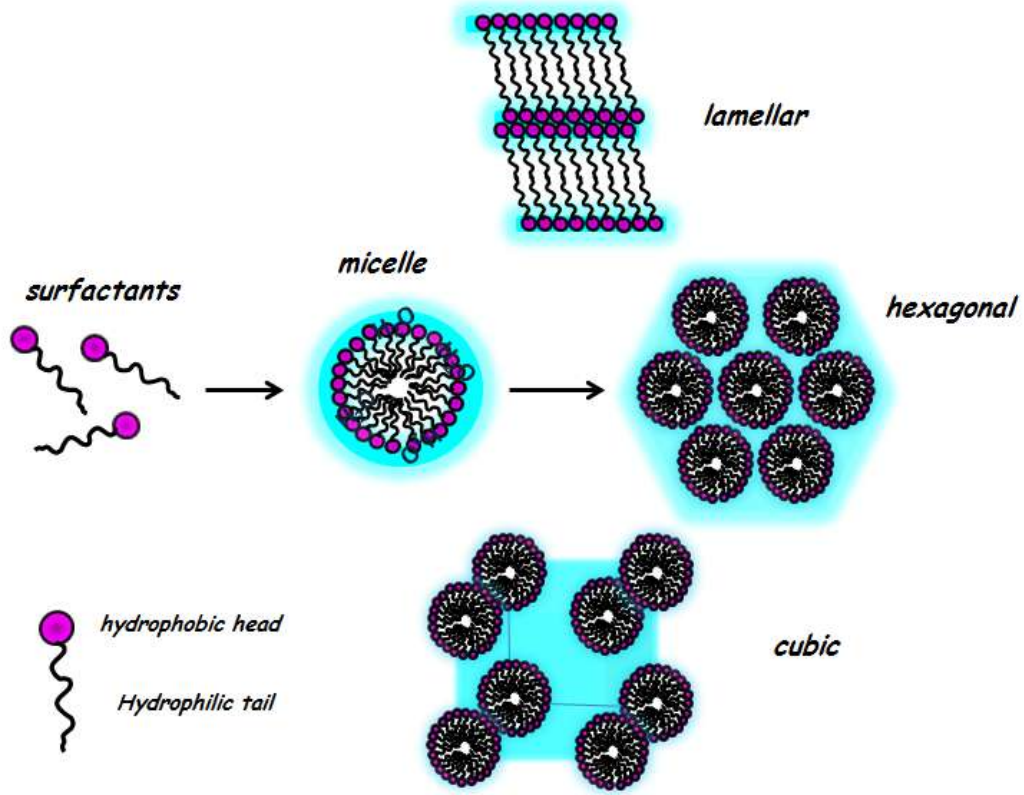

Figure 1.3 Frequently observed LLC mesophases in H_2O.

Since the intermolecular forces direct the self-assembly process, and these forces depend on the shape and size of the molecules interacting, the CMC is different for each surfactant. Therefore, every surfactant has their own phase diagram, depending on the change in the temperature and concentration of the solution. Figure 1.4 shows a typical phase diagram of $C_{16}H_{33}N(CH_3)_3Br$ (CTAB) in water. The phase diagram shows different mesostructures, depending on the temperature and concentration of CTAB in water.

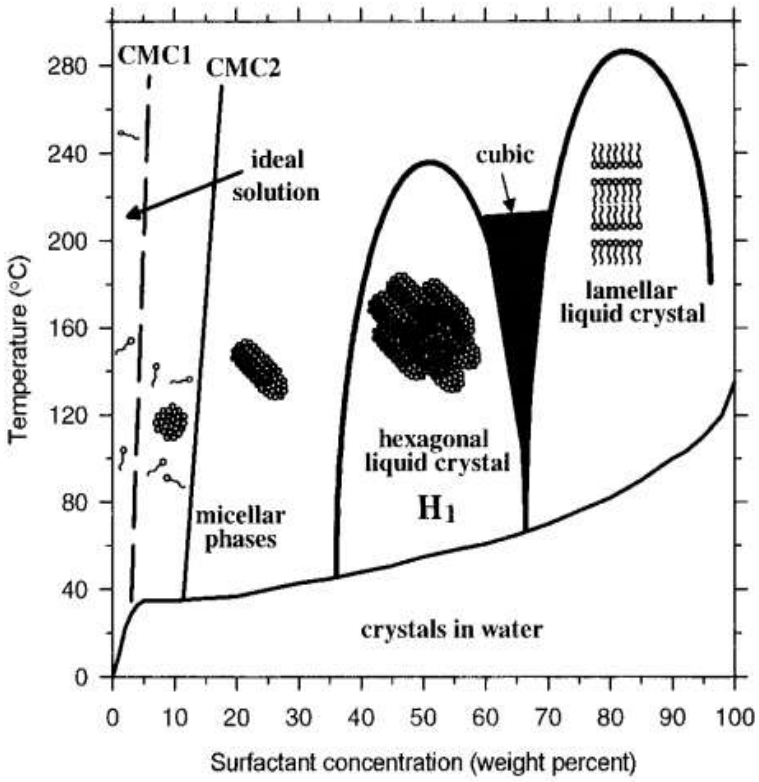

Figure 1.4[1] The phase diagram of CTAB, a cationic surfactant, in water. (CMC1: critical micelle concentration for spherical micelles, CMC2: critical micelle concentration for rod-like micelles).[19]

The phase diagrams have been widely employed to investigate the synthesis of the mesoporous materials. For instance, in 1995, Attard et. al.[7] showed that mesoporous silica could be obtained by the LCT approach by using the already published phase diagram of non-ionic surfactant (C_nEO_m) and water.[20] The tetramethoxysilane (TMOS), as a silica source, was added into the already formed hexagonal mesophase of 50:50 wt% C_nEO_m:water. That means, the silica condensation took place in the hydrophilic domains of a pre-formed LLC mesophase. Using the phase diagrams of surfactants, mesostructured/mesoporous metals and metal oxides have been synthesized using LCT method. The well characterized mesoporous platinum[21], tin[22, 23] and their alloys[24] were synthesized by Attard` s group. Kuroda` s group obtained the mesostructured Ni-Co alloys[25]

[1] Reprinted from Chemistry of Materials, Vol. 8, Raman, N. K.; Anderson, M. T. and Brinker, C. J. "Template-Based Approaches to the Preparation of Amorphous, Nanoporous Silicas." 1682-1701 , (1996), with permission from ACS.

and mesoporous Ni nanoparticles[26] from a LLC mesophase through electroless deposition technique. Stucky` s group showed the synthesis of numerous metal oxides with ordered large pores such as $TiO_2$, $WO_3$, $SnO_2$, $Al_2O_3$, $Nb_2O_5$, $ZrO_2$, $Ta_2O_5$, $HfO_2$, $ZrTiO_4$, $Al_2TiO_5$, and $SiTiO_4$ by the LCT method.[27] Stupp` s group obtained the nanostructured/mesostructured semiconductors, such as ZnS, CdS and CdSe by the LCT approach.[28, 29]

However, in all of these studies that use salt-water-surfactant LLC phases, the metal ion concentrations were very low, around 0.1 M in LLC medium. Therefore, these materials have only been synthesized in the form of very fine, ultra small powders. In presence of such a small amount of salt, in the medium, it is not easy to obtain mesostructured or mesoporous metals or metal oxides or metal chalcogenide films. Note also that the above LLC mesophases are not stable in the presence of high metal salt concentration in the medium. The reason is that in all of these procedures, the LLC phase was used as a cast medium for the inorganic condensation. That means, the LC phase was formed using water as a second component, and the metal salt was added as a third component into the already formed LLC mesophase (ternary system). Since the metal salt does not contribute to formation of the mesostructure, the ternary systems are limited to the solubility of salt in the LC phase. For that reason, the ternary system fails at high metal salt concentrations. Moreover, the ternary mesophases collapse upon evaporation of water from the medium. Therefore, these systems had to be improved further to be used in the synthesis of the mesoporous materials.

1.3 Transition Metal Salt-Surfactant LLC Mesophases

The low metal ion concentration problem in the LLC mesophase has been overcome by Dag` s group in 2001.[30] A new LLC mesophase that has been reported was directly formed by a surfactant and transition metal aqua complex salt.[30] In this assembly process, the coordinated water molecules of a transition metal salt (TMS) mediate the formation of LC phase as in the same way as free water molecules through hydrogen bonding, ($M–OH_2$ ----$(OCH_2CH_2)_n$-R,[30-33] and other weak interactions, schematically shown in Figure 1.5. In the new system, the

TMS to surfactant mole ratio could be increased up to 3.2 for an oligo(ethylene type) surfactant. Many LLC mesophases have been identified for various types of oligo(ethylene oxide) and pluronic type non-ionic surfactants in our group.[34-37]

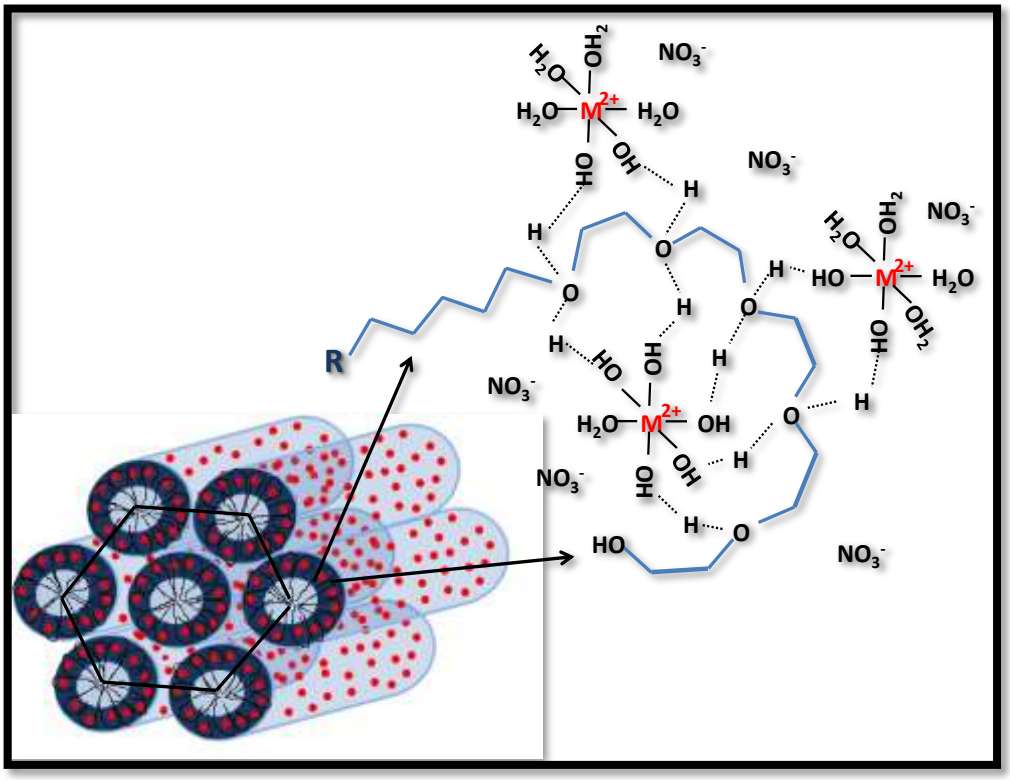

Figure 1.5 Illustration of the structure of LC phase formed directly using TMS as a second component.

Furthermore, using this new LLC system, first mesostructured $Cd_{1-x}Zn_xS$ thin films, where x can be controlled between 0.0 and 1.0 have been synthesized by our group.[37] A salt/pluronic (P85 = poly(ethylene oxide) – poly(propylene oxide) – poly(ethylene oxide) ($PEO_{26}PPO_{40}PEO_{26}$)) mole ratio could be as high as 11.0 in the new LLC phase. Furthermore, these mesophases can be dissolved in a solvent, such as water, ethanol or acetone, and spin or dip coated over a substrate as a LLC thin film that forms upon evaporation of the solvent during the coating process. The ordered LC mesophases form in the $[Cd(H_2O)_4](NO_3)_2$:P85 mole ratio range of 3:1 to 11:1 with a 3D hexagonal structure and *$P6_3/mmc$* space group having unit cell parameters of ***a*** = 99.5 Å and ***c*** = 162.5 Å with a ***c/a*** ratio of 1.633. The mesostructured LLC thin films can be exposed to H_2S gas to obtain mesostructured MS thin films, as shown in Figure 1.6. The high metal ion content

provided some stability to the resulting mesostructured MS thin films.[37] Well homogenized LC mesophases produce cracked, mesostructured films upon completion of the H_2S reaction. The mesostructured CdS thin films that consist of 4.3 nm CdS nanoparticles emit orange light under UV irradiation.

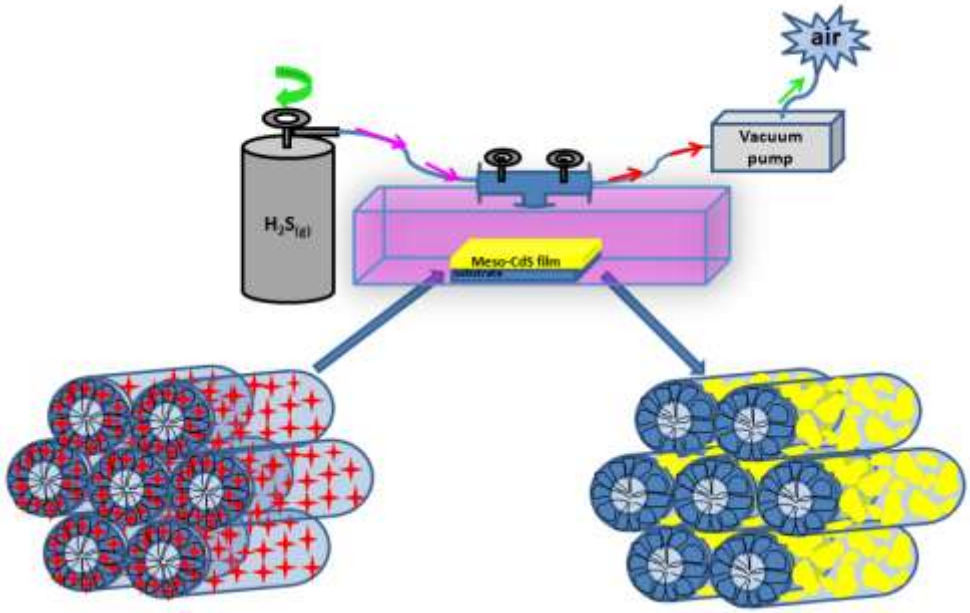

Figure 1.6 Scheme of the H_2S reaction of mesostructured LC phase of $[Cd(H_2O)_4](NO_3)_2$/P85.

However, the metal ion content is still low; therefore the films undergo phase separation in time through the diffusion of excess surfactant molecules out of the mesostructured films. The schematic illustration of the mesostructured MS/MSe film is given in Figure 1.7 (A). As shown in Figure 1.7 (A), the MS nanoparticles are not in contact, and so they can`t form stable inorganic walls around the surfactant domains in the mesostructures. Therefore, the inevitable result is the slow phase separation all over the samples in time due to the release of the excess surfactant molecules out of the mesostructured films.

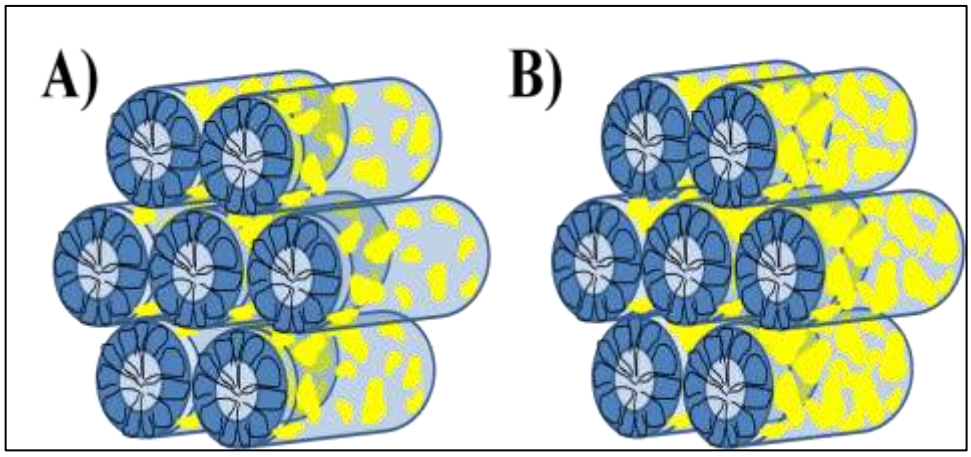

Figure 1.7 Illustration of the mesostructured MS in case of (A) insufficient metal ion density, and (B) high metal ion density, rigid structure.

On the other hand, it is well known that stable and ordered mesostructured silica films can be obtained at 0.6-0.7 Si/EO mole ratios, (corresponding to inorganic/surfactant mole ratio of 7.0 for $C_{12}EO_{10}$ and 30-35 for P85)[38, 39] Therefore, 11.0 Cd(II)/P85 mole ratio is still low compared to Si/EO mole ratio in a stable mesostructured silica film. Therefore, the metal ion concentration has to be increased to 0.6 salt for each EO in our LC systems to achieve stability over phase separation and possibly for a calcination process to obtain stable mesoporous MS or metal selenide, (MSe), see Figure 1.7 (B). However, the solubility limit of TMS in the hydrophilic domains of the LLC phase restricts the TMS concentration to reach to those high amounts.

To overcome the limitations of the TMS:surfactant LLC mesophase, a mixture of a charged surfactant (such as CTAB or sodiumdodecyl sulfate, $C_{12}H_{25}OSO_3Na$, (SDS)) and a non-ionic oligo(ethylene oxide) type surfactant (or Pluronic) has been investigated in detail for the formation of LLC mesophases.[40-45] In the mixtures of two or three surfactants, the assembly is directed through the hydrophobic interactions between alkyl chains of the surfactants and hydration of the alkyl tail-EO interface in the presence of a charged head group. That means, both the hydrophobicity of the core and the hydrophilicity of the EO shell are strengthened upon those interactions. Combining this knowledge with our LC system improved the metal ion to $C_{12}EO_{10}$ mole ratio up to 8.0 in the $[Cd(H_2O)_4](NO_3)_2$-$C_{12}EO_{10}$-CTAB-H_2O LC system.[46] Here, the electrostatic

interactions and hydrogen bonding between the charged surfactants and TMS, as shown in Figure 1.8, provide stability to the LLC mesophase at such high metal ion contents. The new assembly stabilize excessive amount of salt species in the hydrophilic domains through electrostatic interaction between the salt and surfactant domains. As a response of excess salt, the unit cell of the LLC mesophase expands to accommodate excess salt.[46] Further investigations on the salt-surfactant mesophase proved that the salt species are in the molten phase in the LLC mesophase.[47]

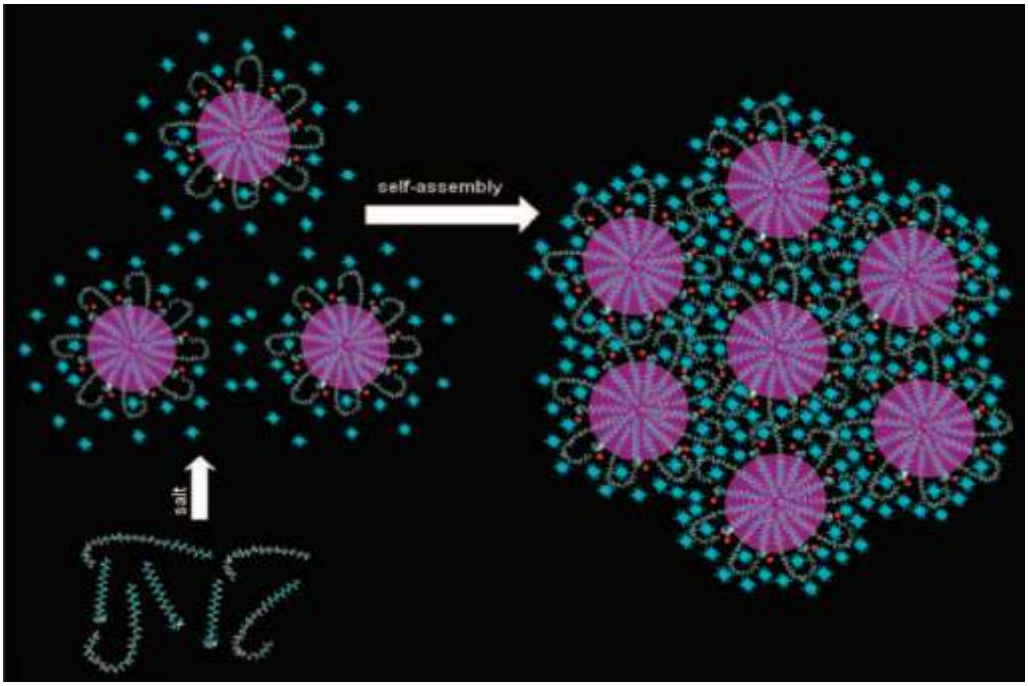

Figure 1.8[2] Schematic illustration of the assembly of hexagonal mesophase. The core (purple regions) is alkyl tails of the charged and neutral surfactants, the ethylene oxides, and the charged head group of the charged surfactant, and metal ions (blue stars) are in the dark domains.[46]

1.4 Hydrated Metal Nitrate Salts as a Good Solvent for the Salt-Surfactant Mesophases

In addition to concentration of the TMS, its counter anion also affects the self-assembly process. The numerous kinds of mesophases have been obtained

[2] Reprinted from Langmuir, Vol. 24, Albayrak, C.; Soylu, A. M. and Dag, Ö. "Lyotropic Liquid-Crystalline Mesophases of $[Zn(H_2O)_6](NO_3)_2$-$C_{12}EO_{10}$-CTAB-H_2O and $[Zn(H_2O)_6](NO_3)_2$-$C_{12}EO_{10}$-SDS-H_2O Systems." 10592-10595, (2008), with permission from ACS.

using pluronics and different TMS, $[M(H_2O)_n]X_m$, where M = Co^{2+}, Ni^{2+}, Cd^{2+}, Zn^{2+} and Mn^{2+} for X = NO_3^-, Cl^-, ClO_4^-).[30-33, 35, 37] However, major investigations on the LLC mesophases and mesostructured solids, so far, are focused on using nitrate salts of various transition metals. Both in the LLC and mesostructured solids, where the salt species are incorporated, and the nitrate ions are usually coordinated to the metal ions. Note that coordination of the counter ion to a metal ion center affects its solubility. The solubility of a salt increases by the decrease in the ionic strength of the solution, where the anions coordinate to the metal centers, (Equation **1**.**1**). Evaporation of uncoordinated water molecules shifts equilibrium to right, resulting in the coordination of nitrate ions to the metal centers, producing the $[Cd(H_2O)_2(O_2NO)]^+$ charged complex.[33]

$$[M(H_2O)_4]^{2+} + 2NO_3^- \rightleftharpoons [M(H_2O)_3(ONO_2)]^+ + H_2O + NO_3^- \quad \text{Equation 1.1}$$

The nitrate ions can coordinate to the metal center as a monodentate, bidentate, or bridged ligand as shown in Figure 1.9. D_{3h} symmetry point group of the free nitrate ion is reduced to C_{2v} symmetry in all of these three types of coordination. The coordination type of nitrate ions can be identified by using FT-IR spectroscopy. Upon coordination, the free nitrate peak at 1360 cm^{-1} splits by 120-160 cm^{-1} in monodentate, 160-210 cm^{-1} in bidentate, and more than 210 cm^{-1} in bridged coordinations.[48] Besides, the shift from 1050 cm^{-1} to 1010-1030 cm^{-1} range, the symmetric stretching mode of nitrate ions can also be monitored by Raman spectroscopy in order to identify the coordination types.[48]

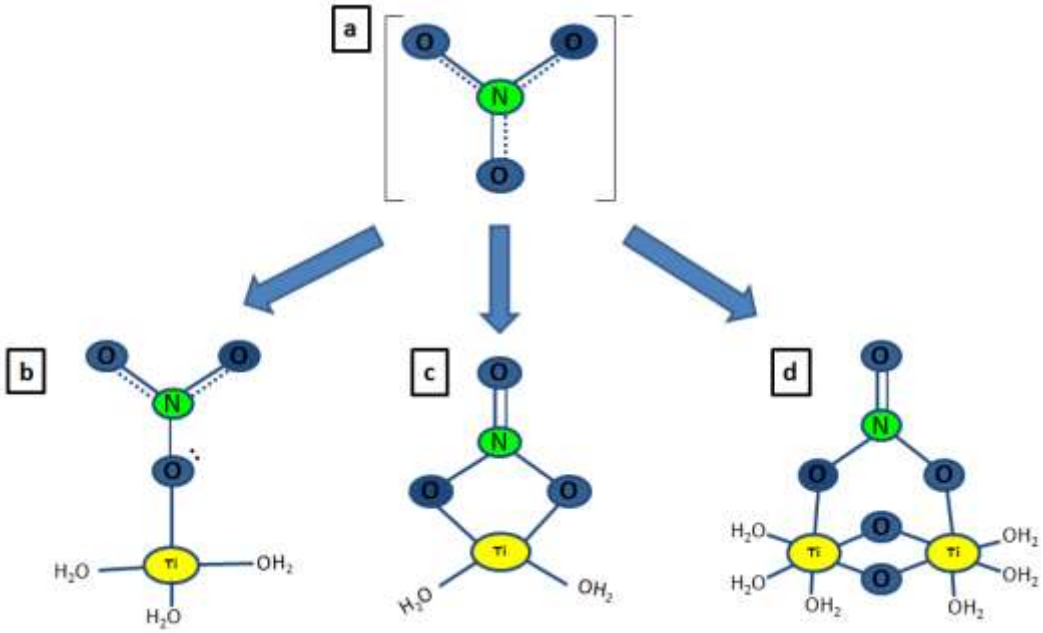

Figure 1.9 Illustration of a) free nitrate, b) monodentate, c) bidentate, and d) bridged coordination of nitrate ion to metal center. (N:nitrogen, O: oxygen, M: metal)

Second driving force for salt species to remain in liquid (or solvated) form in the LLC mesophase is depression of the melting point of salt species in a confined space. This concept will be introduced under the confinement effect in the following section.

1.5 Sol-gel Process

Sol-gel is a wet chemical process, used to produce materials generally metal oxides, starting from a colloidal solution (sol), which works like a precursor of an integrated network (gel) of particles or polymers. The *sol* is a suspension of very small dispersed particles, which are directed by van der Waals interactions and surface charges, rather than gravity, therefore the sol can be stable for a long time. The metal alkoxides and metal salts, such as nitrates, chlorides, and acetates, are generally used as precursors, and they undergo gelation through various types of hydrolysis and polycondensation reactions. The concentration of reagents, pH, temperature, and type of solvent are the main factors to define the final structure of the materials. By sol-gel method, fibers, xerogels, dense films, aerogels, uniform nano, micro sized particles have been produced.[49] The sol-gel process has

been used to synthesize mesoporous titania from titanium alkoxides ($Ti(OC_nH_{2n+1})_4$)[70] or titanium chloride ($TiCl_4$)[27], and mesoporous silica from silicon alkoxides ($Si(OC_nH_{2n+1})_4$)[50] as precursors. The processes, taking place in the hydrophilic domains of micelles and LLC mesophase, are also type of sol-gel processes that take place in a confined space.

The reason of choosing transition metal alkoxides, $M(OR)_z$, as the precursor, is based on their high reactivity provided by high electronegativity of OR groups, which can stabilize the M center in its highest oxidation state, and make it available for nucleophilic attacks.[51, 52] The condensation of titania precursors occurs by consecutive hydrolysis and condensation reactions. In the absence of a catalyst, the hydrolysis and condensation both occur by nucleophilic substitution (S_N) reactions. In the *hydrolysis*, a proton transfer is required from an attacking molecule to an alkoxide or hydroxo-ligand. Removal of the protonated species can end up with an alcohol (*alcoxolation*) or water (*oxolation*) as shown in Equation **1.2**, Equation **1.3**, and Equation **1.4**, and the *condensation* can occur by an olation process (Equation **1.5**): [51, 53]

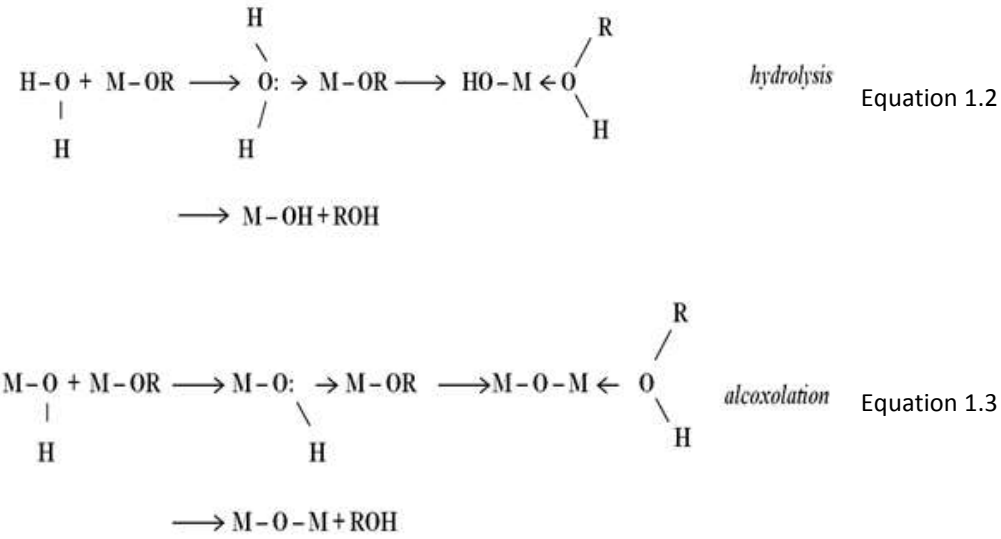

Equation 1.2

Equation 1.3

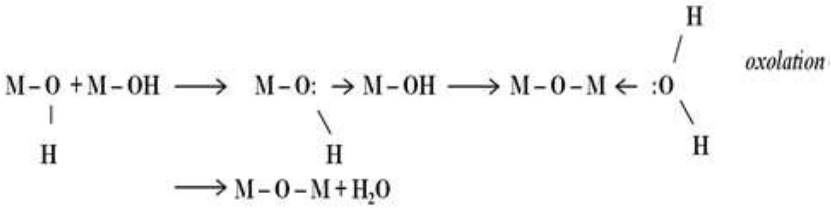

Equation 1.4

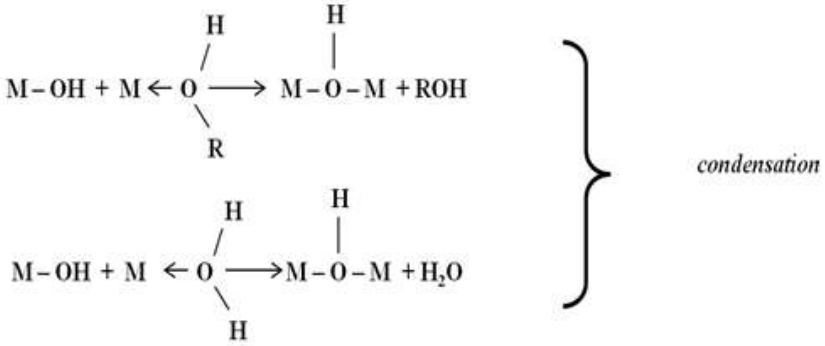

Equation 1.5

An acid or base catalyst affects both the hydrolysis and condensation rates, and the final structure of the metal oxide. The acid catalyzed condensations generally result in monolithic gels[54] or spinnable sols[55, 56] whereas the base catalyzed condensations lead to more compact, highly branched species.[51] In the presence of acids, the negatively charged alkoxide groups are protonated, providing a good leaving group, Equation **1.6**. Therefore, the reaction rate is significantly increased. This enables to eliminate the proton transfer within the transition state. Upon addition of sufficient water, even with ambient humidity, the hydrolysis may go to a completion.[51] Note that in an LCT process, the rate of condensation must be comparable to the rate of assembly of surfactants in the medium.

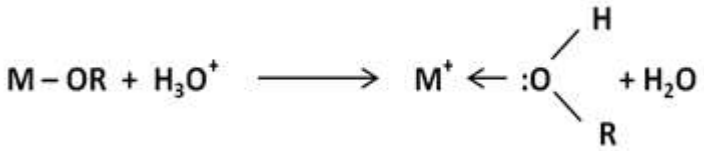

Equation 1.6

1.6 Sol-Gel Process of Titania: Synthesis of Mesostructured Titania Films

The mesostructured titania, named as Ti-TMS1, was first synthesized in 1995 by a modified sol-gel method using titanium alkoxides and phosphate surfactants.[57] Later, mesostructured titania has also been synthesized by controlling the hydrolysis and condensation steps of titania precursors by many groups.[27, 58-63] However, these mesostructured titania collapsed above 300 °C, that is necessary to crystallize titania and to remove organic species. The extent and nature of the crystallinity of titania govern its intrinsic properties for the photocatalysts, photoconductors, electrochromic device, photovoltaic, and sensor applications.[64, 65] Therefore, changing the solvent from ethanol, which is known as a good solvent for these processes due to its good wetting properties, to 1-butanol under an acidic condition and using a pluronic (P123) as a templating agent was a milestone for obtaining well-ordered mesostructured titania in the form of crack-free films.[66, 67] Since ethanol is a short alkyl chain alcohol, it tends to increase the solvation of non-ionic surfactants, and so causing an increase in the CMC. As a result of this, the LC phase could be obtained at only higher amounts of surfactants, and this causes to the solubility problem. Therefore, a long chain alcohol, butanol, could solve this solubility problem by decreasing the CMC of surfactants.[68, 69] Furthermore, a low temperature synthetic path was suggested by Ozin` s group through a mild hydrothermal treatment of ingredients at 100 °C to improve the crystallinity of titania in the stock solution without a need for further heat treatment so that mesostructured nanocrystalline titania could be obtained in the form of a crack-free flexible film.[70] These strategic changes in the procedures were the key steps to obtain ordered transparent mesoporous titania thin films, and the development of this film technology by mesoporous titania.[71-74]

However, use of HCl as an acid source at large quantities was still a problem since the films are contaminated with excessive amount of Cl^- ions that has to be removed from the mesostructured titania for the applications. The minimum temperature for the removal of Cl^- ions is around 200 °C and, the surfactant molecules burn at these temperatures, and contaminates the samples

further. Hence, the acid source has to be changed to an acid that can decompose at lower temperatures, such as HNO_3. The another advantage of use of HNO_3 as an acid source is that the nitrates make an important contribution to the self-assembly process of the organics and inorganics in the medium through coordination to the metal centers.[75]

1.7 Sol-Gel Process of Silica: Synthesis of Mesostructured Silica Films

Silicate gels are prepared from precursors, that are monomeric tetrafunctional alkoxides, under an acidic or basic condition.[49] Three main reactions are often used to explain the sol-gel process of silica as given below, where R is an alkyl group (C_nH_{2n+1}):

$$\equiv Si-OR + H_2O \leftrightarrow \equiv Si-OH + ROH \quad \textit{hydrolysis} \qquad \text{Equation 1.7}$$

$$\equiv Si-OR + HO-Si\equiv \leftrightarrow \equiv Si-O-Si\equiv + ROH \quad \textit{alcohol condensation} \qquad \text{Equation 1.8}$$

$$\equiv Si-OH + HO-Si\equiv \leftrightarrow \equiv Si-O-Si\equiv + H_2O \quad \textit{water condensation} \qquad \text{Equation 1.9}$$

The silica condensation under dilute conditions starts with a hydrolysis step, which is a fast step, and followed by a condensation step. The *hydrolysis* step (Equation **1.7**) starts upon nucleophilic attack of oxygen of water to the silicon atom, and the alkoxide group (OR) is replaced by a hydroxyl group (OH). The siloxane bonds (Si-O-Si) form during condensation reactions, producing an alcohol (Equation **1.8**) or water (Equation **1.9**). The rate of hydrolysis depends on both the length of alkoxide unit and use of a catalyst. The longer the alkoxide chain is, the slower is the hydrolysis rate. The condensation mechanisms of silica have to be investigated in three different pH ranges.[49] The pH 2 can be taken as the first boundary, since it is the point of zero charge (PZC), and the isoelectric point (IEP) of silica, where the electrical mobility of silica is equal to zero. Below

pH 2 is the metastable region for silica condensation, and the condensation rate is directly proportional to concentration of protons in the medium.[76] This long gelation time is advantageous to control the condensation process of silica so that highly ordered mesoporous silica can be obtained under high acidity. In the acid catalyzed condensation, a siliconium ion ($\equiv Si^+$) forms as an intermediate[76] and leads the condensation as shown below in Equation **1.10** and Equation **1.11**, respectively;

$$\equiv Si - OH + H_3O^+ \longrightarrow \equiv Si^+ + 2H_2O$$ Equation 1.10

$$\equiv Si^+ + HO - Si \longrightarrow \equiv Si - O - Si\equiv + H^+$$ Equation 1.11

In the range of pH 2-7, the silica particles are negatively charged and the rate of condensation is proportional to hydroxide ion concentration. In this pH range, the solubility of silica is low causing the particles to stop growing above 2-4 nm.[49] Above pH 7, the silica condensation takes place similar to the pH 2-7 range as shown in the given mechanisms below in Equation **1.12** and Equation **1.13**. However, instead of particle aggregation, highly condensed particles tend to form due to the ionization of all the condensed species.

$$\equiv Si - OH + OH^- \xrightarrow[fast]{} \equiv Si\text{-}O^- + H_2O$$ Equation 1.12

$$\equiv Si - O^- + OH - Si \xrightarrow[slow]{} \equiv Si - O - Si\equiv + OH^-$$ Equation 1.13

Therefore, the acidity and precursor choice are two important factors that control the hydrolysis and condensation reactions which control the order, morphology and size of the mesoporous silica particles. The condensation steps of silica have been investigated in detail by using FTIR, NMR, Raman, XRD and TEM techniques.[49, 77-80] Especially, the hydrolysis step has been identified very well by FTIR and Raman spectroscopy.[77, 79] The degree of silica condensation has been identified by ^{29}Si-NMR.[78] The structure of the mesostructured silica has been determined by using XRD and TEM techniques.[77, 79, 81]

Furthermore, the sol-gel chemistry in a beaker can be combined with molecular self-assembly in a simultaneous evaporation-driven processing procedure called "Evaporation Induced Self-Assembly (EISA)". Therefore, the EISA facilitates the formation of well-organized porous and composite nanostructures from homogenous sols by means of a simple evaporative procedure.

1.8 The EISA Process: Preparation of Mesostructured Thin Films

Compared to many complicated and high-cost methods for the synthesis of the patterned porous or nanocomposite materials in the form of films, fibers, or powders, the evaporation induced self-assembly (EISA) method is quite simple and rapid.[82] Name of the method was initially given by Brinker and his co-workers, who used this technique for the synthesis of mesoporous silica films.[8, 83, 84] The EISA method uses very dilute solutions, and it is, in fact, just a `beaker` chemistry, which is combined with molecular self-assembly in a simultaneous evaporation driven process. The homogenized solution of a surfactant and TMS and/or inorganic precursors, at which $C_o << CMC$, is coated on a substrate that follows a controlled evaporation of solvent, as a result of which the surfactant concentration progressively increases to CMC, and with the further evaporation, a mesophase forms. Therefore, a highly ordered mesostructured thin film is obtained by a simple and rapid process. Dilution of the ingredients provides an excellent homogeneity and diminishes the condensation of inorganic species. The latter is especially important for the non-silica systems because the condensation

step has to be controlled meticulously. Many well-defined mesostructured hybrids have been designed by adjusting the parameters that affect micellization and the formation of a LC mesophase during the condensation of the inorganic species. The mesoporous silica has been designed in various morphologies such as, spheres,[85] monoliths,[86] and thin and thick films.[84, 87-89] Stucky` s group used the EISA method to synthesize the mesoporous transition metal oxide powders such as TiO_2, ZrO_2, Al_2O_3, WO_3 from their MCl_n type precursors by using pluronic surfactants in ethanol.[59, 90] The condensation of inorganic was controlled by in situ developed HCl from MCl_n precursors.

Furthermore, unlike many high-tech methods, the EISA method overcomes many problems that occur during the synthesis of ordered porous thin films. For the patterning of surfaces of materials within a 45-300 nm size range, optical or electron beam lithography are mainly used. The EISA method provided the formation of crack-free, ultrathin, crystalline metal oxide films with highly ordered mesostructure. The film thickness could be finely tuned so that the films with a thickness of one micellar monolayer in height could be obtained in ordered mesophase.[91] Likewise, Sanchez` s group showed the synthesis of $SrTiO_3$, $MgTa_2O_6$ and $Co_xTi_{1-x}O_{2-x}$ ($0 < x < 0.30$) thin films with high homogeneity (optical transparency), 35 vol % porosity and close to 100% nanocrystalline network with 100 m^2g^{-1} surface area by using EISA technique.[92] In general, such kind of films cannot be obtained by intricate physical techniques like molecular beam epitaxy[93] or pulsed laser deposition.[94]

1.9 Mesostructured CdS and CdSe Nanoparticles and Thin Films

The II-VI semiconductor nanoparticles are useful in the area of photocatalysis, photoluminescence, and photonics.[95, 96] Since their electrical and optical properties can be tuned by changing their sizes and shapes below Bohr radius of electron-hole pair in the nanocrystals, there are tremendous efforts on the synthesis of II-VI semiconductors with a narrow size distribution and various types of novel morphologies.[97-100] The CdS and CdSe nanoparticles are the important members of this family. CdS, having a direct band gap of 2.42 eV at

room temperature, is the most promising photosensitive material.[101, 102] Since CdS has strong absorption and emission between blue and red wavelengths of visible light, it may contribute to the advancement of photoelectrochemical devices, electronics, optoelectronics, photodetectors, light emitting diodes, electrically driven lasers, and field effect transistors, etc.[103-108] The CdS and CdSe nanoparticles have been widely prepared by using numerous methods such as, laser ablation, chemical precipitation, solvothermal, photochemical, hydrothermal, and one pot synthesis methods, etc.[109-112]

Many synthesis methods have been suggested to produce CdS nanoparticles with porosity, such as nanoparticles, nanofibers, nanotubes, and nanospheres. For instance, CdS hollow microspheres were obtained by a photochemical method using polystyrene latex spheres as templates, and $CdSO_4$ as cadmium source, and $Na_2S_2O_3$ as both sulfur source and photo-initiator under low-power UV light.[113] These CdS hollow microspheres could successfully photodegradate the methyl blue in the presence of H_2O_2 under UV irradiation.[113]

Mesoporous CdS nanoparticles with an average pore size of 5.4 nm were obtained through ultrasonic mediated precipitation at room temperature, and showed great photocatalytic activity for H_2 generation.[114] If compared to the catalysts synthesized so far, the Pt metal loaded mesoporous CdS has enabled the highest hydrogen production rate of 1415 μmol/h/0.1 g catalyst.[114] The CdS and CdSe micro/nanotubes, nanowires, and nanosponges were prepared by self-sacrificing templating method, and all of them showed an enhanced photocatalytic activity due their high surface-to-volume ratio.[115-118] The uniform spherical CdS and ZnS nanocrystals with an easily controlled diameter have been produced in a combined method of water/oil micro emulsion and γ-ray irradiation at RT.[119] The same method was applied to obtain 40-50 nm CdSe nanospheres in an aqueous solution of $CdCl_2$ and Na_2SeO_3.[120]

Inorganic semiconductors have also been used to create hybrid inorganic-polymer solar cells with higher efficiency than organic photovoltaic devices since charge transfer limitations could be overcame by the high electron mobility in the

inorganic nanocrystals as high electron affinity acceptors.[121] Mesoporous CdS spheres with large surface areas and ordered pore size distribution, obtained by a simple wet chemical method, possessed an enhanced photoelectrochemical properties with a maximum conversion efficiency of 2.39 %, which is higher than the values obtained from the low dimensional CdS nanomaterials.[122] Porous CdSe materials were prepared by spray pyrolysis deposition using sodium selenosulfate, and dissolving the sodium sulfate by-product, increased the porosity in the product.[123] By this technique, the efficient solar cells having a power conversion efficiency of 2.6 % for CdSe, and 1.0 % for CdS at 1 sun illumination could be fabricated.[123] The porosity is not uniform and ordered in these materials, where the layers are formed by the aggregation of 100 nm sized CdSe nanoparticles. However, ordered mesoporous CdSe and CdS nanomaterials with high surface areas are promising for much high power conversion efficiencies.

The mesoporous CdSe nanoparticles with an interconnected network of colloidal nanoparticles were also obtained by aerogel method.[124] The CdSe aerogels were prepared by oxidative aggregation of thiolate capped CdSe nanoparticles, which were transformed into aerogels by supercritical drying so that they could maintain the loosely connected nanoparticles network present in the wet gel. The dried material had a BET surface areas up to 224 m^2/g, and average pore diameter of 16-32 nm.[124]

On the other hand, among those varieties of methods, the LCT method still remains powerful since the unit cell dimensions in the liquid crystalline phases can be adjusted, and rapidly replicated in the products.[28, 29, 84, 125, 126] However, there is not enough investigations on the synthesis of mesoporous CdS and CdSe, especially the surface area and porosity data compared to siliceous materials are still missing. The main reason is the collapse of the mesostructure upon removal of the template in the mesostructured CdS and CdSe. That is why only mesostructured CdS and CdSe exist in the literature.[127] In addition to that, the mesoporous CdS and CdSe nanomaterials mentioned above are in the form of powders, not as transparent films, and the pore walls are too thick, therefore they have bulk properties. The CdS and CdSe nanomaterials synthesized in the form of

films, using TLCT method, are not stable and undergo aggregation and separation of organic and inorganic domains.

Unfortunately, there has been no study so far showing the synthesis of ordered mesoporous CdS or CdSe films. Using the LCT approach, we have shown the first investigation of the mesostructured $Cd_{1-x}Zn_xS$ films from the TMS-P85 LLC template.[37] However, the mesostructure was not rigid enough to maintain its stability against removal of the organic template; they could not be converted into a form of stable mesoporous films. Therefore, we followed a strategy to enhance the stability of the template by a help of polymerizing inorganic reagents, such as silica and titania. Presence of the silica network provided us to synthesize stable mesoporous CdS and CdSe nanoflakes.[128, 129] Finally, the mesoporous CdS and CdSe films could be obtained successfully by the removal of silica walls by chemical etching. The details of these investigations will be presented in the results and discussion section of this thesis.

1.10 Importance of CdS-TiO_2/CdSe-TiO_2 Nanoparticles

The CdS-TiO_2 and/or CdSe-TiO_2 nanocomposites have been attractive topics since these materials display efficient solar energy conversion and good photocatalytic performance.[130-137] The titania is a large band gap semiconductor, 3.2 eV for its anatase phase, and absorbs only in the UV region of the sun light. However, due to its low cost, chemical inertness and photo stability, it has been one of the most targeted materials in the solar energy and photocatalysis areas.[138, 139] Therefore, the titania needs to be combined with a nanocrystalline semiconductor, which highly absorbs in the visible range for an efficient photocatalytic application.[140] The CdS and CdSe nanocrystals can be used as an efficient sensitizer due to their bulk band gaps in the visible region, 2.42 eV and 1.75 eV, respectively. Figure 1.10 is a schematic illustration of an electron transfer from CdS and CdSe nanoparticles to titania. The electron injection from the photoexcited sensitizer, CdS and CdSe, into TiO_2 is a primary step in photocurrent generation process. Therefore, an electronic communication between nanocrystals and titania mainly defines the efficiency of this process. The

mesoporous TiO_2 enables a high surface area template for the CdS and CdSe sensitizers to be deposited directly on the TiO_2 surface without need of any linkers and so, shows efficient photo conductance.[141]

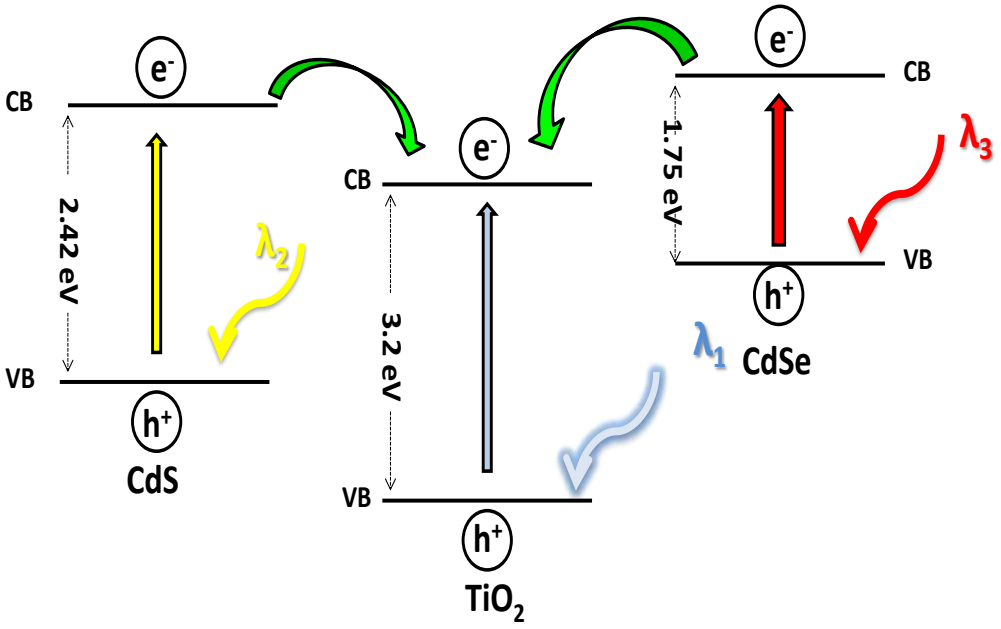

Figure 1.10 The schematic illustration of electron transfer from CdS and CdSe nanoparticles to TiO_2. (VB: valence band, CB: conduction band, λ: wavelength of the light required to produce an electron-hole pair.)

However, the synthesis of mesoporous TiO_2 is not as easy as the mesoporous SiO_2 synthesis due to the tendency of TiO_2 to precipitate and crystallize in the solution, which ends with a collapse of the mesostructure upon removal of the organic template. Only recently successful synthesis of the mesoporous titania films has been introduced.[60, 142] Therefore, there have been very few studies on depositing CdS and CdSe nanoparticles in the mesopores of TiO_2. Zhang` s group used the immobilization of the already sensitized CdSe quantum dots into mesoporous titania. The mole percent of CdSe to TiO_2 was only 3 mol %, because it is very difficult to load the nanoparticles at high concentrations into the pores. Besides, the pores of TiO_2 are blocked by the nanoparticles that also limit its use in many applications.

Therefore, the nanocrystal growth in the mesopores is a superior method, because the nanocrystals can be homogenously distributed in the pores at much

higher concentrations, and the pores will remain open for further processes, like diffusion of molecular species. Pore accessibility plays fundamental role in almost all applications. Stucky`s group introduced a method that can produce 10 mole % CdSe nanocrystals into the mesoporous TiO_2 with a high absorption in the visible region.[143] We showed that the mesostructured CdS or CdSe-TiO_2 transparent thin films can be obtained up to a 25 mole % homogenously distributed CdS and CdSe nanoparticles in the channels of the mesostructured TiO_2 by combining the EISA and LCT method.[75] Recently, we have also found out that around 86 mole % CdS and CdSe nanocrystals can be chemically deposited into the channels of the mesoporous TiO_2 by the condensation of the TiO_2 in the presence of TMS content of $[Cd(H_2O)_4](NO_3)_2$-$C_{12}EO_{10}$-CTAB-butanol or ethanol LC system.[144] The transparent crack free mesoporous CdS (CdSe)-TiO_2 films have high absorbance in the visible range, and their absorbance can be easily increased by increasing the thickness of the films coated on a substrate. The details of these investigations will be presented in the results and discussion section of this thesis.

1.11 Synthesis of CdS and CdSe Nanoparticles in the Mesoporous Silica

As mentioned above, the CdS and CdSe nanomaterials are among the class of high potential optical and electronic semiconductors. Therefore, their properties can be enhanced if they can be converted into ordered mesoporous films with high crystallinity. However, since the synthesis of crystalline mesoporous CdS or CdSe materials are very difficult, the mesoporous silica have been chosen as potential template to grow the nanocrystalline mesoporous CdS or CdSe.[145-147]

In 2003, Zhao et. al.[50] has announced the synthesis of ordered and crystalline mesoporous CdS nanoarrays by using SBA-15 silica as a template and a cadmium thioglycolate as both Cd and S source. After complete removal of the silica template using NaOH solution, the CdS nanowire arrays showed the same replica of its silica template.[50] The pores of the mesoporous silica were used as a micro-reactor to synthesize the CdS nanoparticles exclusively with high crystallinity. Sizes of the CdS nanocrystals were mainly defined by the pore size of the silica template, and removal of the template by HF solution gave the CdS

nanocrystals encapsulated microcapsules.[148] Another study shows the synthesis of MCM-41-CdS composite, which was prepared by localization of CdS nanoparticles capped by both amine and surfactant molecules inside cylindrical silica pores. During incorporation, MCM-41 long range order is just slightly modified.[149] In general, the method used to produce CdS or CdSe-SiO_2 composites has usually been loading of the CdS and CdSe nanoparticles into the already synthesized mesoporous silica template.[150-153]

All of these methods mentioned above require a second or third step during the preparation of CdS or CdSe in the mesoporous silica. Because size and shape of the nanoparticles are not uniform, they are not homogeneously distributed in the silica pores. We have recently developed a new synthesis pathway for the mesoporous CdS(or CdSe)-SiO_2 thin films with homogenously distributed CdS and CdSe nanoflakes in the pore walls of silica up to 79 % w/w CdSe to silica ratio.[129] This topic is one of the sections of this thesis, and will be discussed further in the last section.

1.12 Confinement Effects on The Electronic and Thermal Properties of Solids

Nanosized materials are of great scientific interest due to their size dependent optical and thermal properties, which can be quite different from their bulk counterparts. As the size of the material approaches to nano-scale, the surface-area-to-volume, SA/V, ratio increases drastically. Therefore, there will be a huge increase in the percentage of surface atoms and the intrinsic properties of interior of nanocrystals make optical and thermal properties of the material to be size-dependent. [154]

The size-dependency of electronic and optical properties of nanosized semiconductors can be explained by *quantum confinement effect (QCE).* [154] The QCE is observed when the size of a semiconductor is reduced below exciton (electron-hole pair) Bohr radius. The excitonic states are the bound states of an electron-hole (e-h) pair, which are attracted to each other by Coulomb force. An exciton forms when a semiconductor absorbs a photon, which excites an electron

from the valence band into the edge of the conduction band, and leaves the positively-charged hole in the valence band and electron in the hydrogenic levels below conduction band. The distance between the hole and electron can be as large as the exciton Bohr radius in a semiconductor nanocrystal. The QCE is observed when the excitons in a semiconductor are confined in a potential well, which is the region surrounding the local minimum of potential energy. A quantum well confines an e-h pair in one dimension, nanowires in two dimensions, and quantum dots in three dimensions. When the size of the materials reaches the exciton Bohr radius, the e-h pair cannot move freely, and the energy spectrum turns into discrete rather than being continuous. As a result of this, the band gap becomes size dependent, and it is observed as a blue shift in the absorption spectra as the particle size decreases.

Therefore, the measured band gaps can be used to calculate the particle size of semiconductor nanoparticles. The effective-mass model (EMM) is a reliable theoretical calculation in order to find out the radius of the semiconductor nanoparticle from its band gap value.[97] The overall equation is given as;

$$E^* = E_g^{bulk} + \frac{\hbar^2\pi^2}{2er^2}\left(\frac{1}{m_e m_0} + \frac{1}{m_h m_0}\right) - \frac{1.8e}{4\pi\varepsilon\varepsilon_0 r} - \frac{0.124e^3}{\hbar^2\left(4\pi\varepsilon\varepsilon_0\right)^2}\left(\frac{1}{m_e m_0} + \frac{1}{m_h m_0}\right)^{-1} \quad \text{Equation 1.14}$$

where E_g is the bulk band gap (eV), r is the particle size (Å), h ($\hbar = h/2\pi$) is the Planck` s constant divided by 2π, m_e is the effective mass of electron, m_h is the effective mass of hole, m_0 is the free electron mass (9.110×10^{-31} kg), ϵ_0 is the permittivity of free space ($8.85418782 \times 10^{-12}$ $C^2N^{-1}m^{-2}$), ϵ is the dielectric constant, e is the charge on the electron (1.602176×10^{-19} C). The second term on the right hand side of the equation is consistent with the particle in a box quantum confinement model, and adds the quantum localization of energy of effective mass of electron. The effective mass of electron and hole is characteristic to the semiconductor type and dimension. The third term is due to the screened coulomb interaction between electron and hole, and lowers the bulk band gap energy by $\mathbf{r^{-1}}$ factor. The last term is the salvation energy loss and usually ignored due to its negligibly small contribution.

The nanoscale materials have very high SA/V ratio compared to their bulk phases, which also alter their thermal properties. The melting point decrease is one of the results of this confinement effect.[155] The high SA/V ratio means that a large number of surface atoms are involved in defining the chemical and physical properties of the material. Since the surface atoms have less neighboring atoms to bond compared to bulk atoms, they have lower cohesive energy. According to Lindemann`s criterion, the melting temperature of a material is proportional to its cohesive energy since the cohesive energy defines the amount of thermal energy necessary to free the atom from a solid.[156] Therefore, the melting point decreases for the nanoparticles due to their very high SA/V ratio.[157] The change in melting point by the change in size of a material can be calculated theoretically through classical thermodynamic analysis by Gibbs-Thomson equation;[158]

$$\Delta T = \frac{2\gamma_{sl} v T_0}{\Delta H_f d} \qquad \text{Equation 1.15}$$

where ΔH_f is the bulk heat of fusion, γ_{sl} is the solid-liquid interface energy, v is the molar volume, T_0 is the bulk melting point, and d is the particle diameter. The Gibbs-Thomson equation can be simplified as;[159]

$$\Delta T = \frac{K}{d} \qquad \text{Equation 1.16}$$

where K is the Gibbs-Thomson coefficient assuming different values for different substances, and for different interfacial geometries such as spherical, cylindrical or planar. Vargas-Florencia et. al.[158] showed that the melting point depression of a confined inorganic salt hydrate can be used as a sensitive probe to measure the pore size and size distribution of a porous material. They measured the pore size distributions of porous glasses through the observation of the melting of a pore-confined $[Zn(H_2O)_6](NO_3)_2$. Recently, it has been proved that confining the salt species in the hydrophilic domains of a LLC mesophase of $[Zn(H_2O)_6](NO_3)_2 - C_{12}EO_{10}$ system drastically depresses the melting point of the salt, and causes the salts to transform into liquid phase.[47] The advantage of this property is that the

molten phase of the salt species can be used as a solvent to mediate the self-assembly of the surfactants in the LLC mesophase. Furthermore, confining Zn(II) and Cd(II) salts in channel spaces between the surfactant molecules and silica or titania matrixes through LLC mesophase of $[M(H_2O)_x](NO_3)_2$-$C_{12}EO_{10}$ system has provided us to synthesize highly ZnO and CdO loaded mesoporous silica or titania materials, respectively.[128, 129, 144] Here, the molten phase of Zn(II) and Cd(II) salts acts as a nonvolatile secondary solvent in the assembly process and therefore, such a high concentration of salts can be kept in a solid silica or titania matrix, and the mesostructure can be maintained until all salts are converted into their oxides.

In this thesis, the basic aim is to synthesize mesoporous MS and MSe by means of LCT. For this purpose, the thesis work is mainly divided into two general parts; liquid crystalline and materials parts. In the first chapter, the liquid crystalline part, the synthesis of the mesostructured MS-P85 thin films from the $[M(H_2O)_4](NO_3)_2$-P85-H_2O or ethanol solutions and the phase separation problems will be mentioned. Then, the problems during calcination of these mesostructured MS-P85 films are given in detail. Following, the synthesis of mesostructured MS thin films, and the problems during H_2S reactions, and the phase separations after H_2S reactions, and their behavior under calcination process are clarified. In the second chapter, rigidifying the mesostructure with TiO_2, the synthesis of stable CdS and CdSe nanoparticles in the channels of mesostructured titania films by exposing the mesostructured Cd(II)-TiO_2 films are given. To further increase the CdS (or CdSe)/TiO_2 mole ratio in the films, synthesis of mesoporous CdS (or CdSe)-TiO_2 thin films by exposing the mesoporous TiO_2-CdO (or ZnO) thin films, which were prepared from a solution of $[M(H_2O)_x](NO_3)_2$-CTAB-HNO_3-C_2H_5OH-$C_{12}EO_{10}$- $Ti(OC_4H_9)_4$ (M is Zn(II) or Cd(II) and x is 6 for Zn(II) and 4 for Cd(II) salts), to H_2S/H_2Se reactions at RT has been described in detail. In the last chapter, synthesis of the mesoporous SiO_2-MS (or MSe) thin films (where M is Zn(II) or Cd(II)) by exposing the mesoporous SiO_2-CdO(or ZnO) films, which were prepared from clear solutions of $[M(H_2O)_x](NO_3)_2$-H_2O-CTAB-HNO_3-$C_{12}EO_{10}$-TMOS (M is Zn(II) or Cd(II) and x is 6 for Zn(II) and 4 for Cd(II) salts) and calcined at 450 °C, to H_2S or H_2Se

gaseous at RT and the reaction kinetics of H_2S (or H_2Se) reactions with the mesoporous SiO_2-CdO(or ZnO) films will be presented. Finally, the synthesis of mesoporous CdS (or CdSe) from mesoporous SiO_2-CdS (or CdSe) through a chemical etching of silica under a dilute solution of HF, and how the mesoporous CdS nanoparticles have been modified by capping with a polymer in a dilute solution to gain photoluminescence will be discussed.

CHAPTER II

EXPERIMENTAL

2.1 Materials

All chemicals and solvents were reagent grade and used as received without any further treatment.

Surfactants used throughout this work, the triblock copolymers having a poly(ethylene oxide) – poly(propylene oxide) – poly(ethylene oxide) blocks, (EO_n-PO_n-EO_n) so called pluronics; P85 ($EO_{26}PO_{40}EO_{26}$) with a M_w of 4600 g/mol and P123 ($EO_{20}PO_{70}EO_{20}$) with a M_w of 5750 g/mol were generously donated by BASF Corp. and used without further treatment, and 10-lauryl ether, $CH_3(CH_2)_{11}(OCH_2CH_2)_{10}OH$, (designated as $C_{12}EO_{10}$, M_w = 626.9 g/mol) and cetyl trimethyl-ammonium bromide, $C_{16}H_{33}N(CH_3)_3Br$, (designated as CTAB, Mw = 364.45 g/mol) are commercially available from Aldrich, Germany.

The other chemicals used are: cadmium(II) nitrate tetrahydrate ($[Cd(H_2O)_4](NO_3)_2$, 99%, Fluka), zinc(II) nitrate hexahydrate ($[Zn(H_2O)_6](NO_3)_2$, 98%, Aldrich), hydrogen sulfide (H_2S, 99.5%, Aldrich), hydrogen selenide (H_2Se, 99.99%, Air Products), ethanol (C_2H_5OH, 99.9%, Merck), hydrochloric acid (HCl, %37, Reidel-de Haën), nitric acid (HNO_3, %65, Reidel-de Haën) and 1-butanol (C_4H_9OH, %99, Fluka), titanium tetrabutoxide ($Ti(OC_4H_9)_4$,%98, Aldrich), tetramethylorthosilicate (TMOS, %99 pure, Aldrich).

2.2 Synthesis of Materials

2.2.1 Preparation of $[Cd(H_2O)_4](NO_3)_2$:P85 LC Thin Films:

The lyotropic liquid crystalline phase of $[Cd(H_2O)_4](NO_3)_2$ was prepared by stirring a mixture of 1.0 g P85 and a salt with appropriate salt to pluronic mole ratio ($[Cd(H_2O)_4](NO_3)_2$/P85 = 7:1 – 11:1) in 10.0 mL ethanol overnight at RT.

For example, in order to prepare n:1 mole ratio of $[Cd(H_2O)_4](NO_3)_2$:P85 solution, first, dissolve 1.0 g P85 in a vial using 10.0 mL ethanol by stirring for 30 minutes on a magnetic stirrer until the solution becomes clear. Then, add m g $[Cd(H_2O)_4](NO_3)_2$, where m is equal to 0.067*n (0.067 = 308.47/4600 Mwt of $[Cd(H_2O)_4](NO_3)_2$/Mwt of P85) to the above solution and let the solution mix overnight at RT in order to obtain homogenized solution.

Then, prepare the films by spin coating of 1.0 mL of above solution on a substrate by spinning at 2000 rpm for 1 minute. For a smooth coating, first, inject the solution on a substrate, and then spin at a desired speed. Quartz, glass and silicon (100) substrates were used to perform measurements using various techniques. The LC films are stable for a long period of time on any substrate.

2.2.2 Synthesis of CdS/P85 Thin Films:

Expose and keep the $[Cd(H_2O)_4](NO_3)_2$:P85 LC thin film under 300 torr H_2S gas for 15 minutes at RT in an evacuated reaction chamber (see Figure 1.3.2). Upon completion of the reaction, evacuate excess H_2S gas inside the reaction chamber by using a rotary pump for 5 minutes.

2.2.3 Preparation of $[Cd(H_2O)_4](NO_3)_2 - C_{12}EO_{10}$ – CTAB LC Thin Films:

A solution of $[Cd(H_2O)_4](NO_3)_2$ was prepared by stirring (overnight at RT) a mixture of 1.0 g $C_{12}EO_{10}$, appropriate amount of cadmium nitrate hexahydrate ($[Cd(H_2O)_4](NO_3)_2/C_{12}EO_{10}$ mole ratio was changed from 3 to 15) and appropriate amount of CTAB (CTAB/$C_{12}EO_{10}$ mole ratio was changed from 0.75 to 2.0) in a 10.0 mL distilled water. The mole ratios and amounts of $[Cd(H_2O)_4](NO_3)_2$ and CTAB used for the preparation of $[Cd(H_2O)_4](NO_3)_2 - C_{12}EO_{10}$ – CTAB LC thin films are given in Table 2.1 and Table 2.2.

Table 2.1 The mole ratios and amounts of $[Cd(H_2O)_4](NO_3)_2$ used for the preparation of $[Cd(H_2O)_4](NO_3)_2 – C_{12}EO_{10}$ – CTAB solutions.

Cd(II)/$C_{12}EO_{10}$ mole ratio	**amount of $[Cd(H_2O)_4](NO_3)_2$ for 1 g of $C_{12}EO_{10}$ (g)**
3	1.478
6	2.956
8	3.942
9	4.435
10	4.927
13	6.406
15	7.391

Table 2.2 The mole ratios and amounts of CTAB used for the preparation of [Cd(H2O)4](NO3)2 – C12EO10 – CTAB solutions.

CTAB/$C_{12}EO_{10}$ mole ratios	**amount of CTAB for 1 g of $C_{12}EO_{10}$ (g)**
0.75	0.437
1.0	0.582
1.25	0.728
1.5	0.873
2	1.164

For example, in order to prepare 13:1 mole ratio of $[Cd(H_2O)_4](NO_3)_2/C_{12}EO_{10}$ solution with a 2:1 mole ratio of CTAB/$C_{12}EO_{10}$; first,

dissolve 1.0 g $C_{12}EO_{10}$ 10.0 mL distilled water by stirring 30 minutes on a magnetic stirrer until the solution becomes clear. Then, add 1.164 g CTAB to the solution and stir for another 15 minutes until all the surfactants are completely dissolved. Finally, add 6.406 g $[Cd(H_2O)_4](NO_3)_2$ to that mixture and let the solution mix overnight in a closed vial at RT.

Then, in order to prepare the films, spin coat 1 mL of above solutions on a substrate first at 500 rpm for 5 seconds and then at 1500 rpm for 20 seconds. For a smooth coating, first, inject the solution on a substrate, and then spin at a desired speed. Quartz, glass and silicon (100) substrates were used to perform measurements using various techniques.

2.2.4 Synthesis of Mesostructured CdS - $C_{12}EO_{10}$ – CTAB Thin Film:

Expose and keep the above film under a 300 torr H_2S in an evacuated reaction chamber for 15 minutes at RT. Then, evacuate the excess H_2S gas by using a rotary pump for 5 minutes.

2.2.5 Synthesis of Cd(II) Modified Titania Thin Films :

A mixture of $[Cd(H_2O)_4](NO_3)_2$ – P123 – $Ti(OC_4H_9)_4$ – 1-butanol – HNO_3 solution was prepared with Cd(II)/P123 mole ratio range of 2 to 15 at a Ti(IV)/P123 mole ratio of 60 with 1.0 g of HNO_3 in 6.0 g of 1-butanol. The mole ratios and amounts of $[Cd(H_2O)_4](NO_3)_2$ used for 0.65 g P123 in order to prepare Cd(II) modified Titania thin films are given in Table 2.3.

Table 2.3 The mole ratios and amounts of $[Cd(H_2O)_4](NO_3)_2$ used for 0.65 g P123 for the preparation of Cd(II) modified Titania thin films.

Cd(II)/P123 mole ratios	amount of $[Cd(H_2O)_4](NO_3)_2$ for 0.65 g P123 (g)
2	0.07
5	0.175
10	0.35
13	0.455
15	0.525

For example, in order to prepare 13:1 mole ratio of $[Cd(H_2O)_4](NO_3)_2$:P123 solution, first, add 0.650 g P123 into 6.000 g of 1-butanol and stir until the solution becomes clear. Then, add 0.455 g $[Cd(H_2O)_4](NO_3)_2$ and stir the mixture overnight on a magnetic stirrer at RT. To above clear solution, add 1.000 g of concentrated HNO_3, and cool the mixture in an ice-bath for 1.5 minutes. Finally, add 2.280 g titania precursor to that mixture, and let the solution mix for 6 hours by constant stirring in a closed vial at RT.

Then, in order to prepare the films, spin coat 1 mL of above solution on a substrate by first spinning at 500 rpm for 5 seconds and then at 1500 rpm for 20 seconds. For a smooth coating, first, inject the solution on a substrate, and then spin at a desired speed. Quartz, glass and silicon (100) substrates were used to perform measurements using various techniques. As soon as films were prepared, put the films in a humidity oven with a 50 % relative humidity (RH) at 30 °C for 12 h and then at a 130 °C for 4 hrs in an oven. These samples were denoted as meso-xCd(II)-yTiO_2, where x and y are the initial Cd(II)/P123 and Ti(IV)/P123 mole ratios.

2.2.6 Synthesis of CdSe Nanoparticles in Mesostructured Titania:

Expose and keep above films under ~ 39 torr of 5% H_2Se, in a N_2 atmosphere for 1 minute in an evacuated vacuum chamber. Upon completion of the reaction, due to environmental considerations, evacuate the excess H_2Se gas first into a trap, which has CuO-loaded mesoporous silica, for 2 minutes. The unreacted H_2Se gas is converted into CuSe nanoparticles so that only N_2 gas is pumped out using a rotary pump for 5 minutes. These samples were abbreviated as meso-x$CdSe$-yTiO_2, where x and y are the initial Cd(II)/P123 and Ti(IV)/P123 mole ratios. (**Synthesis of CuO Loaded Mesoporous Silica:** Stir mesoporous silica beads around 1 μm sizes for 15 minutes in a saturated $CuCl_2.2H_2O$ solution and then, wash several times with distilled water through vacuum filtration, and then calcine at 450 °C.)

2.2.7 Synthesis of meso-TiO_2-MO (M = Zn(II) and Cd(II) Thin and Thick Films:

Prepare a mixture of a desired amount of $[Zn(H_2O)_6](NO_3)_2$ or $[Cd(H_2O)_4](NO_3)_2$, 0.291g CTAB (1.0 CTAB/$C_{12}EO_{10}$ mole ratio), 0.500 g $C_{12}EO_{10}$ and 7.0 g ethanol, and stir the mixture for 1 day to get a clear solution. To above clear solution; add 0.500 g of concentrated HNO_3 (12 M) and stir for another 5 minutes. Finally, add 1.9 g of $Ti(OC_4H_9)_4$ to the mixture and stir for additional 5 Mminutes. The solution must be homogenous and clear before spin coating over a substrate.

In order to prepare the films, spin coat 1 mL of above fresh solution on a substrate at 2000 rpm for 30 seconds. For a smooth coating, first, inject the solution on a substrate, and then spin at a desired speed. Immediately after spin coating the films, put the samples into an oven at 70 ^oC and calcine to 450 ^oC using a temperature controlled oven at 1 ^oC/min increments. The calcined sample was labeled as meso-Zn_2TiO_4 (the Zn(II)/$C_{12}EO_{10}$ mole ratio has been changed among 2, 4, 6, and 8 at constant Ti(IV)/$C_{12}EO_{10}$ mole of 7.0 and 1.0 CTAB/$C_{12}EO_{10}$ mole ratio). The meso-$CdTiO_3$ films were also prepared using

above procedure, and the Cd(II)/$C_{12}EO_{10}$ mole ratio has been changed among 2, 4, and 6 at a constant Ti(IV)/$C_{12}EO_{10}$ mole of 7.0 and 1.0 CTAB/$C_{12}EO_{10}$ mole ratio.

For a larger amount of meso-TiO_2-MO, thick meso-TiO_2-MO films were prepared by spray coating of the above solution on glass slides. The spray coatings were carried using a spray gun (Max Extra H-2000) operated using 3 bar dry air. After spray coating, put the films immediately into an oven at 70 ^oC and calcine to 450 ^oC using a temperature controlled furnace at 1 ^oC/min increments.

2.2.8 Synthesis of meso-TiO_2-CdS Thin Film:

Expose the above meso-$CdTiO_3$ thin film to a 300 torr H_2S gas in an evacuated reaction chamber for 15 minutes at RT to obtain meso-TiO_2-CdS thin film. Then, evacuate the reaction chamber by using a rotary pump for 5 min prior to removing the sample.

2.2.9 Synthesis of meso-TiO_2-CdSe Thin Films:

Expose the above meso-$CdTiO_3$ thin film to a 300 torr of 5 % H_2Se gas (diluted with pure N_2 gas) in an evacuated reaction chamber for 15 minutes at RT to obtain meso-TiO_2-CdSe thin film. Then, due to environmental considerations, transfer the excess H_2Se gas first into a trap, which has CuO-loaded mesoporous silica, for 2 minutes to convert the excess H_2Se into CuSe nanoparticles. Then, evacuate the unreacted gas by using a rotary pump for 5 min before removing the sample.

2.2.10 Synthesis of meso-TiO_2-ZnSe Thin Film:

Expose and keep the meso-Zn_2TiO_4 thin film under a 300 torr of 5 % H_2Se gas (diluted with pure N_2 gas) in an evacuated reaction chamber for 15 minutes to obtain meso-TiO_2-ZnSe thin films. Then, due to environmental considerations, transfer the excess H_2Se gas first into a trap, which has CuO-loaded mesoporous silica, for 2 minutes to convert the excess H_2Se into CuSe nanoparticles. Then, evacuate the reaction chamber by using a rotary pump for 5 min before removing the sample.

2.2.11 Synthesis of meso-SiO_2-MO (M = Zn(II) and Cd(II) Thin Film:

Prepare a mixture of a desired amount of $[Zn(H_2O)_6](NO_3)_2$ or $[Cd(H_2O)_4](NO_3)_2$, 0.291g CTAB (1.0 CTAB/$C_{12}EO_{10}$ mole ratio), 0.500 g $C_{12}EO_{10}$ and 4.5 g deionized water, and stir the mixture for 1 day to get a clear solution. To the above clear solution, add 0.050 g of concentrated HNO_3 (12 M) and stir for another 5 minutes. Finally, add 0.850 g of TMOS to the mixture and stir for additional 5 minutes. The solution must be homogenous and clear before spin coating over a substrate.

In order to prepare the films, spin coat 1 mL of above fresh solution on a substrate at 1200 rpm for 1 minute. For a smooth coating, first, inject the solution on a substrate, and then spin over the spin coater at a desired speed. Immediately after spin coating the films, put into an oven at 55 °C for Zn(II) and 65 °C for Cd(II) samples, and calcine to 450^oC using a temperature controlled furnace at 1 ^oC/min increments in order to obtain mesoporous silica-zinc oxide (denoted as meso-SiO_2-nZnO) and mesoporous silica-cadmium oxide (denoted as meso-SiO_2-nCdO) thin films, respectively, in which n is the Zn(II)/$C_{12}EO_{10}$ or Cd(II)/$C_{12}EO_{10}$ mole ratio and has been changed among 2, 4, 6, and 8 at a constant SiO_2/$C_{12}EO_{10}$ mole ratio of 7.0 with 1.0 CTAB/$C_{12}EO_{10}$ mole ratio.

2.2.12 Synthesis of meso-SiO_2-CdS and meso-SiO_2-ZnS Thin Films:

Expose and keep the meso-SiO_2-nCdO and meso-SiO_2-nZnO thin films under a 300 torr H_2S gas in an evacuated reaction chamber for overnight at RT for a complete metal sulfide, MS, reaction. Then, evacuate the reaction chamber using a rotary pump for 5 min before removing the sample. The films were labeled as meso-SiO_2-CdS and meso-SiO_2-ZnS.

2.2.13 Synthesis of meso-SiO_2-CdSe and meso-SiO_2-ZnSe Thin Films:

Expose and keep the meso-SiO_2-nCdO and meso-SiO_2-nZnO thin films under 300 torr of 5 % H_2Se gas (diluted with pure N_2 gas) in an evacuated reaction chamber for 1 h at RT for a complete metal selenide, MSe, reaction. Then, due to environmental considerations, evacuate the excess H_2Se gas in the

reaction chamber, which has CuO loaded mesoporous silica, for 2 min to convert the excess H_2Se into CuSe nanoparticles. Then, pump out the unreacted gas using a rotary pump for 5 min before removing the sample. The films were labeled as meso-SiO_2-CdSe and meso-SiO_2-ZnSe.

2.2.14 Synthesis of Mesoporous CdS:

Put a few drops of 4 % HF solution over the meso-SiO_2-CdS films for 1 second. Then, wash the films several times with deionized water. The crashed film pieces of mesoporous CdS were collected for the characterization. In order to collect large amounts of mesoporous CdS, scrap around 20 thin films of meso-SiO_2-CdS prepared on glass substrates. Etch the meso-SiO_2-CdS powder in a 10 mL 4 % HF solution, and centrifuge at 5000 rpm for 30 minutes. Upon precipitating the mesoporous CdS powder (denoted as meso-CdS), decant the liquid part. Wash the mesoporous CdS powder several times using deionized water by centrifugation and decantation. Finally, dry the meso-CdS powder at 100 °C.

2.2.15 Synthesis of Mesoporous CdSe:

Put a few drops of 4 % HF solution over the meso-SiO_2-CdSe films for 1 second. Then, wash the films several times with deionized water. The crashed film pieces of mesoporous CdSe were collected for the characterization. In order to collect large amounts of mesoporous CdSe powder, scrap around 20 thin films of meso-SiO_2-CdSe prepared on glass substrates. Etch the meso-SiO_2-CdS powders in a 10 mL 4 % HF solution, and centrifuge at 5000 rpm for 30 minutes. Upon precipitating the mesoporous CdSe (denoted as meso-CdSe) powder, decant the liquid part. Wash the meso-CdSe powder several times using deionized water by centrifugation and decantation. Finally, dry the meso-CdSe powder at 100 °C.

2.2.16 Synthesis of Mesoporous CdS-PEI:

Dissolve 1.0 mg of etched meso-CdS and excess amount of PEI (polyethyleneimine) in an absolute ethanol. Keep the PEI and meso-CdS solution in a sonicator for 5 minutes. Upon evaporation of the solvent, photoluminescent

(PL) PEI modified meso-CdS (denoted as meso-CdS-PEI) was obtained. Disperse the meso-CdS-PEI in deionized water for the PL measurements.

2.3 Instrumentation

2.3.1 X-Ray Diffraction (XRD)

The XRD patterns were recorded by using Rigaku Miniflex diffractometer equipped with a high power Cu Kα source operating at 30 kV/15 mA, generating X-rays with λ = 1.5405 Å, and a Scintillator NaI (T1) detector with a Be window. The samples were prepared on glass substrates for the XRD measurements. The measurements were performed at small angles between 0.5 and 5, 2θ range with a 1 °/minute scan rate in order to observe the meso-order. High angle regions, between 15 and 60° 2Θ range, were recorded in order to observe the nanocrystalline phases of metal oxides, metal sulfides, and metal selenides.

2.3.2 FT-IR Spectroscopy

The FT-IR spectra were obtained using a Bruker Tensor 27 model FT-IR spectrometer. A DigiTectTM DLATGS detector was used with a resolution of 4 cm^{-1} and 128 scans in 400-4000 cm^{-1} range for all the samples. The samples were prepared on IR transparent Si(100) wafers for the FT-IR measurements.

2.3.3 UV-Vis Spectroscopy

The UV-Vis spectra were recorded on a Varian Cary 5 and Thermo Scientific Evolution160 double beam spectrophotometer with a 100 nm/min speed and a resolution of 0.2 nm over a wavelength range from 200 nm to 800 nm in absorbance mode. The substrates were quartz or glass depending on the wavelength range of the measurements. The powder samples were measured by preparing KBr pellets.

2.3.4 Raman Spectroscopy

The micro Raman spectra were recorded by using a LabRam Model confocal Raman microscope with a 300 mm focal length. The spectrometer is

equipped with both HeNe laser operated at 20 mW, polarized 500:1 with a wavelength of 632.817 nm, and dipole-pumped solid state laser operated at 50 mW, polarized 100:1 with a wavelength of 532.1 nm, and a 1024 x 256 element CCD camera. The signal collected is transmitted via a fiber optic cable into a spectrometer with 600 or 1800 g/mm gratings. The spectra were collected by manually placing the probe tip near the desired point of the sample on a silicon wafer.

2.3.5 Scanning Electron Microscopy (SEM) and Energy Dispersive X-Ray Spectroscopy (EDS)

The SEM images were recorded using Zeiss EVO-40, operated at 20 kV with a Bruker AXS XFlash EDS detector 4010 attached to the same microscope and Nova NanoSEM 430, operated at 20 kV. The samples on the silicon wafers were attached to the aluminum sample holders by using carbon adhesive tabs.

2.3.6 Transmission Electron Microscope (TEM)

The TEM images were recorded on FEI Technai G2 F30, operated at 200 kV and JEOL JEM 2100F Field Emission Gun TEM operated at 200kV. The calcined thin film samples were scraped from the substrates and grinded well in a mortar with a few drops of absolute ethanol, and then dispersed in a large amount of absolute ethanol. A drop of above solution is put on a TEM grid and then immediately dried on a heater at 50° C.

2.3.7 N_2 Sorption Measurements

The N_2 (77.4 K) sorption measurements were performed with a TriStar 3000 automated gas adsorption analyzer (Micrometrics) in a relative pressure range P/P_0, the saturation pressure P_0 was measured over 120 min intervals. The powder sample was obtained by scraping about 20 glass slides of each thin film. The sample was dehydrated under (~10^{-2} torr) vacuum for 3 hrs at 250 °C to remove adsorbed water and other volatile species from the pores before N_2 sorption measurements.

2.3.8 Photoluminescence Measurements

The photoluminescence of the meso-CdS-PEI that was dispersed in deionized water in a quartz cell was measured using Varian Cary Eclipse fluorescence spectrophotometer. An excitation wavelength of 365 nm was used and the PL was recorded from 380 to 700 nm. The excitation and emission slit widths were both set to 10 nm.

CHAPTER III

RESULTS AND DISCUSSION

3.1 Liquid crystalline part

3.1.1 Calcination of $[Cd(H_2O)_4](NO_3)_2$: P85 LC Samples

In our former studies, we reported the synthesis of the first mesostructured MS thin films, where M is Cd(II) or Zn(II) or $Cd_{1-x}Zn_x$ for x between 0.0 and 1.0, by using $[M(H_2O)_n](NO_3)_2$-P85 LC system.[37] The $[M(H_2O)_n](NO_3)_2$/P85 mole ratio could be as high as 11.0 in the mesostructured LC thin films. Exposing the mesostructured M(II)/P85 LC thin films to H_2S gas produces transparent mesostructured MS (MS/P85) thin films. However, the MS/P85 films undergo phase separation in time through the diffusion of excess surfactant molecules out of the mesophase as a result of low MS content in the medium.

Based on the aim of the thesis, the mesostructured MS/P85 films were still worth to be used to develop a method for the synthesis of mesoporous MS films. Even though the MS/P85 samples, prepared using up to 11.0 M(II)/P85 mole ratio, undergo phase separation in time due to low MS content in the medium, the 11.0 M(II)/P85 mole ratio was still the highest in the literature. Therefore, the calcination processes of the mesostructured MS/P85 films were performed to remove the organic species from the medium and to obtain mesoporous MS films. The results were analyzed after calcination process as follows. Analyzing thermal behavior at various temperatures might lead us to a path for stabilizing the mesostructured MS or $[M(H_2O)_n](NO_3)_2$-P85 films during calcination process. Therefore, we first calcined the fresh CdS/P85 films at 350 °C by heating the samples under ambient conditions with 1 °C/min increments.

Figure 3.1 shows the IR spectra of fresh CdS/P85 film (solid line), and after its calcination (dashed line). The IR spectrum of the calcined CdS film indicates that all organic species could be removed from the medium and also shows that 350 °C would be enough for the calcination process.

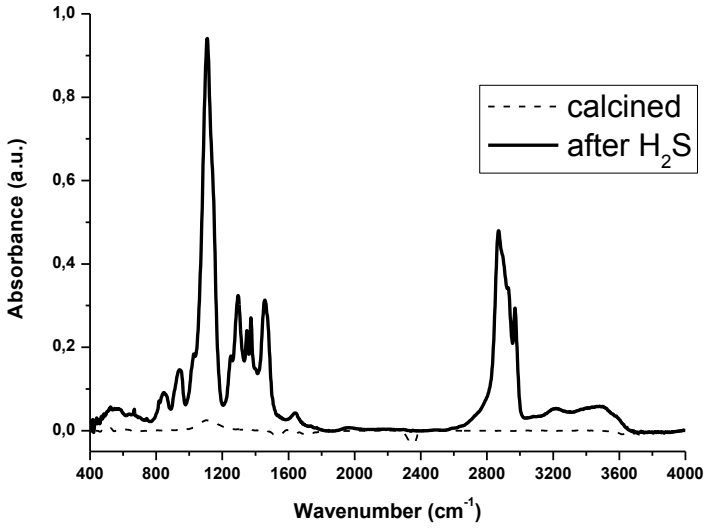

Figure 3.1 FTIR spectra of fresh CdS/P85 film (solid line), and after calcination (dashed line).

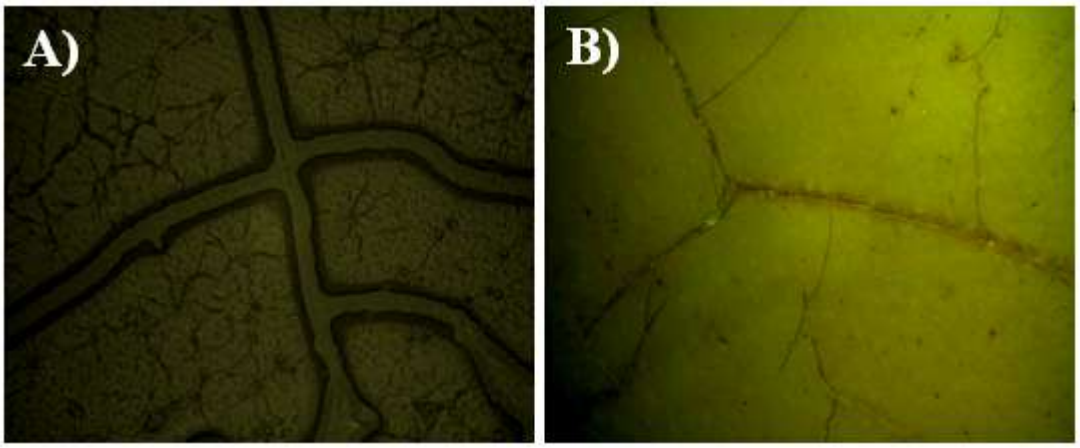

Figure 3.2 OM images of CdS/P85 films (A) before and (B) after calcination up to 350 °C.

Figure 3.2 shows the optical microscopy (OM) images of the CdS/P85 films before (A) and after (B) calcination. The crack patterns formed all over the films upon exposure to H_2S gas. The crack formation all over the sample is a proof of formation of a solid MS film. However, even though the crack patterns were retained during the calcination step (see Figure 3.2 (B)), the mesoorder could not be retained (see Figure 3.4, XRD pattern). The diminished transparency and brown color indicate formation of the bulk CdS and CdO.

The UV-Vis spectra of fresh CdS/P85 and calcined CdS films are given in Figure 3.3 (A). The high baseline of calcined CdS film in the visible region is due to formation of bulk CdO particles, which give brown color to the films. The band gap of the calcined CdS film is same as its bulk band gap, 2.42 eV (see Figure 3.3 (B)) indicating that the CdS particles grow further and form larger CdS particles, whose particle sizes are bigger than 10 nm, during the calcination step.

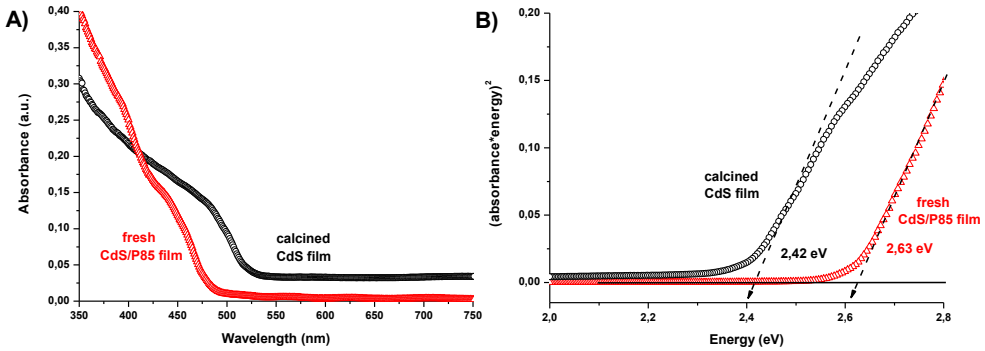

Figure 3.3 (A) UV-Vis spectra, and (B) (Absorbance*energy)^2 vs. Energy plot of the fresh CdS/P85 and calcined CdS films (as labeled in the spectra).

Figure 3.4 is the XRD pattern of the CdS films after calcination process. The peaks at 2Θ = 26.6, and 44° belong to wurtzite CdS nanoparticles (ICDD # 00-010-0454), and 33, 38, and 55° belong to cubic (NaCl structure) CdO nanoparticles (ICDD # 00-005-0640). The broad diffraction line at 2Θ = 26.6 gives a particle size of 10.3 nm, calculated using the Scherrer's equation;

$$D = \frac{0.9\ \lambda}{B\cos\Theta} \qquad \text{Equation 3.1}$$

where D is the diameter of the particles in Å, λ is the wavelength of X-ray source, 1.54078 Å, B is the corrected full width at half maximum in radian, and Θ is half of the angle of diffraction of the (100) plane at 2Θ = 33.0 in the XRD pattern in Figure 3.4. The CdO particles are calculated to be around 63 nm from the peak at 2Θ = 38. During the calcination, some of the CdS nanoparticles aggregate and grow into bulk CdS, and some are converted into cadmium oxide and form bulk CdO. The inset in Figure 3.4 is the XRD pattern of calcined CdS films at small

angles, indicating that the films do not have mesostructure after the calcination process.

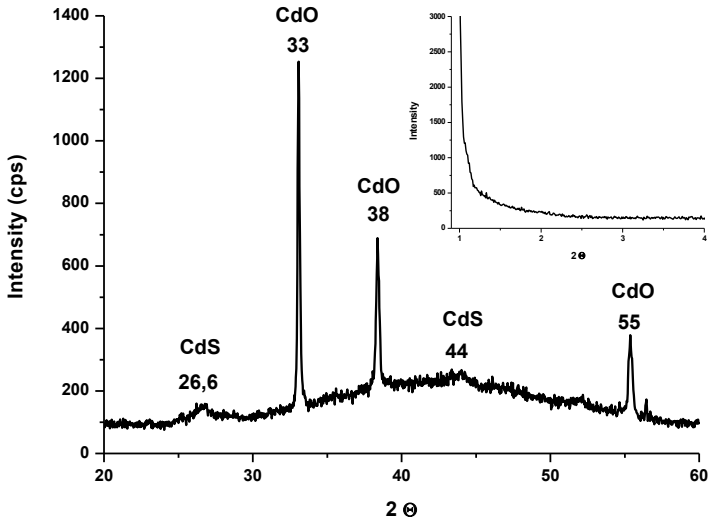

Figure 3.4 The wide angle XRD pattern of the CdS films upon calcination at 350 °C. The inset is the XRD pattern at small angles.

The SEM images of the calcined CdS films, Figure 3.5, show that the uniformity of the film and crack patterns could be retained during calcination. However, crystalline nanoparticles were formed all over the film, see Figure 3.5.

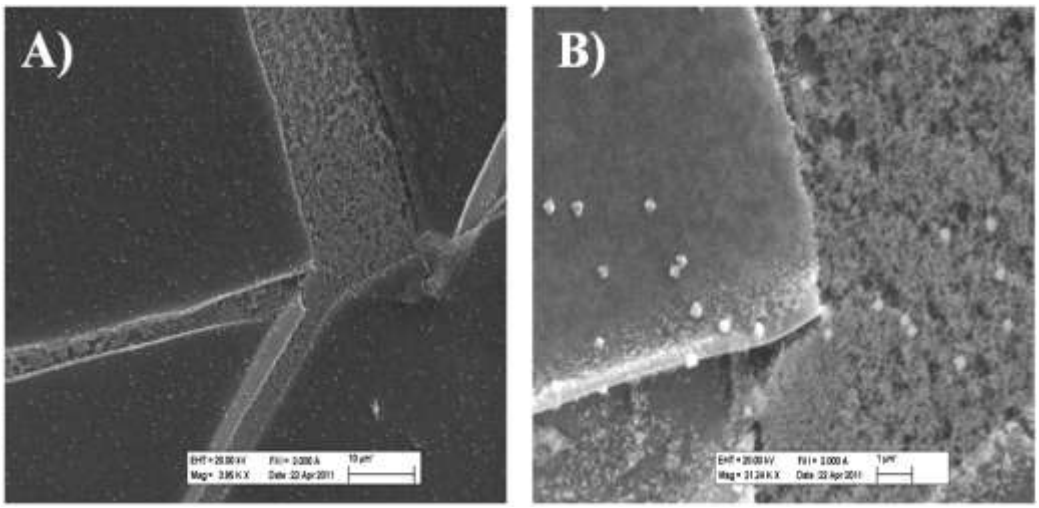

Figure 3.5 SEM images of the calcined CdS films with A) 10 µ, and B) 1 µ scale bars.

The EDX data shows that the Cd/S ratio is around 3, Figure 3.6. The Cd/S intensity ratio of bulk CdS is 1.0. High Cd signal is due to the presence of CdO particles, because almost 2/3 of the CdS nanoparticles were converted to their oxides during calcination under air.

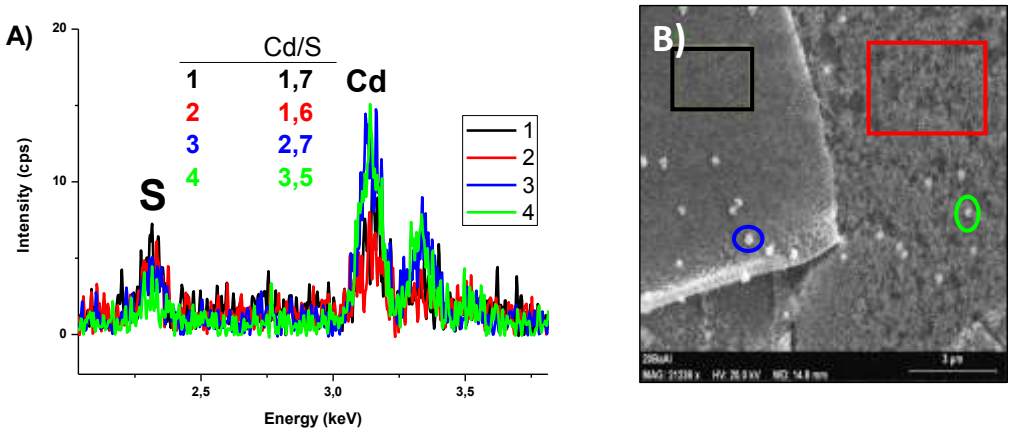

Figure 3.6 The EDX spectra of the calcined CdS film, showing the Cd/S ratio at different points on the film, and B) the SEM image of the calcined CdS film showing the areas that EDX were recorded.

The following results were obtained from the calcined CdS films, prepared using 7:1 Cd(II)/P85 mole ratio. Even though the CdS nanoparticles formed a stable mesostructured film when the mesostructured Cd(II)/P85 films are exposed to H_2S reactions, their stability cannot be retained during the calcination at 350 °C. Again, while the organic species are removed from the medium, the CdS nanoparticles aggregate and form bulk CdS. Besides, some of the CdS particles start converting into bulk CdO particles. Unfortunately, the remaining CdS film does not have any significant porosity, which is also proved by N_2 sorption measurements. Here, the main problem is the aggregation of CdS nanoparticles. This is due to the fact that the inorganic content in the mesostructured MS films is low to provide stability. Hence, during the calcination process, no rigid pore-wall can be formed in the films to prevent aggregation of the CdS nanoparticles. Therefore, as the organic species burn out from the medium, the CdS nanoparticles first start gathering, and then at higher temperatures, they convert into form bulk CdO.

Therefore, we have investigated various other approaches to obtain stable mesoporous CdS films. The liquid crystalline mesostructured Cd(II)/P85 films have been investigated during calcination to determine the temperature, where the mesophase collapse and nitrates are eliminated. If the temperature is known, at which most of the nitrates are removed from the medium while retaining the mesostructure, then the film can be first calcined to that temperature, and then reacted under H_2S atmosphere. Therefore, we expected to obtain relatively more stable mesostructured CdS films that could be calcined at high temperatures to remove the surfactants. In brief, the prestabilized CdS films could prevent the aggregation of the CdS particles so that mesoporous CdS films could be obtained.

Therefore, we have analyzed the thermal behavior of the mesostructured Cd(II)/P85 binary LC film. The IR spectra of the mesostructured Cd(II)/P85 film were collected during controlled heating of the sample, 1 °C/min, given in Figure 3.7 (A) and (B). Figure 3.7 (A) shows the peaks at 1292 and 1477 cm^{-1}, which are due to NO_3^- ions coordinated to Cd(II) ions. Figure 3.7 (B) shows the peaks in the range of 2800 and 3000 cm^{-1}, which are due to the stretching modes of C-H bonds of the surfactant. The spectral changes show that the films has to be aged at least up to 175 °C in order to remove around 50 % of the NO_3^- ions and to 225 °C in order to remove around 80% of the surfactant from the medium. The peaks due to nitrate coordinated to Cd^{2+} ions (Cd(II)-$(O_2NO)_x$) at around 1310 and 1460 cm^{-1} gradually lose their intensities while a new peak at around 1580 cm^{-1} arose. The likely origin of this peak is the formation of cadmium hydroxide species that has coordinated nitrate ions ($Cd(OH)_{x-n}$-$(O_2NO)_n$). These spectral changes clearly show that the formation of CdO/$Cd(OH)_{x-n}$-$(O_2NO)_n$ species start forming at around 175 °C.

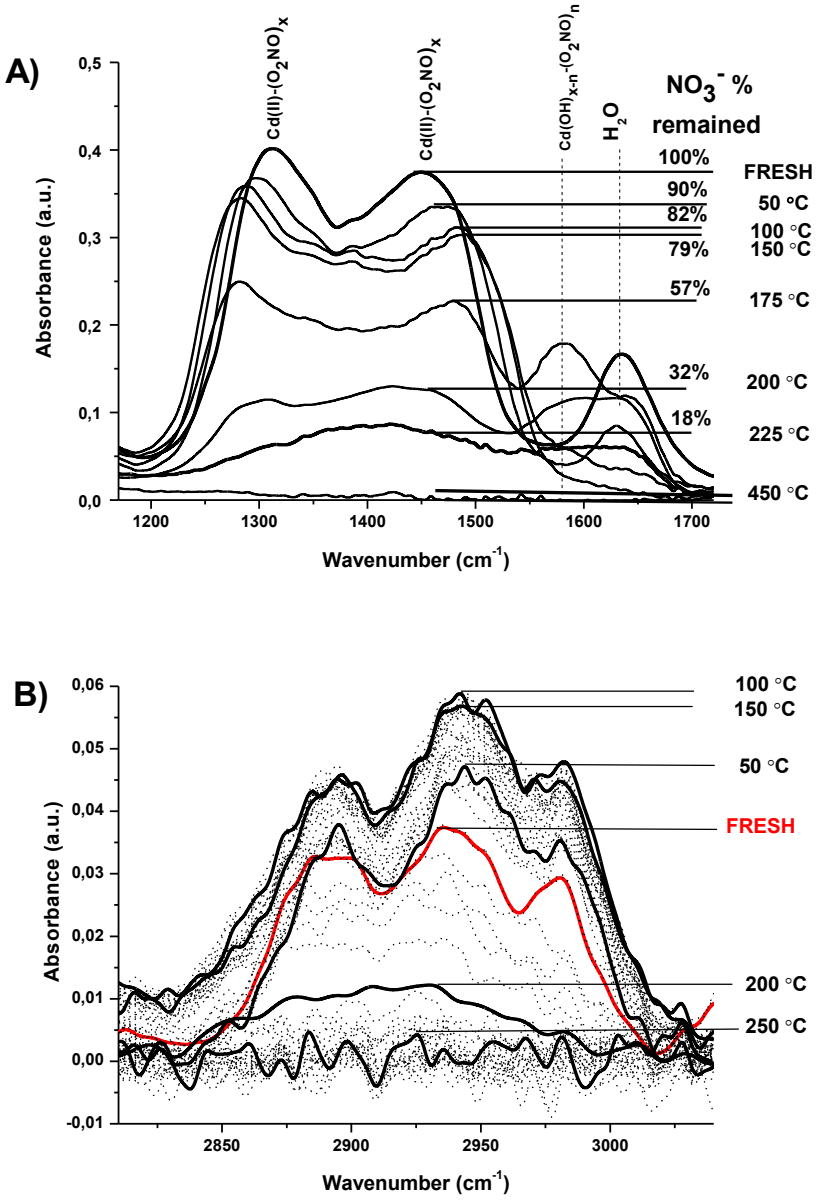

Figure 3.7 FTIR spectra of 11 Cd(II)/P85 film at various temperatures, A) peaks at 1292 and 1477 cm^{-1} due to coordinated NO_3^-, and B) peaks at 2874 and 2930 cm^{-1} due to C-H stretching.

The spectra in Figure 3.7 (B) clearly show that the peaks in the range of 2800 and 3000 cm^{-1}, which are due to the stretching modes of C-H bonds of the surfactant, significantly disappear at around 200 °C. Therefore, in order to remove most of the surfactants from the medium, the samples must be calcined at least to 200 °C.

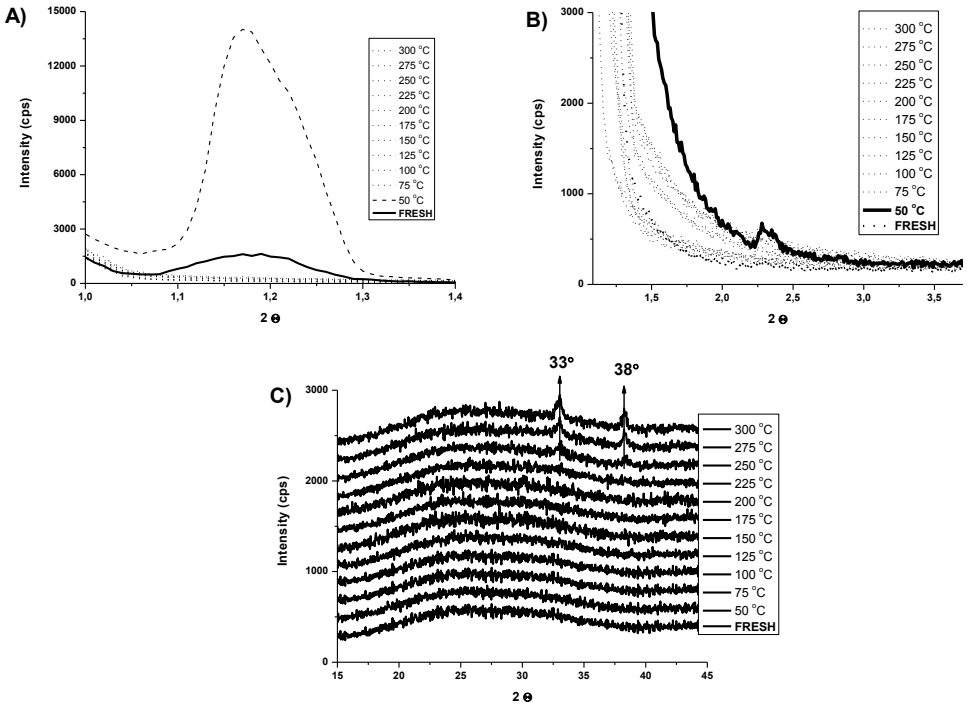

Figure 3.8 The XRD patterns of 11 Cd(II)/P85 LC film at various temperatures. A) low angle, B) low angle, and C) high angle.

In order to improve the system we increased the salt/P85 mole ratio to 11.0 and performed similar experiments. The XRD patterns of 11 Cd(II)/P85 LC film were recorded at various temperatures in order to monitor the thermal stability of the mesostructure. Figure 3.8A shows that the mesoorder is already lost above 50 °C so that the mesophase likely melts at around 50 °C. In Figure 3.8C, the diffraction lines at 33° and 38°, 2Θ due to CdO appear at around 225 °C showing that the Cd(II) species are converted into CdO at around 225 °C.

Unfortunately, there is no intermediate temperature between RT and 350 °C in order to stabilize the mesostructure prior to the H_2S reaction before further calcination to remove the surfactant species. Since the high order in the mesostructure is almost lost above 50°C, there is no meaning of doing H_2S reactions at high temperatures since it will form large CdS nanoparticles.

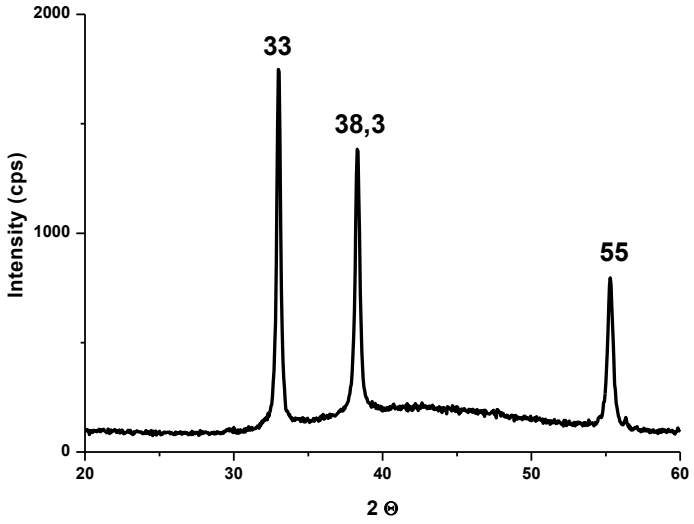

Figure 3.9 The XRD pattern of Cd(II)/P85 film at 11.0 mole ratio after calcined to 350 °C.

Therefore, the LLC films were put to calcination oven at RT and applied controlled calcination by 1 °C/min up to 350 °C. Of course, it was unavoidable for Cd(II) ions to form bulk CdO particles in such a fluidic medium. The problem of low inorganic content still exists here, as well. The XRD pattern of the calcined CdO is given in Figure 3.9. The CdO particles are around 32 nm according to Scherrer's equation.

The SEM images, in Figure 3.10, show the aggregated particles, which were also identified by EDX to be CdO. The N_2 sorption measurements and analysis of the data show no porosity. It means that calcined 11:1 Cd(II)/P85 mesostructured films collapse upon calcination and form bulk CdO crystallites.

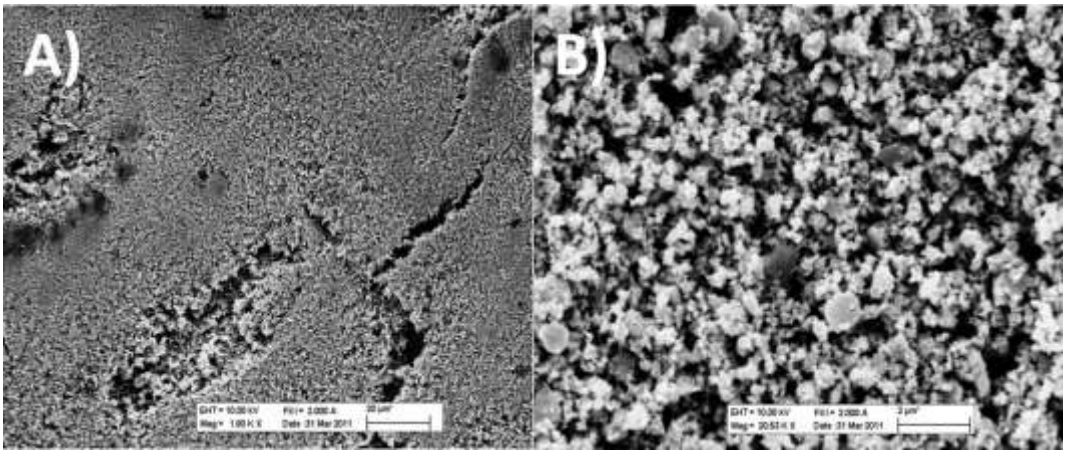

Figure 3.10 SEM images of 11 Cd(II)/P85 films after calcined to 350 °C, with A) 20 µ, and B) 2 µ resolution.

However, the mesophase of the 7:1 Cd(II)/P85 is relatively more stable than 11:1 Cd(II)/P85. At this composition, the phase is stable up to 100 °C, see their small angle XRD pattern in Figure 3.11 (A) and (B). As explained in the FTIR section, at 100 °C, ~80 % of coordinated NO_3^- ions and all the surfactant species are still present in the medium. Therefore, it is necessary to heat the samples at least up to 175 °C in order to remove ~50 % of the coordinated NO_3^- ions, Cd(II)-$(O_2NO)_x$, and let them exchange with OH^- ions, $Cd(OH)_{x-n}$-$(O_2NO)_n$. The formation of $Cd(OH)_{x-n}$-$(O_2NO)_n$ species might lead to condensation of $Cd(OH)_x$ species, and so formation of mesoporous CdO during calcination. However, at 175 ^oC, the mesostructure is also lost for this composition; see Figure 3.11 (A) and (B). The bulk CdO particles appear at around 250°C, Figure 3.11 (C). From the Scherrer's equation, the CdO particles were calculated to be 32 nm.

The SEM images in Figure 3.12 (A) and (B) also show presence of the bulk CdO particles that were also analyzed using EDX data. Besides, the N_2 sorption data also support the formation of bulk structure. The N_2 sorption data show no porosity with a very low surface area. Therefore, the presence of a more stable mesophase is not a sufficient criterion to stabilize the mesostructure to calcination. Since the metal ion density is very low and there is no other supporting reagent in the medium, aggregation of the particles and collapse of the mesoorder are unavoidable.

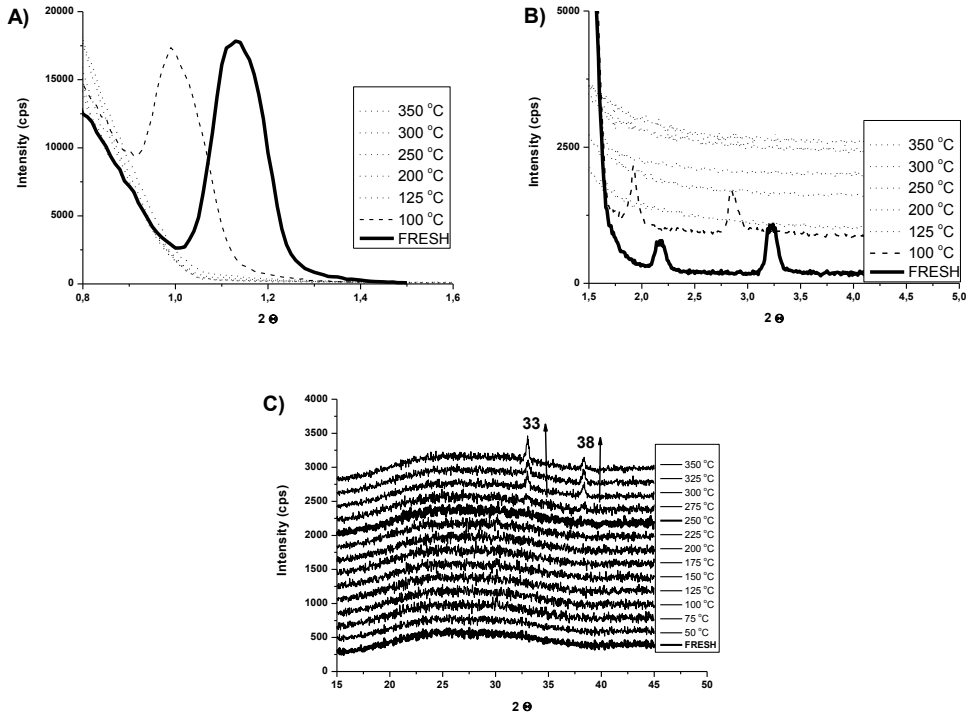

Figure 3.11 XRD pattern of 7 Cd(II)/P85 LC film calcined up to various temperatures. A) low angle, B) low angle, and C) high angle.

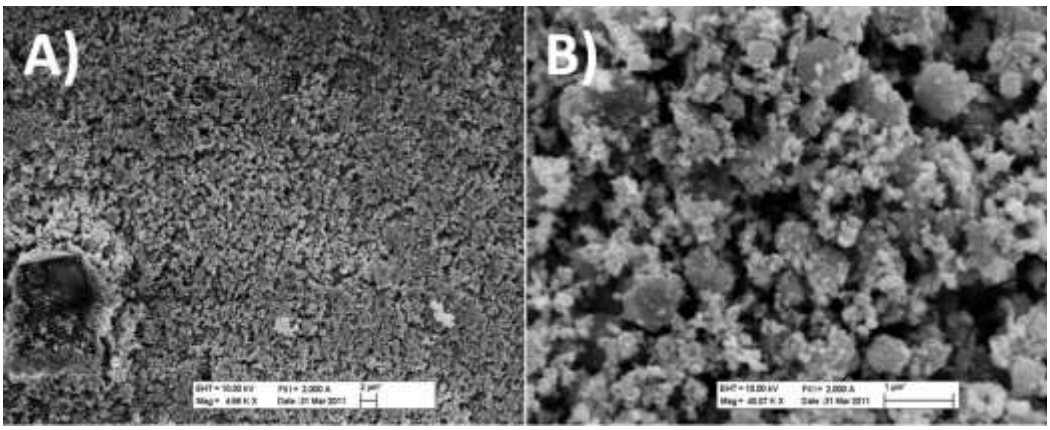

Figure 3.12 SEM images of 7 Cd(II)/P85 films after calcined to 350 °C, with A) 2 μ, and B) 1 μ resolution.

The stable mesoporous films of SiO_2 have been synthesized by many groups by using LCT method.[7, 160-162] As mentioned already in the previous chapter, theoretically, the required amount of SiO_2 in a nonionic surfactant system to synthesize a stable mesoporous film is around 6-7 $SiO_2/C_{12}EO_{10}$ mole ratio, and

it corresponds to around 60-80 SiO_2/P85 mole ratio. That means the metal ion density should be increased up to around 60 metal ion/P85 mole ratios while retaining the LLC mesophase. Hence, it can be expected that the LLC template would be rigid enough during calcinations so that we would be able to synthesize the mesoporous MO thin films from which the synthesis of the mesoporous MS or MSe thin films would be possible. Therefore, the thermal behavior of 60 Cd(II)/P85 composition has been investigated using FTIR spectroscopy and XRD techniques by heating the sample at a rate of 1 °C/min. The FTIR spectra were almost similar to low salt compositions, given in Figure 3.13 (A) and (B). In order to remove 50 % of the NO_3^- ions, we had to calcine the films at least to 175 °C, see Figure 3.13 (A). The peaks due to nitrate coordinated to Cd^{2+} ions (Cd(II)-$(O_2NO)_x$) at around 1310 and 1460 cm^{-1} gradually lose their intensities while a new peak at around 1580 cm^{-1} arose. The likely origin of this peak is the formation of cadmium hydroxide species that has coordinated nitrate ions ($Cd(OH)_{x-n}$-$(O_2NO)_n$). These spectral changes clearly show that the formation of CdO/$Cd(OH)_{x-n}$-$(O_2NO)_n$ species start forming at around 175 °C (see page 49). The spectra in Figure 3.13 (B) clearly show that the peaks in the range of 2800 and 3000 cm^{-1}, which are due to the stretching modes of C-H bonds of the surfactant, significantly disappear at around 200 °C. Therefore, in order to remove most of the surfactants from the medium, the samples must be calcined at least to 200 °C.

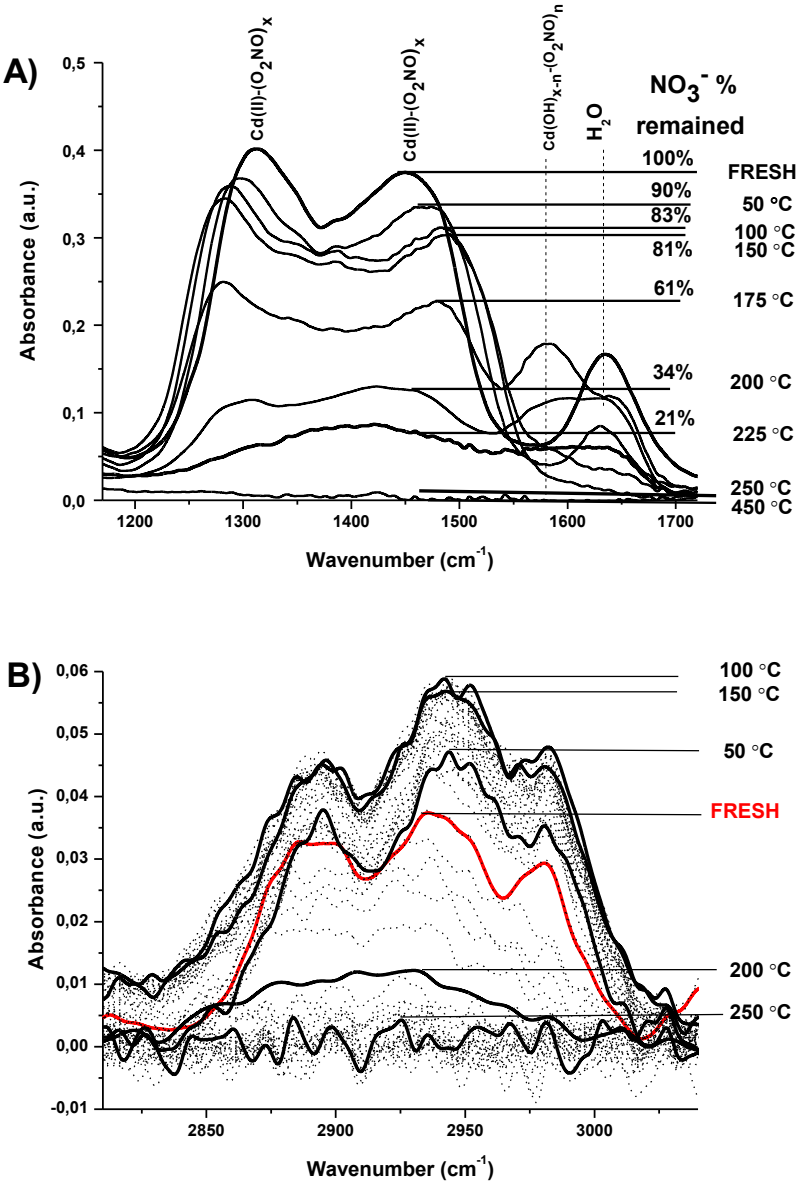

Figure 3.13 IR spectra of 60 Cd(II)/P85 film at various temperatures, A) peaks at 1292 and 1477 cm^{-1} due to coordinated NO_3^-, and B) peaks at 2874 and 2930 cm^{-1} due to C-H stretching.

At 60 Cd(II)/P85 mole ratio, no LLC mesophase was observed either at RT or at high temperatures by XRD measurements. We calcined the films under POM to see if there is a formation of mesostructure at higher temperatures. Notice that the hexagonal mesophase is briefringent between crossed polarized under the POM. The POM images in Figure 3.14 were recorded at 25° C (A), 185° C (B), 190° C (C), and 300° C (D). There was no observable change until 185°C, and above this, some features appear in the images. The heating step up to 185^{o}C did

not show any structural changes. From the XRD and POM results, it is clear that there is no formation of salt crystals. It is likely that the salt species are in their molten phase. Therefore, based on the assumption of formation of cadmium hydroxide species that has coordinated nitrate ions ($Cd(OH)_{x-n}$-$(O_2NO)_n$) from the FTIR analysis given above, we expected that even though the mesoorder does not form at any temperature, the CdO/$Cd(OH)_{x-n}$-$(O_2NO)_n$ species formed in the molten phase could be polymerized during slow heating process to form rigid walls and prevent aggregation during controlled calcinations. However, the calcination still resulted in bulk CdO domains with no porosity. It seems that the preformed CdO particles in the medium during calcination did not form the mesostructure, and subsequently, aggregation of the CdO particles could not be prevented.

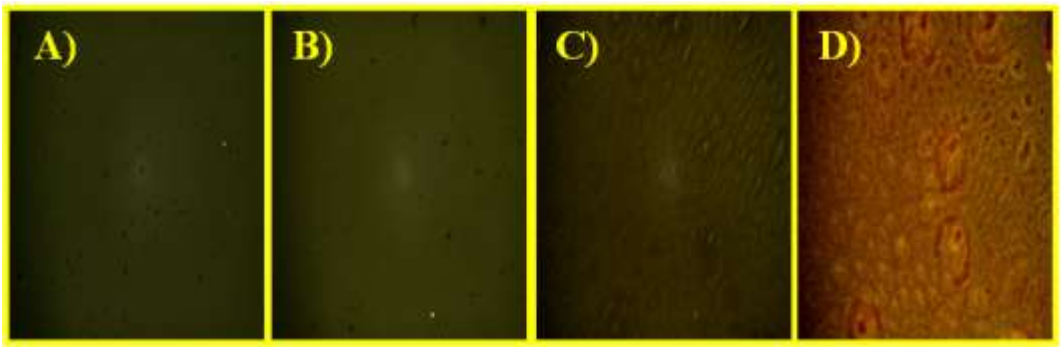

Figure 3.14 POM images of 60 Cd(II)/P85 films at A) 25 °C, B) 185 °C, C) 190 °C, and D) 300 °C.

Therefore, from those calcination experiments above, it has been found that the metal ion concentration definitely affects the stability during the calcination step. If it is low, there is no way to overcome aggregation of particles and formation of bulk domains. At the same time, increasing only the metal ion content is not enough to provide this required stability. Even though the metal ion content is increased to 60:1 Cd(II)/P85, the medium is still fluidic. Since the medium is still fluidic enough, the CdO or CdS particles gather and lead to the same result. There is no mesophase at such high salt concentrations.

In our group, parallel to this work, LLC mesophase of salt-two surfactants is investigated in detail and found out that in the presence of a charged surfactant,

the mesophase of $C_{12}EO_{10}$ can take up 8.0 moles of salt per mole of $C_{12}EO_{10}$. This is equivalent to the inorganic/organic ratio in the synthesis of mesoporous silica using LCT method. Therefore, the two surfactant salt system was also investigated under the topic of this thesis.

3.1.2 $[Cd(H_2O)_4](NO_3)_2$ – $C_{12}EO_{10}$ – CTAB LC templates for meso - MS(Se) synthesis

By cooperation of a charged surfactant (CTAB) with $C_{12}EO_{10}$ during self-assembly of LLC mesophase, the metal ion to $C_{12}EO_{10}$ mole ratio could be increased up to 8.0 salt/$C_{12}EO_{10}$ mole ratio, which is a record high metal ion density in an LLC mesophase in the literature.[46] The mesostructured films at those salt concentrations are relatively more stable than the ones explained above. Hence, this new LLC mesophase might be used to obtain mesostructured CdS/CdSe films, and then calcined to give mesoporous CdS/CdSe films.

$[Cd(H_2O)_4](NO_3)_2$ – $C_{12}EO_{10}$ – CTAB system forms LLC mesophase up to 15 Cd(II)/$C_{12}EO_{10}$ mole ratio by adjusting the CTAB/$C_{12}EO_{10}$ mole ratio (salt concentration increases with increasing CTAB concentration in the medium) as shown in Figure 3.15. As the salt concentration increases in the LLC mesophase, the small angle x-ray diffraction line shifts to smaller angles indicating the larger d-spacing in the mesostructure, Figure 3.15 The larger d-spacing is most probably due to expansion of hydrophilic ethylene oxide (EO) parts of the mesophase. Above 15 Cd(II)/ $C_{12}EO_{10}$, there is no LLC mesophase and even increasing the CTAB amount does not help to improve salt concentration in the LLC mesophase.

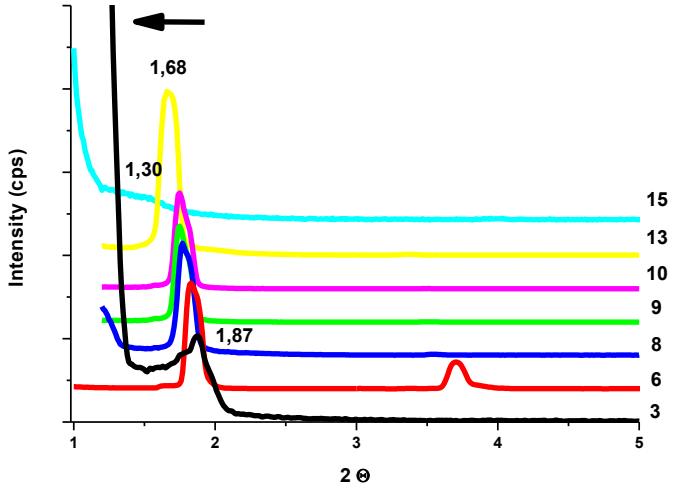

Figure 3.15 XRD patterns of LLC mesophase of $[Cd(H_2O)_4](NO_3)_2$ – $C_{12}EO_{10}$ – CTAB films at Cd(II)/ $C_{12}EO_{10}$ mole ratio of 3, 6, 8, 9, and 10.

Even though the LLC mesophase of $[Cd(H_2O)_4](NO_3)_2 - C_{12}EO_{10} - CTAB$ system forms up to 15 $Cd(II)/C_{12}EO_{10}$ mole ratio, it is stable up to 8 $Cd(II)/C_{12}EO_{10}$ mole ratio and less stable in the range of 8 to 15 $Cd(II)/C_{12}EO_{10}$ mole ratio. The stability of the film samples can be monitored by recording XRD patterns of aged samples in time. In 40 minutes, the XRD line 1.66°, 2Θ shifts to higher angle while its intensity decreases and a new diffraction line arised at 2.0° and shifts to higher angle while its intensity increases, see Figure 3.16 (A). The same trend is observed for the second XRD line at 3.37°, 2Θ. After 1 h, as shown in Figure 3.16 (B), the second XRD line decreases in intensity while the third XRD line arises and increases in intensity and shifts to a lower angle in time. The higher angle XRD patterns are shown in Figure 3.16 (C). The XRD lines arise at 2Θ of 13.64, 17.45, 27.47, 35.28, and 38.26°, which are due to the formation of $[Cd(H_2O)_6](NO_3)_2$ crystals all over the film. The LLC mesophase, first, releases the excess salt; therefore, the XRD lines shift to higher angle, in the small angle region, due to decrease in d-spacing upon shrinkage of EO corona region. After 1 h, the lines arise at 2Θ of 5.28, 10.67, and 15.72°, which are due to CTAB crystals. As the CTAB amount decreases in the mesophase, d-spacing increases due to expansion of EO corona region. Hence, the shift in the lines at 2.02 to 1.87°, 2Θ are due to the release of excess CTAB out of the mesophase. The new composition at some salt and CTAB concentration stabilizes in 1 day.

It is also observed that there is a linear correlation between the CTAB concentration used in the synthesis and salt concentration that is contained in the LLC system (Figure 3.17). Addition of CTAB improves the salt uptake of the LLC system so that LLC mesophase can form up to 13 $Cd(II)/C_{12}EO_{10}$ mole ratio.

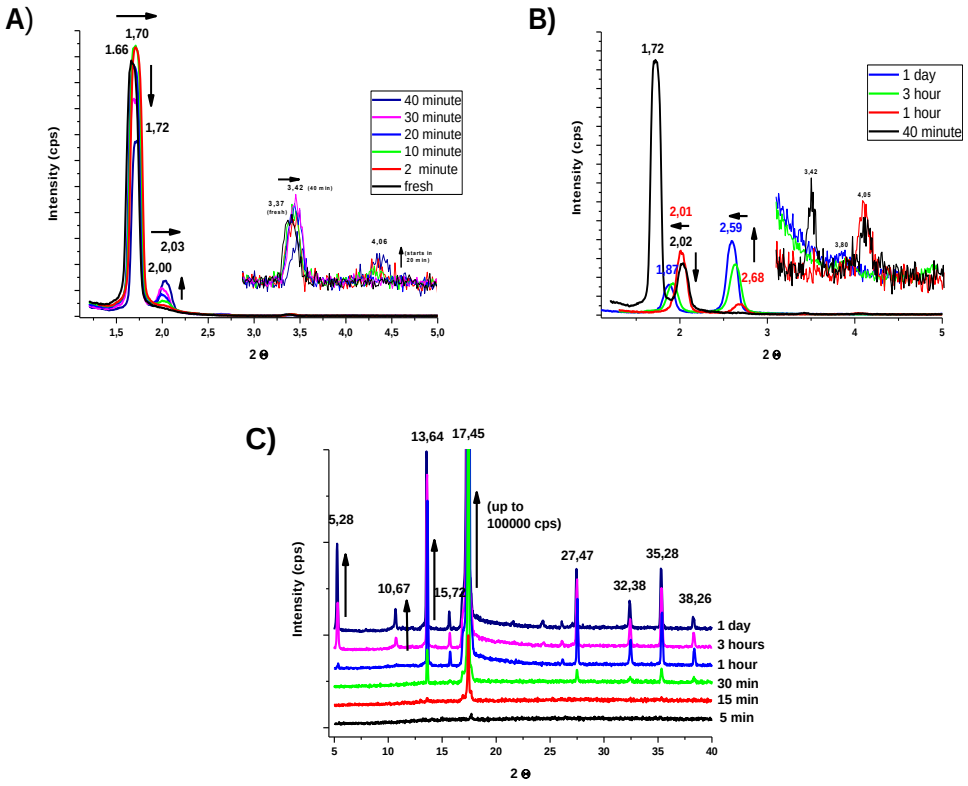

Figure 3.16 The XRD patterns of LLC mesophase of 13 Cd(II)/$C_{12}EO_{10}$ of $[Cd(H_2O)_4](NO_3)_2$ – $C_{12}EO_{10}$ – CTAB in time. A) As prepared to 40 minutes, and B) from 40 minutes to 1 day aged; C) 5 minutes to 1 day aged sample, in the high angle region (aging times are given in the figures).

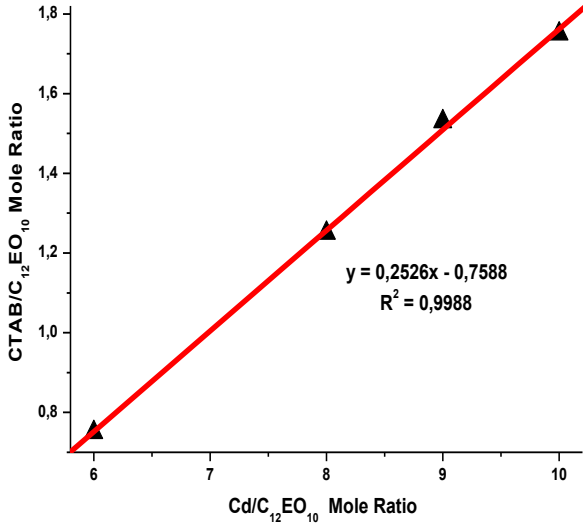

Figure 3.17 CTAB/$C_{12}EO_{10}$ ratio versus Cd(II)/$C_{12}EO_{10}$ mole ratio plot of $[Cd(H_2O)_4](NO_3)_2$ – $C_{12}EO_{10}$ – CTAB LC mesophases.

At constant salt concentration, the d-spacing linearly decrease as CTAB amount increases, see Figure 3.18 (A). The d-spacing linearly increases as the salt concentration increases at a constant CTAB concentration; see Figure 3.18 (B). The decrease in d-spacing is due to the shrinkage of the hydrophilic ethylene oxide surfactant domains with the addition of CTAB, and the increase is due to expansion of EO corona upon addition of salt into the medium.[46]

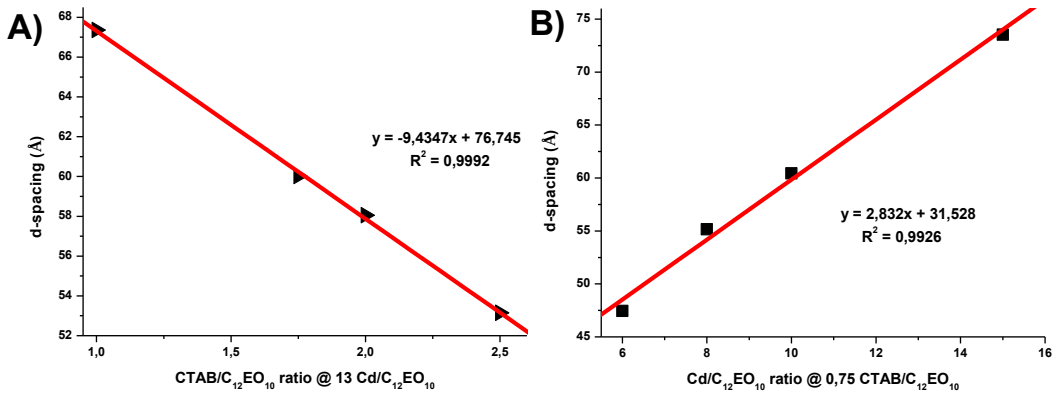

Figure 3.18 Linear dependence of d-spacing versus A) CTAB/$C_{12}EO_{10}$ ratio for 13 Cd(II)/$C_{12}EO_{10}$, and B) Cd(II)/$C_{12}EO_{10}$ ratio for 0.75 CTAB/$C_{12}EO_{10}$ for $[Cd(H_2O)_4](NO_3)_2$ – $C_{12}EO_{10}$ – CTAB LC mesophases.

These trends can be used to calculate the salt and CTAB concentration of formed mesophase after the excess salt and CTAB were leached out of the mesophase as given above for 13 Cd(II)/$C_{12}EO_{10}$ and n CTAB/$C_{12}EO_{10}$, where n changes from 1.00 to 2.5, (Table 3.1). The shift from 1.66 to 2.01° is due to decrease in d-spacing from 5.3 nm to 4.4 nm indicating the formation of mesophase at around 9.73 salt concentrations. The shift from 2.01 to 1.87° is due to increase in d-spacing from 4.4 nm to 4.7 nm indicating the decrease of CTAB concentration of the mesophase to 2.15. When the change in the XRD pattern of the films is analyzed for 13 Cd(II)/$C_{12}EO_{10}$, it can be clearly seen that increase in CTAB amount improves the salt uptake in the LLC mesophase. At 1.0 CTAB/ $C_{12}EO_{10}$ mole ratio, Cd(II)/ $C_{12}EO_{10}$ mole ratio in the mesophase decreases to 5.35 after crystallization, and CTAB/$C_{12}EO_{10}$ mole ratio decreases to 0.59 whereas at

2.5 CTAB/ $C_{12}EO_{10}$ mole ratio, the LLC mesophase can stabilize at 9.73 Cd(II)/$C_{12}EO_{10}$ and 2.15 CTAB/$C_{12}EO_{10}$ mole ratios. However, the presence of above 2.5 CTAB concentrations does not improve the salt uptake of the mesophase anymore (it is likely that 2.5 CTAB/$C_{12}EO_{10}$ mole ratio is upper limit of this LLC mesophase).

Table 3.1 The change in the XRD peak positions and d-spacings of $[Cd(H_2O)_4](NO_3)_2 - C_{12}EO_{10}$– CTAB LC film samples for 13 Cd(II)/ $C_{12}EO_{10}$ ratio in time.

Cd(II)/ $C_{12}EO_{10}$ as prepared	**CTAB/ $C_{12}EO_{10}$** as prepared	**fresh 2Θ**	**d (Å)**	**2nd 2Θ**	**d (Å)**	**3rd 2Θ**	**d (Å)**	**Cd/ $C_{12}EO_{10}$** after cryst	**CTAB/ $C_{12}EO_{10}$** after cryst
13	1.00	1.31	67.36	1.93	45.72	1.78	49.57	5.35	0.59
13	1.75	1.47	60.02	1.88	46.94	1.75	50.42	8.38	1.38
13	2.00	1.52	58.05	1.92	45.96	1.73	51.00	8.73	1.46
13	2.25	1.64	53.80	1.89	46.69	1.82	48.48	10.49	2.06
13	2.5	1.66	53.16	2.01	43.90	1.87	47.19	9.73	2.15

We have to emphasize once more that increasing the salt concentration is necessary in order to improve the rigidity of the LLC mesophase so that we can prevent the phase separation during or after the H_2A (A is S or Se) reaction. Therefore, carrying the H_2A reactions at salt concentrations of 13 Cd(II)/$C_{12}EO_{10}$ and analyzing the resulting samples are important. However, as the metal ion density increases in the mesophase, there is a significant decrease at the metal ion amount reacted with H_2S (Figure 3.19). At 8 Cd(II)/$C_{12}EO_{10}$ concentration, 80% Cd(II) ions reacted with H_2S but for 10 Cd(II)/$C_{12}EO_{10}$ concentration, it is only 10%, which means that Cd(II) ions cannot be converted to their sulfides almost at all.

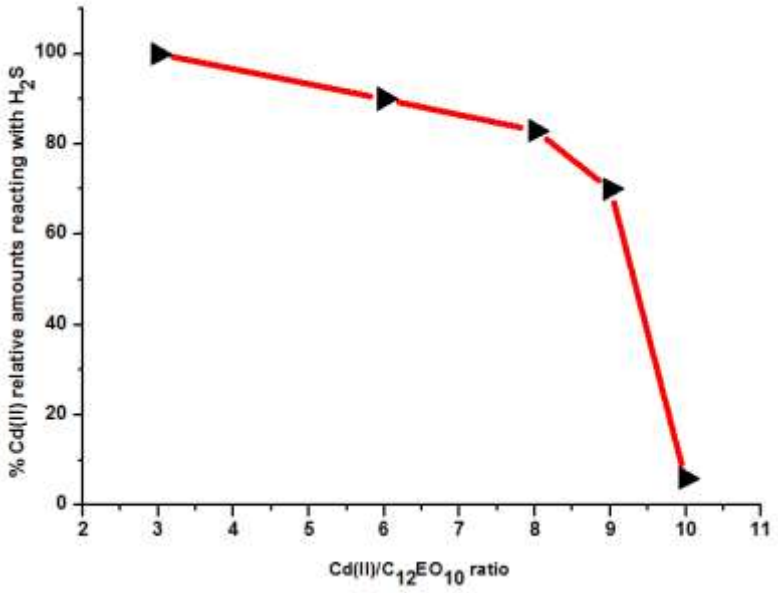

Figure 3.19 Calibration plot of % Cd(II) relative amounts reacting with H_2S gas at different Cd(II)/$C_{12}EO_{10}$ ratios in the $[Cd(H_2O)_4](NO_3)_2$ – $C_{12}EO_{10}$ – CTAB LC films.

FTIR analysis of the films before and after H_2S reactions reveals relative amounts of metal ions reacting with H_2S (Figure 3.20). The peaks at 1300 and 1460 cm^{-1} indicate the bidentate coordination of nitrate ions to Cd^{2+} ions. Intensity of those peaks decrease as Cd^{2+} ions react with H_2S while they are converted to their sulfides and the coordinated nitrate ions become free or eliminated as HNO_3. During H_2S reactions, hydronium ions of H_2S form nitric acid. Huge amount of nitric acid forms and shifts the equilibrium to the left in Equation **3.2**. The intensity of peaks at 1300 and 1460 cm^{-1} increases since nitric acid causes decomposition of the CdS particles back to their nitrates.

$$Cd^{2+} + 2NO_3^- + H_2S \rightleftharpoons CdS_{(s)} + 2HNO_{3(aq)} \qquad \text{Equation 3.2}$$

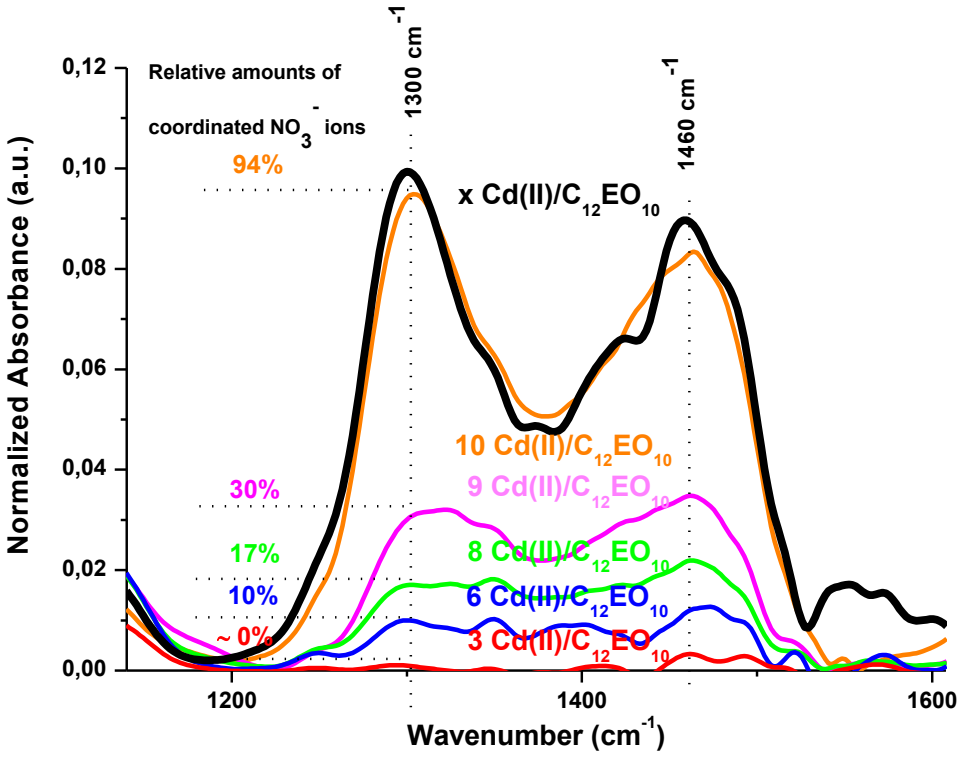

Figure 3.20 FT-IR analysis of films before (x Cd(II)/$C_{12}EO_{10}$) and after H_2S reactions at x = 3, 6, 8, 9, and 10 Cd(II)/$C_{12}EO_{10}$ mole ratios in the N-O stretching region 1200-1600 cm^{-1}. The numbers are the relative numbers of the coordinated NO_3^- ions remain in the media after H_2S reactions.

Moreover, the phase separation occurs upon exposure to the H_2S gas as shown in Figure 3.21. The numbers inside the colored chambers in Figure 3.21(C) are the EDS results of the Cd to S atomic ratio. The Cd to S atomic ratio is not homogenous all over the film. Therefore, we can say that adding CTAB to metal/$C_{12}EO_{10}$ LLC system increases the metal ion density further. However, high amount of metal concentration itself does not solve the stability problem against H_2S reactions or calcination procedures.

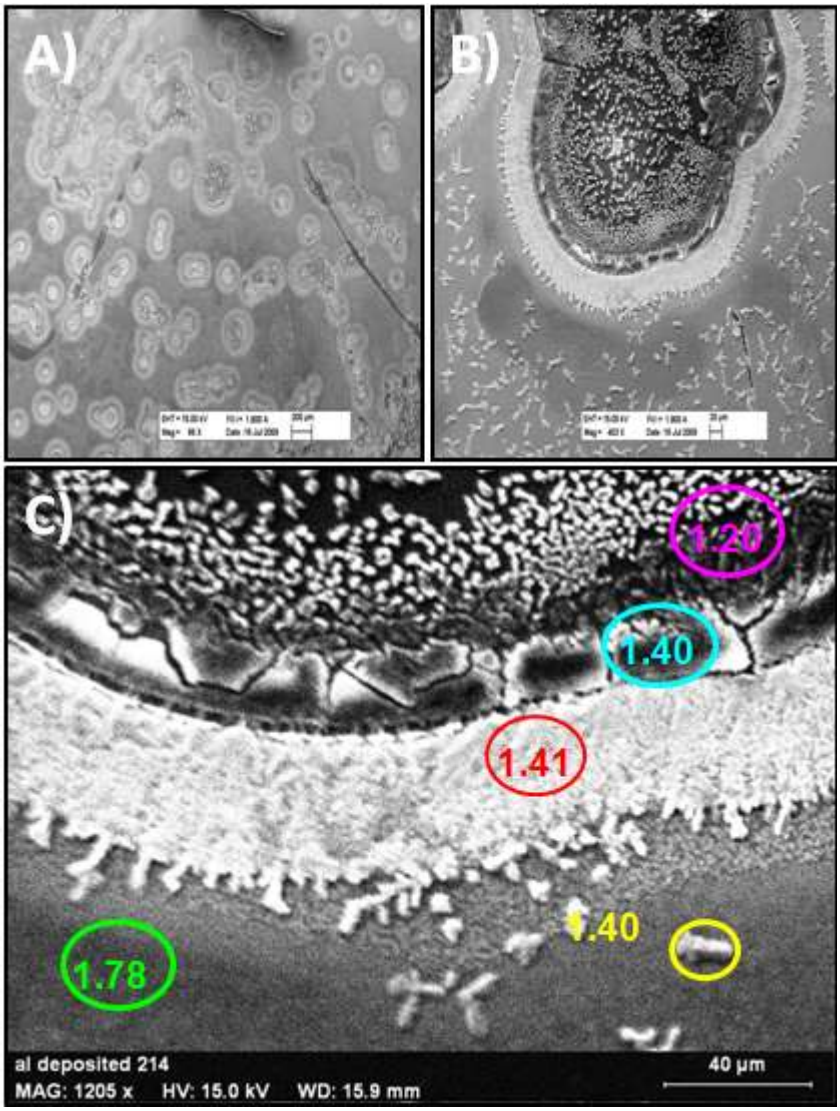

Figure 3.21 (A), (B), and (C) are the SEM images of the $[Cd(H_2O)_4](NO_3)_2$ – $C_{12}EO_{10}$ – CTAB LC film sample at 13 Cd(II)/$C_{12}EO_{10}$ after exposed to H_2S. The numbers in (D) are EDS results of Cd to S ratio.

Furthermore, when the LLC films at high salt concentrations were heated to high temperatures (around 90^{o}C), it was observed that the first XRD line detected shifted to higher angles. For $[Cd(H_2O)_4](NO_3)_2$–$C_{12}EO_{10}$–CTAB LC film with a 13Cd(II)/$C_{12}EO_{10}$, the line shifted from 1.66° to 1.93° indicating the decrease in d-spacing (Figure 3.22). Therefore, the CTAB amount contributing to the formation of LC mesophase increases and so the stability of the sample can be increased further. Hence, we expected that performing the H_2S reactions at high temperatures around 90 ^{o}C should provide more rigid metal sulfide films since the template would be more rigid and removal of HNO_3 under vacuum should be

possible. However, the results did not improve at all, most probably due to low metal ion concentration and very fast conversion of sulfides back to their nitrates.

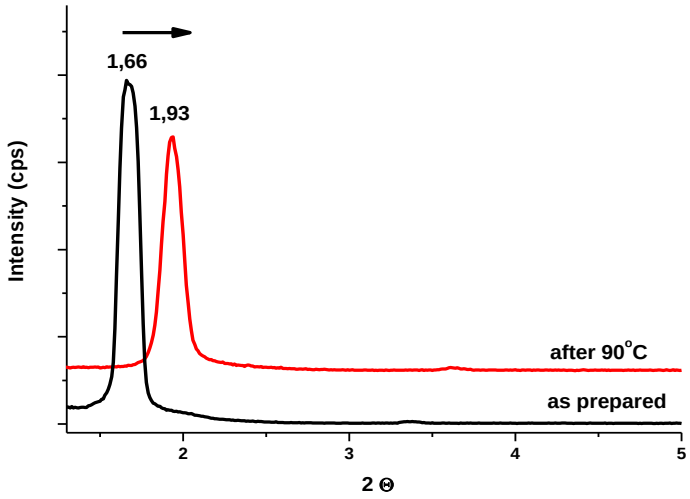

Figure 3.22 XRD pattern of $[Cd(H_2O)_4](NO_3)_2$ – $C_{12}EO_{10}$ – CTAB LC film sample at 13 Cd(II)/$C_{12}EO_{10}$ as prepared and after heating at 90 °C.

These results have been used to define the problem of the synthesis of mesostructured and mesoporous MS (or MSe) thin films by exposing the LLC mesophase to H_2S (or H_2Se). It has always been recognized that the metal ion density in the mesophase had to be increased in order to rigidify and eliminate the phase separation. However, while increasing the metal ion density, presence of NO_3^- leads to the formation of a huge amount of nitric acid upon H_2A reactions and causes conversion of CdS (or CdSe) back to cadmium nitrate. Hence, in order to form stable MS or MSe nanoparticles, nitrate ions have to be removed from the medium before or during the H_2A reactions. The only well known way to get rid of the nitrate ions is to age the sample at high temperatures.

Hence, all these results reveal that the mesoporous MO or MS or MSe films cannot be obtained directly from TMS/Surfactant binary LLC system. The LLC system has to be strengthened with an agent that can polymerize during self-assembly and form rigid inorganic walls in the hydrophilic shell during calcination so that the aggregation of MO or MS or MSe domains can be prevented. For that purpose, titania and silica can be the candidates to investigate

such a problem because they can polymerize during self-assembly of the mesophase to form stable mesoporous films of MO or MS or MSe.

3.2 Rigidifying Mesostructure with TiO_2

3.2.1 Synthesis of Stable Mesostructured CdS-TiO_2 and CdSe-TiO_2 Coupled Semiconductor Thin Films

The rigidity of the mesostructured materials obtained from an LLC phase is mainly based on the nature of the inorganic precursors used. The presence of inorganic precursors, which can polymerize makes a significant contribution to the rigidity of the mesostructure. Most transition metal salts, such as $[Cd(H_2O)_4](NO_3)_2$ and $[Zn(H_2O)_6](NO_3)_2$, do not polymerize under acidic/neutral conditions while some of inorganic compounds such as titanium alkoxides can polymerize in an aqueous medium. Another key factor defining the rigidity of the mesostructure is the amount of polymerizing inorganic agent used in the medium. The LLC mesophase starts rigidifying, when enough polymerizing inorganic agent is added to the medium.

Here, the polymerizing agent was chosen to be titanium butoxide due to its highly controlled condensation in a solution, and utility in many applications such as catalysis, photocatalysis, optics, sensing and energy conversion, etc. The $[Cd(H_2O)_4](NO_3)_2$/P123 LLC system was known to have LLC mesophase between 2 and 13 Cd(II)/P123 mole ratios. Therefore, using the LLC phase of salt/P123 as a template, the Ti(IV)/P123 mole ratio have been gradually increased up to 80 mole ratio at all compositions of $[Cd(H_2O)_4](NO_3)_2$ between 2 and 13 Cd(II)/P123 mole ratios. P123 was used as a surfactant, because the synthesis of mesostructured titania films had been well established. The main factors to be considered and optimized are the choice and the amount of acid used in the medium, relative humidity, temperature, and time of aging since they extensively affect the condensation of titania.

The acid source used so far has been HCl in the literature[27, 163, 164] in order to control the condensation of titania precursors.[165] However, we found out that HCl causes separation of salt crystallites in the $[Cd(H_2O)_4](NO_3)_2$/P123 LC system at high salt concentrations. Therefore, HNO_3 has been used throughout this investigation.

Following these considerations, it has been found out by changing the Cd(II)/P123 mole ratios between 2 and 13, and Ti(IV)/P123 mole ratio between 0 and 80, rigid mesostructured titania could be obtained over 35 Ti(IV)/P123 mole ratios at all salt compositions.[166] As the ratio of titania in the medium is increased, the samples go through phase transitions from LLC like matter to soft matter to rigid matter.[166] While the amount of titania determines the type of phase, the amount of Cd(II) determines the order of the mesostructure. At low salt and titania source concentrations, up to 2 mole ratio of Cd(II)/P123 and 15 mole ratio of Ti(IV)/P123, a phase separation occurs upon aging films revealing LC like behaviors. At a titania concentration above 20, plastic-like materials so called soft matter are formed. Above 15 Cd(II)/P123 mole ratios, completely disordered materials are formed.

Above 35 Ti(IV)/P123 mole ratios, the samples are still disordered at ambient conditions. Therefore, the meso-order had to be improved by controlling the conditions necessary for titania condensation. It is known that the rigid mesostructured titania materials can be synthesized by controlling the relative humidity of the medium.[67, 164] The reason is that the formation of Ti-O-Ti bonds is directed trough consecutive hydrolysis and condensation steps in a very short time.[165] On the other hand, pH of the medium must be adjusted to be acidic enough (pH~1) during the condensation step of titania species. Taking those into considerations, amount of HNO_3 and humidity were optimized to obtain ordered mesostructures, which were monitored using XRD measurements. The optimum values were set to be 1.0 g HNO_3 and 12 hrs of aging at a 50 % relative humidity (RH) at 30 °C. Finally, very stable, highly ordered mesostructured titania materials were synthesized with a desired amount of Cd(II) species. These conditions effectively polymerize titania species and as a result provide rigidity to the material to diminish aggregation of titania or salt species. Besides of that, since the nitrate ions play important roles by coordinating to titania, it also helps to overcome the aggregation problem. Based on those reasons, the rigid mesostructured titania materials prepared under optimized conditions were the best candidates for the synthesis of stable mesostructured CdSe-TiO_2 films called

meso-xCdSe-yTiO_2 at which x is the mole ratio of Cd(II)/P123 (changed from 2 to 13) and y is the mole ratio of TiO_2/P123, 60.

Therefore, stable CdS and CdSe nanoparticles can be synthesized in the channels of mesostructured titania films by exposing the mesostructured Cd(II)-TiO_2 films to H_2S and H_2Se, respectively under a N_2 atmosphere.[75] The Cd(II) ions have been incorporated into the channels of mesostructured titania by evaporation induced self-assembly (EISA) approach. Well-ordered mesostructured Cd(II) titania films, called meso-Cd(II)-TiO_2, form up to 15 Cd/P123 mole ratio for a 60 mole ratio of Titania/P123. The order of the meso-xCd(II)-60TiO_2 thin films was enhanced by aging at 50% relative humidity (RH) at RT for 12 hrs. Relatively 90% of the nitrate ions were removed from the medium by further aging the samples at 130° C for 4 hrs. According to XRD analysis, the mesostructure was retained during aging and H_2S/H_2Se reactions (Figure 3.23). The diffraction line(s) gradually shifts to a higher angle, typically the small angle line at 0.95° (92.9 Å d-spacing) shifts to 1.22° (72.4 Å d-spacing) upon aging and shifts slightly to a lower angle or remains the same after H_2S (or H_2Se) treatment. The shift of the peaks towards higher angles can be explained as a contraction of structure due to further condensation of the titania walls and most probably formation of some $Cd(OH)_2$ and/or CdO species, and shift back to lower angle due to expansion of the structure by the formation of CdS (or CdSe) nanoparticles in the walls.

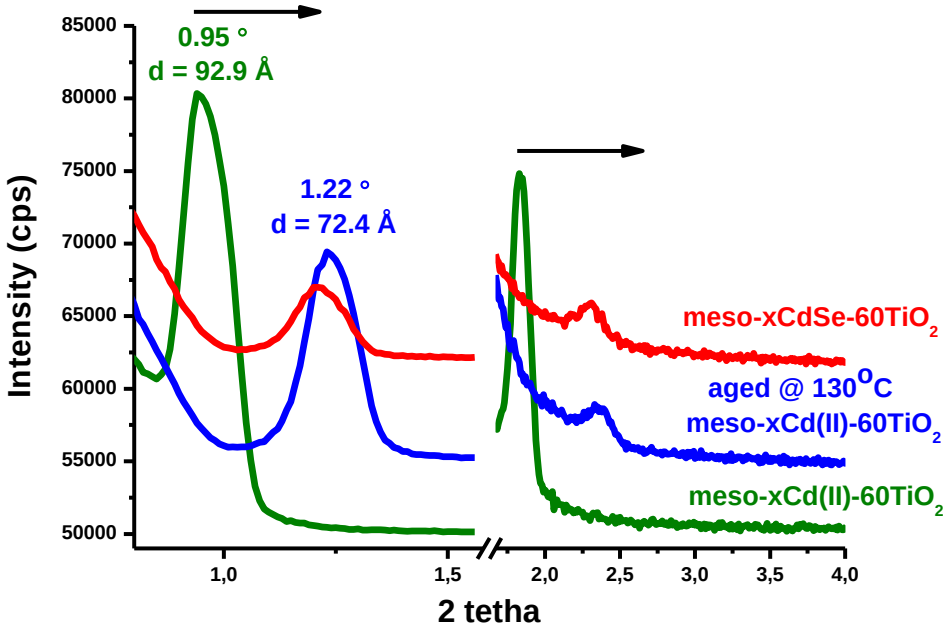

Figure 3.23 XRD patterns of oriented meso-xCd(II)-60TiO_2 thin films after aging at RT at 50 % RH for 12 hrs (bottom), after aged at 130 °C for 4 hrs (middle), and after exposed to H_2Se reactions (top).

The formation of well-ordered channels oriented parallel to the film surface with curling channel patterns were proved by the TEM images (Figure 3.24 (A)). Those images were obtained from the samples calcined at 350 ˚C, because the uncalcined samples are sensitive under the electron beam in the microscope. The spacing between the channels are 7.3 nm, corresponding to (100) planes of the hexagonal meso-13CdO-60TiO_2 samples. Figure 3.24 (A) is the TEM image of the sample before H_2Se reactions. Figure 3.24 (B) is the HRTEM image of a sample exposed to H_2Se reaction with a 5 nm scale bar and the crystalline CdSe nanoparticles are observed all over the sample. Figure 3.24 (*i*) and (*ii*) are the inverse FFT images of the selected areas in Figure 3.24 (B), and belong to (110) planes of cubic CdSe nanoparticles with a 4.29 Å spacing. The inverse FFT image of the selected area in Figure 3.24 (*iii*) belongs to (101) planes of anatase TiO_2 with 3.49 Å spacing.

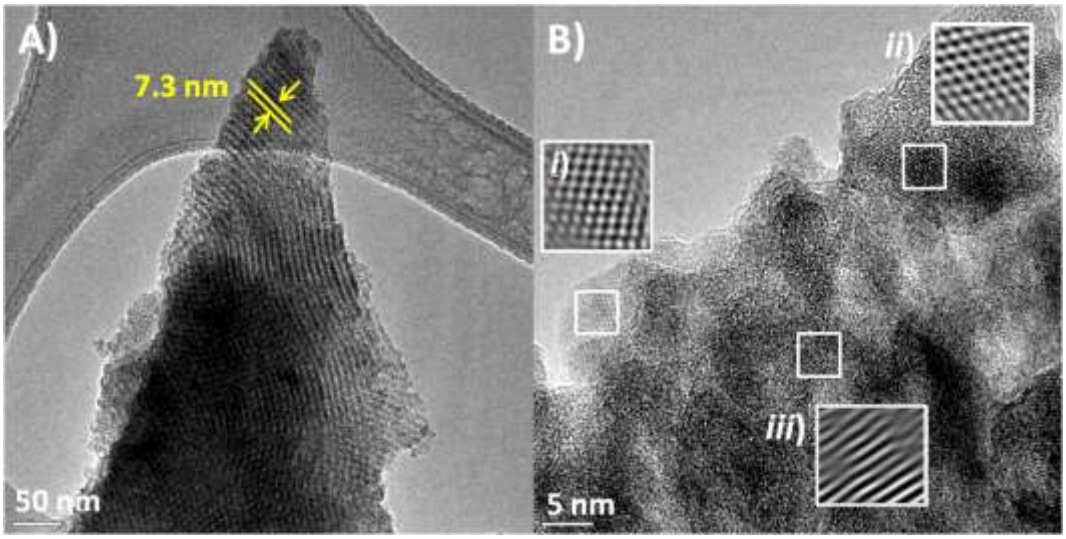

Figure 3.24 TEM images of (A) meso-13CdO-60TiO_2 with 50 nm scale bar and, (B) meso-13CdSe-60TiO_2 with 5 nm scale bar, *i*), *ii*) and *iii*) inverse FFT images of the selected areas in b).

The presence of the high mesoorder in the calcined meso-13CdSe-60TiO_2 films were also proved by the small angle XRD line at 2Θ = 2.06, Figure 3.25 (A). This XRD line corresponds to 4.2 nm d spacing according to Bragg`s law;

$$n\lambda = 2d\sin\Theta \qquad \text{Equation 3.3}$$

where n is an integer, λ is wavelength of X-ray source 1.54078 Å, d is the spacing between the planes in the atomic lattice, and Θ is the angle between the incident ray and the diffracting planes. Since the d spacings between the channels were measured to be 7.3 nm from the TEM images given above, the XRD line at 2.06° must be the second diffraction line (corresponding to (200) planes of the mesophase), and the first XRD line must be observed at around 1.00° which corresponds to 8.0 nm d spacing and (100) planes of the mesostructure. The first line could not be resolved because the x-rays from the source overlap in this region. The high angle XRD pattern were also recorded using around 50 thin films of meso-13CdO-60TiO_2, which were calcined to 350 °C, and scraped to collect powder, and then exposed to H_2Se to obtain meso-13CdSe-60TiO_2. As shown in Figure 3.25 (B), meso-13CdSe-60TiO_2 gives broad diffraction lines at 25.6, 42.0, and 49.5, 2Θ, corresponding to (111), (220), and (311) planes of zinc blend CdSe

nanocrystallites (ICDD Card # 00-019-0191). The other diffraction lines belong to TiO_2 but they cannot be assigned properly due to broad character of the lines.

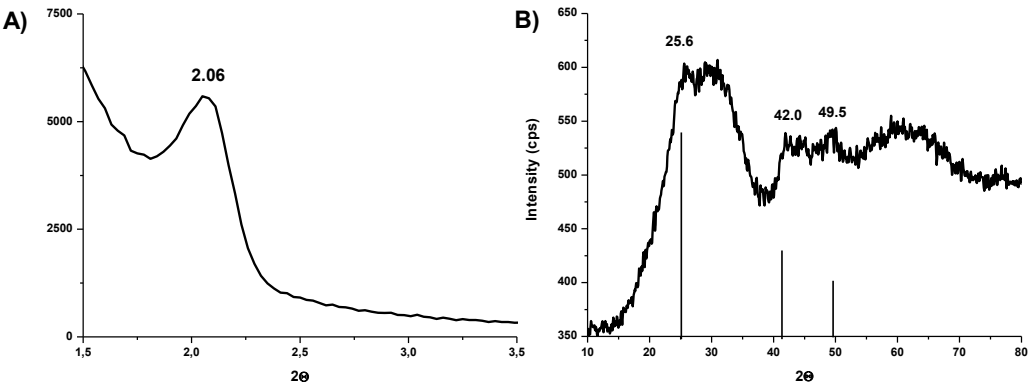

Figure 3.25 A) The small angle and B) high angle XRD pattern of meso-13CdSe-60TiO_2 calcined to 350 °C.

Raman spectrum of meso-13CdSe-60TiO_2 calcined at 350 °C shows the peaks due to the crystalline phase of TiO_2. The peaks, in Figure 3.26, at 144 cm^{-1} (E_g), 198 cm^{-1} (E_g), 397 cm^{-1} (B_{1g}), 516 cm^{-1} (B_{1g}), and 639 cm^{-1} (E_g) are the bands due to anatase phase of titania and the peaks at 261 cm^{-1}, 448 cm^{-1} (E_g), 612 cm^{-1} (A_{1g}), and 832 cm^{-1} (B_{2g}) are the bands due to rutile phase of titania in the meso-13CdSe-60TiO_2.[167] At temperatures around 350 °C, it is unlikely to form rutile phase of titania. However, from the Raman spectrum, the presence of rutile phase of titania can also be inferred from the Raman spectrum in Figure 3.26.

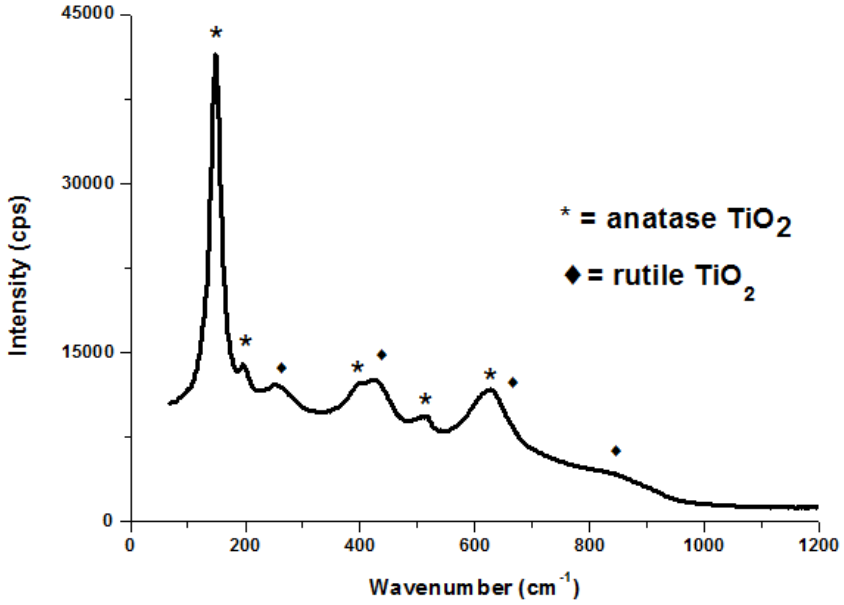

Figure 3.26 Raman spectrum of meso-13CdSe-60TiO_2 calcined to 350 °C.

The meso-13CdSe-60TiO_2 samples calcined to 350 °C were further analyzed using N_2 sorption data. The meso-13CdSe-60TiO_2 powder prepared for XRD measurement was also used for the N_2 sorption measurement. Figure 3.27 (A) shows the N_2 sorption isotherms of meso-13CdSe-60TiO_2 with a Barrett-Joyner-Halenda (BJH) (pore volume is 0.69 cm^3/g) pore size distribution plot. The N_2 sorption isotherm is type IV with a hysteresis loop, characteristic for the mesoporous materials. The BET (Brunauer-Emmett-Teller) surface area is ~ 112 m^2/g. The apexes of pore size distribution plot correspond to 6.5 nm, and it supports the TEM analysis and XRD measurements given above. Figure 3.27 (B) is the t-plot of the N_2 adsorption branch, collected from meso-13CdSe-60TiO_2. The t-plot helps to determine the existence of micro- and/or mesopores throughout the sample. The upward deviation observed in the t-plot passing through the origin indicates the presence of only mesopores, downward deviation indicates the presence of only micropores, and a downward deviation followed by an upward deviation indicates the presence of both micro- and mesopores in the sample.[168-171] Therefore, t-plot in Figure 3.27 (B) clearly indicates the presence of only mesopores through the meso-13CdSe-60TiO_2 samples.

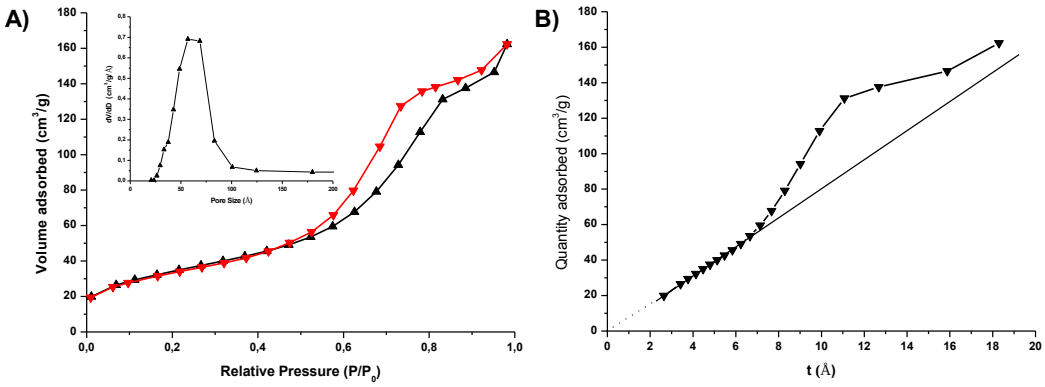

Figure 3.27 A) The N_2 (77.4 K) sorption isotherm with pore size distribution plot as inset and B) t-plot of the N_2 sorption data collected from meso-13CdSe-60TiO_2 calcined to 350 °C.

We have used cadmium nitrate salt and nitric acid as metal and acid source, respectively, because the nitrate ions have a low removal temperature and the transition metal nitrate salts have higher solubility. And nitrate ions play important roles in the self-assembly process by coordinating to metal ion, which can be tracked using IR technique (Figure 3.28). The peaks at 1290 and 1475 cm^{-1} with a splitting energy of 185 cm^{-1} indicate the coordination of nitrate ions as bidentate to Cd(II) sites. And the peaks at 1290 and 1560 cm^{-1} with the splitting energy of 270 cm^{-1} indicate the bidentate or bridged coordination of nitrate ions to Ti(IV) sites on the pore walls.[48]

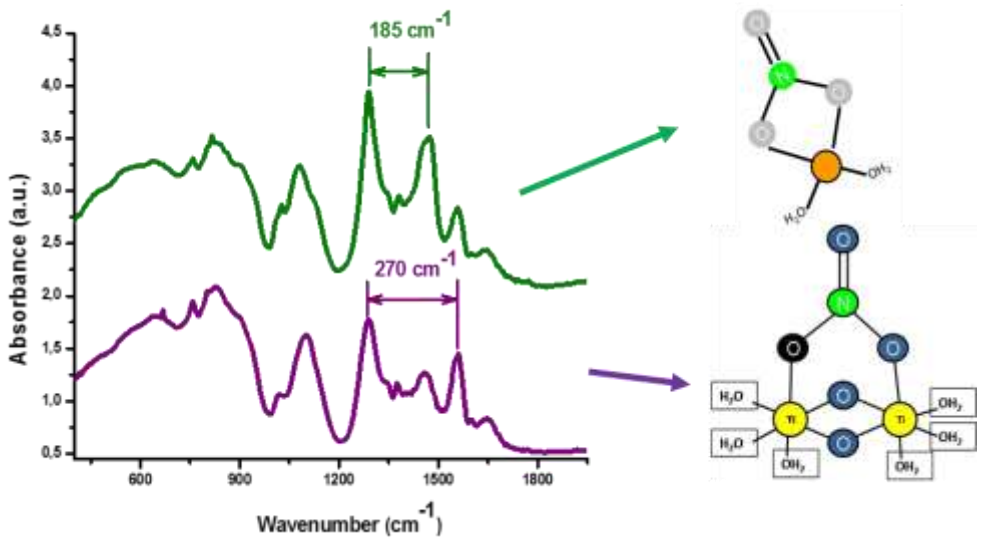

Figure 3.28 FTIR spectra of mesostructured samples of 13 Cd(II)/P123 and 60 TiO_2/P123 (top), and 2 Cd(II)/P123 and 80 TiO_2/P123 (bottom).

However, if the mesostructured cadmium titania films is exposed to H_2S or H_2Se reactions in the presence of such a huge amount of nitrate ions, a large amount of nitric acid forms as determined by the increase in the FTIR stretching peaks of the coordinated NO_3^- peaks to the Cd(II) metal centers at around 1290 and 1475 cm^{-1}. The CdS and CdSe nanoparticles are converted back to their nitrates upon reaction with nitric acid. Therefore, we have to remove the nitrate ions before or right after the H_2S or H_2Se reactions in order to stabilize the mesostructured CdS or CdSe titania films, denoted as meso-CdS-TiO_2 or meso-CdSe-TiO_2, respectively.

Further aging of the as prepared samples at 130° removes up to 90% of nitrate ions from the medium prior to H_2S or H_2Se reactions. The FTIR analysis enabled to monitor the behavior of nitrate ions during aging and H_2S or H_2Se reactions (Figure 3.29).

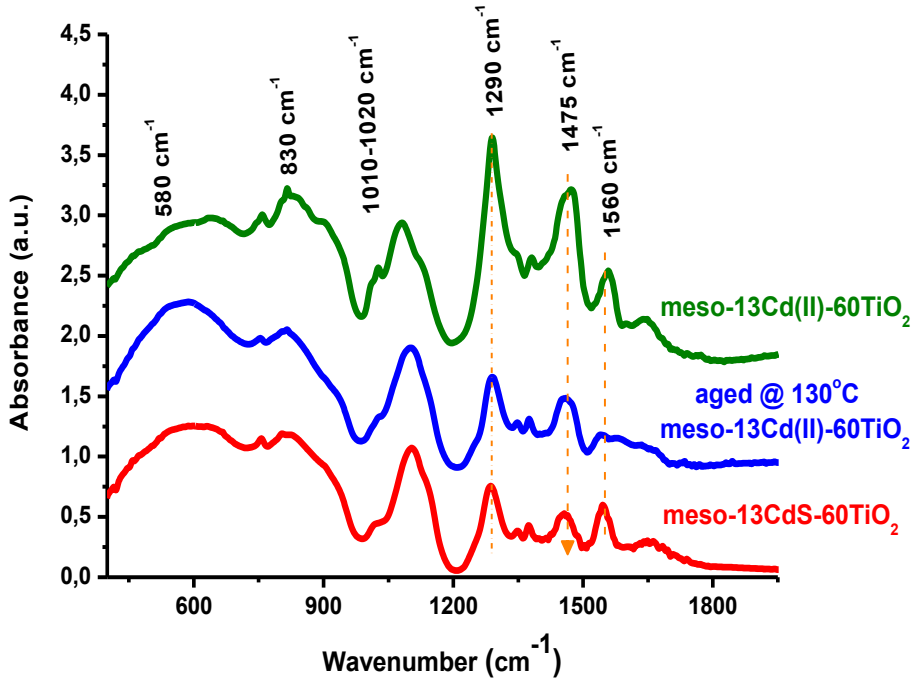

Figure 3.29 FTIR spectra of meso-13Cd(II)-60TiO_2 films as fresh (top), after aged at 130 °C (middle), and exposed to H_2S or H_2Se reactions (bottom).

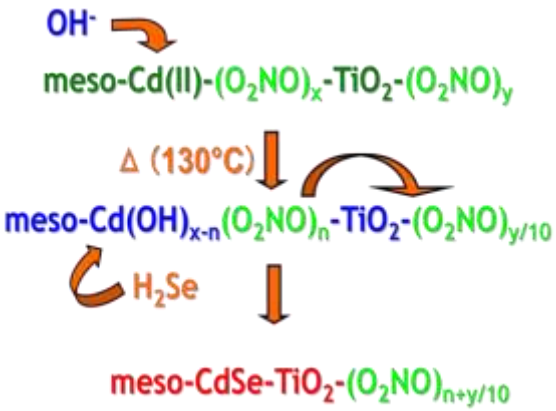

Figure 3.30 Schematic illustration of ions exchange during 130 °C aging and H_2Se reaction steps of meso-13Cd(II)-60TiO_2.

During the aging step at 130°C, the peak intensity at 1475 cm^{-1} decreases because some hydroxide ions exchange with the nitrate ions coordinated to cadmium ions as represented in Figure 3.30. And decrease of the intensity of peak at 1560 cm^{-1} is due to decomposition of nitrate ions from Ti(IV) sides. Upon

reaction with H_2S or H_2Se, the peak at 1475 cm^{-1} mostly diminishes and the peak at 1560 cm^{-1} is almost completely recovered. And the common peak at 1290 cm^{-1} remains almost unaltered after all these treatments. These indicate that nitrate ions coordinated to cadmium ions are transferred to titania sides upon formation of CdS or CdSe nanoparticles. Therefore, stable mesostructured CdS or CdSe titania films can be synthesized.

UV absorption spectral changes during aging also reveal the behavior of nitrate ions during aging and H_2S/H_2Se reactions (Figure 3.31). The absorption band at around 204 nm is due to nitrate ions and loses intensity during aging and H_2S/H_2Se reactions. The broad band around 250 nm, which is due to titania, slightly red shifts as a result of further condensation of titania species. Throughout aging, an isosbestic point forms at 230 nm, see Figure 3.31. Therefore, whole process can be called as single-step decomposition of the nitrate ions from the medium.

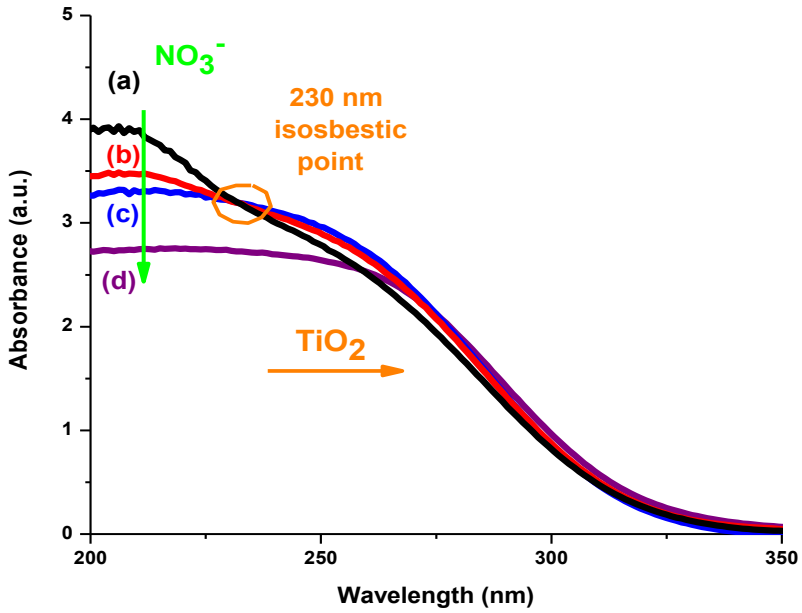

Figure 3.31 UV-Vis absorption spectra of fresh (a), 2 hrs aged at 130 °C (b), 4 hrs aged at 130 °C (c) meso-13Cd(II)-60TiO_2, and after exposing the sample to H_2Se reactions (d).

The films, after H_2Se treatment, were further investigated to elucidate the electronic structure using of the CdSe domains. Due to quantum size effect, the absorption edge shows a blue shift compared to bulk CdSe, indicating formation of CdSe nanoparticles (see Figure 3.32). On the right hand side, the plot of direct gap fitting gives the band gap energy of 2.36 eV for the CdSe nanoparticles. Darma and Sharma`s tight binding model can be used to calculate the particle size from their band gap values by the given empirical formula below;

$$\Delta E_g = a_1 e^{-d/b_1} + a_2 e^{-d/b_2} \qquad \text{3.2.1.1.1.1.1.1.1 Equation 3.4}$$

where d is the diameter, a_1, a_2, b_1, and b_2 are the electronic parameters characteristic to the semiconductor.[172] The particle size of CdSe nanoparticles were calculated as 3.7 nm by using the given parameters a_1, a_2, b_1, b_2 as 7.62, 6.63, 2.07, and 28.88 for the CdSe nanocrystallites.[172] The absorption edges of the aged meso-x$CdSe$-60TiO_2 slightly red shifts compared to the fresh samples.

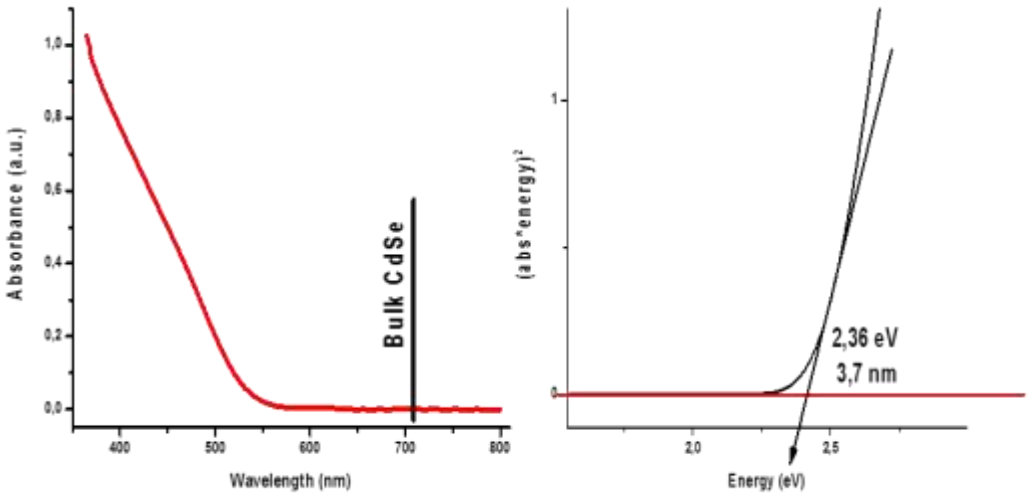

Figure 3.32 UV-Vis absorption spectra of meso-13CdSe-60TiO_2 film samples (on the left hand side) and band gap plot of this absorption spectra (on the right hand side).

We did not observe any problem during H_2S reactions that means the reaction atmosphere or duration does not change the result and does not produce

any side products like any compounds of sulfides. However, use of H_2Se is a little problematic. EDS analysis showed us that if H_2Se reactions are performed under oxygen atmosphere, large amount of Se species form (Figure 3.33 (A)), which is also identified by Raman spectroscopy from the presence of a peak at 250 cm^{-1} (Figure 3.34.bottom) originating from Se. Since this is an oxidation process ($Se^{2-} \rightarrow Se^0 + 2e^-$), H_2Se reaction has to be carried out under a non-oxidizing environment. Therefore, no Se species formed, when the reaction was carried out under a nitrogen atmosphere (Figure 3.33 (B) and (C)) and all the Cd(II) ions were converted into CdSe nanoparticles (Figure 3.34.top). The three peaks at 207, 412, and 618 cm^{-1} are due to the longitudinal optical (LO) mode[173] and its overtones (2LO and 3LO), respectively, of the CdSe nanoparticles. The red shift of the LO frequency from its bulk value is due to phonon confinement and also indicates the formation of CdSe nanoparticles.[173] However, the samples are beam sensitive under a green laser, used for the Raman measurements. The CdSe nanoparticles decompose under the beam into Se (see Figure 3.33 (C)). The observed irreversible degradation of CdSe to Se under green laser in the presence of oxygen indicates that there is an electron injection from CdSe nanoparticles to TiO_2 walls.[133] However, the degradation process can be stopped if the measurement is carried under N_2 atmosphere, see Figure 3.33 (C).

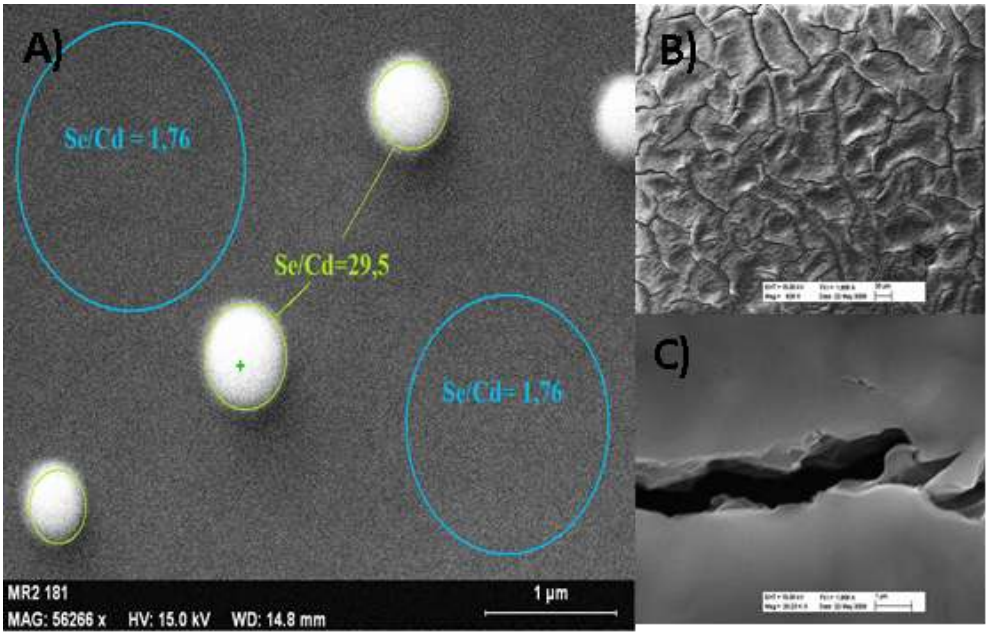

Figure 3.33 SEM images of the meso-13Cd(II)-60TiO_2 film samples after H_2Se reaction A) under oxidizing environment, B) and C) under N_2 atmosphere.

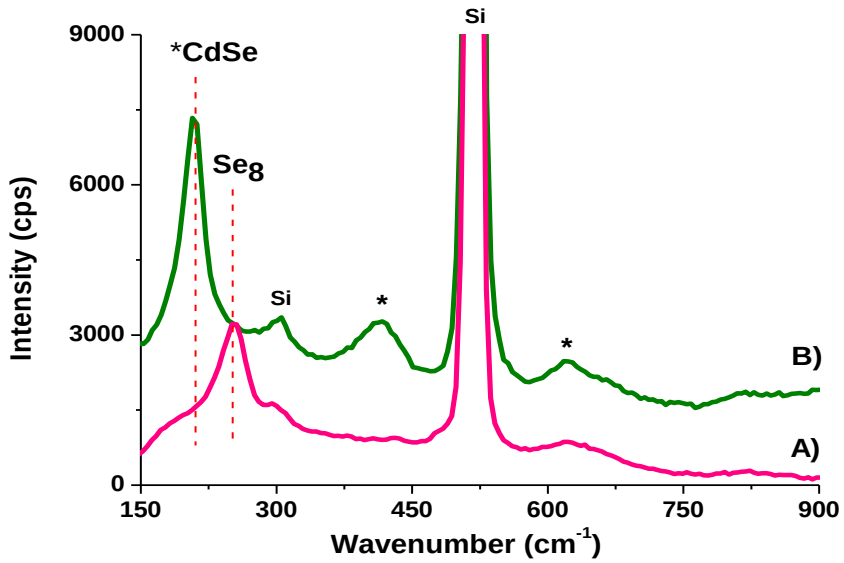

Figure 3.34 Raman spectra of the meso-13Cd(II)-60TiO_2 film samples after H_2Se reaction A) under an oxidizing environment and B) under N_2 atmosphere.

The Raman spectral changes can be explained as electron injection from the excited CdSe nanoparticles into TiO_2.[133] The mechanism, behind this

photodegradation, is illustrated below (Figure 3.35). The electron injection from the conduction band of CdSe nanoparticles to the conduction band of the TiO_2 is favorable. In the presence of air, injected electrons are scavenged by surface adsorbed oxygen. The excess holes left in the valence band of the CdSe nanoparticles induce their anodic corrosion and so, causes irreversible degradation of the CdSe into Se. However, in the case of SiO_2, electron injection from the CdSe nanoparticles is not favorable due to large band gap of SiO_2 and also, in a vacuum environment, no degradation is observed. All those results support the role of TiO_2 and oxidizing environment for photodegradation of the CdSe nanoparticles. Since the meso-xCdSe-60TiO_2 film samples show such behavior under green laser, it means that the CdSe nanoparticles and TiO_2 walls are in close contact with each other. This result is very important for such materials to be used in photovoltaic applications.

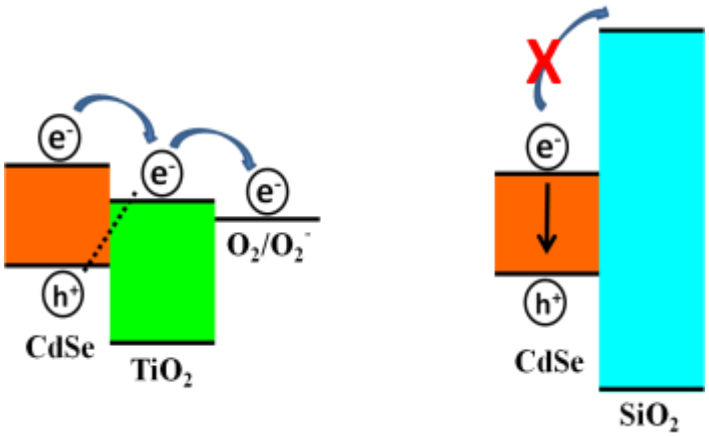

Figure 3.35 Illustration of band energies of TiO_2 and SiO_2 in comparison with CdSe.

During Raman measurements of the CdSe nanoparticles in the mesostructured titania, it was observed that under a green laser, λ_{exc} = 532 nm, the intensity of peak at 207 cm^{-1} originating from CdSe nanoparticles, decreased in time while a new peak at 250 cm^{-1} due to Se, arised in time in an oxygen atmosphere at RT (Figure 3.36). The color of the spots exposed to laser changed from transparent orange to dark brown during this transformation. The power of the laser beam changed the rate of that transformation significantly. The higher is the power of the laser beam, the shorter the degradation time of the CdSe to Se is.

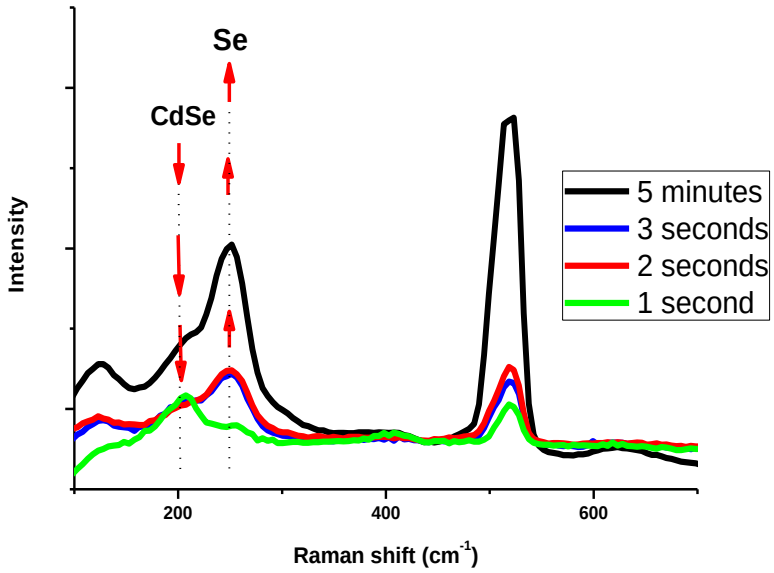

Figure 3.36 The Raman spectra of the meso-13CdSe-60TiO_2 film sample under green laser (λ_{exc} = 532 nm) with time.

The films, reacted with H_2Se under N_2 atmosphere with an optimized pressure and reaction duration, were further analyzed using EDS parallel to Raman measurements. The control of time and pressure of H_2Se reaction effectively changes the ratio of Cd/Se. Therefore, those parameters were identified for each sample according to Raman and EDS results since the formation of CdSe could be approved by Raman and the complete reaction could be proved by EDS analysis of the Cd/Se ratio. The bulk pure CdSe was used as a reference to determine the Cd/Se ratio. As shown in Figure 3.37, the Cd/Se ratio was the same, around 0.9, in the bulk CdSe and the meso-10CdSe-60TiO_2 films.

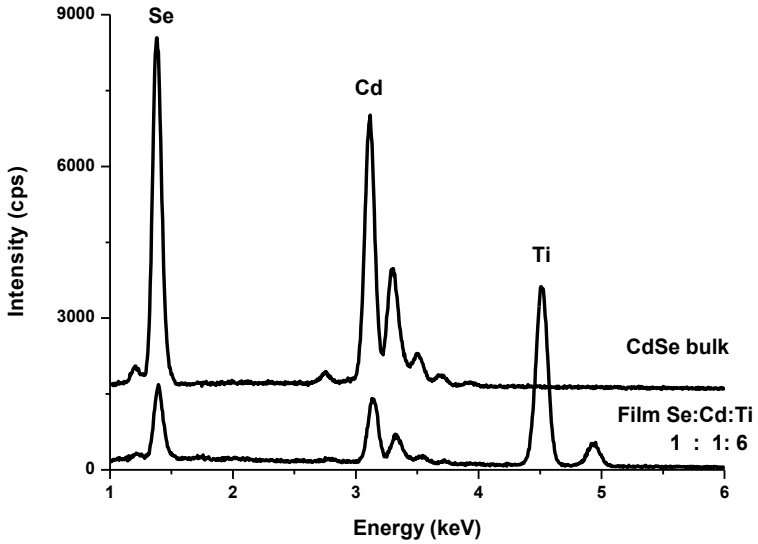

Figure 3.37 The EDS data of bulk CdSe as a reference (top), and meso-10CdSe-60TiO_2 thin film sample (bottom).

The meso-xCdS-60TiO_2, x between 2 and 13, were also prepared by just exposing aged meso-xCd(II)-60TiO_2 films to H_2S atmosphere. Compared to H_2Se reactions, no problem during H_2S reactions, such as formation of any side products, control of gas pressure or reaction duration has been encountered. The photodegradation of the CdS nanoparticles under green laser was much slower.

3.2.2 Synthesis of mesoporous-TiO_2-MX (M = Cd(II), Zn(II) and X = (S^{2-}, Se^{2-}))

As already explained in the LLC chapter, in a two surfactant (CTAB and $C_{12}EO_{10}$) LLC mesophase, the metal ion to $C_{12}EO_{10}$ mole ratio could be increased up to 8.0 salt/$C_{12}EO_{10}$ mole ratio,[46] where the LLC mesostructured films at those salt concentrations are quite stable. It is also known that a 7 SiO_2/$C_{12}EO_{10}$ mole ratio is sufficient to obtain stable mesoporous SiO_2 films.[174] As it will be explained in detail in the next chapter, combining these two methods successfully enabled the synthesis of mesoporous MO-SiO_2 (M is Cd(II) and Zn(II)) thin films in one pot. The mesoporous MO-SiO_2 could be used as precursors to produce mesoporous SiO_2-MS (or MSe) thin films under a H_2S (or H_2Se) atmosphere at RT.[128]

Even though controlling the condensation of titania precursors is more difficult than the condensation of silica precursors, the method developed in this thesis enabled controlled hydrolysis and condensation of $Ti(OC_4H_9)_4$ under optimized conditions of the solvent type and amount. Excessive amount of metal salts, Zn(II) and Cd(II), can be inserted into the channels between titania walls and surfactant domains. The melting point of salts depressed due to the confinement effect, and the melted salt species behave like a secondary solvent in the medium. Even though the primary solvent, ethanol, evaporates from the medium during the preparation of the films by spin coating method, the molten phase of salt still remains in the medium, and acts as a secondary solvent to preserve the mesostructure until they are all converted into their oxides to form the mesoporous framework. Therefore, the controlled condensation of TiO_2 at 7 TiO_2/$C_{12}EO_{10}$ mole ratio dissolved in a mixture of TMS-$C_{12}EO_{10}$-CTAB at high salt concentrations could be used to synthesize metal rich mesoporous TiO_2-MO films (denoted as meso-TiO_2-nMO, n is the M(II)/$C_{12}EO_{10}$ mole ratio) from which the mesoporous TiO_2-MS(or MSe) films (denoted as meso-TiO_2-nMS (or MSe)) were successfully obtained.[175]

The meso-TiO_2-nMS (or MSe) thin films were obtained by exposing the meso-TiO_2-nCdO(or ZnO) films to H_2S or H_2Se gaseous at RT. The meso-TiO_2-

CdO (or ZnO) films were prepared with a thickness of around 400 – 600 nm by spin coating a clear solution of $[M(H_2O)_x](NO_3)_2$-CTAB-HNO_3-C_2H_5OH-$C_{12}EO_{10}$- $Ti(OC_4H_9)_4$ (M is Zn(II) or Cd(II) and x is 6 for Zn(II) and 4 for Cd(II) salts), where the TMS/$C_{12}EO_{10}$ mole ratio, n, has been taken as 2, 4 and, 6, and calcining the films from 70 °C to 450 °C by 1 °C/min increments.[175] This new method can be named as "molten phase assisted self-assembly" (MASA) since the hydrolysis and condensation of titania precursor take place in a molten phase formed by the excessive amount of transition metal salt confined in the nano-spaces between surfactant molecules and titania walls.[175] The characterization of the meso-TiO_2-CdS, meso-TiO_2-CdSe, and meso-TiO_2-ZnSe films were performed using spectroscopy, microscopy, and diffraction techniques.

1.1.1.1 XRD analysis of meso-Zn_2TiO_4, meso-TiO_2-ZnSe, meso-$CdTiO_3$, meso-TiO_2-CdS and meso-TiO_2-CdSe

XRD is a powerful tool here to analyze the crystal structure of the materials formed after calcination and H_2S/H_2Se reactions. In order to collect x-ray diffraction patterns of the samples, around 20 thin films prepared on glass substrates were scraped to obtain enough powder for the measurements. The calcined meso-TiO_2-ZnO (or CdO), did not diffract at small angles. This indicates that structure is either mesoporous disordered or no mesostructure at all. The formation of mesostructure was confirmed by TEM and N_2 sorption measurements (see later). The meso-TiO_2-ZnO, at 6 Zn(II)/$C_{12}EO_{10}$ mole ratio gives broad diffraction lines at 30.0, 34.7, 42.7, 53.5, 56.5, 62.0, and 72.4°, 2Θ corresponding to (220), (311), (400), (422), (511), (440), and (533) planes of the Zn_2TiO_4 called zinc titanate, Figure 3.38, and the sample is represented as meso-Zn_2TiO_4 (ICDD PDF #00-025-1164, space group of Fd3m). This shows that the Zn(II) ions are forming the zinc titanates on the titania walls during the calcination step, instead of forming separate ZnO nanoparticles coating on the titania walls. Since the Zn(II)/Ti(IV) mole ratio in those samples is around 0.87, Zn_2TiO_4/TiO_2 mole ratio should be 3/4 in the meso-Zn_2TiO_4. The Scherrer` s

equation gives a particle size that is around 2.4 nm, and it can be considered as the pore-wall thickness in the meso-Zn_2TiO_4.

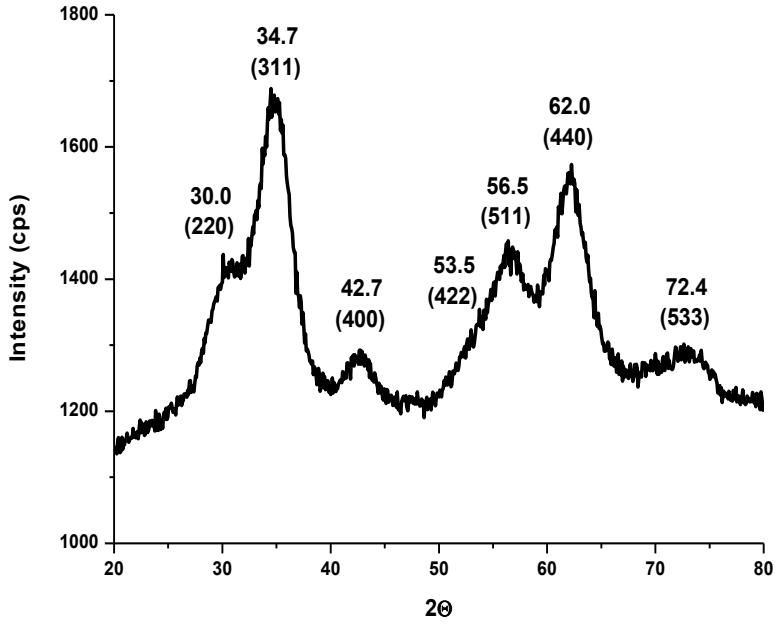

Figure 3.38 The XRD of meso-TiO_2-ZnO after calcination. (6 Zn(II)/$C_{12}EO_{10}$ mole ratio)

After exposing the meso-Zn_2TiO_4 to H_2Se, it is converted to meso-TiO_2-ZnSe. Then, the meso-TiO_2-ZnSe is aged under tungsten light at ambient conditions for around 3 days, and due to favorable electron injection from conduction band of ZnSe to the conduction band of TiO_2, photodegradation of ZnSe leads to an irreversible conversion of ZnSe into Se metal in the presence of oxygen.[133] The material formed after this photodegradation process has been called as meso-TiO_2-Se. Figure 3.39 displays the XRD patterns of the meso-TiO_2-ZnO, meso-TiO_2-ZnSe, and meso-TiO_2-Se. Since we did not know whether ZnSe and TiO_2 domains phase separate after exposed to H_2Se or photodegradation, it is very difficult to assign the broad XRD lines. Therefore, we took the differences of the XRD patterns of each material from the other, and figured out their form and structure. It is clear from the difference patterns that the photodegradation of ZnSe to Se is not complete, Figure 3.40. The XRD pattern of the ZnSe nanoparticles can be obtained by subtracting the XRD pattern of meso-TiO_2-Se from meso-

TiO_2-ZnSe, which is shown in Figure 3.40. These analysis shows that either the conversion of ZnSe to Se is very limited or Se species are amorphous that Se diffraction lines are not observed in the XRD patterns. The diffraction lines at 27.0, 45.0, and 53.0°, 2Θ were assigned to (111), (220), (311) planes of a zinc blend ZnSe nanoparticle with a F-43m(216) space group (PDF # 00-037-1463). The size of ZnSe nanoparticles are calculated to be 2.5 nm from the Scherrer`s equation. The difference pattern of meso-TiO_2-ZnSe and ZnSe should give the XRD pattern of TiO_2, see the bottom diffraction pattern in Figure 3.40. The diffraction lines at 27.0, 36.0, 54.0, and 62.0 were assigned as (110), (101), (211), and (002) planes of a rutile TiO_2 nanoparticles with P42/mnm(136) space group (PDF # 04-003-0648). Those results show us that after exposing the meso-Zn_2TiO_4 to the H_2Se gas, meso-zinc titanate does not remain in the form of titanates anymore, and interestingly it transforms into cubic ZnSe nanoparticles and TiO_2 crystalline domains in the rutile phase. Those results were also supported with Raman analysis (see later).

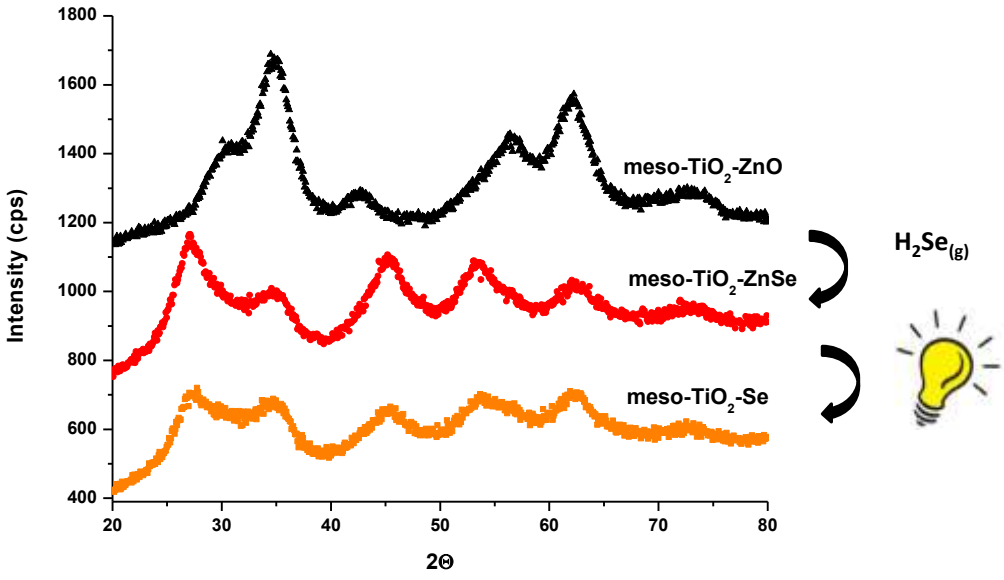

Figure 3.39 The XRD pattern of meso-TiO_2-ZnO (top), meso-TiO_2-ZnSe (middle), and meso-TiO_2-Se (bottom).

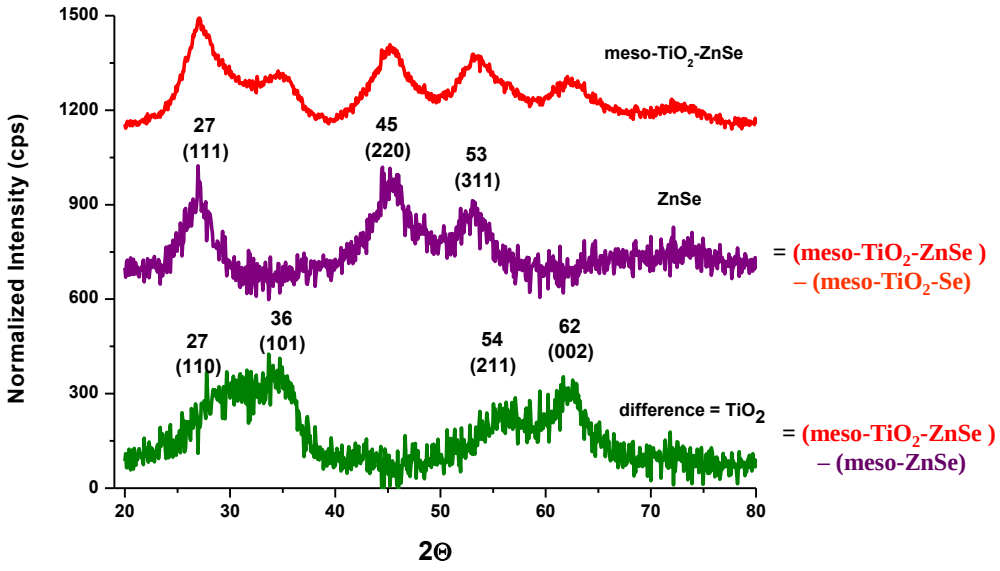

Figure 3.40 The XRD pattern of meso-TiO_2-ZnSe (top), ZnSe (middle), and TiO_2 (bottom).

The XRD patterns of meso-TiO_2-CdO (after calcination), meso-TiO_2-CdS (after exposed to H_2S), and meso-TiO_2-CdSe (after exposed to H_2Se) are given in Figure 3.41. As expected, the diffraction lines are very broad most probably due to very small size of the nanoparticles. However, the significant change in the XRD patterns can be clearly seen upon conversion of cadmium oxide to its sulfide or selenide. The crystal structure of CdS nanoparticles can be barely assigned to zinc blend from the diffraction lines at 26.02, 43.31, and 51.45°, 2Θ corresponding to the (111), (220), and (311) planes (PDF # 00-010-0454). For the meso-TiO_2-CdSe, the diffraction lines at 25.35, 42.00, and 49.69°, 2Θ correspond to the (111), (220), and (311) planes of cubic CdSe with a F43m(216) space group (PDF # 00-019-0191).

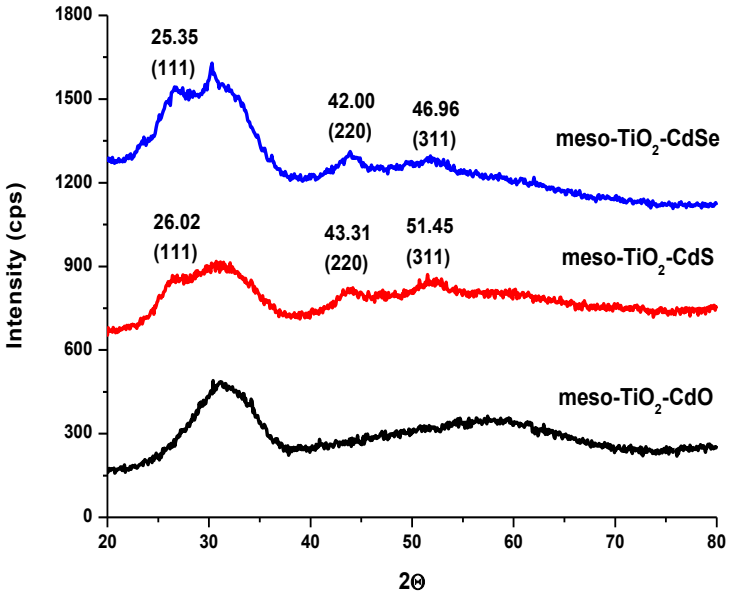

Figure 3.41 The XRD pattern of meso-TiO_2-CdO (bottom), meso-TiO_2-CdS (middle), and meso-TiO_2-CdSe (top).

Since it is very hard to find out the crystal structure of the meso-CdO-TiO_2 from the XRD pattern given above in Figure 3.41 due to its very broad nature, we calcined the meso-CdO-TiO_2 samples to higher temperatures to enable further crystallization and growth of the oxides, assuming the crystal structure will not change. The XRD pattern of the meso-CdO-TiO_2 heated at 550 °C, in Figure 3.42, displays diffraction lines at 17.92, 20.43, 22.96, 31.10, 34.20, 36.14, 38.87, 40.17, 41.60, 46.90, 47.29, 50.72, 53.30, 53.75, 59.30, and 61.21°, 2Θ corresponding to the (003), (101), (012), (104), (110), (015), (113), (021), (024), (116), (018), (214), and (300) planes of rhombohedral structure of $CdTiO_3$ (PDF card # 00-029-0277).

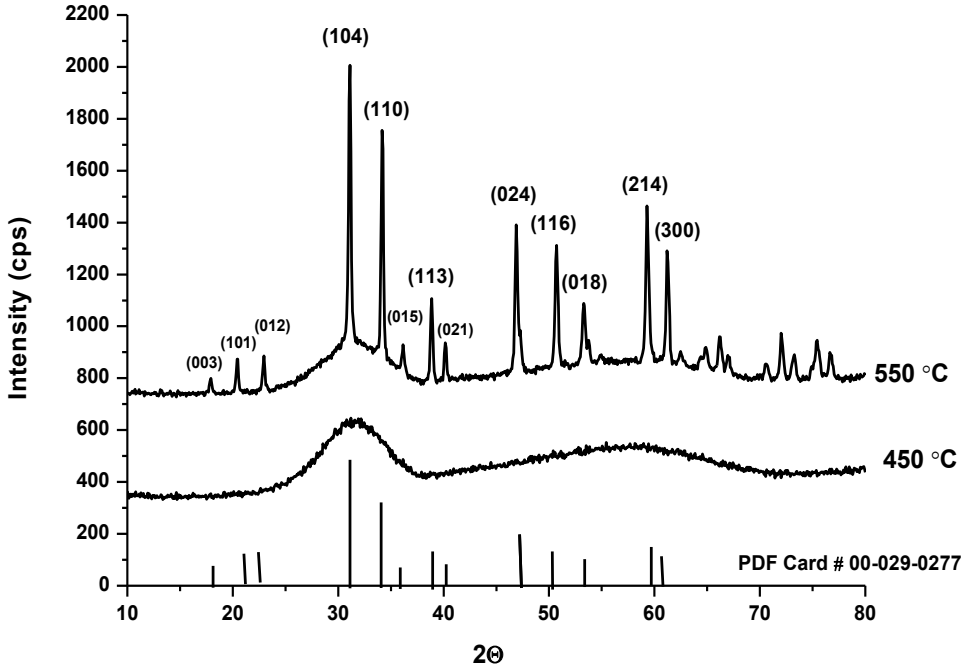

Figure 3.42 The XRD pattern of meso-TiO_2-CdO calcined to 450 °C(bottom), and 550 °C (top).

1.1.1.2 RAMAN analysis of meso-Zn_2TiO_4, meso-TiO_2-ZnSe, meso-$CdTiO_3$, meso-TiO_2-CdS and meso-TiO_2-CdSe

Besides the XRD technique, the Raman spectroscopy is also very useful to clarify the crystal structures formed after H_2S (or H_2Se) exposures. The Raman spectral analysis of the phases of titania and metal sulfides and metal selenides has been extensively studied. The Table 3.2 gives the list of peaks observed for rutile, anatase, and brookite phases of TiO_2 in their Raman spectra. The Raman spectra of meso-TiO_2-ZnO and meso-TiO_2-ZnSe are given in Figure 3.43. The phase transition during H_2Se exposure can be clearly seen. The Raman peaks at 447 cm^{-1} (E_g) and 612 cm^{-1} (A_{1g}) are assigned to rutile phase of titania.[167]

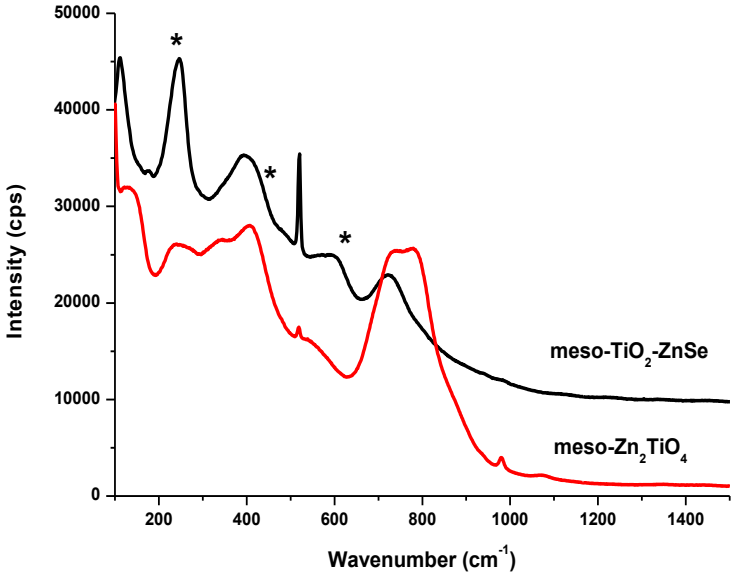

Figure 3.43 Raman spectra of meso-Zn_2TiO_4 (bottom), and meso-TiO_2-ZnSe (top).

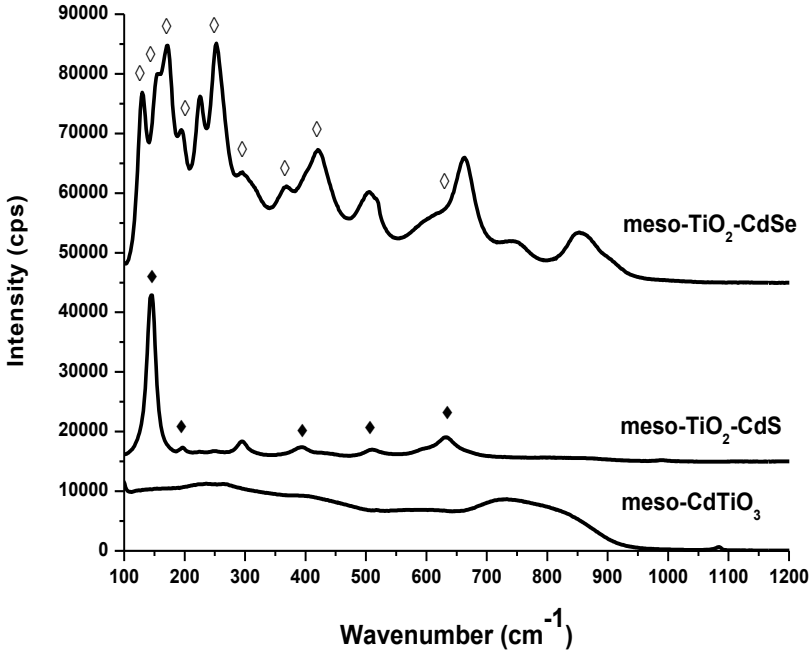

Figure 3.44 Raman spectra of meso-$CdTiO_3$ (bottom), meso-TiO_2-CdS (middle), and meso-TiO_2-CdSe (top), (♦ : anatase TiO_2, ◊ : brookite TiO_2).

From the XRD patterns, it is difficult to figure out the crystal structure of titania formed after H_2S (or H_2Se). However, Raman peaks were strong enough to assign their structures. There are significant differences between meso-TiO_2-CdS and meso-TiO_2-CdSe, see Figure 3.44. The peaks at 144 cm^{-1} (E_g), 198 cm^{-1} (E_g), 397 cm^{-1} (B_{1g}), 507 cm^{-1} (B_{1g}), and 639 cm_{-1} (E_g) are the bands due to anatase phase of titania of meso-TiO_2-CdS, middle spectrum in Figure 3.44. The peaks at 128 cm^{-1} (A_{1g}), 153 cm^{-1} (A_{1g}), 172 cm^{-1} (B_{3g}), 195 cm^{-1} (A_{1g}), 247 cm^{-1} (A_{1g}), 288 cm^{-1}, 366 cm^{-1} (B_{2g}), 396 cm^{-1} (B_{2g}) and 639 cm^{-1} (A_{1g}) are assigned to brookite structure of titania[167] in the meso-TiO_2-CdSe, top spectrum in Figure 3.44. Interestingly, while the H_2S reaction transforms to anatase, H_2Se reactions converts $CdTiO_3$ to brookite structure. The reason or mechanism of those transformations are not known and needs detailed work.

Table 3.2 Raman spectra of synthetic titania polymorphs (cm^{-1}) [167]

Rutile	***Anatase***	***Brookite***
		128 (s)
		135 (w)
143 (w)	144 (vs) E_g	153 (vs)
	198 (w) E_g	172 (sh)
		195 (w)
235(b, m) combination		214 (w)
273 (sh)		247 (m)
320 (w)	320(vw) combination	288 (w)
357 (w)		322 (w)
		366 (w)
	397(m) B_{1g}	396 (sh)
449 (s) E_g		412(w)
		454 (w)
		461 (w)
610 (s) A_{1g}	516 (m) A_{1g}, B_{1g}	502 (w)
		545 (w)
		585 (w)
	639 (m) E_g	636 (s)
	695(vw) combination	
832 (w) B_{2g}	795 (w) B_{1g} overtone	

1.1.1.3 UV-Vis analysis of meso-Zn_2TiO_4, meso-TiO_2-ZnSe, meso-$CdTiO_3$, meso-TiO_2-CdS and meso-TiO_2-CdSe

The MASA method produces transparent and crack-free thin films. Figure 3.45 (A) is the UV-Vis absorption spectra of meso-$CdTiO_3$, meso-TiO_2-CdS and meso-TiO_2-CdSe thin films. The band gaps of CdS and CdSe particles were evaluated by using direct band gap fitting of the UV-Vis absorption spectra, as shown in Figure 3.45 (B). The band gaps of the meso-$CdTiO_3$, meso-TiO_2-CdS, and meso-TiO_2-CdSe nanoparticles are 3.88 eV, 2.84 eV, and 2.40 eV, respectively. From the band gap values, the sizes of the CdS and CdSe nanoparticles were calculated to be 2.0 and 2.3 nm, respectively, by using Bruss effective mass model (EMM).[176] The evaluated particle sizes indeed explain the reasoning behind the observed broad XRD patterns.

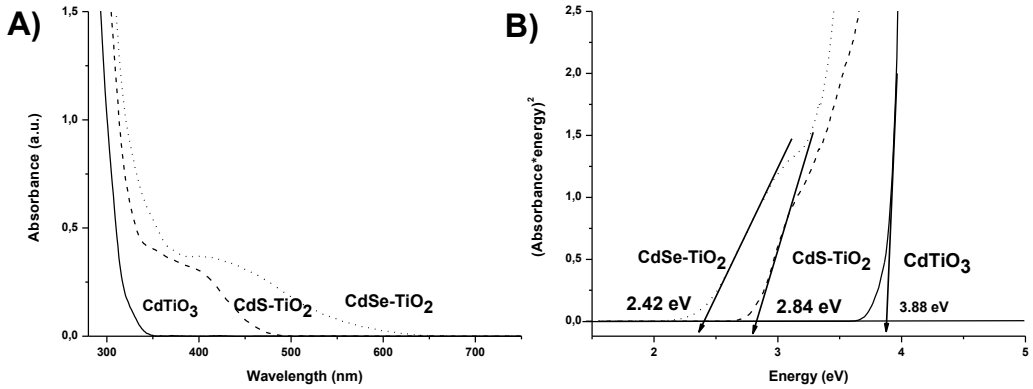

Figure 3.45 A) The UV-Vis absorption spectrum of meso-TiO_2-CdO, meso-TiO_2-CdS and meso-TiO_2-CdSe thin films. B) The plot of (abs*energy)$_2$ versus energy.

Figure 3.46 (A) is the UV-Vis absorption spectra of meso-Zn_2TiO_4, and meso-TiO_2-ZnSe thin films. The ZnSe nanoparticles have 3.13 eV band gap value and it corresponds to around 2.0 nm particle size according to Bruss` EMM.

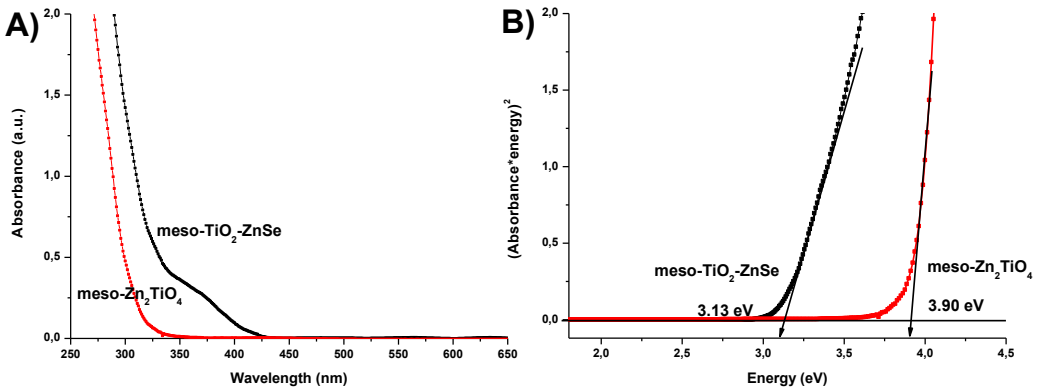

Figure 3.46 A) The UV-Vis absorption spectrum of meso-Zn_2TiO_4, and meso-TiO_2-ZnSe thin films. B) The plot of (abs*energy)^2 versus energy.

Moreover, the MASA method can be used to obtain multilayered transparent films so that one can control the amount of absorption. The multilayered films were prepared by multiple spin coating followed by calcination for each layer. The multiple spin coated film was exposed to H_2S or H_2Se at once. The reactions were as fast as in the case of one layered films. This was an important observation that the films are porous and openings of the pores are accessible. As shown in Figure 3.47 (A) and (B), the absorbance gradually increases with increasing the number of layers in the films. In Figure 3.48 (A) and (B), the gradual increase of the color contrast can be seen on the photos of those films, whose UV-Vis absorption spectra are given in Figure 3.47 (A) and (B). The qualities of the films as being transparent and crack-free make them preferable candidates for various applications such as the solar-cells.

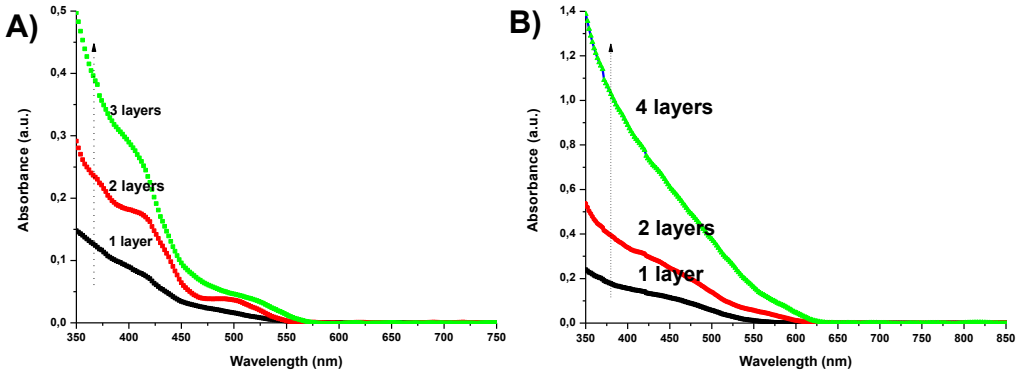

Figure 3.47 The UV-Vis absorption spectra of A) 1, 2 and 3 layers of meso-TiO_2-CdS, and B) 1, 2, and 4 layers of meso-TiO_2-CdSe thin films.

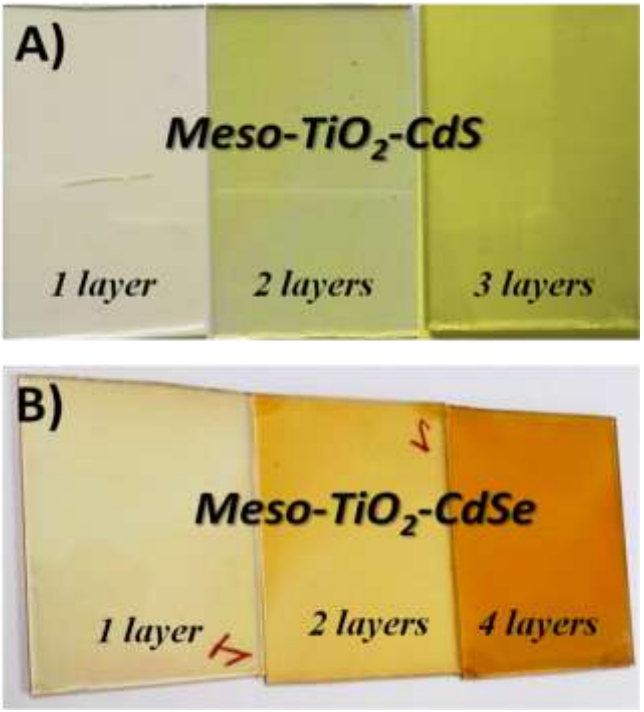

Figure 3.48 The photos of A) 1, 2, and 3,layered meso-TiO_2-CdS films, and B) 1, 2, and 4 layered meso-TiO_2-CdSe films.

3.2.2.1 N_2 sorption data of meso-$CdTiO_3$ and meso-TiO_2-CdSe and its analysis

The films were further analyzed using N_2 sorption data. Around 20-30 glass of the meso-$CdTiO_3$ films prepared on glass substrates were scraped and about 10 mg powder sample were collected to obtain N_2 sorption data. For the N_2

sorption measurements of meso-TiO_2-CdSe, meso-TiO_2-CdO powders were exposed to H_2Se. Figure 3.49 shows the N_2 sorption isotherms of meso-$CdTiO_3$ and meso-TiO_2-CdSe with pore size distribution plots. The N_2 sorption isotherms characteristics type IV with a hysteresis loop for both $CdTiO_3$ and CdSe cases. The BET surface area changes from 35 m^2/g to 6 m^2/g upon converting meso-$CdTiO_3$ to meso-TiO_2-CdSe. The Barrett-Joyner-Halenda (BJH) pore-volume changes from 0.46 cm^3/g to 0.096 cm^3/g upon converting meso-$CdTiO_3$ to meso-TiO_2-CdSe. This shows a large pore blocking after H_2Se reaction or during dehydration process prior to N_2 sorption measurement. The apexes of pore size distribution plots correspond to 8.5 nm for meso-$CdTiO_3$ and 7.5 nm for meso-TiO_2-CdSe.

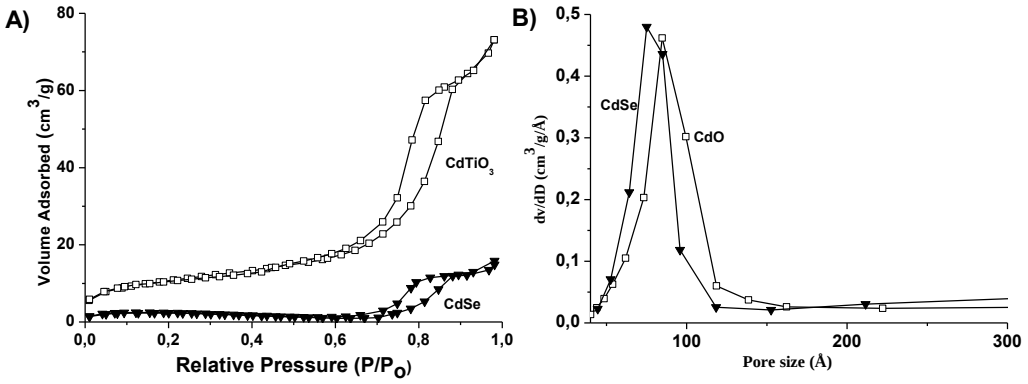

Figure 3.49 A) The N_2 (77.4 K) sorption isotherm and B) pore size distribution plots of meso-$CdTiO_3$ and meso-TiO_2-CdSe.

3.2.2.2 TEM analysis of meso-TiO_2-CdSe, meso-TiO_2-ZnSe, and meso-TiO_2-CdS

Figure 3.50 shows a series of TEM images obtained from meso-TiO_2-6CdSe, meso-TiO_2-4ZnSe, and meso-TiO_2-6CdS thin films. The nanocrystalline domains are clearly shown all over the sample, Figure 3.50 (a). The inset (b) in Figure 3.50 (a) is the inverse FFT image representing (111) plane of a cubic CdSe nanocrystals with a 3.525 Å spacing, and the inset (c) is the inverse FFT image, showing the (022) plane of a brookite TiO_2 nanocrystal with a 2.24 Å spacing, Figure 3.50 (a). The structural analysis of the CdSe and TiO_2 domains from the HRTEM image in Figure 3.50 (a) supports the XRD and Raman analysis given

above. The sponge like, disordered pores with around 10 nm sizes, which are marked yellow, are observed in Figure 3.50 (d). The sponge like porosity is clearly observed in the dark and bright field images of meso-TiO_2-CdSe films, given in Figure 3.50 (e) and (f), respectively. The EDS mappings are obtained for the Ti, Cd, and Se elements from the same region in Figure 3.50 (e) and (f). The homogenous distribution of the Ti, Cd, and Se metals proves that the CdSe domains are homogeneously distributed in the meso-TiO_2-CdSe films. Figure 3.50 (j) is the TEM image obtained from the meso-TiO_2-ZnSe, which clearly shows nanocrystalline domains all over the sample. Figure 3.50 (k) is the magnified image of the selected region in Figure 3.50 (j). The inverse FFT image of the selected area in the inset in Figure 3.50 (l) belongs to (110) planes of the rutile TiO_2 nanocrystal with 3.24 Å spacing, and the other inverse FFT image in Figure 3.50 (m) belongs to (211) plane of the cubic ZnSe nanocrystal with 2.31 Å spacing. This image in Figure 3.50 (k) supports our assumption about the morphology of the samples that upon transformation of zinc titanate to the ZnSe and TiO_2 crystalline domains under H_2Se reaction in the pore walls of amorphous TiO_2. The TEM image obtained from the meso-TiO_2-CdS films is shown in Figure 3.50 (n). The inverse FFT image in Figure 3.50 (o) is due to the (111) planes of cubic CdS crystals with 3.36 Å spacing in the selected area, and the inverse FFT image in Figure 3.50 (p) is due to the presence of (100) planes of anatase TiO_2 with 3.74 Å spacing in the selected area in Figure 3.50 (n).

The structural analysis from the TEM images support the results obtained from XRD and Raman spectroscopy that meso-$CdTiO_3$ is converted to cubic CdSe and brookite TiO_2 under H_2Se reaction, and converted to cubic CdS and anatase TiO_2 under H_2S reaction, and the meso-Zn_2TiO_4 is converted to cubic ZnSe and rutile TiO_2 nanocrystallites under H_2Se reaction at RT. The reason or reaction mechanism of the conversion of titanates into one of the three phases of nanocrystalline titania is not known, and the further studies are required to find out.

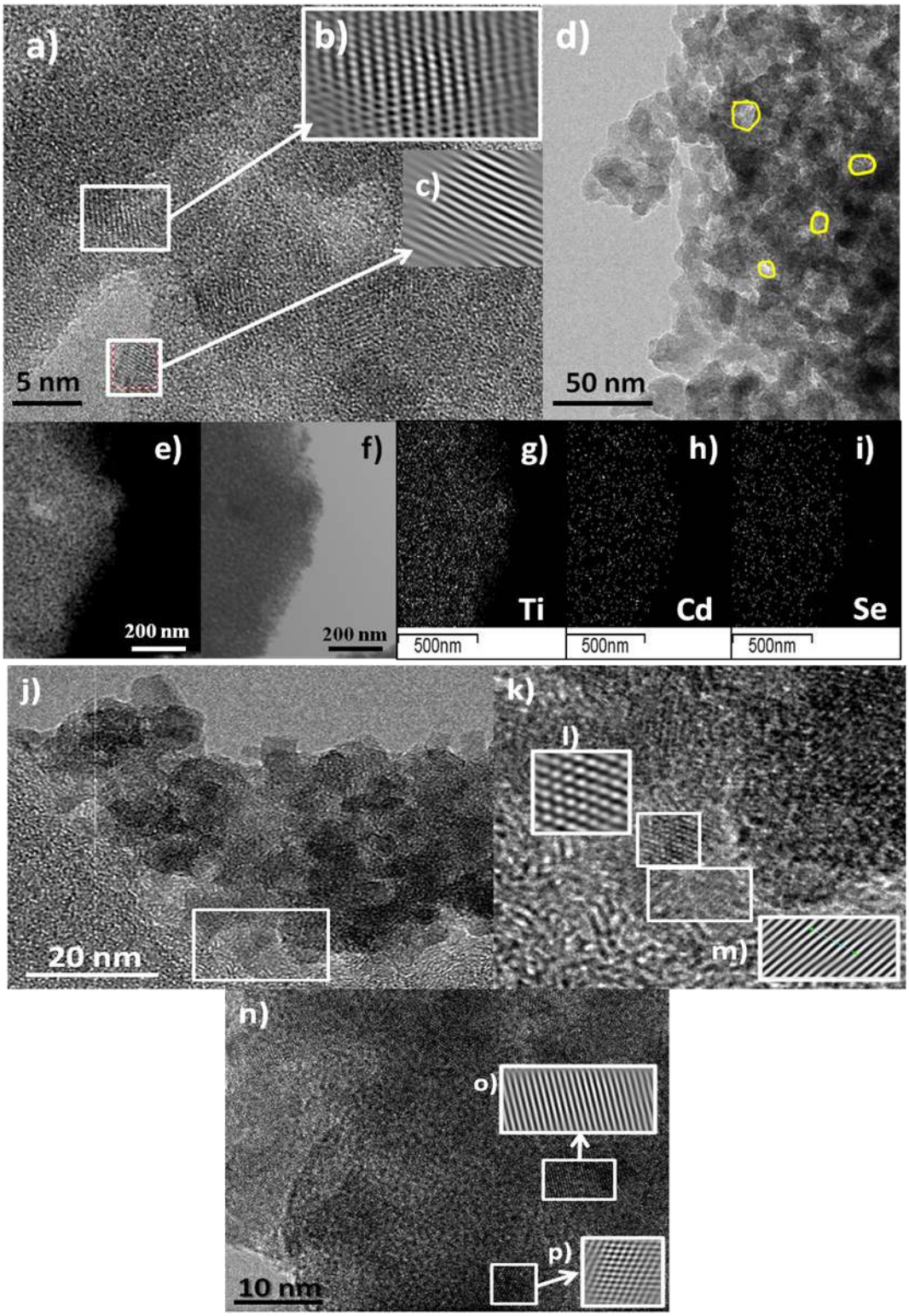

Figure 3.50 TEM images of a) and d) meso-TiO_2-CdSe with 5 nm and 50 nm scale bars, respectively, b) and c) inverse FFT images of the selected areas in a. e) dark field and f) bright field TEM images of meso-TiO_2-CdSe, EDS mapping for g) Ti, h) Cd and i) Se in meso- TiO_2-CdSe, j) TEM image of meso-TiO_2-ZnSe with 20 nm scale bar, k) magnified image of the selected area in pannel j. l) and m) inverse FFT images of the selected areas in pannel k. n) TEM image of meso-TiO_2-CdS with 10 nm scale bar.

Figure 3.51 is a schematic illustration of a reaction between meso-$CdTiO_3$ and H_2S (or H_2Se). In the oxide precursors, represented in the schema on the right hand side, the titanates, zinc titanate or cadmium titanate, coat the amorphous titania pore walls. After H_2S (or H_2Se) reactions, metal titanates are converted into nanocrystalline TiO_2 and metal sulfide (or selenide) domains as represented in the schema on the left hand side. They are still in contact and still coating the amorphous titania pore walls, as represented in Figure 3.51.

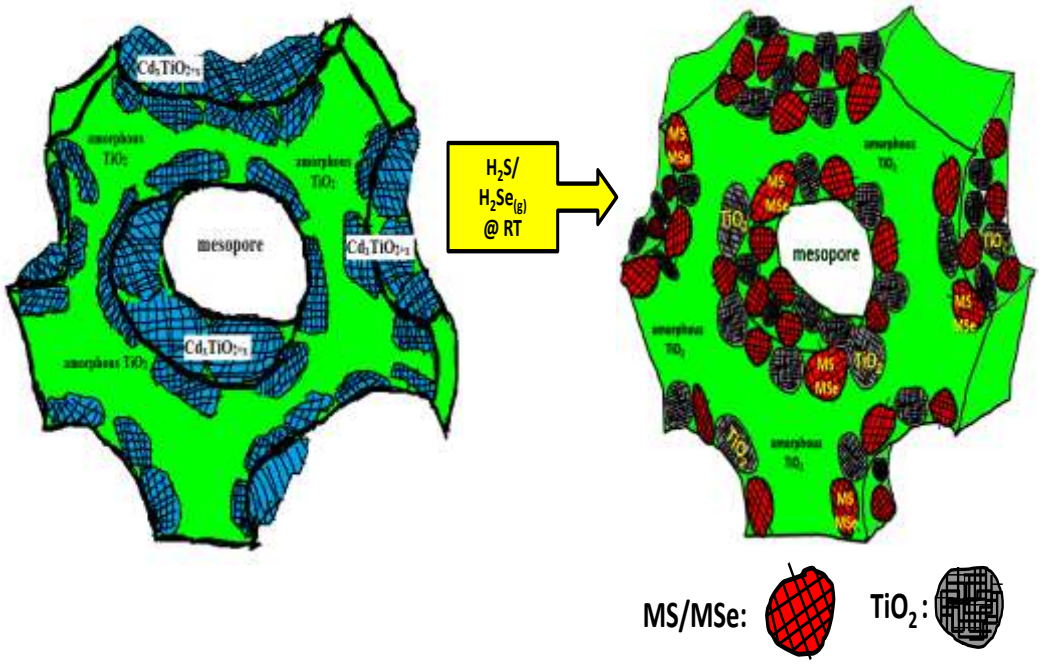

Figure 3.51 Schematic illustration of the synthesis path for the H_2S (or H_2Se) and meso-$CdTiO_3$.

3.3 Rigidifying the mesostructure with SiO_2

3.3.1 Synthesis of rigid mesoporous SiO_2-CdS/CdSe/ZnS/ZnSe

It has been well established that 7 $SiO_2/C_{12}EO_{10}$ mole ratio works very well for the synthesis of mesoporous SiO_2 film.[174] And, it has also been shown that metal salt concentration in a LLC mesophase can be increased up to 8.0 salt/$C_{12}EO_{10}$ mole ratio by using a second charged surfactant, CTAB.[46] At such a high metal salt concentration, the metal salt exists in the molten phase in the hydrophilic domains of the LLC mesophase because of the confinement effect.[47] The molten phase of salt ions acts as a non-volatile solvent to mediate the surfactant molecules into a metastable salt-surfactant-silica mesostructured thin film. The salt-surfactant LLC mesophase is used to confine as high as 60 or 71 w/w % salt species (ZnX or CdX, respectively) between the silica species and surfactant domains in the channels of mesostructured silica, and uniformly ZnO or CdO coated mesoporous SiO_2-ZnO or SiO_2-CdO thin films can be obtained upon calcination process.[128] Based on the UV-Vis absorption spectra and HRTEM analysis, it was shown that the calcined meso-SiO_2-ZnO and meso-SiO_2-CdO thin films contain uniformly coated 1.4 -1.7 nm thick crystalline metal oxide nano-islands on the pore walls of mesoporous silica films. The nano-islands of the CdO and ZnO nanocrystallites coat the pore walls of mesoporous silica films spatially with a ~100 % and ~50% surface coverage, respectively. In principle, the method developed here is based on combination of the salt-surfactant LLC mesophase and EISA method. The advantage of the high salt concentration in the salt-surfactant system is that it acts like a primary solvent as it is in the molten phase. And, the primary solvent, molten phase of salt does not evaporate while the secondary solvent, water, evaporates during the EISA process. This makes this salt-surfactant LLC mesophase differ from the traditional EISA method. During the assembly of salt-surfactant-silica system, the amount of charge surfactant, CTAB, and the effect of confined space have a key importance. In the molten phase, the surface charges of the molten salt domains are compensated by the CTAB. And, confining such high amount of metal salt ions between the silica walls and

surfactant domains in the mesostructured thin films causes a depression of freezing point of the salts used.

High concentration of TMS is achieved in the LLC mesophase of TMS/$C_{12}EO_{10}$/CTAB system through confining the salt ions between the surfactant domains as in the form of molten phase. However, the salt species are not stable at RT under ambient conditions in the mesophase. Through aging or calcination processes, they tend to leach out and form bulk metal oxides rather than producing the mesoporous metal oxides. However, a mixture of a silica precursor and molten in the presence of surfactant and solvent form LLC mesophase during evaporation of solvent, water, and forms rigid mesostructures over time. However, the mesostructure is still not stable at RT, and it is necessary to keep the fresh films above the melting point of the salts, used. The molten salt confined mesostructured silica is stable over 55-60 °C and to calcination, and forms mesoporous metal oxide-silica thin film, dumped meso-SiO_2-nCdO and meso-SiO_2-nZnO (where n is salt/$C_{12}EO_{10}$ mole ratio). The films were prepared by spin coating a clear solution of $[M(H_2O)_x](NO_3)_2$-H_2O-CTAB-HNO_3-$C_{12}EO_{10}$-TMOS (M is Zn(II) or Cd(II) and x is 6 for Zn(II) and 4 for Cd(II) salts) over various substrates, where the salt/$C_{12}EO_{10}$ mole ratio, n, has been changed between 2 and 8, and by calcining the films to 450 °C.[128] The thickness of the oxide films are around 600 nm (details of the meso-SiO_2-nMO synthesis and characterization have been extensively discussed by Karakaya`s M.Sc. thesis[177] and Karakaya et.al[128]).

The meso-SiO_2-nCdO and meso-SiO_2-nZnO films were used as a precursor to obtain mesoporous silica metal sulfide and metal selenide (denoted as meso-SiO_2-nCdS(or CdSe) and meso-SiO_2-nZnS(or ZnSe)) thin films by exposing to H_2S or H_2Se atmosphere at RT. The films were characterized using XRD, UV-Vis, FT-IR, Raman, N_2 sorption, SEM, EDS, and TEM techniques.

The conversion process of MO to MS or MSe and growth of the particles could be monitored using spectroscopy, microscopy, and diffraction techniques.

The results were very useful to understand the formation mechanism of MS or MSe from their oxides by H_2S or H_2Se reactions at RT.

3.3.2 Analysis of the Particles and Particle Size during the Synthesis of meso-SiO_2-ZnS, meso-SiO_2-ZnSe, meso-SiO_2-CdS, and meso-SiO_2-CdSe

The meso-SiO_2-CdO (or ZnO) samples were exposed to H_2S or H_2Se several times for short reaction durations; each exposure times were 15 minutes for the H_2S and 1 minute for the H_2Se reactions. Most probably, due to stronger acidity of H_2Se, it reacts more aggressively with both meso-SiO_2-ZnO and CdO samples than H_2S. Therefore the H_2Se reactions were carried in much shorter intervals than that of the H_2S reactions. The MS (or MSe) particle growth in mesoporous silica from their oxides was followed using UV-Vis, FTIR, Raman, and EDS techniques.

3.3.2.1 UV-Vis Analysis of the H_2S and H_2Se Reactions with meso-SiO_2-MO

Figure 3.52 shows the spectral changes in UV-Vis absorption spectra, obtained from the H_2S and H_2Se reactions of the meso-SiO_2-nCdO films. The gradual red shift in the absorption edge is seen clearly as the H_2S or H_2Se exposure time increase, Figure 3.52 (A) and (B), respectively. That means, MS and MSe particles grow in size as they are kept under H_2S or H_2Se atmosphere. Since the rate of these reactions are slow enough at RT, the growth of MS and MSe domains in mesoporous silica can be monitored and the degree of conversion can easily be controlled.

The band gaps of the MS and MSe nanoparticles were calculated by using direct band gap fitting method in each steps. The band gaps of meso-SiO_2-CdS change from 2.66 eV to 2.58 eV and the band gaps of meso-SiO_2-CdSe change from 2.44 eV to 2.08 eV during the reactions. The thickness of the MS (or MSe) domains was calculated by using Bruss expression and the band-gaps by assuming that the lateral growth exists in MS/MSe nanoparticles as nanosheets. The reason for this assumption will be discussed in the following sections.[176] The thicknesses of the CdS and CdSe domains gradually increased from 2.4 nm to 2.7 nm, and 2.1

nm to 3.0 nm, respectively, in time as shown in the plots, see Figure 3.52 (C) and (D).

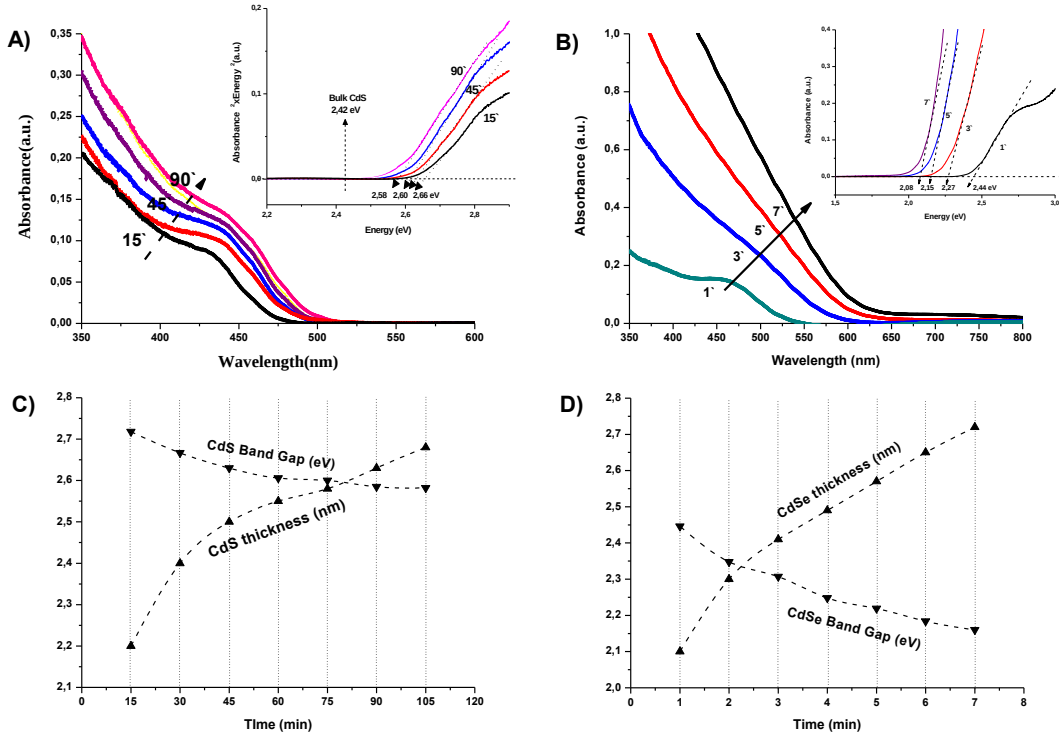

Figure 3.52 UV-Vis absorption spectra of A) meso-SiO_2-6CdS after different H_2S reaction durations, shown as numbers on the spectra in unit of minutes, and B) meso-SiO_2-6CdSe after different H2Se reaction durations, shown as numbers on the spectra in unit of minutes, and the plot of band gap and thicknesses change versus reaction time for C) CdS and D) CdSe domains in the meso-SiO_2-6CdS and meso-SiO_2-6CdSe, respectively.

3.3.2.2 FTIR Analysis of the H_2S and H_2Se Reactions with meso-SiO_2-MO

Spectral changes in the FTIR spectra, recorded during the H_2S (or H_2Se) reactions also give important information regarding to the progressive growth of the MS (or MSe), respectively. Figure 3.53 (A) and (B) show FTIR spectral changes upon exposing the meso-SiO_2-6CdO samples to H_2S and H_2Se for several times. The peaks at around 850-1000 cm^{-1} and 450-550 cm^{-1} are characteristic for the meso-SiO_2-nCdO (or ZnO) samples. These peaks are due to νSi-O stretching mode that appears upon attaching of Si-O to zinc or cadmium (Si-O-Zn/ or Cd) and ZnO or CdO stretching modes, respectively. The peaks at 992 and 496 cm^{-1} are characteristic for the meso-SiO_2-6CdO samples and shifted gradually to

around 1063 cm^{-1} and 477 cm^{-1} in both H_2S and H_2Se reactions, Figure 3.53 (A) and (B).

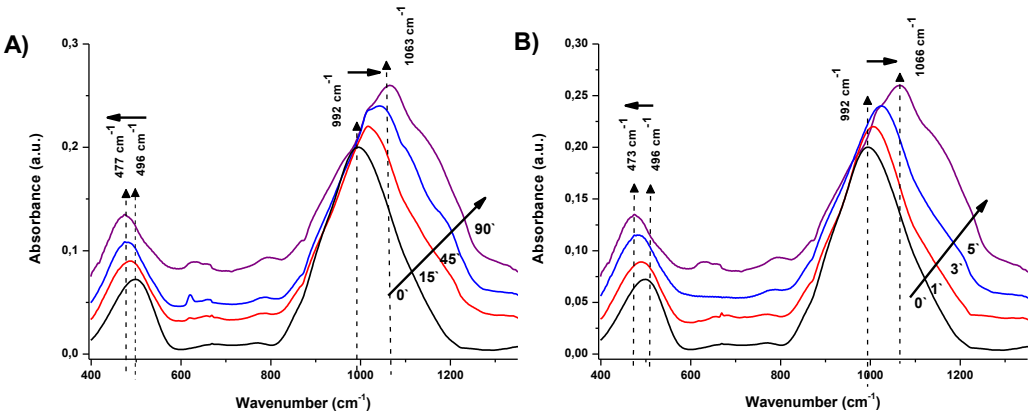

Figure 3.53 FTIR spectra of A) meso-SiO_2-6CdS after different H_2S reaction durations, shown as numbers on the spectra in unit of minutes, and B) meso-SiO_2-6CdSe after different H_2Se reaction durations, shown as numbers on the spectra in unit of minutes.

This gradual shift of FTIR peaks given above is due to change in stretching mode of vSi-O-Cd(or Zn) and CdO or ZnO during this progressive growth of MS and MSe. Hence, it can be proposed that H_2S (or H_2Se) reactions started at the top surface of the outer layers of CdO and ZnO domains, and progressed by the diffusion of the H_2S (or H_2Se) through those layers as they are more exposed to H_2S (or H_2Se). Based on those observations, it can be said that vSi-O-Cd and Zn interface modes are very sensitive to the thickness of the MO-MS (or MSe) layers, and the composition.

3.3.2.3 Raman Analysis of the H_2S and H_2Se Reactions with meso-SiO_2-MO

Raman spectroscopy, provides information about the vibrational modes of materials so that it can be used to characterize the substances.[178, 179] If there is a resonance effect from the electronic states, which are close to laser frequency used for the Raman measurements, intensity of the Raman modes increase, by a factor of 10^6 in some cases, so that the spectra can be obtained using small amount of sample. The resonance raman spectra (RRS) of meso-SiO_2-CdS and meso-SiO_2-CdSe were recorded under a laser with a 532 nm excitation wavelength, see Figure 3.54 (A) and (B). The spectra were recorded on a silicon wafer, where the

peak at 520 cm^{-1} is due to silicon. The Raman spectra of the *meso*-SiO_2-CdS, *meso*-SiO_2-CdSe films in Figure 3.54 (A) and (B) display intense Raman peaks due to longitudinal optical (LO) modes at 300 and 205 cm^{-1}, respectively, with shoulders on their low energy side due to surface modes.[180] The Raman peaks of the CdS and CdSe nanocrystallites are broad compared to bulk silicon peak at 520 cm^{-1}, and they are red shifted compared to their bulk CdS and CdSe due to phonon confinement effect.[181] Furthermore, the peaks due to LO modes gradually increased in intensity, shifted to higher energy and became relatively sharper over the reaction time. That means, the Raman spectra also supported the gradual growth of the CdS and CdSe particles in time. The blue shift (from 300.0 to 302.3 cm^{-1} for CdS, and from 202.5 to 205.8 cm^{-1} for CdSe) and decrease on the full-width-half maximum (from 16.41 to 14.92 cm^{-1} for CdS, and from 19.2 to 17.2 cm^{-1} for CdSe) of the 1LO mode at around 300 cm^{-1} and 205 cm^{-1} are the indicators for the growth of the CdS and CdSe domains over time, respectively.

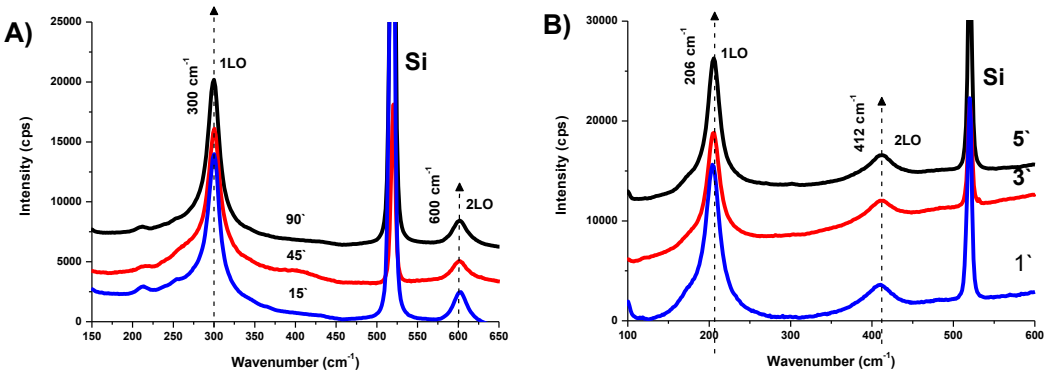

Figure 3.54 Resonance Raman Spectra of A) meso-SiO_2-6CdS after different H_2S reaction durations, shown as numbers on the spectra in unit of minutes, and B) meso-SiO_2-6CdSe after different H_2Se reaction durations, shown as numbers on the spectra in unit of minutes.

3.3.2.4 EDS Analysis of meso-SiO_2-CdS, meso-SiO_2-CdSe, and of meso-SiO_2-ZnS

EDS data of a series of samples were analyzed in order to confirm the gradual increase in the amount of S and Se, while the Si and Cd or Si and Zn signals remain constant during the growth of the CdS, CdSe, ZnS, and ZnSe nanocrystallites.

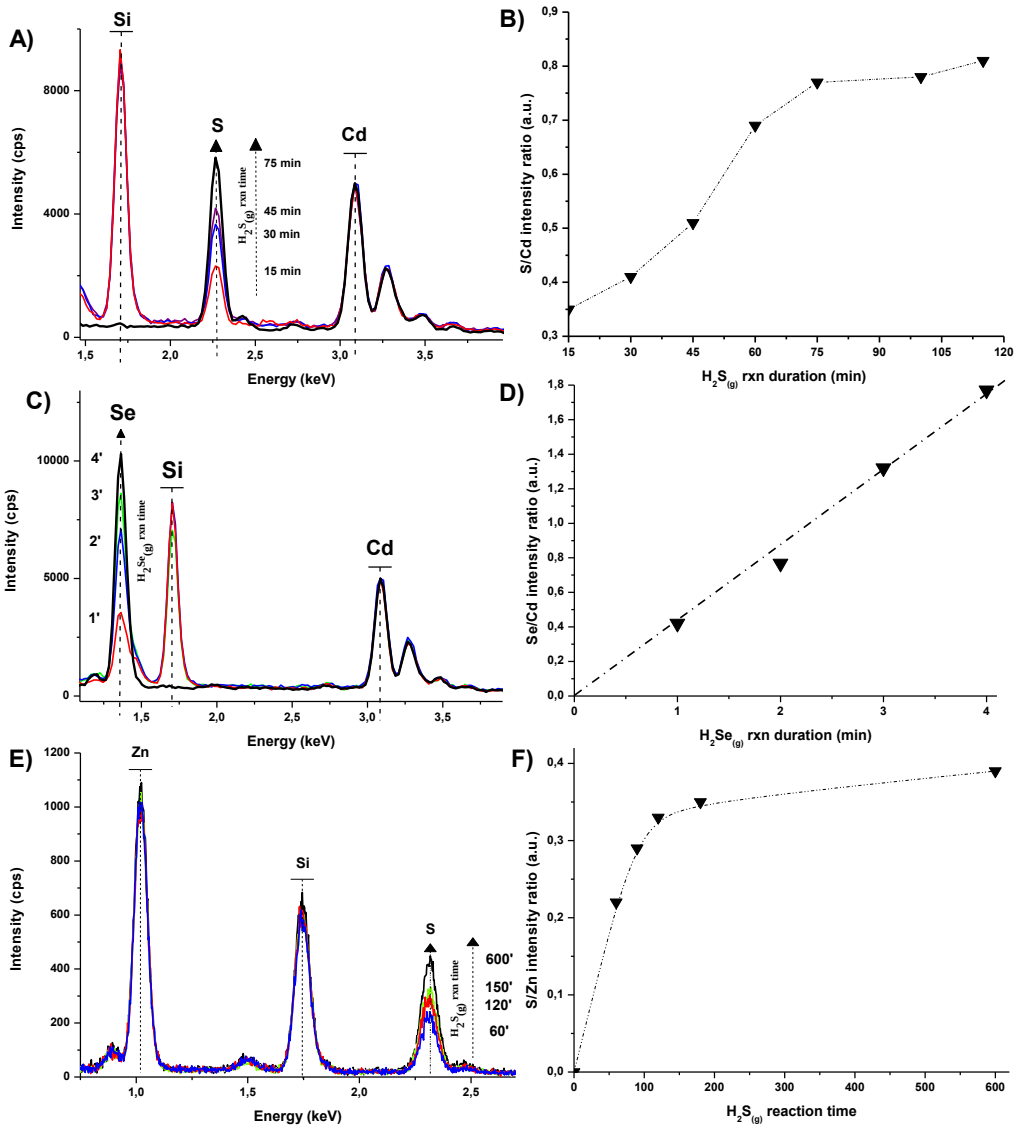

Figure 3.55 The EDS spectra of meso-SiO_2-6CdO over time under an atmosphere of A) H_2S and C) H_2Se (top EDS spectra are the bulk CdS and CdSe, respectively). The plots of B) S/Cd intensity ratio in (A) vs. H_2S reaction duration, and D) Se/Cd intensity ratio in (C) vs. H_2Se reaction duration. E) The EDS spectra of meso-SiO_2-6ZnO over time under H_2S atmosphere (top EDS spectra is the bulk ZnS), and F) The plot of S/Zn intensity ratio in (E) vs. H_2S reaction duration.

The EDS spectra were collected from the same samples used for the FTIR, UV-Vis, and Raman measurements. Small amount of meso-SiO_2-CdO-CdS, meso-SiO_2-CdO-CdSe, and meso-SiO_2-ZnS films were scraped and put onto the SEM stubs at each stage of H_2S and H_2Se reactions for EDS measurements. Figure 3.55 (A) and (C) gives the EDS spectra of meso-SiO_2-6CdO over time under H_2S and H_2Se atmosphere, respectively. The EDS spectra display gradual

increase in S and Se peaks, while the Si and Cd signals remain constant during H_2S or H_2Se reactions, respectively. Figure 3.55 (B) and (D) give the EDS results as S/Cd and Se/Cd intensity ratio over time, respectively. Almost linear increase in the amount of S and Se supported the gradual increase in the particle size of the CdS and CdSe domains during H_2S and H_2Se reactions at RT, respectively. Therefore, composition in the meso-SiO_2-CdO-CdS and meso-SiO_2-CdO-CdSe films can be adjusted by controlling the H_2S and H_2Se exposure time.

The EDS spectra of meso-SiO_2-6ZnO over time under a H_2S atmosphere are given in Figure 3.55 (E). The S/Zn EDS intensity ratio increase during the exposure of the meso-SiO_2-6ZnO thin films to H_2S, Figure 3.55 (F). The S/Zn ratio reaches to a constant value, 0.39 over time. Since the S/Zn EDS intensity ratio is equal to 0.39 in the bulk ZnS, indicating the completion of ZnS reaction.

3.3.2.5 The Growth Kinetics of meso-SiO_2-CdS and meso-SiO_2-CdSe

Huang studied the kinetics of the growth of mercaptoethanol capped ZnS nanoparticles under hydrothermal coarsening.[182]

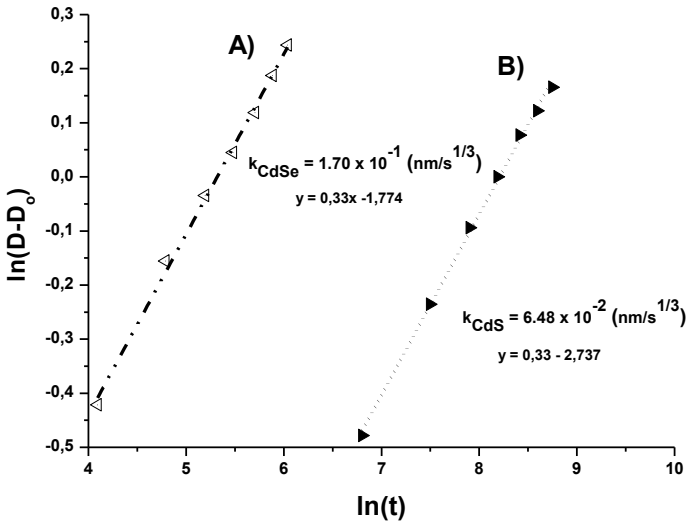

Figure 3.56 The ln(D-Do) versus ln(t) plots of the time dependent thickness data of meso-SiO_2-6(CdO-CdS) (A) and meso-SiO_2-6(CdO-CdSe) (B).

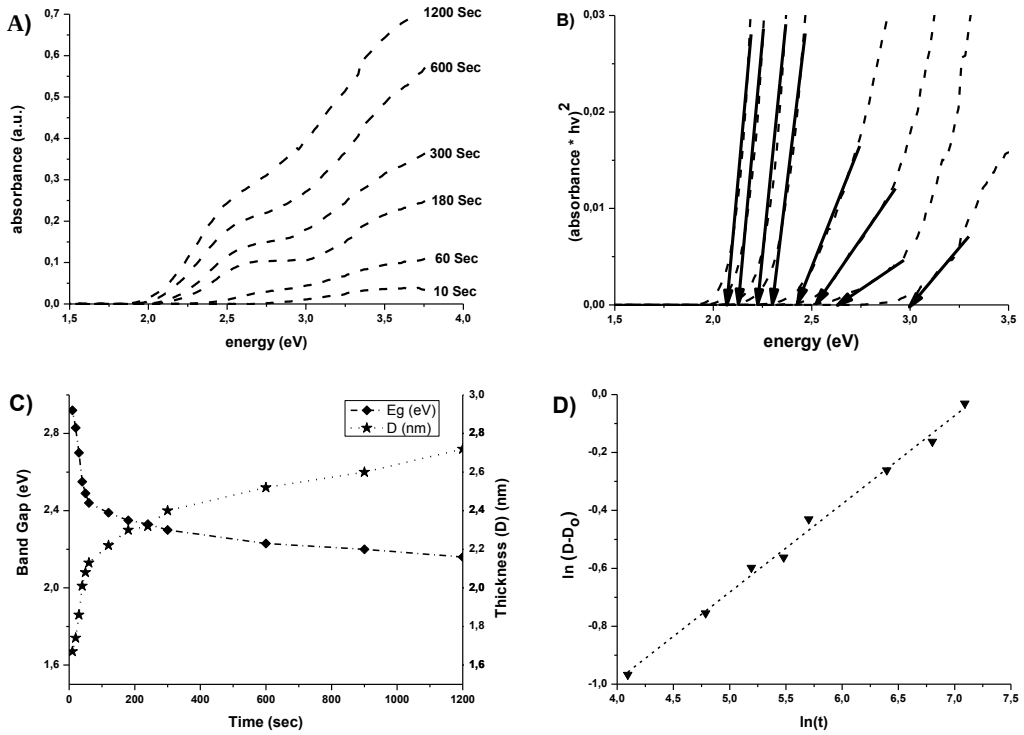

Figure 3.57 A) The UV-Vis absorption spectral changes during H_2Se reaction of meso-SiO_2-6CdO, B) the (absorbance*hv)^2 versus energy plots, C) the band-gap and particle size versus time plots, and D) plot of ln(D-D_o) versus ln(t).

Based on the results of their observations, the change in thickness of the MS (or MSe) nanoparticles over time can be analyzed through the Equation **3.4**;

$$D\text{-}D_o = kt^{1/n} \qquad \text{Equation 3.4}$$

where D and D_o are the particle sizes at time t and t_o, respectively, and k is the material constant, and n is characteristic to the growth mechanism. For n = 2, the diffusion of ions along the matrix-particle boundary controls the crystal growth, for n = 3, the volume diffusion of ions in the matrix controls the crystal growth, and for n = 4, the dissolution kinetics at the particle-matrix interface dominates during the crystal growth.

In order to determine the growth mechanism of MS (or MSe) in our system, we used the thickness data of MS (or MSe) at different times of the H_2S

(or H_2Se) reactions as given in Figure 3.52 (C) and (D). From the plot of ln(D-Do) versus time, in Figure 3.56, n is calculated to be 3.0 for both H_2S and H_2Se reactions of meso-SiO_2-6(CdO-CdS(or CdSe)) for suggested D_o value of 1.50 nm for CdS, and 1.44 nm for CdSe. Up to D_0 values suggested above, it can be assumed that the reaction rates are very fast up to those thicknesses and so, the reaction mechanism cannot be observed under current methods. In order to define the D_o values, UV-Vis spectra of meso-SiO_2-6(CdO-CdSe) with very small amounts of H_2Se for a very short reaction periods have been collected. As shown in Figure 3.57, the initial reaction is very fast so that a few CdSe layers form almost immediately up to a thickness of around 1.4-1.5 nm. Therefore, the D_o values are decided to be 1.50 nm for CdS and 1.44 nm for CdSe nanoparticles.

Hence, it can be suggested that the CdS and CdSe nanoparticles grow by volume diffusion of ions through the inner layers. The initial stages of the reactions are very fast up to the D_o values calculated above, and cannot be monitored in detail by the current methods. However, as the growth of the CdS and CdSe nanoparticles approaches to the silica-cadmium oxide interface, the reaction occurs at much slower rate than the reactions at the outer layers of silica-cadmium oxide. The silica-cadmium oxide interface is the least reactive region. The EDS, FT-IR, and UV-Vis absorption spectral changes indicate that at each stage of the reactions, SiO_2-n(CdO-CdS(or CdSe)) and SiO_2-n(ZnO-ZnS(or ZnSe)) films are in the form of sponge-like mesoporous thin films as the CdO or ZnO thickness decreases over time.

3.3.2.6 TEM Analysis of meso-SiO_2-CdS, meso-SiO_2-CdSe, and of meso-SiO_2-ZnS

Figure 3.58 shows the TEM images collected from three sets of partially H_2S and H_2Se reacted samples, denoted as meso-SiO_2-6(ZnO-ZnSe), meso-SiO_2-6(CdO-CdS), and meso-SiO_2-6(CdO-CdSe). As compared to the image in Figure 3.58 (a), which belongs to meso-SiO_2-6ZnO, the crystalline metal sulfide or metal selenide domains follow the pattern of the silica walls during H_2S or H_2Se reactions as in the case of metal oxides.[128]

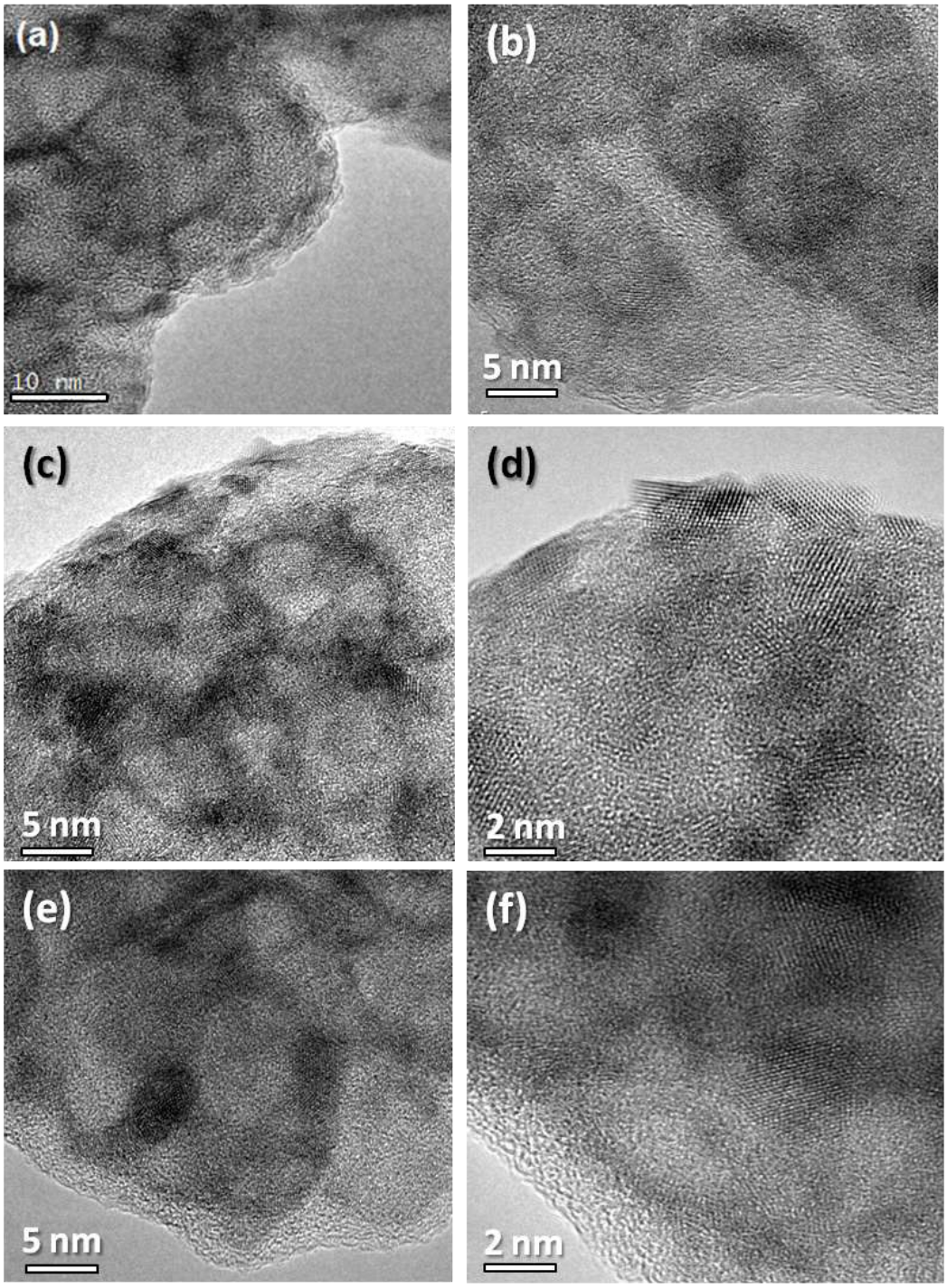

Figure 3.58 TEM images of the meso-SiO_2-6ZnO (a) before and (b) after partially H_2Se reacted films (meso-SiO_2-6(ZnO-ZnSe)), (c) and (d) after partially H_2S reacted films of meso-SiO_2-6(CdO-CdS, (e) and (f) after partially H_2Se reacted films of meso-SiO_2-6(CdO-CdSe).

The meso-SiO_2-(MO-MS (or MSe)) films have the disordered/non-uniform sponge-like pore structure with the size range of 3-20 nm (mesopores), composed of a few nanometer thick crystalline metal sulfide or metal selenide nano-islands, which are relatively the darker regions in the images. As described by the spectroscopic techniques the H_2S or H_2Se reactions start at the top surface of the outer layers of the metal oxides, and diffuse through the inner layers until Si-O-M interface. TEM images prove that during those partial reactions, there is no change in the overall pore morphology.

3.3.3 The Cleavage of Metal – Oxygen – Silicon Bond

So far, by analyzing the H_2S and H_2Se reactions of the meso-SiO_2-nCdO (or ZnO) thin films over time through using various techniques, it is verified that the CdO and ZnO domains react with H_2S or H_2Se and converted into their sulfides and selenides at RT. By controlling the reaction durations, the particle size of the MS (or MSe) domains could be controlled as well. The results showed us that the reactions started at the outer layers of metal oxides and as the samples are more exposed to H_2S (or H_2Se) gas, metal sulfides or metal selenides grow further through inner layers over time. Further analyses were required to figure out the whole growth mechanism. From the recent works[128] we knew that the precursor metal oxides are nano-crystalline and are nicely coated over the silica walls in the mesoporous silica. Even though the zinc oxide can be partially coated over the silica walls like nano-islands in meso-SiO_2-nZnO, the cadmium oxide can efficiently coat the whole silica walls in the meso-SiO_2-nCdO. Here, by using spectroscopic, microscopic and diffraction techniques complementarily, we found out that all the metal oxides in the mesoporous silica could be successfully converted into their sulfides or selenides by forming the metal sulfide or metal selenide nanosheets over the silica walls.

3.3.3.1 EDS Analysis of meso-SiO_2-CdS and meso-SiO_2-CdSe

EDS data have been used to confirm the complete conversion of metal oxides to their sulfides (or selenides) by using their pure bulk compounds as references. Figure 3.59 (A) and (B) gives the EDS spectra of the meso-SiO_2-6CdS

and meso-SiO_2-6CdSe, respectively. Since there is no side product from those reactions, 1.1 S/Cd and 2.0 Se/Cd intensity ratios in the bulk CdS and CdSe, respectively, were used as a guarantee of the complete conversion of the metal oxides to metal sulfide or metal selenide. Then, analyzing those samples with FTIR and TEM techniques enlightened us about the reaction mechanism.

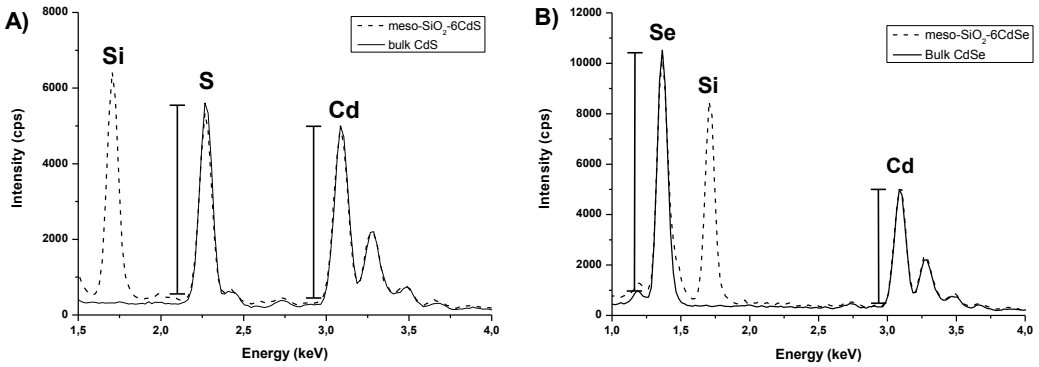

Figure 3.59 The EDS spectra of A) meso-SiO_2-6CdS with pure bulk CdS, and B) meso-SiO_2-6CdSe with pure bulk CdSe.

3.3.3.2 FTIR Analysis of meso-SiO_2-CdS and meso-SiO_2-CdSe

Figure 3.60 (A) and (B) are the FTIR spectra of the meso-SiO_2-6CdS and meso-SiO_2-6CdSe, respectively. These were the samples in which the complete conversion of metal oxides to their sulfides and selenides were confirmed by EDS analysis as explained above. We observed that the FTIR spectra of the completely reacted samples coincide well with the spectrum of the pure mesoporous silica, see Figure 3.60 (A) and (B). In the FTIR spectra of meso-SiO_2-nCdO, the peaks at around 992 cm^{-1} and 500 cm^{-1} are due to the νSi-O stretching mode of the surface silicon-oxygen bonds, attached to a cadmium (Si-O-Cd) (same is observed for Si-O-Zn) and silica deformation modes and/or ZnO or CdO stretching modes, respectively.[128] Upon complete conversion of the metal oxide to metal sulfide or metal selenide, the peak at 992 cm^{-1} in the meso-SiO_2-nCdO shifts to 1080 cm^{-1}, which corresponds to the pure silica stretching mode, and the peak at 500 cm^{-1} in the meso-SiO_2-nCdO shifts to 465 cm^{-1}, which corresponds to the pure silica breathing modes, see Figure 3.60. In Section 3.3.2.2, we explained the gradual shift of those peaks over time as the metal sulfides (or selenides) grew further.

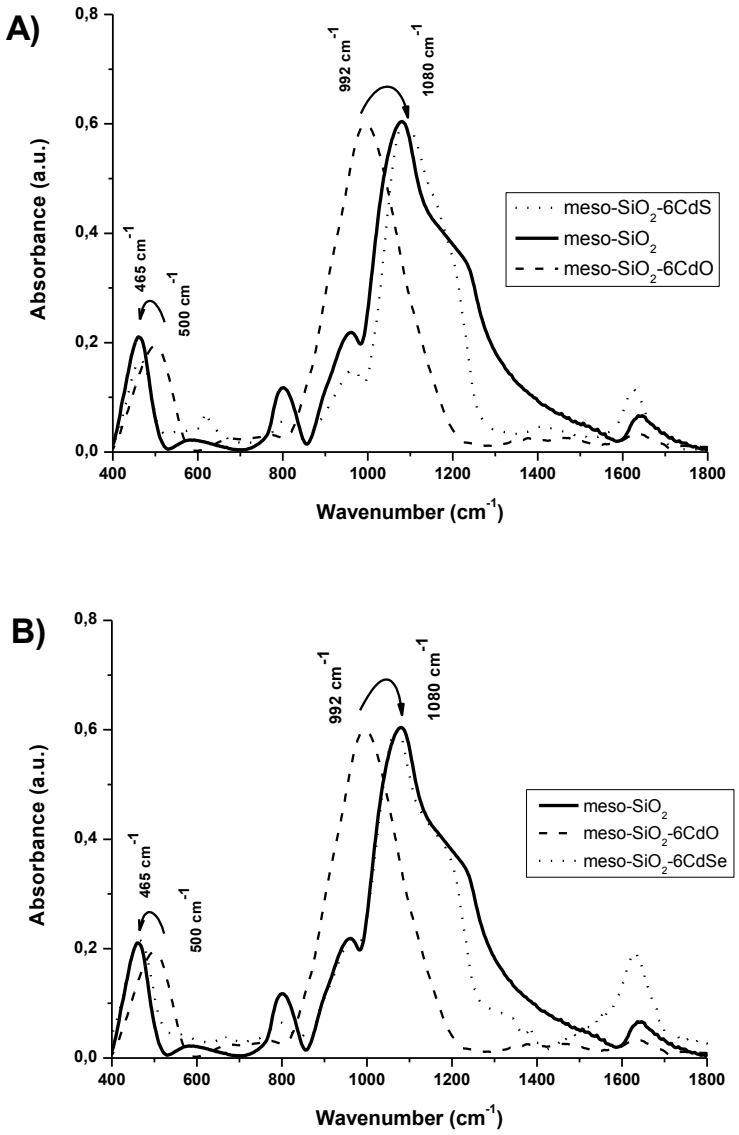

Figure 3.60 FTIR spectra of meso-SiO_2-6CdO, pure meso-SiO_2 and A) meso-SiO_2-6CdS and B) meso-SiO_2-6CdSe after complete conversion.

Therefore, it can be confidently suggested for the reaction mechanism that; the metal oxides at the top surfaces of the outer layer are the first which are converted to MS or MSe under H_2S or H_2Se atmosphere, and the growth of the MS or MSe proceeds further through the inner layers of the metal oxide domains as they are more exposed to H_2S or H_2Se gas, and the last layer, which is the M-O-Si interface, reacts finally and so, the M-OSi bond breaks, giving an FTIR spectrum, which is very similar to the pure mesoporous silica. Similar spectral

changes were observed for the meso-SiO_2-nZnO and H_2S or H_2Se reactions, and they will be given in Section 3.3.4.3 (see later). The equation of the reactions can be given as;

$$\text{meso-SiO}_2\text{-nCdO} + \text{H}_2\text{S} \rightarrow \text{meso-SiO}_2\text{-nCdS} + \text{nH}_2\text{O} \quad \text{Equation 3.5}$$

$$\text{meso-SiO}_2\text{-nCdO} + \text{H}_2\text{Se} \rightarrow \text{meso-SiO}_2\text{-nCdSe} + \text{nH}_2\text{O} \quad \text{Equation 3.6}$$

$$\text{meso-SiO}_2\text{-nZnO} + \text{H}_2\text{S} \rightarrow \text{meso-SiO}_2\text{-nZnS} + \text{nH}_2\text{O} \quad \text{Equation 3.7}$$

$$\text{meso-SiO}_2\text{-nZnO} + \text{H}_2\text{Se} \rightarrow \text{meso-SiO}_2\text{-nZnSe} + \text{nH}_2\text{O} \quad \text{Equation 3.8}$$

3.3.3.3 TEM Analysis of meso-SiO_2-CdS and meso-SiO_2-CdSe

The HRTEM images from different samples, namely meso-SiO_2-6CdS, meso-SiO_2-6CdSe, and meso-SiO_2-6ZnSe for the complete H_2S and H_2Se reactions are shown in Figure 3.61. The homogenous distribution of the crystalline domains can be seen throughout the films. If compared to the TEM images of partially reacted samples in Figure 3.58, in the completely reacted samples, the sizes of domains are bigger than the partially reacted ones. The crystalline domains have the sizes of 15 nm and 3 nm all over the sample due to the MS or MSe nano-flakes grown along the pore axis and thickness axis, respectively. Since we observe a blue shift on the UV-Vis absorption-edge of the particles, which are indeed in 10-25 nm sizes, e-h pairs must be confined at least in one of their axis. Therefore, based on the blue-shift in the UV-Vis absorption-edge, and the plate like crystalline MS or MSe domains observed in the TEM images, it can be suggested that the MS or MSe domains form in the shape of nano-flakes. This also consists with the CdO and ZnO nanoislands in meso-SiO_2-CdO and meso-SiO_2-ZnO and the growth mechanism suggested above.

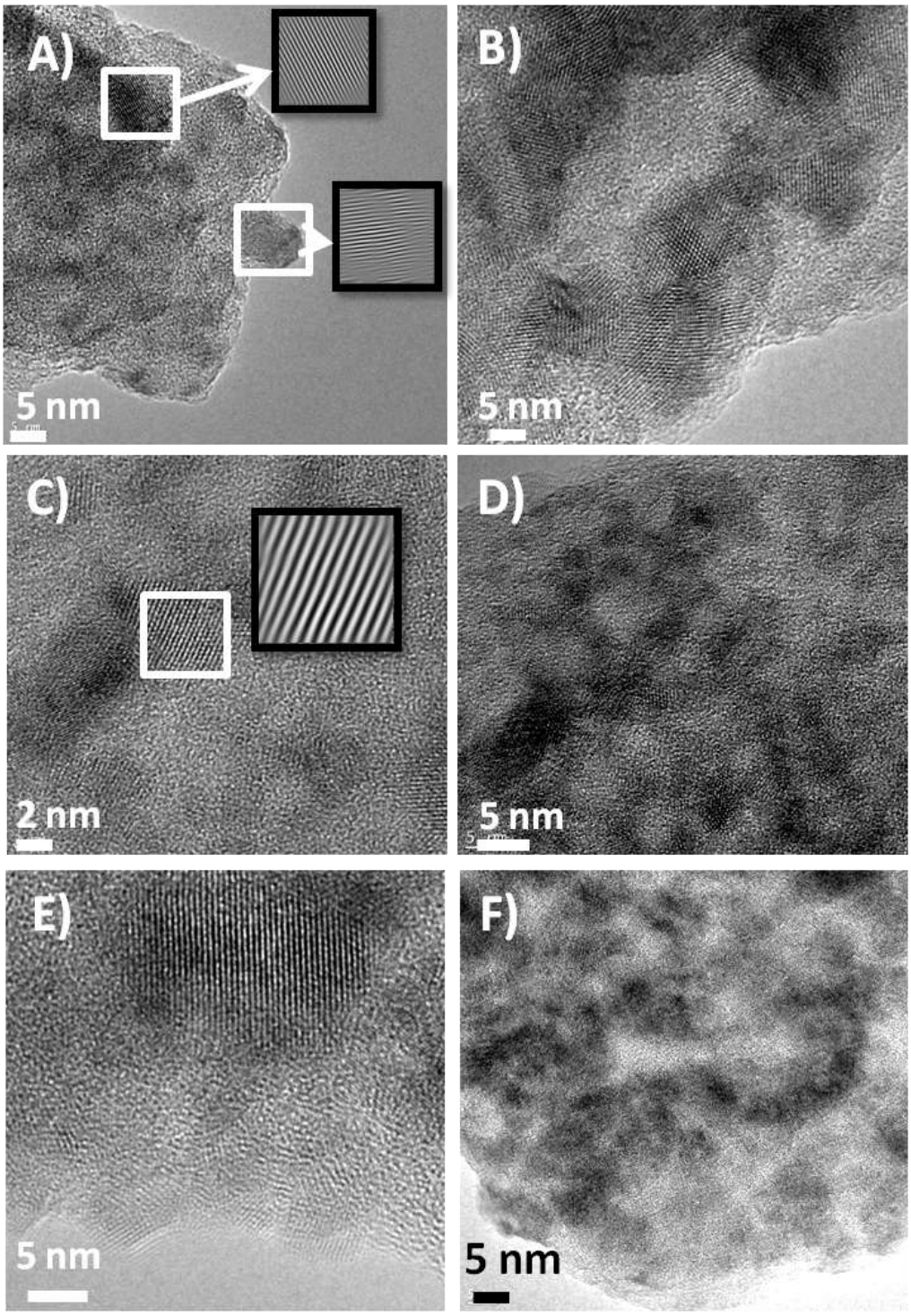

Figure 3.61 TEM images of complete H_2S reaction of meso-SiO_2-6CdS samples with A) 5 nm and B) 5 nm scale bar; complete H_2Se reaction of meso-SiO_2-6CdSe samples with C) 2 nm and D) 5 nm scale bar; complete H_2Se reaction of meso-SiO_2-6ZnSe samples with E) 5 nm and F) 5nm scale bar.

The insets in Figure 3.61 (A) and (C) are the inverse FFT images of the selected regions. The insets in Figure 3.61 display lattice fringes, which are spaced by 0.336 nm, belong to the (111) planes of zinc blend CdS domains. 10-20 nm sized CdS nanoflakes distributed in the film are observed in Figure 3.61 (B). The inverse FFT in Figure 3.61 (C) displays the lattice fringes, spaced by 0.182 nm, of the (311) planes of the zinc blend CdSe nano-flakes. The (111) planes of the zinc blend ZnSe nano-flakes can be seen in Figure 3.61 (E). The TEM images also support that all metal oxides can be converted into metal sulfides (or selenides), and they maintain the morphology of the oxide precursor thin films.

3.3.3.4 N_2 Sorption Data Analysis of meso-SiO_2-CdS and meso-SiO_2-ZnS

Figure 3.62 shows the N_2 sorption isotherms and pore size distribution plots of the meso-SiO_2-6CdS and meso-SiO_2-6ZnS samples. The data were collected from the powders collected by scraping around 20-30 thin films of meso-SiO_2-6CdS and meso-SiO_2-6ZnS prepared on glass slides. The N_2 sorption data in Figure 3.62 (A) and (C) shows a type IV isotherm and hysteresis loops, and these are characteristic for the mesoporous materials. Therefore, the partially reacted or completely reacted meso-SiO_2-6CdS and meso-SiO_2-6ZnS samples maintain their mesoporosity. The BET surface area and the BJH pore-volume of the meso-SiO_2-6CdO increase, upon complete conversion to CdS, from 55 to 90 m^2/g and from 0.16 to 0.30 cm^3/g, respectively. However, the BET surface area and the BJH pore-volume of the meso-SiO_2-6ZnO decreases, upon complete conversion to ZnS, from 175 to 75 m^2/g and 0.40 to 0.26 cm^3/g, respectively.

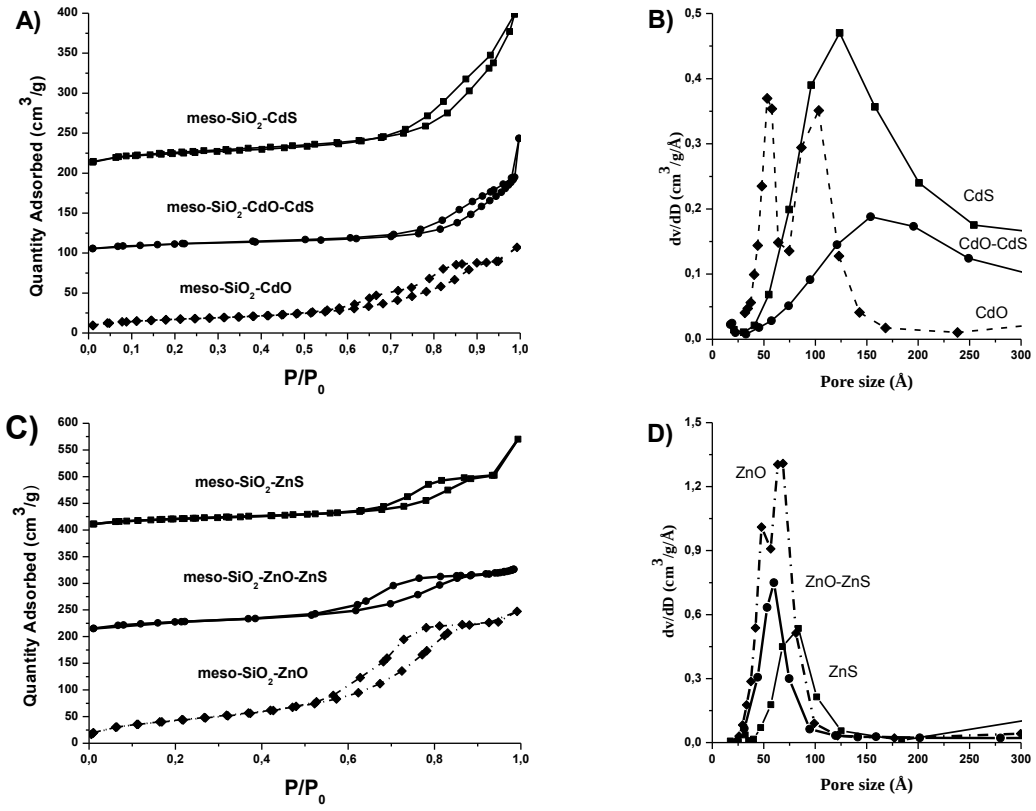

Figure 3.62 A) and C) The N_2 (77.4 K) sorption isotherms and B) and D) pore size distribution plots of before, partially, and full H_2S reactions of meso-SiO_2-6CdS and meso-SiO_2-6ZnS, respectively.

The t-plots are useful to determine if there are micro- and/or mesopores throughout the sample. The slight downward deviation exists in the 4-6 Å range in the t-plots of the adsorption isotherms of both meso-SiO_2-6CdO and meso-SiO_2-6ZnO before H_2S reaction is due to the presence of some microporosity throughout the samples, see Figure 3.63. The downward deviation disappears in the t-plots of meso-SiO_2-6(CdO-CdS) samples after partial H_2S reaction of the meso-SiO_2-6CdO. However, downward deviation in the t-plots of meso-SiO_2-6CdS reappears upon complete conversion of CdO to CdS. This is most probably because of the formation of more micropores between the silica walls and metal sulfide domains. The reason for this is that the CdS nanoflakes are pealed out upon breakage of the Si-O-Cd bond at the O_3Si-O-CdO_3 interface in the meso-SiO_2-nCdS upon complete H_2S reaction. The t-plots of meso-SiO_2-6ZnS do not display downward deviation before or partial or complete H_2S reaction, and so

there is no microporocity throughout those samples. The reason might be the difference between the degree of coating of silica walls with the metal oxides in the meso-SiO_2-nCdO and meso-SiO_2-nZnO precursors. The percentage of the coating of the silica walls by CdO and ZnO are 35 % and 90 % in the meso-SiO_2-6CdO and meso-SiO_2-6ZnO samples, respectively.[128]

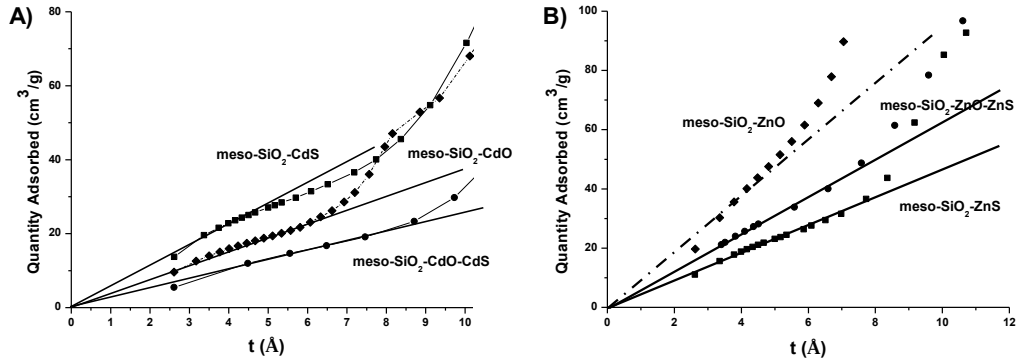

Figure 3.63 A) and B) t- plots of the N_2 sorption data collected from the meso-SiO_2-6CdS and meso-SiO_2-6ZnS samples before, partially, and complete H_2S reactions, respectively.

3.3.4 The dependence of particle size in meso-SiO_2-nZnS, meso-SiO_2-nZnSe, meso-SiO_2-nCdS, and meso-SiO_2-nCdSe on n

In Section 3.3.3, it is explained that the H_2S (or H_2Se) attacks the metal oxides starting from the top surfaces of the outer layers to the inner layers until M-O-Si interface and complete conversion of metal oxides to metal sulfides (or metal selenides) occurs upon the breakage of that M-O bond at the interface. Also, the particle size of metal sulfide (or selenide) can be totally controlled by H_2S (or H_2Se) reaction periods over time. The morphology of the metal oxide silica precursors is maintained during conversion of metal oxides into their sulfides (or selenides).

Furthermore, we observed that the particle sizes of MS (or MSe) also depend on the amount of MO in the meso-SiO_2-nMO. The H_2S (or H_2Se) reactions were carried using the meso-SiO_2-nCdO (or ZnO) samples, where n is M(II)/$C_{12}EO_{10}$ mole ratio as 2, 4, 6, and 8. The samples were characterized by using UV-Vis, FTIR, Raman, EDS, SEM, and TEM techniques.

3.3.4.1 UV-Vis Analysis of meso-SiO_2-CdS, meso-SiO_2-CdSe, meso-SiO_2-ZnS and meso-SiO_2-ZnSe

Figure 3.64 displays UV-Vis absorption spectra, which were recorded using thin films, prepared over quartz or glass substrates, of all 4 sets of samples after H_2S and H_2Se reactions. The band-gap values of the samples are given as the insets in the plots in Figure 3.64 (B), (D), (F), and (H). The absorption edges are at between 2.79 and 2.66 eV in the meso-SiO_2-nCdS, 2.45 and 2.02 eV in the meso-SiO_2-nCdSe, and 3.43 and 2.90 eV in the meso-SiO_2-nZnSe, and 4.07 and 3.90 eV in the meso-SiO_2-nZnS with increasing n, are all blue shifted from their bulk counter parts due to quantum size effect (the bulk values are 2.42, 1.74, 2.70 eV, and 3.68 eV, respectively). The UV-Vis absorption edges of all samples show gradual red-shifts with increasing n in the meso-SiO_2-nZnS, meso-SiO_2-nZnSe, meso-SiO_2-nCdS, or meso-SiO_2-nCdSe, indicating gradual increase of the ZnS, ZnSe, CdS, or CdSe thicknesses, with increasing n in the meso-SiO_2-nZnS, meso-SiO_2-nZnSe, meso-SiO_2-nCdS, or meso-SiO_2-nCdSe, respectively. From the band-gap values, the thicknesses of the MS or MSe domains were calculated by using the effective mass model developed by Bruss et. al.[176]

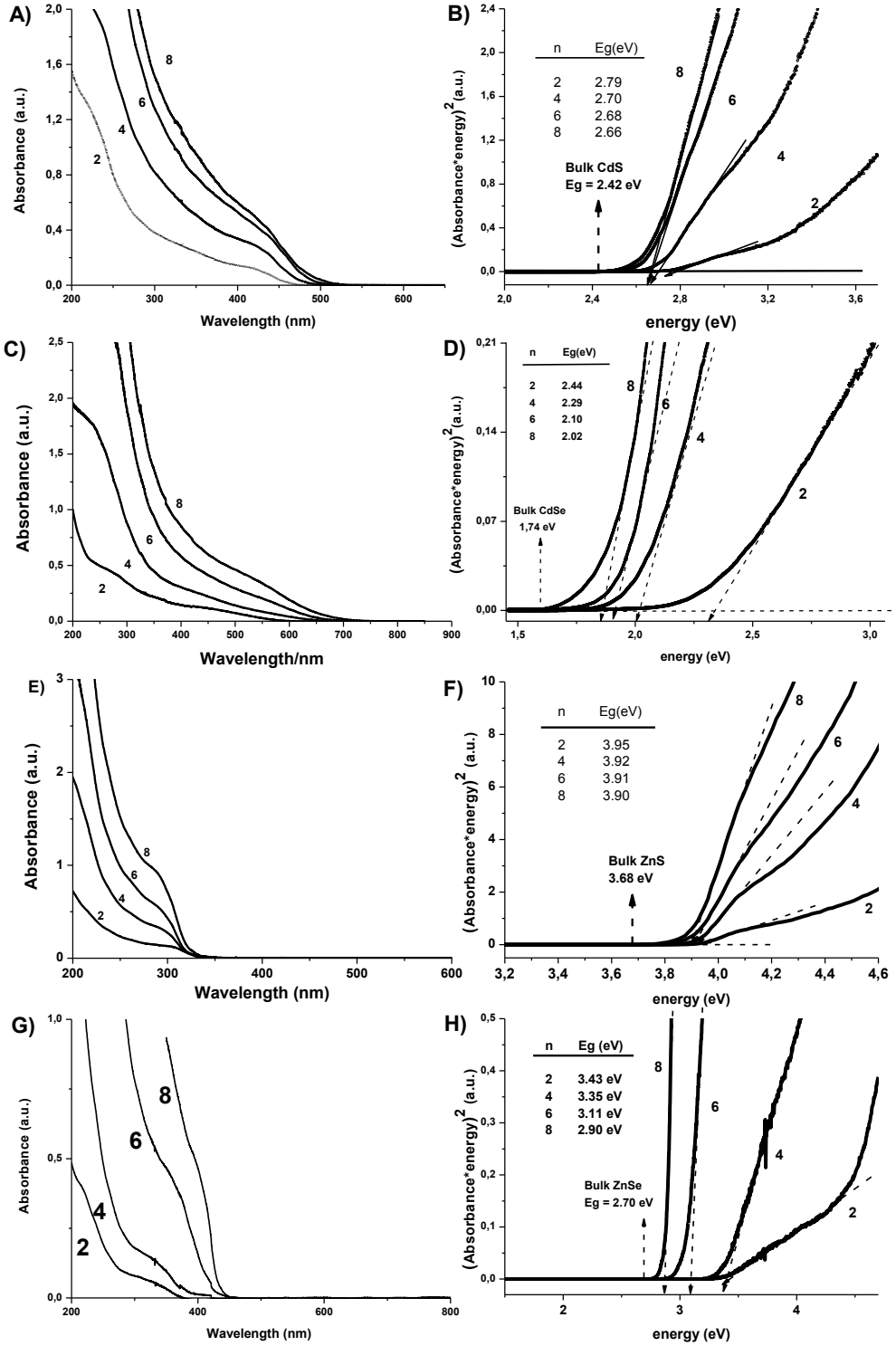

Figure 3.64 A) meso-SiO_2-nCdS, C) meso-SiO_2-nCdSe, E) meso-SiO_2-nZnS, and G) meso-SiO_2-nZnSe UV-Vis absorption spectra, and B) meso-SiO_2-nCdS, D) meso-SiO_2-nCdSe, F) meso-SiO_2-nZnS, and H) meso-SiO_2-nZnSe direct band-gap relation (absorbance*energy)^2 versus energy plots where n = 2, 4, 6, and 8.

Table 3.3 Electronic parameter for the indicated crystalline direct gap semiconductors, E is the dielectric coefficient at optical frequencies. The effective masses are in units of the free electron mass. *Eg* is the bulk band gaps.[176]

	CdS	CdSe	ZnSe	ZnS
E_g	2.42	1.75	2.74	3.68
m_e	0.19	0.13	0.17	0.40
m_h	0.8	0.45	1.44	0.61
Є	5.7	10.6	8.3	5.2

The electronic parameters used to calculate the thicknesses of MS or MSe domains are given in . According to the band-gap values measured, the thickness of the CdS layers change from 2.0 to 2.5 nm, CdSe layers change from 2.8 to 3.2 nm, ZnSe layers change from 1.3 to 2.0 nm, and ZnS layers change from 1.0 to 1.3 nm in the meso-SiO_2-nCdSe, meso-SiO_2-nCdSe, meso-SiO_2-nZnSe, and meso-SiO_2-nZnS, respectively, with an increasing n from 2 to 8. The results also support our reaction mechanism in the previous chapter. The H_2S or H_2Se reactions with meso-SiO_2-nCdO and meso-SiO_2-nZnO samples, starts from the outer layer of both oxides and continues until all oxides are converted into their sulfides or selenides through lateral growth.

3.3.4.2 EDS Analysis of meso-SiO_2-CdS, meso-SiO_2-CdSe and meso-SiO_2-ZnS

Figure 3.65 gives the EDS analysis of the meso-SiO_2-nCdS, meso-SiO_2-nCdSe, and meso-SiO_2-nZnS samples used for the UV-Vis absorption spectra. The linear increase of the Zn/Si and Cd/Si EDS intensity ratios measured by EDS versus their prepared mole ratios, with an increase in n from 2 to 8, proved the homogeneity of the meso-SiO_2-nCdS (or CdSe) and meso-SiO_2-nZnS (or ZnSe). In all samples, the complete conversion was ensured by the EDS data that the S/Cd intensity ratio is 1.1 as in its bulk CdS, the Se/Cd intensity ratio is 2.0 as in its bulk CdSe, and the S/Zn intensity ratio is 0.39 as in its bulk ZnS.

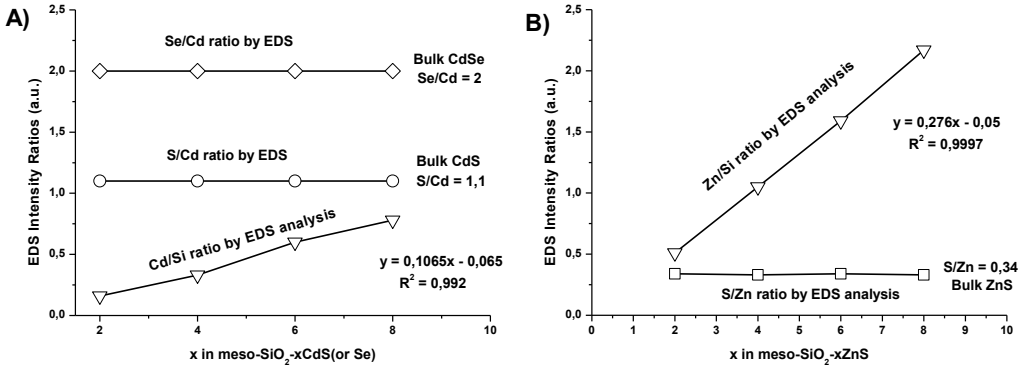

Figure 3.65 A) Se/Cd, S/Cd and Cd/Si EDS intensity ratios versus n in meso-SiO_2-nCdS (and Se), respectively, B) the S/Zn and Zn/Si intensity ratios versus n in meso-SiO_2-nZnS.

3.3.4.3 FTIR Analysis of meso-SiO_2-ZnS and meso-SiO_2-ZnSe

Figure 3.66 (A) and (B) show the FTIR spectra of the meso-SiO_2-nZnS and meso-SiO_2-nZnSe for the n values among 2 and 8 Zn(II)/$C_{12}EO_{10}$ mole ratio. The FTIR spectral changes upon complete conversion of meso-SiO_2-nCdO to meso-SiO_2-nCdS and meso-SiO_2-nCdSe were already given above in Section 3.3.3.2. Here, those FTIR spectra were taken from the samples whose UV-Vis spectra and EDS analysis were given above in Sections 3.3.4.1 and 3.3.4.2.

For all set of samples, these spectra were recorded to confirm a complete conversion of the ZnO domains to ZnS or ZnSe domains upon exposing the samples to H_2S or H_2Se for long enough. The peaks at 926 and 536 cm^{-1} are due to Si-O-Zn bond at the O_3Si-O-ZnO_3 interface in the meso-SiO_2-nZnO samples. The shift of those peaks from 926 to 1067 cm^{-1}, and 536 to 456 cm^{-1}, which correspond to the pure silica stretching and breathing modes, respectively, indicate the complete conversion of ZnO to ZnS (or ZnSe) in the meso-SiO_2-ZnS (or ZnSe) samples. That means, as in the case of meso-SiO_2-CdS (or CdSe), the peaks due to Si-O-Zn disappear and pure silica peaks appear when ZnO domains are completely converted into ZnS (or ZnSe). It is obvious that the Si-O-Zn bonds break at the O_3Si-O-ZnO_3 interface upon complete reaction. Therefore, one can use the FTIR technique in order to check whether the H_2S or H_2Se reaction is completed or not.

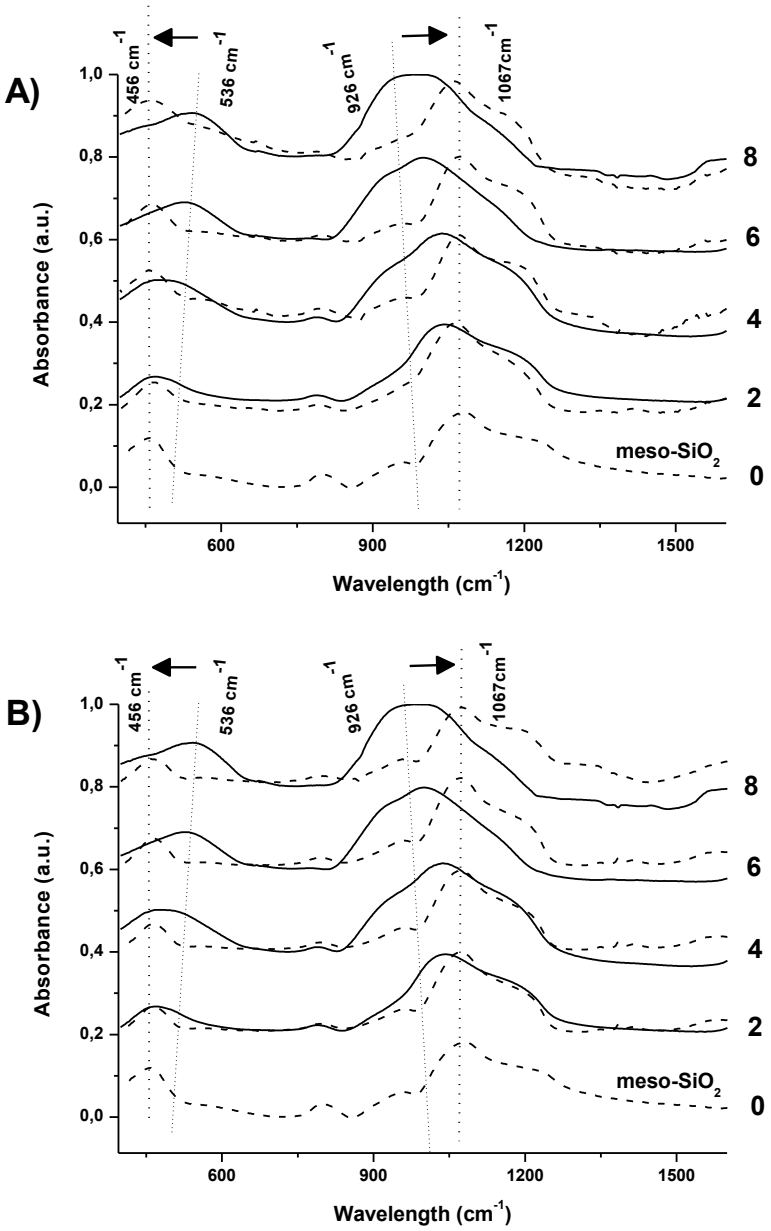

Figure 3.66 FTIR spectra of meso-SiO_2 (dashed line, at the bottom), meso-SiO_2-nZnO (solid line) with A) meso-SiO_2-nZnS (dashed line) and B) meso-SiO_2-nZnSe (dashed line) for n = 2, 4, 6, 8 (shown on the spectra).

3.3.4.4 Raman Analysis of meso-SiO2-CdS, meso-SiO_2-CdSe and meso-SiO_2-ZnSe

The Raman spectra were also recorded for the whole sets of completely converted meso-SiO_2-nCdS (or CdSe), Figure 3.67. The CdS nanoparticles in

meso-SiO_2-nCdS could be identified by its 1LO and 2LO modes at 295 and 590 cm^{-1}, respectively (see Figure 3.67 (A)). The CdSe nanoparticles in the meso-SiO_2-nCdSe could be identified by its 1LO and 2LO modes at 205 and 410 cm^{-1}, respectively (see Figure 3.67 (B)). The ZnSe nanoparticles in the meso-SiO_2-nZnSe could be identified by its 1LO mode at 255 cm^{-1} (see Figure 3.67 (C)) with shoulders on their low energy sides due to surface modes.[180] However, due to resonance effect in the spectra, it is hard to make comment on the particle size change upon change on n. The red shift of the peaks compared to their bulk counterparts indicates the existence of the phonon confinement effect. Due to the red shift and the surface modes, which are observed as a shoulder on the low energy side of the 1LO modes, it can be said that nanostructured MS or MSe domains form in the samples.[181]

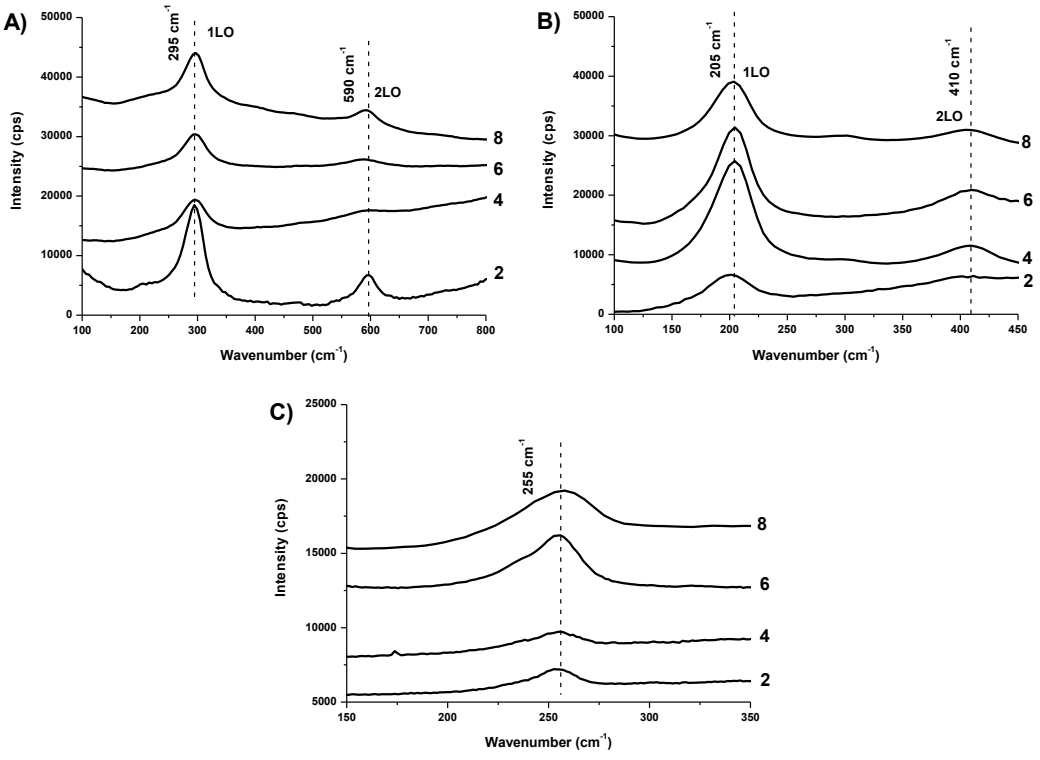

Figure 3.67 The RRS of A) meso-SiO_2-nCdS, B) meso-SiO_2-nCdSe, and C) meso-SiO_2-nZnSe for n = 2, 4, 6, 8 (numbers shown on the spectra).

3.3.4.5 SEM Images of meso-SiO_2-CdSe

The morphology and structural details of the films were investigated using SEM and TEM techniques. Figure 3.68 shows a set SEM and HRSEM images of the samples. The SEM images support the smoothness of the films with micro cracks formed during the calcination process due to the stress. Disordered and non-uniform mesopores with a size range of 4 to 6 nm can be clearly observed in the images. Note that the morphology of the films does not change during H_2S (or H_2Se) reactions and same at all concentrations of metal oxides.

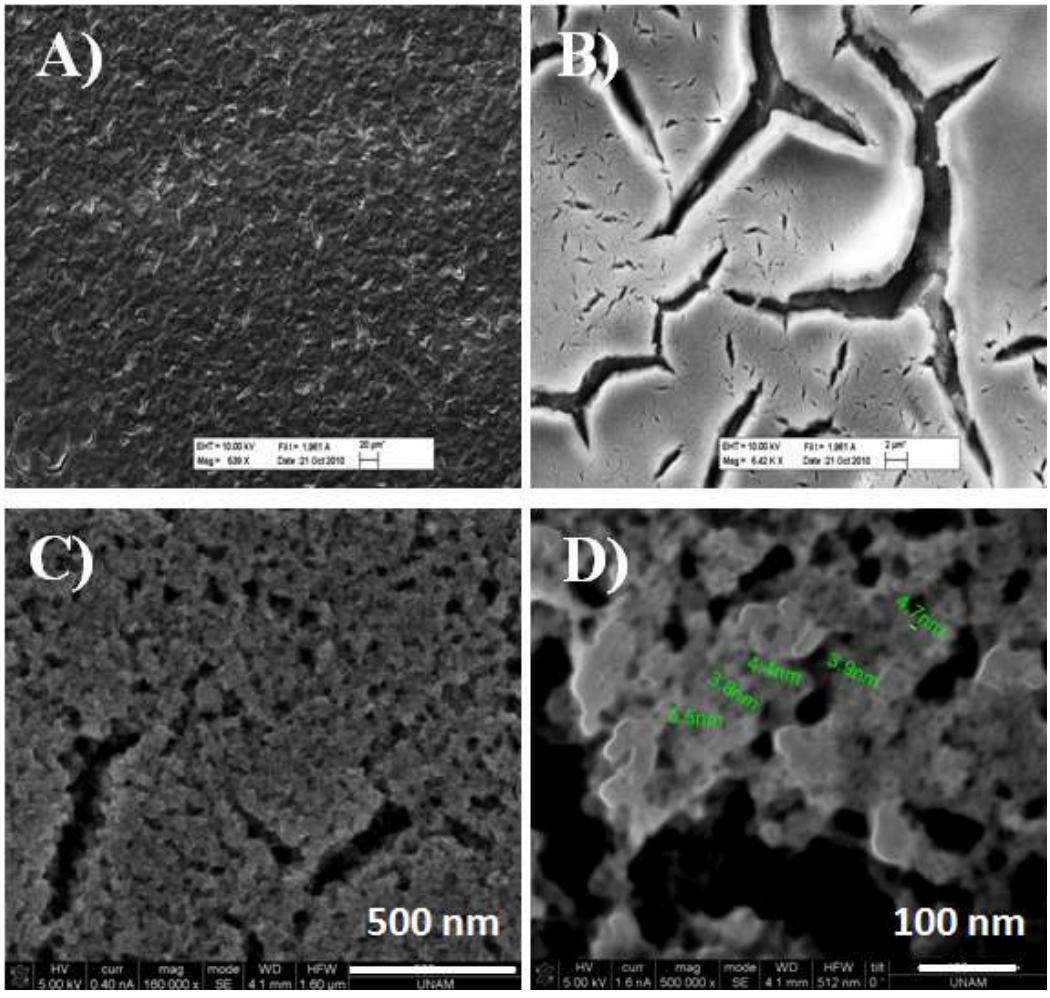

Figure 3.68 The SEM images of meso-SiO_2-6CdSe film with A) 20 µ, B) 2 µ scale bars and HRSEM images of meso-SiO_2-6CdSe film with C) 500 nm and D) 100 nm scale bars.

The overall process during the H_2S (or H_2Se) reactions of meso-SiO_2-CdO can be represented schematically (see Figure 3.69). The white regions with the square drawings represent the CdO nano-islands over the silica pore-walls, and

the amorphous silica walls are represented with the purple regions in Figure 3.69. Upon complete reaction of those CdO domains with H_2S (or H_2Se), the final product is represented at the bottom in Figure 3.69. The orange domains are the CdSe nano-flakes. Since the bond at the Si-O-Cd interface breaks upon complete reaction, the CdSe nano-flakes peal out from the silica surfaces as represented in the schematic in Figure 3.69.

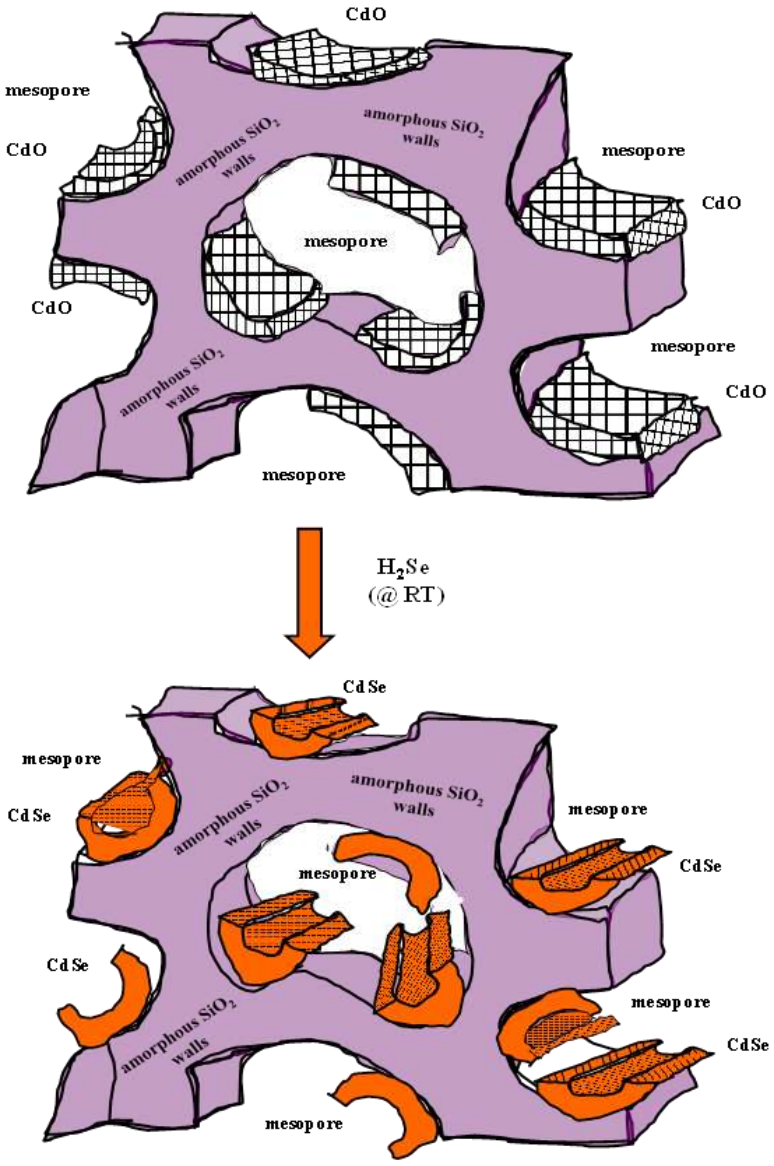

Figure 3.69 Schematic illustration of the synthesis path for the H2Se and meso-SiO_2-CdO.

3.3.5 The synthesis of meso-CdS and meso-CdSe Nanoflakes

In the first part of the thesis, the difficulties of synthesizing mesoporous MS/MSe directly from the salt-surfactant LC mesophase are mentioned. The reason proposed as that the inorganic part of the mesophase in the salt-surfactant system was not rigid enough to maintain its structure during the calcination process. Therefore, the inorganic part had to be supported with an additional polymerizing inorganic reagent. For that purpose, silica was chosen to be the best candidate. It can provide rigidity to allow the mesostructure to maintain its structure during calcination so that we could finally obtain mesoporous silica coated with MS (or MSe). Furthermore, the great advantage of silica is that it can be etched out from the medium. Therefore, we could obtain perfectly smooth and transparent MS (or MSe) nanoflakes in the form of mesoporous MS or MSe thin films. In order to prove the formation of pure mesoporous MS and MSe nanoflakes, they will be analyzed further in detail by using SEM and N_2 sorption analysis.

First of all, we tried etching the silica from meso-SiO_2-CdS (or CdSe) films over silicon or glass substrate using 2M NaOH solution, using a procedure in the literature.[183] However, this process produced unavoidable silica side-products. During etching process of silica in 2M NaOH solution, as silica was etched from the films, they were re-depositing back into the films, as most probably Na_2SiO_3 particles, see the following equation;

$$SiO_2 + 2NaOH \rightarrow Na_2SiO_3 + H_2O \qquad \text{Equation 3.9}$$

Since we were working with films coated on the substrates, those side-products could not be eliminated from the films by simple washing process. Therefore, we used very dilute HF solution to etch the silica from the medium. The reaction of HF with silica has a side-product of volatile and soluble H_2SiF_6. The etched films were characterized by EDS, TEM and UV-Vis analysis as follows.

3.3.5.1 SEM Images of Etched Films

Figure 3.70 shows the SEM images of the meso-SiO_2-6CdS and the meso-SiO_2-6CdSe after HF etching. For the etching process, the meso-SiO_2-6CdS (or CdSe) films were scraped from the glass substrates, and 4 % HF aqueous solution was dropped onto the powder collected. As clearly seen in the SEM images in Figure 3.70, the sponge-like surface morphology of the films is still maintained after the etching process. The SEM image in Figure 3.70 (B) is the magnified section from the white square in the image in Figure 3.70 (A). The uniformity and the porosity can be clearly seen in Figure 3.70 (B). A similar film thickness, around 400 nm, before and after HF etching indicates the homogenous distribution of the CdS (or CdSe) nanoflakes throughout the films. The micron sized film domains of CdSe in Figure 3.70 (C) indicate that whole meso-SiO_2-6CdSe film cracks into small pieces of films after HF treatment. However, sizes of the mesoporous CdSe pieces were still in micron range.

However, the HF etching of the meso-SiO_2-6ZnS (or ZnSe) films could not maintain the porosity (see Figure 3.71). The etching process of the meso-SiO_2-6ZnS (or ZnSe) films caused the formation of S (or Se) species, which were identified by EDS analysis, all over the films.

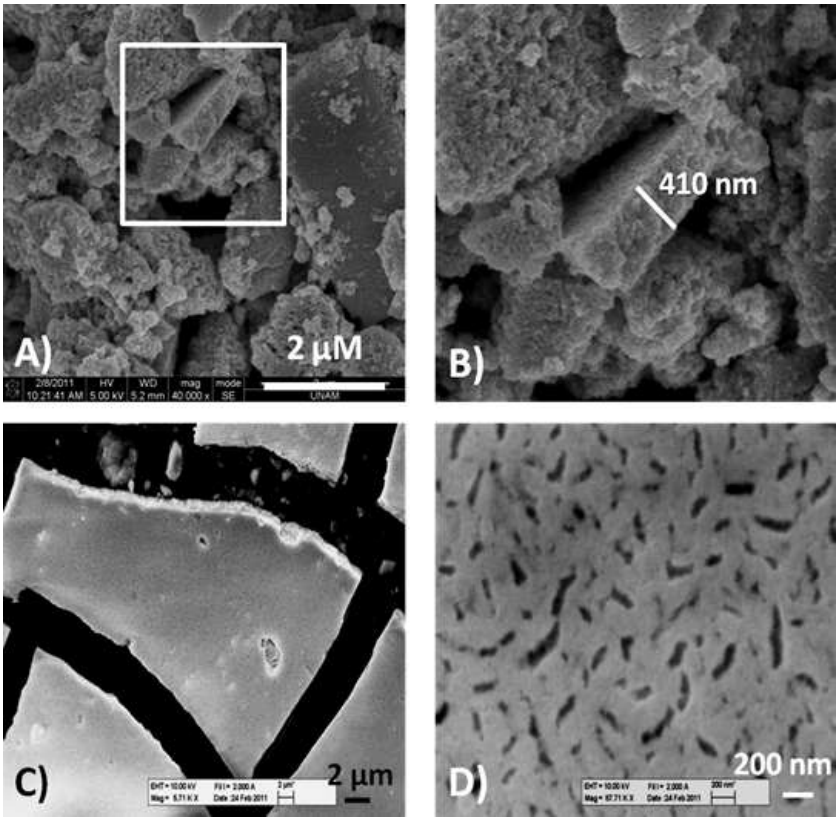

Figure 3.70 SEM images of A) and B) meso-SiO_2-6CdS, and C) and D) meso-SiO_2-6CdSe after HF etching. The image in B) is the magnified section, marked with a white square in A).

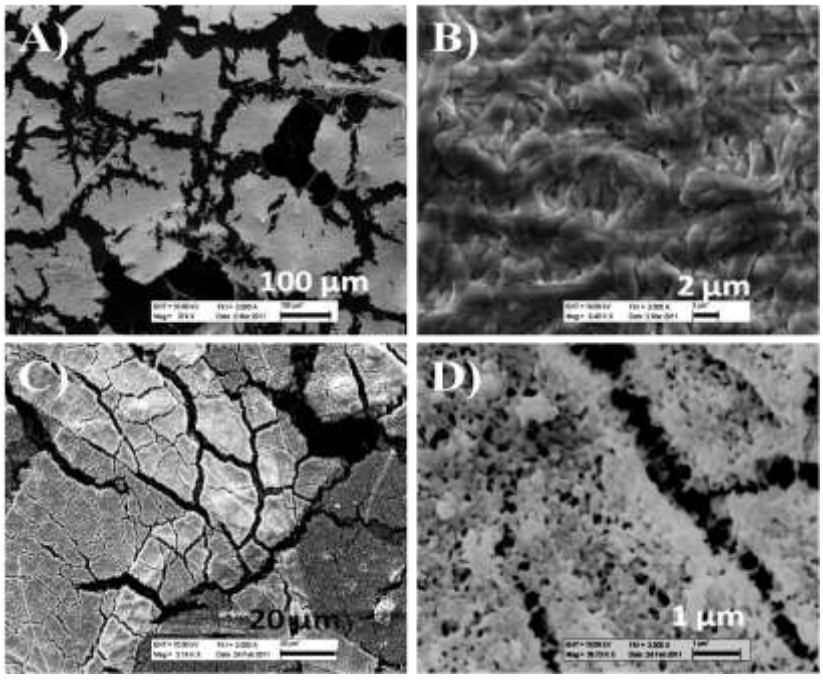

Figure 3.71 SEM images of A) and B) meso-SiO_2-6ZnS, and C) and D) meso-SiO_2-6ZnSe after HF etching.

3.3.5.2 EDS Analysis of Etched Films

After etching the films with 4% HF solution, even though the whole film on the glass substrate were broken into pieces, they were still transparent and yellow colored thin film pieces of the meso-CdS (or CdSe). Moreover, EDS analysis was performed to ensure that all silica was etched from the medium and S/Cd (or Se/Cd) ratio in the CdS (or CdSe) domains were not changed. Figure 3.72 (A) and (B) show the EDS data of the meso-SiO_2-6CdS and meso-SiO_2-6CdSe films (and bulk CdSe) before and after etching in aqueous HF solution, respectively. The EDS analyses of the films were made on the samples scraped from the films and placed over carbon tapes so there was no overlapping of silicon coming from the substrate. The Cd and S (or Se) peaks perfectly fitted into one another and Si peak totally disappeared after etching. The result obviously indicates that silica could be removed from the medium while keeping the CdS (or CdSe) nanoparticles as thin films.

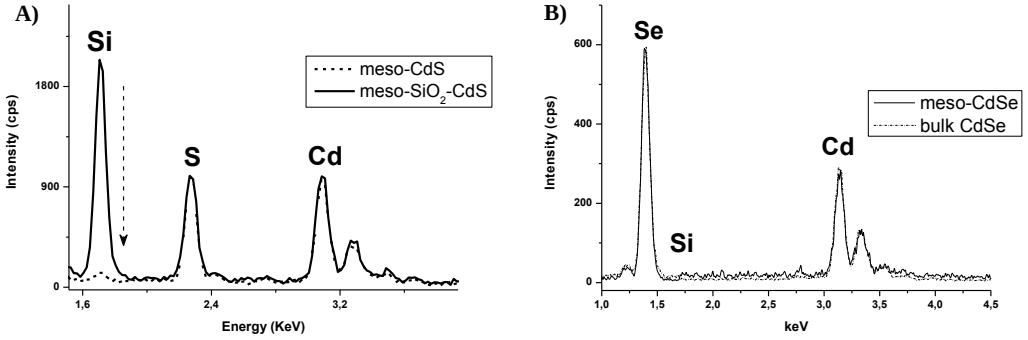

Figure 3.72 EDS analysis of A) meso-SiO_2-6CdS film before (solid line) and after (dashed line) etching in aqueous HF solution, and B) meso-SiO_2-6CdSe film after (solid line) etched with HF and bulk CdSe(dashed line).

However, as seen in Figure 3.73 (A) and (B), the etching process of the meso-SiO_2-6ZnS (or ZnSe) films caused the formation of S (or Se) species. As Si dissolves in the dilute HF solution, ZnS (or ZnSe) dissolves as well, remaining the S or Se species throughout the films.

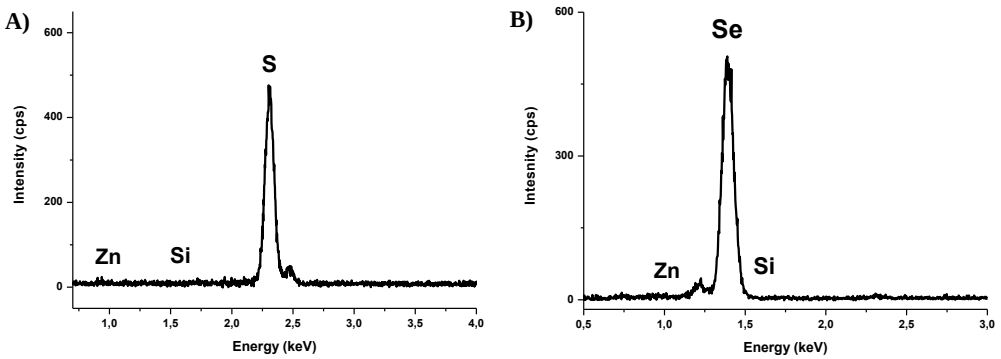

Figure 3.73 EDS analysis of A) meso-SiO_2-6ZnS and B) meso-SiO_2-6ZnSe films after HF etching.

3.3.5.3 UV-Vis Analysis of meso-CdS

The UV-Vis spectra of the meso-SiO_2-6CdS film before and after etching in a 2.0 M NaOH solution are given in Figure 3.74. The UV-Vis spectra show almost no change after etching process indicating the presence of all CdS nanoparticles remained in the film without changing its shape and size. Note also that the absorption edge of CdS depends both on the shape and size of the particles. It is important to note that the absorption edge did not shift at all after etching in aqueous NaOH solution. There is no color change, no decomposition, no aggregation, or no further growth after etching process. Therefore, it can be concluded that duty of silica in the assembly of meso-SiO_2-nMO(or MS or MSe) samples is to provide the rigid walls for the metal oxides and metal sulfides (or selenides) to be coated smoothly over, so that no aggregation during calcination process and H_2S (or H_2Se) reactions occurs. However, we need to do further analysis to make sure if the remaining MS (or MSe) domains were rigid enough to maintain any porosity.

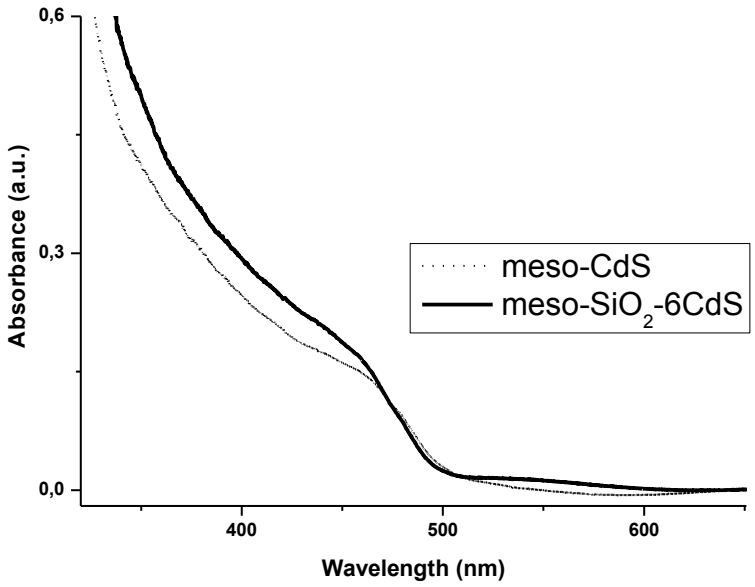

Figure 3.74 The UV-Vis absorption spectra of meso-SiO_2-6CdS film before (solid line) and meso-CdS after (dashed line) etching with $NaOH_{(aq)}$ solution.

3.3.5.4 N_2 Sorption Analysis of meso-CdS

The porosity of the etched samples was further investigated by N_2-sorption measurements. Figure 3.75 (A) shows the N_2 sorption isotherms of meso-SiO_2-6CdS before and after HF etching. Both of the N_2-sorption data, before and after HF treatment, display type-IV isotherm, which is characteristic to mesoporous materials. Even though the pore shape and size did not change much upon etching process, the surface area and pore volume of the etched meso-CdS decreased to 50 m^2/g and 0.16 cm^3/g, respectively. The reason of the decrease in surface area and pore volume must be the loss of accessible silica surfaces in the samples upon etching. According to the t-plots of those isotherms in Figure 3.75 (B), some micropores are formed in the meso-CdS samples upon removal of silica from the medium.

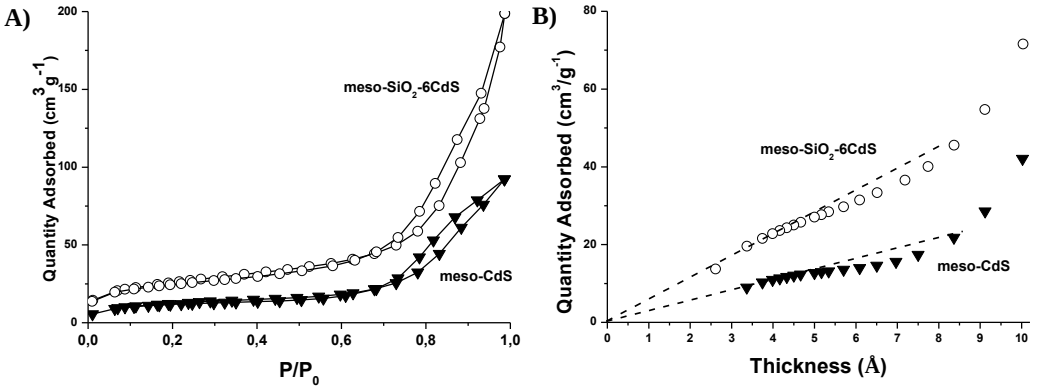

Figure 3.75 A) N_2 sorption isotherms of meso-SiO_2-6CdS before and after HF etching, B) the t-plots obtained from the adsorption isotherms in A).

3.3.5.5 TEM Images of meso-CdS

TEM images of the meso-SiO_2-6CdS samples after etching are given in Figure 3.76. From these images, it is reasonable to say that the CdS domains did not agglomerate upon removing the silica walls. The large CdS nano-flakes can be seen with a size of 10 to 25 nm in Figure 3.76 (A) and (E). The inverse FFT of the selected regions in Figure 3.76 (A) is given in Figure 3.3.24 (B) and (C). The lattice spots and fringes in the darker regions of the images can be clearly seen in the FFT and inverse FFT of the TEM images. The lattice fringes at both of these inverse FFT images are spaced by 0.336 nm and it corresponds to the (111) planes of the zinc blend structure of CdS. The CdS particles are random and dispersed as in the meso-SiO_2-6CdS films so that the removal of silica upon etching did not change their distribution through the film.

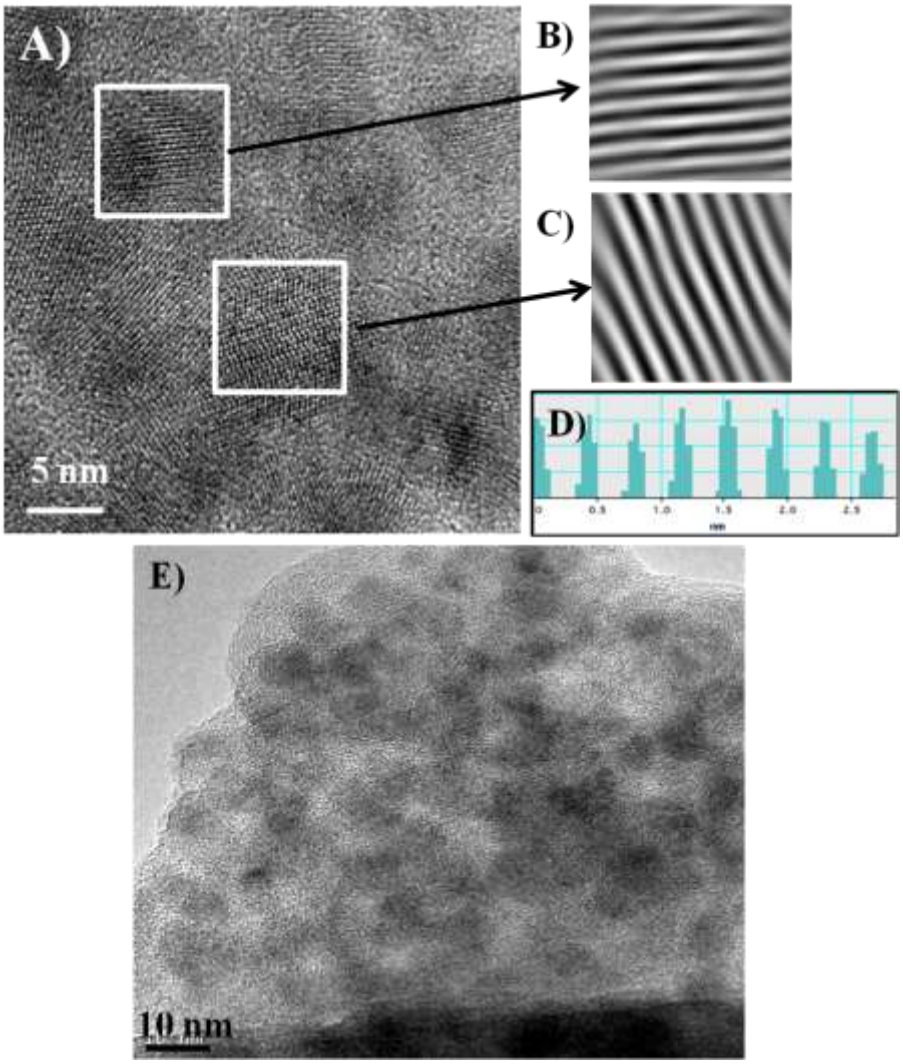

Figure 3.76 TEM images of meso-SiO_2-6CdS after etching with A) 5 nm and E) 10 nm scale bar. B) and C) Inverse FFT of the selected regions in A), and D) Histogram of the B) and C).

3.3.5.6 Photoluminescence of meso-CdS

The photoluminescence properties of meso-CdS particles were also investigated by capping the CdS nanoparticles with a capping agent, PEI (polyethyleneimine). Figure 3.77 shows photographs of PEI modified CdS, denoted as meso-CdS-PEI, PEI, and meso-CdS under a 365 nm UV light. Since the only PEI and meso-CdS are colorless under 365 nm, the bright blue color of meso-CdS-PEI obviously indicates that the PEI modification could provide the photoluminescence property to meso-CdS-PEI films. The broad PL peak at 455 nm must be due to band gap emission showing us that all the surface traps could

be capped by PEI, Figure 3.77 (d). Since the solution had some cloudiness, the scattered light caused the tail shown in absorption spectrum.

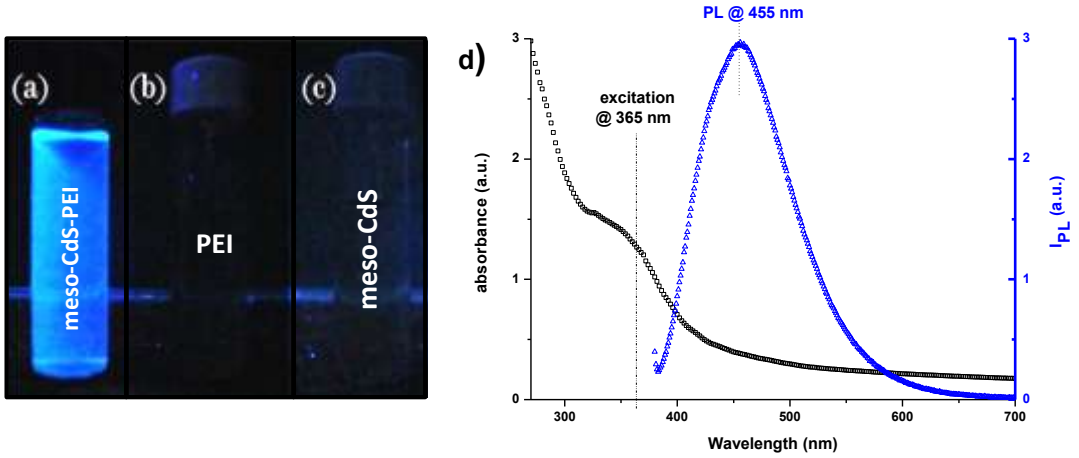

Figure 3.77 Photographs, under 365 nm UV lamp, of water dispersions of (a) meso-CdS-PEI, (b) PEI, and (c) meso-CdS. (d) The UV-Vis absorption and PL spectra of meso-CdS-PEI.

CHAPTER IV

CONCLUSION

In this thesis, the mesoporous CdS (meso-CdS) and mesoporous CdSe (meso-CdSe) nanoflakes were synthesized by means of the LCT approach. The thermal behavior of binary $[Cd(H_2O)_4](NO_3)_2$/P85 and $[Cd(H_2O)_4](NO_3)_2/C_{12}EO_{10}$/CTAB LLC systems, H_2Se reactions of mesostructured Cd(II)-TiO_2-P123 films, H_2S and H_2Se reactions of meso-$CdTiO_3$ and H_2Se reactions of meso-Zn_2TiO_4, H_2S and H_2Se reactions of meso-SiO_2-CdO and meso-SiO_2-ZnO have been investigated.

It has been found out that the binary $[Cd(H_2O)_4](NO_3)_2$/P85 and $[Cd(H_2O)_4](NO_3)_2/C_{12}EO_{10}$/CTAB LLC mesophases and mesostructured CdS/P85 films are not stable to calcination and leads to formation of the bulk CdO or CdS nanoparticles for various reasons as discussed in the first part of this thesis.

Adding a titania or silica precursor to the salt-surfactant LLC mesophases improved stability of the resulting structure by forming rigid titania or silica walls against aggregation and growth of metal oxide at high calcination temperatures. Well-ordered, stable and rigid mesostructured Cd(II) titania films can be formed, up to 15.0 Cd(II)/P123 mole ratio in the presence of 60 mole ratio of Ti(IV)/P123 in these samples. The fresh samples require aging under 50% humidity at 30 °C to enhance the order of the mesostructure, and further aging at 130 °C removes about 90 % of the nitrate ions (originating from both acid and metal ion sources). Note that nitrate ions form HNO_3 under H_2Se atmosphere and decompose the CdSe nanoparticles. Exposing the mesostructured nitrate free Cd(II)-TiO_2 films to H_2Se under a N_2 atmosphere produces stable CdSe nanoparticles in the channels of the mesostructured titania films. The control of H_2Se pressure, inert atmosphere, and duration time of reaction play significant roles on the synthesis of pure CdSe-TiO_2 films. However, the CdSe nanoparticles undergo irreversible degradation to Se

under green laser in the presence of air upon electron injection from CdSe to TiO_2.

The hydrolysis and condensation of $Ti(OC_4H_9)_4$ can also be carried out in a molten phase formed by excessive amount of $[Cd(H_2O)_4](NO_3)_2$ or $[Zn(H_2O)_6](NO_3)_2$ confined in the hydrophilic domains of the mesophases of $C_{12}EO_{10}$ and CTAB. The assembly process is called `molten salt assisted self-assembly` (MASA). The MASA method can be used to produce sponge like mesoporous $CdTiO_3$ and Zn_2TiO_4 films with a controlled calcination. The calcined meso-$CdTiO_3$ thin films produce homogeneously distributed zinc blend 2.0 to 2.3 nm CdS and CdSe nanocrystallites over the nanocrystalline anatase and brookite TiO_2 pore walls by upon H_2S (meso-TiO_2-CdS) and H_2Se (meso-TiO_2-CdSe) reactions at RT, respectively. The reaction of meso-Zn_2TiO_4 under a H_2Se atmosphere yields ~2.0 nm zinc blend ZnSe nanocrystallites over the nanocrystalline rutile TiO_2 pore walls (meso-TiO_2-ZnSe). The absorption intensity of the crack free transparent meso-TiO_2-MS (or MSe) thin films can be adjusted by preparing multiple layered films through multiple spin coating followed by calcination each layer.

The mesoporous SiO_2-CdS, SiO_2-CdSe, SiO_2-ZnS, and SiO_2-ZnSe thin films, in which the pore walls are made up of SiO_2 and MS or MSe nanoflakes can be synthesized by reacting mesoporous SiO_2-CdO and SiO_2-ZnO thin film precursors with H_2S and H_2Se gases at RT. The sponge like meso-SiO_2-nCdO and meso-SiO_2-nZnO films can be formed as CdO and ZnO nano-islands, coated up to ~100 % and ~50 % surface coverage over the SiO_2 walls, respectively, through the MASA method followed by a controlled calcination. The conversion of MO to MS or MSe proceeds from the outer layers of MO to inner layers until cleavage of the M-O-Si interface. Both H_2S and H_2Se reactions can be kinetically controlled by controlling the exposure times. The initial reactions at the outer layers of MO are very fast. The CdS and CdSe nanoparticles grow by volume diffusion of ions through the inner layers, and as the growth of the CdS and CdSe nanoparticles approaches to the silica-cadmium oxide interface, the reaction occurs at much slower rate than the reactions at the outer layers of silica-cadmium oxide. The

silica-cadmium oxide interface is the least reactive region. The thickness and size of the MS or MSe nanoflakes also depend on the amount of MO in the meso-SiO_2-MO precursor. Etching the SiO_2 walls of meso-SiO_2-CdS and meso-SiO_2-CdSe in a dilute HF solution produces mesoporous CdS (meso-CdS) and mesoporous CdSe (meso-CdSe) nanoflakes that can be modified using PEI (polyethyleneimine), to obtain bright blue photoluminescent meso-CdS-PEI.

CHAPTER V

REFERENCES

1. Terminology, I. M. S. 1972. Colloidal and Surface Chemistry.

2. Kresge, C. T.; Leonowicz, M. E.; Roth, W. J.; Vartuli, J. C. and Beck, J. S. "Ordered Mesoporous Molecular Sieves Synthesized by a Liquid-Crystal Template Mechanism." *Nature* **1992,** 359, (6397), 710-712.

3. Behrens, P. "Mesoporous Inorganic Solids." *Advanced Materials* **1993,** 5, (2), 127-132.

4. Huang, L.; Wang, Z.; Sun, J.; Miao, L.; Li, Q.; Yan, Y. and Zhao, D. "Fabrication of Ordered Porous Structures by Self-Assembly of Zeolite Nanocrystals." *Journal of the American Chemical Society* **2000,** 122, (14), 3530-3531.

5. Moore, P. B. and Shen, J. "An X-Ray Structural Study of Cacoxenite, A Mineral Phosphate." *Nature* **1983,** 306, (5941), 356-358.

6. Dessau, R. M.; Schlenker, J. L. and Higgins, J. B. "Framework Topology of AlPO4-8: The First 14-ring Molecular Sieve." *Zeolites* **1990,** 10, (6), 522-524.

7. Attard, G. S.; Glyde, J. C. and Goltner, C. G. "Liquid-Crystalline Phases as Templates for the Synthesis of Mesoporous Silica." *Nature* **1995,** 378, (6555), 366-368.

8. Yang, H.; Kuperman, A.; Coombs, N.; Mamiche-Afara, S. and Ozin, G. A. "Synthesis of Oriented Films of Mesoporous Silica on Mica." *Nature* **1996,** 379, (6567), 703-705.

9. Tang, Y. S.; Cai, S. J.; Jin, G. L.; Wang, K. L.; Soyez, H. M. and Dunn, B. S. "Direct MBE Growth of SiGe Dots on Ordered Mesoporous Glass-coated Si Substrate." *Thin Solid Films* **1998,** 321, (1-2), 76-80.

10. Dag, Ö.; Ozin, G. A.; Yang, H.; Reber, C. and Bussière, G. "Photoluminescent Silicon Clusters in Oriented Hexagonal Mesoporous Silica Film." *Advanced Materials* **1999,** 11, (6), 474-480.

11. Plyuto, Y.; Berquier, J.-M.; Jacquiod, C. and Ricolleau, C. "Ag Nanoparticles Synthesised in Template-Structured Mesoporous Silica Films on a Glass Substrate." *Chemical Communications* **1999,** (17), 1653-1654.

12. Xie, Z.; Henderson, E. J.; Dag, O. m.; Wang, W.; Lofgreen, J. E.; Kübel, C.; Scherer, T.; Brodersen, P. M.; Gu, Z.-Z. and Ozin, G. A. "Periodic Mesoporous Hydridosilica − Synthesis of an "Impossible" Material and Its Thermal Transformation into Brightly Photoluminescent Periodic Mesoporous Nanocrystal Silicon-Silica Composite." *Journal of the American Chemical Society* **2011,** 133, (13), 5094-5102.

13. Dag, Ö.; Henderson, E. J.; Wang, W.; Lofgreen, J. E.; Petrov, S.; Brodersen, P. M. and Ozin, G. A. "Spatially Confined Redox Chemistry in Periodic Mesoporous Hydridosilica–Nanosilver Grown in Reducing Nanopores." *Journal of the American Chemical Society* **2011**.

14. Collings, J. **1990.** *Liquid Crystals*. Princeton: University Press.

15. Collings, P. J. and Hired, M. **1997.** *Introduction to Liquid Crystals*. Taylor&Francis.

16. Meyers, D. **1991.** Surfaces, Interfaces, and Collids; Principles and Applications. VCH.

17. Marinov, V. S. and Matsuura, H. "Raman Spectroscopic Study of Temperature Dependence of Water Structure in Aqueous Solutions of a Poly(Oxyethylene) Surfactant." *Journal of Molecular Structure* **2002,** 610, (1-3), 105-112.

18. Tanford, C. **1980.** The hydrophobic effect: Formation of Micelles and Biological Membranes;second ed. New York: Wiley.

19. Raman, N. K.; Anderson, M. T. and Brinker, C. J. "Template-Based Approaches to the Preparation of Amorphous, Nanoporous Silicas." *Chemistry of Materials* **1996,** 8, (8), 1682-1701.

20. Mitchell, D. J.; Tiddy, G. J. T.; Waring, L.; Bostock, T. and McDonald, M. P. "Phase Behaviour of Polyoxyethylene Surfactants with Water. Mesophase Structures and Partial Miscibility (Cloud Points)." *Journal of the Chemical Society, Faraday Transactions 1: Physical Chemistry in Condensed Phases* **1983,** 79, (4), 975-1000.

21. Attard, G. S.; Corker, J. M.; Göltner, C. G.; Henke, S. and Templer, R. H. "Liquid-Crystal Templates for Nanostructured Metals." *Angewandte Chemie International Edition in English* **1997,** 36, (12), 1315-1317.

22. Attard, G. S.; Bartlett, P. N.; Coleman, N. R. B.; Elliott, J. M.; Owen, J. R. and Wang, J. H. "Mesoporous Platinum Films from Lyotropic Liquid Crystalline Phases." *Science* **1997,** 278, (5339), 838-840.

23. H. Whitehead, A.; M. Elliott, J.; R. Owen, J. and S. Attard, G. "Electrodeposition of Mesoporous Tin Films." *Chemical Communications* **1999,** (4), 331-332.

24. Attard, G. S.; Leclerc, S. A. A.; Maniguet, S.; Russell, A. E.; Nandhakumar, I. and Bartlett, P. N. "Mesoporous Pt/Ru Alloy from the Hexagonal Lyotropic Liquid Crystalline Phase of a Nonionic Surfactant." *Chemistry of Materials* **2001,** 13, (5), 1444-1446.

25. Yamauchi, Y.; Yokoshima, T.; Momma, T.; Osaka, T. and Kuroda, K. "Fabrication of Magnetic Mesostructured Nickel-Cobalt Alloys from Lyotropic Liquid Crystalline Media by Electroless Deposition." *Journal of Materials Chemistry* **2004,** 14, (19), 2935-2940.

26. Yamauchi, Y.; Momma, T.; Yokoshima, T.; Kuroda, K. and Osaka, T. "Highly Ordered Mesostructured Ni Particles Prepared from Lyotropic Liquid Crystals by

Electroless Deposition: The Effect of Reducing Agents on The Ordering of Mesostructure." *Journal of Materials Chemistry* **2005,** 15, (20), 1987-1994.

27. Yang, P.; Zhao, D.; Margolese, D. I.; Chmelka, B. F. and Stucky, G. D. "Generalized Syntheses of Large-Pore Mesoporous Metal Oxides with Semicrystalline Frameworks." *Nature* **1998,** 396, (6707), 152-155.

28. Tohver, V.; Braun, P. V.; Pralle, M. U. and Stupp, S. I. "Counterion Effects in Liquid Crystal Templating of Nanostructured CdS." *Chemistry of Materials* **1997,** 9, (7), 1495-1498.

29. Braun, P. V.; Osenar, P. and Stupp, S. I. "Semiconducting Superlattices Templated by Molecular Assemblies." *Nature* **1996,** 380, (6572), 325-328.

30. Çelik, Ö. and Dag, Ö. "A New Lyotropic Liquid Crystalline System: Oligo(ethylene oxide) Surfactants with $[M(H_2O)_n]X_m$ Transition Metal Complexes." *Angewandte Chemie International Edition* **2001,** 40, (20), 3799-3803.

31. Dag, Ö.; Alayoğlu, S.; Tura, C. and Çelik, Ö. "Lyotropic Liquid-Crystalline Phase of Oligo(ethylene oxide) Surfactant/Transition Metal Salt and the Synthesis of Mesostructured Cadmium Sulfide." *Chemistry of Materials* **2003,** 15, (14), 2711-2717.

32. Dag, Ö.; Alayoğlu, S. and Uysal, İ. "Effects of Ions on the Liquid Crystalline Mesophase of Transition-Metal Salt:Surfactant (C_nEO_m)." *The Journal of Physical Chemistry B* **2004,** 108, (24), 8439-8446.

33. Dag, Ö.; Samarskaya, O.; Tura, C.; Günay, A. and Çelik, Ö. "Spectroscopic Investigation of Nitrate−Metal and Metal−Surfactant Interactions in the Solid $AgNO_3/C_{12}EO_{10}$ and Liquid-Crystalline $[M(H_2O)n](NO_3)_2/C_{12}EO_{10}$ Systems." *Langmuir* **2003,** 19, (9), 3671-3676.

34. Albayrak, C.; Gülten, G. and Dag, Ö. "Phase Separation in Liquid Crystalline Mesophases of $[Co(H_2O)_6]X_2$:P65 Systems (X = NO_3^-, Cl^-, or ClO_4^-)." *Langmuir* **2006,** 23, (2), 855-860.

35. Demirörs, A. F.; Eser, B. E. and Dag, Ö. "Liquid Crystalline Mesophases of Pluronics (L64, P65, and P123) and Transition Metal Nitrate Salts ($[M(H_2O)_6](NO_3)_2$)." *Langmuir* **2005,** 21, (9), 4156-4162.

36. Demirörs, A. F.; Arslan, M. and Dag, Ö. "The Effect of Anions of Transition Metal Salts on The Structure of Modified Mesostructured Silica Films and Monoliths." *Microporous and Mesoporous Materials* **2007,** 98, (1-3), 249-257.

37. Türker, Y. and Dag, Ö. "Synthesis of Mesostructured Metal Sulfide Films Using $[M(H_2O)_n](NO_3)_2$:P85 (M = Cd(II) and Zn(II)) Liquid Crystalline Mesophases." *Journal of Materials Chemistry* **2008,** 18, (29), 3467-3473.

38. Dag, Ö.; Verma, A.; A. Ozin, G. and T. Kresge, C. "Salted Mesostructures: Salt-Liquid Crystal Templating of Lithium Triflate-Oligo(Ethylene Oxide) Surfactant-Mesoporous Silica Nanocomposite Films and Monoliths." *Journal of Materials Chemistry* **1999,** 9, (7), 1475-1482.

39. Samarskaya, O. and Dag, Ö. "Silver Nitrate/Oligo(ethylene Oxide) Surfactant/Mesoporous Silica Nanocomposite Films and Monoliths." *Journal of Colloid and Interface Science* **2001,** 238, (1), 203-207.

40. Aramaki, K.; Hossain, M. K.; Rodriguez, C.; Uddin, M. H. and Kunieda, H. "Miscibility of Block Copolymers and Surfactants in Lamellar Liquid Crystals." *Macromolecules* **2003,** 36, (25), 9443-9450.

41. Herrington, K. L.; Kaler, E. W.; Miller, D. D.; Zasadzinski, J. A. and Chiruvolu, S. "Phase Behavior of Aqueous Mixtures of Dodecyltrimethylammonium bromide (DTAB) and Sodium dodecyl sulfate (SDS)." *The Journal of Physical Chemistry* **1993,** 97, (51), 13792-13802.

42. Matsubara, H.; Muroi, S.; Kameda, M.; Ikeda, N.; Ohta, A. and Aratono, M. "Interaction between Ionic and Nonionic Surfactants in the Adsorbed Film and Micelle. 3. Sodium Dodecyl Sulfate and Tetraethylene Glycol Monooctyl Ether." *Langmuir* **2001,** 17, (25), 7752-7757.

43. Matsubara, H.; Ohta, A.; Kameda, M.; Ikeda, N. and Aratono, M. "Interaction between Ionic and Nonionic Surfactants in the Adsorbed Film and Micelle. Dodecylammonium Chloride and Tetraethylene Glycol Monooctyl Ether." *Langmuir* **2000,** 16, (20), 7589-7596.

44. Matsubara, H.; Ohta, A.; Kameda, M.; Villeneuve, M.; Ikeda, N. and Aratono, M. "Interaction between Ionic and Nonionic Surfactants in the Adsorbed Film and Micelle: Hydrochloric Acid, Sodium Chloride, and Tetraethylene Glycol Monooctyl Ether." *Langmuir* **1999,** 15, (17), 5496-5499.

45. Poyraz, A. S.; Albayrak, C. and Dag, Ö. "The Effect of Cationic Surfactant and Some Organic/Inorganic Additives on the Morphology of Mesostructured Silica Templated by Pluronics." *Microporous and Mesoporous Materials* **2008,** 115, (3), 548-555.

46. Albayrak, C.; Soylu, A. M. and Dag, Ö. "Lyotropic Liquid-Crystalline Mesophases of $[Zn(H_2O)_6](NO_3)_2{-}C_{12}EO_{10}{-}CTAB{-}H_2O$ and $[Zn(H_2O)_6](NO_3)_2{-}C_{12}EO_{10}{-}SDS{-}H_2O$ Systems." *Langmuir* **2008,** 24, (19), 10592-10595.

47. Albayrak, C.; Özkan, N. and Dag, Ö. "Origin of Lyotropic Liquid Crystalline Mesophase Formation and Liquid Crystalline to Mesostructured Solid Transformation in the Metal Nitrate Salt−Surfactant Systems." *Langmuir* **2011,** 27, (3), 870-873.

48. Nakamato, K. **1997.** Infrared and Raman Spectra of Inorganic and Coordination Compounds Part-A. John Wiley & Sons, Inc. .

49. Brinker, C. J. and Scherer, G. W. **1990.** *Sol-Gel Science: The Physics and Chemistry of Sol-Gel Processing*. Academic Press, Inc. .

50. Gao, F.; Lu, Q. and Zhao, D. "Synthesis of Crystalline Mesoporous CdS Semiconductor Nanoarrays Through a Mesoporous SBA-15 Silica Template Technique." *Advanced Materials* **2003,** 15, (9), 739-742.

51. Livage, J.; Henry, M. and Sanchez, C. "Sol-gel Chemistry of Transition Metal Oxides." *Solid State Chemistry* **1988,** 18, 259-341.

52. Hubert-Pfalzgraf, L. G. "Alkoxides as Molecular Precursor for Oxide-Based Inorganic Materials: Opportunities for New Materials." *New Journal of Chemistry* **1987,** 11, 663-675.

53. Sanchez, C.; Livage, J.; Henry, M. and Babonneau, F. "Chemical Modification of Alkoxide Precursors." *Journal of Non-Crystalline Solids* **1988,** 100, (1-3), 65-76.

54. Yoldas, B. E. "Hydrolysis of Titanium Alkoxide and Effects of Hydrolytic Polycondensation Parameters." *Journal of Material Science* **1986,** 21, 1087.

55. Sakka, S. and Kamiya, K. "Glasses from Metal Alcoholates." *Journal of Non-Crystalline Solids* **1980,** 42, (1-3), 403-421.

56. Kamiya, K.; Tanimoto, K. and Yoko, T. "Preparation of TiO_2 Fibres by Hydrolysis and Polycondensation of $Ti(O—i\text{-}C_3H_7)_4$." *Journal of Materials Science Letters* **1986,** 5, (4), 402-404.

57. Antonelli, D. M. and Ying, J. Y. "Synthesis of Hexagonally Packed Mesoporous TiO_2 by a Modified Sol–Gel Method." *Angewandte Chemie International Edition in English* **1995,** 34, (18), 2014-2017.

58. Khushalani, D.; A. Ozin, G. and Kuperman, A. "Glycometallate Surfactants Part 2: Non-Aqueous Synthesis of Mesoporous Titanium, Zirconium and Niobium Oxides." *Journal of Materials Chemistry* **1999,** 9, (7), 1491-1500.

59. Yang, P.; Zhao, D.; Margolese, D. I.; Chmelka, B. F. and Stucky, G. D. "Block Copolymer Templating Syntheses of Mesoporous Metal Oxides with Large Ordering Lengths and Semicrystalline Framework." *Chemistry of Materials* **1999,** 11, (10), 2813-2826.

60. Grosso, D.; de A. A. Soler-Illia, G. J.; Babonneau, F.; Sanchez, C.; Albouy, P. A.; Brunet-Bruneau, A. and Balkenende, A. R. "Highly Organized Mesoporous Titania Thin Films Showing Mono-Oriented 2D Hexagonal Channels." *Advanced Materials* **2001,** 13, (14), 1085-1090.

61. Soler-Illia, G. J. d. A. A.; Louis, A. and Sanchez, C. "Synthesis and Characterization of Mesostructured Titania-Based Materials through Evaporation-Induced Self-Assembly." *Chemistry of Materials* **2002,** 14, (2), 750-759.

62. Crepaldi, E. L.; Soler-Illia, G. J. d. A. A.; Grosso, D.; Cagnol, F.; Ribot, F. and Sanchez, C. "Controlled Formation of Highly Organized Mesoporous Titania Thin Films: From Mesostructured Hybrids to Mesoporous Nanoanatase TiO_2." *Journal of the American Chemical Society* **2003,** 125, (32), 9770-9786.

63. Dag, Ö.; Soten, I.; Çelik, Ö.; Polarz, S.; Coombs, N. and Ozin, G. A. "Solventless Acid-Free Synthesis of Mesostructured Titania: Nanovessels for Metal Complexes and Metal Nanoclusters." *Advanced Functional Materials* **2003,** 13, (1), 30-36.

64. Hagfeldt, A. and Graetzel, M. "Light-Induced Redox Reactions in Nanocrystalline Systems." *Chemical Reviews* **1995,** 95, (1), 49-68.

65. Soler-Illia, G. J. d. A. A.; Sanchez, C.; Lebeau, B. and Patarin, J. "Chemical Strategies To Design Textured Materials: from Microporous and Mesoporous Oxides to Nanonetworks and Hierarchical Structures." *Chemical Reviews* **2002,** 102, (11), 4093-4138.

66. Luo, H.; Wang, C. and Yan, Y. "Synthesis of Mesostructured Titania with Controlled Crystalline Framework." *Chemistry of Materials* **2003,** 15, (20), 3841-3846.

67. Choi, S. Y.; Mamak, M.; Coombs, N.; Chopra, N. and Ozin, G. A. "Thermally Stable Two-Dimensional Hexagonal Mesoporous Nanocrystalline Anatase, Meso-nc-TiO2: Bulk and Crack-Free Thin Film Morphologies." *Advanced Functional Materials* **2004,** 14, (4), 335-344.

68. Armstrong, J.; Chowdhry, B.; Mitchell, J.; Beezer, A. and Leharne, S. "Effect of Cosolvents and Cosolutes upon Aggregation Transitions in Aqueous Solutions of the Poloxamer F87 (Poloxamer P237): A High Sensitivity Differential Scanning Calorimetry Study." *The Journal of Physical Chemistry* **1996,** 100, (5), 1738-1745.

69. Su, Y.-l.; Wei, X.-f. and Liu, H.-z. "Influence of 1-Pentanol on the Micellization of Poly(ethylene oxide)−Poly(propylene oxide)−Poly(ethylene oxide) Block Copolymers in Aqueous Solutions." *Langmuir* **2003,** 19, (7), 2995-3000.

70. Haseloh, S.; Choi, S. Y.; Mamak, M.; Coombs, N.; Petrov, S.; Chopra, N. and Ozin, G. A. "Towards Flexible Inorganic "Mesomaterials": One-Pot Low Temperature Synthesis of Mesostructured Nanocrystalline Titania." *Chemical Communications* **2004,** (13), 1460-1461.

71. Choi, S. Y.; Mamak, M.; Speakman, S.; Chopra, N. and Ozin, G. A. "Evolution of Nanocrystallinity in Periodic Mesoporous Anatase Thin Films." *Small* **2005,** 1, (2), 226-232.

72. Choi, S. Y.; Lee, B.; Carew, D. B.; Mamak, M.; Peiris, F. C.; Speakman, S.; Chopra, N. and Ozin, G. A. "3D Hexagonal (R-3m) Mesostructured Nanocrystalline Titania Thin Films: Synthesis and Characterization." *Advanced Functional Materials* **2006,** 16, (13), 1731-1738.

73. Liu, K.; Fu, H.; Shi, K.; Xiao, F.; Jing, L. and Xin, B. "Preparation of Large-Pore Mesoporous Nanocrystalline TiO_2 Thin Films with Tailored Pore Diameters." *The Journal of Physical Chemistry B* **2005,** 109, (40), 18719-18722.

74. Wang, K.; Morris, M. A. and Holmes, J. D. "Preparation of Mesoporous Titania Thin Films with Remarkably High Thermal Stability." *Chemistry of Materials* **2005,** 17, (6), 1269-1271.

75. Okur, H. I.; Türker, Y. and Dag, Ö. "Synthesis of Stable Mesostructured Coupled Semiconductor Thin Films: meso-CdS-TiO_2 and meso-CdSe-TiO_2." *Langmuir* **2009,** 26, (1), 538-544.

76. Iler, R. K. **1979.** *The Chemistry of Silica*. New York: Wiley.

77. Baccile, N.; Teixeira, C. V.; Amenitsch, H.; Villain, F.; Lindén, M. and Babonneau, F. "Time-Resolved in Situ Raman and Small-Angle X-ray Diffraction Experiments: From Silica-Precursor Hydrolysis to Development of Mesoscopic Order in SBA-3 Surfactant-Templated Silica†." *Chemistry of Materials* **2007,** 20, (3), 1161-1172.

78. Sassi, Z.; Bureau, J. C. and Bakkali, A. "Structural Characterization of the Organic/Inorganic Networks in the Hybrid Material (TMOS–TMSM–MMA)." *Vibrational Spectroscopy* **2002,** 28, (2), 251-262.

79. Kim, Y. "Infrared Spectroscopy Study of Low-Dielectric-Constant Fluorine-Incorporated and Carbon-Incorporated Silicon Oxide Films." *J. Appl. Phys.* **2001,** 90, (7), 3367.

80. Liu, J.; Fan, F.; Feng, Z.; Zhang, L.; Bai, S.; Yang, Q. and Li, C. "From Hollow Nanosphere to Hollow Microsphere: Mild Buffer Provides Easy Access to Tunable Silica Structure." *The Journal of Physical Chemistry C* **2008,** 112, (42), 16445-16451.

81. Mesa, M.; Sierra, L. and Guth, J. L. "Contribution to the Study of the Formation Mechanism of Mesoporous SBA-15 and SBA-16 Type Silica Particles in Aqueous Acid Solutions." *Microporous and Mesoporous Materials* **2008,** 112, (1-3), 338-350.

82. Brinker, C. J.; Lu, Y.; Sellinger, A. and Fan, H. "Evaporation-Induced Self-Assembly: Nanostructures Made Easy." *Advanced Materials* **1999,** 11, (7), 579-585.

83. Yang, H.; Coombs, N.; Dag, Ö.; Sokolov, I. and Ozin, G. A. "Free-Standing Mesoporous Silica Films; Morphogenesis of Channel and Surface Patterns." *Journal of Materials Chemistry* **1997,** 7, (9), 1755-1761.

84. Lu, Y.; Ganguli, R.; Drewien, C. A.; Anderson, M. T.; Brinker, C. J.; Gong, W.; Guo, Y.; Soyez, H.; Dunn, B.; Huang, M. H. and Zink, J. I. "Continuous Formation of Supported Cubic and Hexagonal Mesoporous Films by Sol-Gel Dip-Coating." *Nature* **1997,** 389, (6649), 364-368.

85. Lu, Y.; Fan, H.; Stump, A.; Ward, T. L.; Rieker, T. and Brinker, C. J. "Aerosol-Assisted Self-Assembly of Mesostructured Spherical Nanoparticles." *Nature* **1999,** 398, (6724), 223-226.

86. Melosh, N. A.; Lipic, P.; Bates, F. S.; Wudl, F.; Stucky, G. D.; Fredrickson, G. H. and Chmelka, B. F. "Molecular and Mesoscopic Structures of Transparent Block Copolymer−Silica Monoliths." *Macromolecules* **1999,** 32, (13), 4332-4342.

87. Klotz, M.; Albouy, P.-A.; Ayral, A.; Ménager, C.; Grosso, D.; Van der Lee, A.; Cabuil, V.; Babonneau, F. and Guizard, C. "The True Structure of Hexagonal Mesophase-Templated Silica Films As Revealed by X-ray Scattering: Effects of Thermal Treatments and of Nanoparticle Seeding." *Chemistry of Materials* **2000,** 12, (6), 1721-1728.

88. Soler-Illia, G. J. A. A.; Crepaldi, E. L.; Grosso, D.; Durand, D. and Sanchez, C. "Structural Control in Self-Standing Mesostructured Silica Oriented Membranes and Xerogels." *Chemical Communications* **2002,** (20), 2298-2299.

89. Zhao, D.; Yang, P.; Melosh, N.; Feng, J.; Chmelka, B. F. and Stucky, G. D. "Continuous Mesoporous Silica Films with Highly Ordered Large Pore Structures." *Advanced Materials* **1998,** 10, (16), 1380-1385.

90. Bach, U.; Lupo, D.; Comte, P.; Moser, J. E.; Weissortel, F.; Salbeck, J.; Spreitzer, H. and Gratzel, M. "Solid-State Dye-Sensitized Mesoporous TiO2 Solar Cells with High Photon-to-Electron Conversion Efficiencies." *Nature* **1998,** 395, (6702), 583-585.

91. Brezesinski, T.; Groenewolt, M.; Gibaud, A.; Pinna, N.; Antonietti, M. and Smarsly, B. "Evaporation-Induced Self-Assembly (EISA) at Its Limit: Ultrathin, Crystalline Patterns by Templating of Micellar Monolayers." *Advanced Materials* **2006,** 18, (17), 2260-2263.

92. Grosso, D.; Boissiere, C.; Smarsly, B.; Brezesinski, T.; Pinna, N.; Albouy, P. A.; Amenitsch, H.; Antonietti, M. and Sanchez, C. "Periodically Ordered Nanoscale Islands and Mesoporous Films Composed of Nanocrystalline Multimetallic Oxides." *Nat Mater* **2004,** 3, (11), 787-792.

93. Chu, M.-W.; Szafraniak, I.; Scholz, R.; Harnagea, C.; Hesse, D.; Alexe, M. and Gosele, U. "Impact of Misfit Dislocations on the Polarization Instability of Epitaxial Nanostructured Ferroelectric Perovskites." *Nat Mater* **2004,** 3, (2), 87-90.

94. Chambers, S. A. and Farrow, R. F. C. V. *Mater. Res. Soc. Bull.* **2004,** 28, 729-733.

95. Kamat, P. V. and Meisel, D. "Nanoparticles in Advanced Oxidation Processes." *Current Opinion in Colloid & Interface Science* **2002,** 7, (5-6), 282-287.

96. Yusuf, H.; Kim, W.-G.; Lee, D. H.; Aloshyna, M.; Brolo, A. G. and Moffitt, M. G. "A Hierarchical Self-Assembly Route to Three-Dimensional Polymer−Quantum Dot Photonic Arrays." *Langmuir* **2007,** 23, (10), 5251-5254.

97. Brus, L. "Electronic wave functions in semiconductor clusters: experiment and theory." *The Journal of Physical Chemistry* **1986,** 90, (12), 2555-2560.

98. Peng, X.; Manna, L.; Yang, W.; Wickham, J.; Scher, E.; Kadavanich, A. and Alivisatos, A. P. "Shape Control of CdSe Nanocrystals." *Nature* **2000,** 404, (6773), 59-61.

99. Manna, L.; Scher, E. C. and Alivisatos, A. P. "Synthesis of Soluble and Processable Rod-, Arrow-, Teardrop-, and Tetrapod-Shaped CdSe Nanocrystals." *Journal of the American Chemical Society* **2000,** 122, (51), 12700-12706.

100. Peng, Z. A. and Peng, X. "Mechanisms of the Shape Evolution of CdSe Nanocrystals." *Journal of the American Chemical Society* **2001,** 123, (7), 1389-1395.

101. Arango, A. C.; Johnson, L. R.; Bliznyuk, V. N.; Schlesinger, Z.; Carter, S. A. and Hörhold, H. H. "Efficient Titanium Oxide/Conjugated Polymer Photovoltaics for Solar Energy Conversion." *Advanced Materials* **2000,** 12, (22), 1689-1692.

102. Wang, L.; Liu, Y.; Jiang, X.; Qin, D. and Cao, Y. "Enhancement of Photovoltaic Characteristics Using a Suitable Solvent in Hybrid Polymer/Multiarmed CdS Nanorods Solar Cells." *The Journal of Physical Chemistry C* **2007,** 111, (26), 9538-9542.

103. Hsu, Y.-J.; Lu, S.-Y. and Lin, Y.-F. "Spontaneous Reduction of Metal Ions Initiated by Ethylenediamine-Capped CdS Nanowires: A Sensing Mechanism Revealed." *Chemistry of Materials* **2008,** 20, (9), 2854-2856.

104. Kundu, S. and Liang, H. "Photochemical Synthesis of Electrically Conductive CdS Nanowires on DNA Scaffolds." *Advanced Materials* **2008,** 20, (4), 826-831.

105. Duan, X.; Huang, Y.; Agarwal, R. and Lieber, C. M. "Single-Nanowire Electrically Driven Lasers." *Nature* **2003,** 421, (6920), 241-245.

106. Murai, H.; Abe, T.; Matsuda, J.; Sato, H.; Chiba, S. and Kashiwaba, Y. "Improvement in The Light Emission Characteristics of CdS:Cu/CdS Diodes." *Applied Surface Science* **2005,** 244, (1-4), 351-354.

107. Ma, R.-M.; Dai, L. and Qin, G.-G. "High-Performance Nano-Schottky Diodes and Nano-MESFETs Made on Single CdS Nanobelts." *Nano Letters* **2007,** 7, (4), 868-873.

108. Wang, Y.; Ramanathan, S.; Fan, Q.; Yun, F.; Morkoc, H. and Bandyopadhyay, S. "Electric Field Modulation of Infrared Absorption at Room Temperature in Electrochemically Self Assembled Quantum Dots." *Journal of Nanoscience and Nanotechnology* **2006,** 6, (7), 2077-2080.

109. Marandi, M. and et al. "A Photochemical Method for Controlling the Size of CdS Nanoparticles." *Nanotechnology* **2005,** 16, (2), 334.

110. Hua, T. and Ying-Jie, Z. "Synthesis of CdS Nanocrystals Based on Low-temperature Thermolysis of One Single-Source Organometallic Precursor." *Nanotechnology* **2006,** 17, (3), 845.

111. A.A, L. "Formation of Colloidal GaAs and CdS Quantum Dots by Laser Ablation in Liquid Media." *Applied Surface Science* **2005,** 248, (1-4), 209-212.

112. Hung, A. M.; Konopliv, N. A. and Cha, J. N. "Solvent-Based Assembly of CdSe Nanorods in Solution." *Langmuir* **2011**.

113. Huang, Y.; Sun, F.; Wu, T.; Wu, Q.; Huang, Z.; Su, H. and Zhang, Z. "Photochemical Preparation of CdS Hollow Microspheres at Room Temperature and Their Use in Visible-Light Photocatalysis." *Journal of Solid State Chemistry* **2011,** 184, (3), 644-648.

114. Sathish, M. and Viswanath, R. P. "Photocatalytic Generation of Hydrogen Over Mesoporous CdS Nanoparticle: Effect of Particle Size, Noble Metal and Support." *Catalysis Today* **2007,** 129, (3-4), 421-427.

115. Wang, Q.; Chen, G.; Zhou, C.; Jin, R. and Wang, L. "Sacrificial Template Method for The Synthesis of CdS Nanosponges and Their Photocatalytic Properties." *Journal of Alloys and Compounds* **2010,** 503, (2), 485-489.

116. Miao, J.-J.; Ren, T.; Dong, L.; Zhu, J.-J. and Chen, H.-Y. "Double-Template Synthesis of CdS Nanotubes with Strong Electrogenerated Chemiluminescence." *Small* **2005,** 1, (8-9), 802-805.

117. Li, Q. and Penner, R. M. "Photoconductive Cadmium Sulfide Hemicylindrical Shell Nanowire Ensembles." *Nano Letters* **2005,** 5, (9), 1720-1725.

118. Li, Y.; Wang, Z.; Ma, X.-d.; Qian, X.-f.; Yin, J. and Zhu, Z.-K. "Large-Scale CdX (X=S, Se) Microtube Arrays on Glass Substrate: Transformation of CdOHCl Microrod Arrays by a Simple Template-Sacrificing Solution Method." *Journal of Solid State Chemistry* **2004,** 177, (12), 4386-4393.

119. Xu, C.; Ni, Y.; Zhang, Z.; Ge, X. and Ye, Q. "Synthesis and Characterization of Spherical MS (M=Cd, Zn) Nanocrystalline in a Quaternary W/O Microemulsion by γ-ray Irradiation." *Materials Letters* **2003,** 57, (20), 3070-3076.

120. Hu, Y.; Chen, J.; Chen, W. and Ning, J. "Preparation of Hollow CdSe Nanospheres." *Materials Letters* **2004,** 58, (22-23), 2911-2913.

121. Yu, G.; Gao, J.; Hummelen, J. C.; Wudl, F. and Heeger, A. J. "Polymer Photovoltaic Cells: Enhanced Efficiencies via a Network of Internal Donor-Acceptor Heterojunctions." *Science* **1995,** 270, (5243), 1789-1791.

122. Xia, C.; Wang, N. and Kim, X. "Mesoporous CdS Spheres for High-Performance Hybrid Solar Cells." *Electrochimica Acta* **2011,** 56, (25), 9504-9507.

123. Im, S. H.; Lee, Y. H. and Seok, S. I. "Photoelectrochemical Solar Cells Fabricated from Porous CdSe and CdS Layers." *Electrochimica Acta* **2010,** 55, (20), 5665-5669.

124. Arachchige, I. U. and Brock, S. L. "Sol−Gel Assembly of CdSe Nanoparticles to Form Porous Aerogel Networks." *Journal of the American Chemical Society* **2006,** 128, (24), 7964-7971.

125. Motte, L.; Billoudet, F.; Lacaze, E. and Pileni, M.-P. "Self-Organization of Size-Selected, Nanoparticles Into Three-Dimensional Superlattices." *Advanced Materials* **1996,** 8, (12), 1018-1020.

126. Stupp, S. I. and Braun, P. V. "Molecular Manipulation of Microstructures: Biomaterials, Ceramics, and Semiconductors." *Science* **1997,** 277, (5330), 1242-1248.

127. Schüth, F. "Non-siliceous Mesostructured and Mesoporous Materials†." *Chemistry of Materials* **2001,** 13, (10), 3184-3195.

128. Karakaya, C.; Türker, Y.; Albayrak, C. and Dag, Ö. "Assembly of Molten Transition Metal Salt–Surfactant in a Confined Space for the Synthesis of Mesoporous Metal Oxide-Rich Metal Oxide–Silica Thin Films." *Chemistry of Materials* **2011,** 23, (12), 3062-3071.

129. Türker, Y.; Karakaya, C. and Dag, Ö. "Fabrication of Mesoporous Metal Chalcogenide Nanoflake-Silica Thin

Films and Spongy Mesoporous CdS and CdSe " *Chemistry A European J.* **2011,** in press.

130. Gratzel, M. "Photoelectrochemical Cells." *Nature* **2001,** 414, (6861), 338-344.

131. Robel, I.; Subramanian, V.; Kuno, M. and Kamat, P. V. "Quantum Dot Solar Cells. Harvesting Light Energy with CdSe Nanocrystals Molecularly Linked to Mesoscopic TiO_2 Films." *Journal of the American Chemical Society* **2006,** 128, (7), 2385-2393.

132. Kim, J.; Choi, S.; Noh, J.; Yoon, S.; Lee, S.; Noh, T.; Frank, A. J. and Hong, K. "Synthesis of CdSe−TiO_2 Nanocomposites and Their Applications to TiO_2 Sensitized Solar Cells." *Langmuir* **2009,** 25, (9), 5348-5351.

133. Tvrdy, K. and Kamat, P. V. "Substrate Driven Photochemistry of CdSe Quantum Dot Films: Charge Injection and Irreversible Transformations on Oxide Surfaces†." *The Journal of Physical Chemistry A* **2009,** 113, (16), 3765-3772.

134. Yun, H. J.; Lee, H.; Kim, N. D.; Lee, D. M.; Yu, S. and Yi, J. "A Combination of Two Visible-Light Responsive Photocatalysts for Achieving the Z-Scheme in the Solid State." *ACS Nano* **2011,** 5, (5), 4084-4090.

135. Liu, Y.; Zhou, H.; Zhou, B.; Li, J.; Chen, H.; Wang, J.; Bai, J.; Shangguan, W. and Cai, W. "Highly Stable CdS-Modified Short TiO_2 Nanotube Array Electrode for Efficient Visible-Light Hydrogen Generation." *International Journal of Hydrogen Energy* **2011,** 36, (1), 167-174.

136. Antoniadou, M.; Daskalaki, V. M.; Balis, N.; Kondarides, D. I.; Kordulis, C. and Lianos, P. "Photocatalysis and Photoelectrocatalysis Using (CdS-ZnS)/TiO_2 Combined Photocatalysts." *Applied Catalysis B: Environmental* **2011,** 107, (1-2), 188-196.

137. Sudhagar, P.; Jung, J. H.; Park, S.; Lee, Y.-G.; Sathyamoorthy, R.; Kang, Y. S. and Ahn, H. "The Performance of Coupled (CdS:CdSe) Quantum Dot-Sensitized TiO_2 Nanofibrous Solar Cells." *Electrochemistry Communications* **2009,** 11, (11), 2220-2224.

138. O'Regan, B. and Gratzel, M. "A Low-Cost, High-Efficiency Solar Cell Based on Dye-Sensitized Colloidal TiO_2 Films." *Nature* **1991,** 353, (6346), 737-740.

139. Miwa, T.; Kaneco, S.; Katsumata, H.; Suzuki, T.; Ohta, K.; Chand Verma, S. and Sugihara, K. "Photocatalytic Hydrogen Production from Aqueous Methanol Solution with CuO/Al_2O_3/TiO_2 Nanocomposite." *International Journal of Hydrogen Energy* **2010,** 35, (13), 6554-6560.

140. Davis, M. E. "Ordered Porous Materials for Emerging Applications." *Nature* **2002,** 417, (6891), 813-821.

141. Piris, J.; Ferguson, A. J.; Blackburn, J. L.; Norman, A. G.; Rumbles, G.; Selmarten, D. C. and Kopidakis, N. "Efficient Photoinduced Charge Injection from Chemical Bath Deposited CdS into Mesoporous TiO_2 Probed with Time-

Resolved Microwave Conductivity." *The Journal of Physical Chemistry C* **2008,** 112, (20), 7742-7749.

142. Kavan, L.; Rathouský, J.; Grätzel, M.; Shklover, V. and Zukal, A. "Surfactant-Templated TiO_2 (Anatase): Characteristic Features of Lithium Insertion Electrochemistry in Organized Nanostructures." *The Journal of Physical Chemistry B* **2000,** 104, (50), 12012-12020.

143. Bartl, M. H.; Puls, S. P.; Tang, J.; Lichtenegger, H. C. and Stucky, G. D. "Cubic Mesoporous Frameworks with a Mixed Semiconductor Nanocrystalline Wall Structure and Enhanced Sensitivity to Visible Light." *Angewandte Chemie International Edition* **2004,** 43, (23), 3037-3040.

144. Karakaya, C.; Türker, Y. and Dag, Ö. "Molten Assisted Self-Assembly (MASA)-Synthesis of Mesoporous Metal Oxide-Titania, Metal Sulfide-Titania and Metal Selenide-Titania Thin Films." *in preparation* **2011**.

145. Hirai, T.; Okubo, H. and Komasawa, I. "Incorporation of CdS Nanoparticles Formed in Reverse Micelles into Mesoporous Silica." *Journal of Colloid and Interface Science* **2001,** 235, (2), 358-364.

146. Yang, Y.-J.; Tao, X.; Hou, Q. and Chen, J.-F. "Fluorescent Mesoporous Silica Nanotubes Incorporating Cds Quantum Dots for Controlled Release of Ibuprofen." *Acta Biomaterialia* **2009,** 5, (9), 3488-3496.

147. Wang, S.; Choi, D. G. and Yang, S. M. "Incorporation of CdS Nanoparticles Inside Ordered Mesoporous Silica SBA-15 via Ion Exchange." *Advanced Materials* **2002,** 14, (18), 1311-1314.

148. Li, Y.; Zhu, Y.; Yang, X. and Li, C. "Mesoporous Silica Spheres as Microreactors for Performing CdS Nanocrystal Synthesis." *Crystal Growth & Design* **2008,** 8, (12), 4494-4498.

149. Caponetti, E.; Pedone, L.; Saladino, M. L.; Chillura Martino, D. and Nasillo, G. "MCM-41-CdS Nanoparticle Composite Material: Preparation and Characterization." *Microporous and Mesoporous Materials* **2010,** 128, (1-3), 101-107.

150. Chen, S. "Confinement Effects of CdSe Nanocrystals Intercalated into Mesoporous Silica." *Appl. Phys. Lett.* **2010,** 96, (11), 111907.

151. Wang, P.; Zhu, Y.; Yang, X.; Li, C. and Du, H. L. "Synthesis of CdSe Nanoparticles Into The Pores of Mesoporous Silica Microspheres." *Acta Materialia* **2008,** 56, (5), 1144-1150.

152. Shan, Y.; Gao, L. and Zheng, S. "A facile Approach to Load CdSe Nanocrystallites into Mesoporous SBA-15." *Materials Chemistry and Physics* **2004,** 88, (1), 192-196.

153. Parala, H.; Winkler, H.; Kolbe, M.; Wohlfart, A.; Fischer, R. A.; Schmechel, R. and von Seggern, H. "Confinement of CdSe Nanoparticles Inside MCM-41." *Advanced Materials* **2000,** 12, (14), 1050-1055.

154. Alivisatos, A. P. "Perspectives on the Physical Chemistry of Semiconductor Nanocrystals." *The Journal of Physical Chemistry* **1996,** 100, (31), 13226-13239.

155. Hugo, K. C. "Confinement Effects on Freezing and Melting." *Journal of Physics: Condensed Matter* **2001,** 13, (11), R95.

156. Nanda, K. K.; Sahu, S. N. and Behera, S. N. "Liquid-drop Model for the Size-Dependent Melting of Low-Dimensional Systems." *Physical Review A* **2002,** 66, (1), 013208.

157. Frenken, J. W. M. and Veen, J. F. v. d. "Observation of Surface Melting." *Physical Review Letters* **1985,** 54, (2), 134-137.

158. Vargas-Florencia, D.; Petrov, O. and Furó, I. "Inorganic Salt Hydrates as Cryoporometric Probe Materials to Obtain Pore Size Distribution." *The Journal of Physical Chemistry B* **2006,** 110, (9), 3867-3870.

159. Strange, J. H.; Rahman, M. and Smith, E. G. "Characterization of Porous Solids by NMR." *Physical Review Letters* **1993,** 71, (21), 3589-3591.

160. Dapurkar, S. E.; Badamali, S. K. and Selvam, P. "Nanosized Metal Oxides in the Mesopores of MCM-41 and MCM-48 Silicates." *Catalysis Today* **2001,** 68, (1-3), 63-68.

161. Wang, Y. M.; Wu, Z. Y.; Wei, Y. L. and Zhu, J. H. "In situ Coating Metal Oxide on SBA-15 in One-Pot Synthesis." *Microporous and Mesoporous Materials* **2005,** 84, (1-3), 127-136.

162. Tsoncheva, T.; Järn, M.; Paneva, D.; Dimitrov, M. and Mitov, I. "Copper and Chromium Oxide Nanocomposites Supported on SBA-15 Silica as Catalysts for Ethylacetate Combustion: Effect of Mesoporous Structure and Metal Oxide Composition." *Microporous and Mesoporous Materials* **2011,** 137, (1-3), 56-64.

163. Huo, Q.; Margolese, D. I.; Ciesla, U.; Feng, P.; Gier, T. E.; Sieger, P.; Leon, R.; Petroff, P. M.; Schuth, F. and Stucky, G. D. "Generalized Synthesis of Periodic Surfactant/Inorganic Composite Materials." *Nature* **1994,** 368, (6469), 317-321.

164. Soler-Illia, G. J. d. A. A.; Crepaldi, E. L.; Grosso, D. and Sanchez, C. "Block Copolymer-Templated Mesoporous Oxides." *Current Opinion in Colloid & Interface Science* **2003,** 8, (1), 109-126.

165. Velasco, M. J.; Rubio, F.; Rubio, J. and Oteo, J. L. "Hydrolysis of Titanium Tetrabutoxide. Study by FT-IR Spectroscopy." *Spectroscopy Letters* **1999,** 32, (2), 289-304.

166. Okur, H. I. **2009.** The Phase Behaviour and Synthesis of Mesostructured Coupled Semiconductor Thin Films: Meso-CdS-TiO_2. Bilkent University Ankara, Turkey.

167. Tompsett, G. A.; Bowmaker, G. A.; Cooney, R. P.; Metson, J. B.; Rodgers, K. A. and Seakins, J. M. "The Raman Spectrum of Brookite, TiO_2 (Pbca, Z = 8)." *Journal of Raman Spectroscopy* **1995,** 26, (1), 57-62.

168. Naono, H.; Hakuman, M. and Shiono, T. "Analysis of Nitrogen Adsorption Isotherms for a Series of Porous Silicas with Uniform and Cylindrical Pores: A New Method of Calculating Pore Size Distribution of Pore Radius 1–2 nm." *Journal of Colloid and Interface Science* **1997,** 186, (2), 360-368.

169. Silvestre-Albero, A.; Jardim, E. O.; Bruijn, E.; Meynen, V.; Cool, P.; Sepúlveda-Escribano, A.; Silvestre-Albero, J. and Rodríguez-Reinoso, F. "Is There Any Microporosity in Ordered Mesoporous Silicas?" *Langmuir* **2008,** 25, (2), 939-943.

170. Storck, S.; Bretinger, H. and Maier, W. F. "Characterization of Micro- and Mesoporous Solids by Physisorption Methods and Pore-Size Analysis." *Applied Catalysis A: General* **1998,** 174, (1-2), 137-146.

171. Miyazawa, K. and Inagaki, S. "Towards Flexible Inorganic "Mesomaterials": One-Pot Low Temperature Synthesis of Mesostructured Nanocrystalline Titania." *Chemical Communications* **2000,** (21), 2121-2122.

172. Sapra, S. and Sarma, D. D. "Evolution of the Electronic Structure with Size in II-VI Semiconductor Nanocrystals." *Physical Review B* **2004,** 69, (12), 125304.

173. Tanaka, A.; Onari, S. and Arai, T. "Raman Scattering from CdSe Microcrystals Embedded in a Germanate Glass Matrix." *Physical Review B* **1992,** 45, (12), 6587-6592.

174. Akdogan, Y.; Uzum, C.; Dag, O. and Coombs, N. "Synthesis of Solid-Solution of $Cd_{1-x}Zn_xS$ Nanocrystals in the Channels of Mesostructured Silica Films." *Journal of Materials Chemistry* **2006,** 16, (21), 2048-2055.

175. Türker, Y.; Karakaya, C. and Dag, Ö. "Molten Assisted Self-Assembly (MASA)-Synthesis of Mesoporous Metal Oxide-Titania, Metal Sulfide-Titania and Metal Selenide-Titania Thin Films." *in preparation* **2011**.

176. Brus, L. "Electron–Electron and Electron-Hole Interactions in Small Semiconductor Crystallites: The Size Dependence of The Lowest Excited Electronic State." *Journal of Chemical Physics* **1984,** 80, (9), 4403-4409.

177. Karakaya, C. **2012.** Molten Assisted Self Assembly (MASA): Synthesis of Mesoporous silica-ZnO and Mesoporous silica-CdO Thin Films. Bilkent University, Ankara, Turkey.

178. Raman, C. V. "A Change of Wave-length in Light Scattering." *Nature* **1928,** 121, 619.

179. Raman, C. V. and Krishnan, K. S. "A New Type of Secondary Radiation." *Nature* **1928,** 121, 501-502.

180. Dinger, A.; Göppert, M.; Becker, R.; Grün, M.; Petillon, S.; Klingshirn, C.; Liang, J.; Wagner, V. and Geurts, J. "Lattice Dynamics of CdS/ZnSe Strained Layer Superlattices Studied by Raman Scattering." *Physical Review B* **2001,** 64, (24), 245310.

181. Yoffe, A. D. "Semiconductor Quantum Dots and Related Systems: Electronic, Optical, Luminescence and Related Properties of Low Dimensional Systems." *Advances in Physics* **2001,** 50, (1), 1-208.

182. Huang, F.; Zhang, H. and Banfield, J. F. "Two-Stage Crystal-Growth Kinetics Observed during Hydrothermal Coarsening of Nanocrystalline ZnS." *Nano Letters* **2003,** 3, (3), 373-378.

183. Lu, A.-H. and Schüth, F. "Nanocasting Pathways to Create Ordered Mesoporous Solids." *Comptes Rendus Chimie* 8, (3-4), 609-620.